



**FUNCTIONALIZATION OF GRAPHENE THROUGH HYDROTHERMAL TREATMENT TO PRODUCE
HYDROGEL/AEROGEL AND ITS APPLICATIONS**

By

ALVIN LIM TEIK ZHENG

**Thesis Submitted to the Graduate School of Life Science and Systems Engineering, Kyushu
Institute of Technology in Fulfilment of the Requirement for the Degree of Doctor of Philosophy**

SEPTEMBER 2021

DEDICATION

I would like to dedicate this thesis to my family, teachers, and friends for their endless love, support, and encouragement during my troubled times.

This thesis was submitted to the Graduate School of Life Science and Systems Engineering, Kyushu Institute of Technology, and has been accepted as fulfilment of the requirement for the degree of Doctor of Philosophy.

Members of the Supervisory Committee were as follows:

Yoshito Andou, PhD

Associate Professor
Graduate School of Life Science and Systems Engineering
Kyushu Institute of Technology

Teruhisa Ohno, PhD

Professor
Department of Applied Chemistry
School of Engineering
Kyushu Institute of Technology

Toshinari Maeda, PhD

Associate Professor
Graduate School of Life Science and Systems Engineering
Kyushu Institute of Technology

Tamaki Kato, PhD

Associate Professor
Graduate School of Life Science and Systems Engineering
Kyushu Institute of Technology

Supakorn Boonyuen, PhD

Associate Professor
Department of Chemistry
Faculty of Science and Technology
Thammasat University

Declaration by Graduate Student

I hereby confirm that:

- this thesis is my original work;
- quotations, illustrations, and citations have been duly referenced;
- this thesis has not been submitted previously or concurrently for any other degree at any other institutions;
- intellectual-property from the thesis and copyright of thesis are fully-owned by Kyushu Institute of Technology;
- there is no plagiarism or data falsification/fabrication in the thesis, and scholarly integrity is upheld. The thesis has undergone plagiarism detection software.

Signature: _____

Date: 17 September 2021

Name and Student No: ALVIN LIM TEIK ZHENG / 18899042

TABLE OF CONTENTS

	PAGE
DEDICATION	I
APPROVAL	II
DECLARATION	III
ABSTRACT	VI
ACKNOWLEDGEMENT	VIII
LIST OF FIGURES	X
LIST OF TABLE	XIV
LIST OF ABBREVIATION	XVI
CHAPTER	
1 INTRODUCTION AND LITERATURE REVIEW	
1.1 Overview of graphene-based materials	1
1.1.1 Graphene	2
1.1.2 Graphene oxide	2
1.1.3 Reduced graphene oxide	3
1.2 Hydrothermal Preparation of 3D graphene macrostructure	5
1.3 Common remediation method for wastewater	5
1.3.1 Adsorption	5
1.3.2 Photocatalysis	6
1.4 Types of pollutants	7
1.4.1 Synthetic dye	7
1.4.2 Heavy metals ion	8
1.4.3 Emerging contaminants	8
1.5 3D graphene for wastewater remediation	8
1.6 Anti-bacterial disinfection properties of 3D graphene hydrogel	11
1.7 Problem Statement and objectives	13
2 ACCESSING EFFECTS OF ALIPHATIC DICARBOXYLIC ACID TOWARDS THE PHYSICAL AND CHEMICAL CHANGES IN LOW TEMPERATURE HYDROTHERMALLY REDUCED GRAPHENE HYDROGEL	
2.0 Abstract	14
2.1 Introduction	15
2.2 Material and Method	17
2.3 Results and Discussion	18
2.4 Conclusion	32
3 HYDROTHERMALLY REDUCED GRAPHENE HYDROGEL INTERCALATED WITH DIVALENT IONS FOR DYE ADSORPTION STUDIES	
3.0 Abstract	33
3.1 Introduction	34
3.2 Material and Method	36
3.3 Results and Discussion	40
3.4 Conclusion	59
4 DESIGN OF REDUCED GRAPHENE HYDROGEL WITH ALKYLAMINE SURFACE FUNCTIONALIZATION THROUGH IMMERSION/AGITATION METHOD AND ITS ADSORPTION MECHANISM	
4.0 Abstract	60
4.1 Introduction	61
4.2 Material and Method	63
4.3 Results and Discussion	65

4.4	Conclusion	80
5	SYNTHESIS OF SILVER NANOPARTICLES /PORPHYRIN/REDUCED GRAPHENE OXIDE HYDROGEL AS DYE ADSORBENT FOR WASTEWATER TREATMENT	
5.0	Abstract	82
5.1	Introduction	83
5.2	Material and Method	85
5.3	Results and Discussion	87
5.4	Conclusion	104
6	CU₂O/TIO₂ DECORATED ON CELLULOSE NANOFIBER/REDUCED GRAPHENE HYDROGEL FOR ENHANCED PHOTOCATALYTIC ACTIVITY AND ITS ANTIBACTERIAL APPLICATIONS	
6.0	Abstract	105
6.1	Introduction	106
6.2	Material and Method	108
6.3	Results and Discussion	111
6.4	Conclusion	136
7	CONCLUSIONS AND RECOMMENDATIONS	
7.1	Conclusions	138
7.2	Recommendations for future studies	139
	7.2.1 Pre-synthesis/Characterizations	139
	7.2.2 Adsorption and Photocatalysis	139
	7.2.3 Antibacterial applications	140
	REFERENCES	141
	APPENDICES	161
	LIST OF ACHIEVEMENTS	177
	BIOGRAPHY	180

This Abstract is submitted to the Graduate School of Life Science and Systems Engineering, Kyushu Institute of Technology in Fulfilment of the Requirement for the Degree of Doctor of Philosophy

by

ALVIN LIM TEIK ZHENG

FUNCTIONALIZATION OF GRAPHENE THROUGH HYDROTHERMAL TREATMENT TO PRODUCE HYDROGEL/AEROGEL AND ITS APPLICATIONS

ABSTRACT

The depletion of natural and man-made quality water sources has become rampant today. In this study, functionalized three-dimensional (3D) graphene architecture prepared via the facile hydrothermal treatment has been systematically explored as an ingenious strategy in the mitigation of various pollutants; also extending to the mitigation of bacterial infestation. The morphological, structural, thermal, optical, and textural properties of the hydrothermally modified reduced graphene hydrogels (rGH) were systematically studied. In Chapter One, the synthesis methods with a specific focus on hydrothermally prepared 3D graphene structure are discussed. The fundamentals of adsorption and photocatalysis are also explored. The recent findings on the applications of hybrid 3D graphene-based architectures for the remediation of noxious pollutants are also briefly shared. An effort has also been made to collate recent anti-bacterial disinfections applications using hybrid three-dimensional graphene architectures.

In Chapter Two, the effect of dicarboxylic acid as cross-linkers in hydrothermally prepared reduced graphene hydrogel is briefly explored. It was found that a higher specific surface (SSA) of the hydrogel is obtained for shorter chain length DCAs. The subsequent chapter, Chapter Three deals with the evaluation of the intercalation of alkali earth metal divalent ions in hydrothermally prepared graphene hydrogel on the adsorption capability towards cationic dyes, methylene blue, and rhodamine B. In Chapter Four, the functionalization of various alkylamine chain lengths on the surface of graphene hydrogel was carried out using a simple two-step method involving hydrothermal treatment, followed by immersion/agitation treatment. The evaluation of the adsorption capability of the modified hydrogels towards methylene blue (MB) and bisphenol-A (BPA) was carried out. Chapter Five deals with the preparation of a novel self-assembled reduced graphene hydrogel modified with silver nanoparticles (AgNPs) and various porphyrin

complexes. The AgNPs were successfully decorated on the reduced graphene sheets via electrostatic interactions. On the other hand, the interaction of porphyrin complexes with the Ag/rGH is via esterification and π - π interactions. The adsorption capability of the modified hydrogels towards methylene blue (MB) is further evaluated. Chapter Six covers the preparation and characterization of photocatalyst loaded on three-dimensional graphene hydrogel for photocatalytic degradation of methyl orange. The assessment of their antibacterial activity towards *Escherichia coli* showed a promising result. In Chapter Seven, an attempt has been made to conclude on important findings from each chapter. Besides, some recommendations for future studies were proposed to bring added value to this existing research.

This study may not have covered all aspects of hydrothermally prepared graphene hydrogel in terms of the applications in wastewater remediation, but, hopefully, this dissertation could provide a brief overview of the simple yet easy method of hydrothermal to functionalize the reduced graphene hydrogel. Certainly, this PhD dissertation will be useful to new entrants and experienced researchers intending to employ hydrothermally reduced graphene hydrogel in the future for environmental remediation purposes.

ACKNOWLEDGEMENTS

I am greatly indebted to Associate Professor Dr. Yoshito ANDOU, as my main supervisor for I am only able to complete this study through his continuous supervision and support. I wouldn't have continued my PhD studies in Kyutech without his recommendation for the Ministry of Education, Culture, Sports, Science, and Technology (MEXT) scholarship. His unwavering enthusiasm has kept me always engaged with my research, and his kindness helped me to make my years here enjoyable. I have been extremely lucky to have a supervisor who cared so much about my work, and who has been always attentive to my problems. The knowledge I have gained from him would no doubt be invaluable to me in years to come.

My appreciation also extends to my co-supervisors, Associate Professor Dr. Toshinari MAEDA who had assisted in anti-bacterial studies. I am always motivated by his positive vibes, always reminding me to set the bars high. I am also grateful to Professor Dr. Teruhisa OHNO for his valuable advice and guidance on photocatalysis rendered for the completion of this thesis. I am always impressed with his achievement as an esteemed researcher. Not to forget, Associate Professor Dr. Tamaki KATO for his invaluable advice on peptide synthesis. I am thankful to Associate Professor Dr. Supakorn BOONYUEN for allowing me to carry out my internship exchange program in the Department of Chemistry, Thammasat University, Thailand. The opportunity enabled me to improve my knowledge in metal/metal oxide nanoparticle synthesis using natural products. Not to forget, Associate Professor. Dr. Satoshi IIKUBO and Associate Professor. Dr. Toshiki TSUBOTA for their permission to utilize the XRD and Raman instruments in their laboratory, respectively. I would also like to acknowledge Dr. Mori Yasuki for the analysis of the degraded dye compounds using GC-MS. Part of this thesis is already published; hence my appreciation is also extended to the anonymous reviewers who gave valuable suggestions, comments, and positive feedback before publication.

I must express my profound gratitude to fellow Ando Laboratory research group; former and current members (Dr. Kubra EKSILER, Dr. Safarul MUSTAPHA, Izzudin IBRAHIM, Tessei KAWANO, Yuto KAWATA, Lease JACQUILINE, and Ruozhu WANG). They aided me greatly by showing my errors in the entire duration of my study. Completing this work would have been all more difficult were it not for the support and encouragement provided by other members of the Department of Life Science and Systems

Engineering (Dr. Hisham N. FARRAG, Taku OMURA, Dr. ZHU Jiangyu, Sarah SABIDI, and Dr. Halimatun Saadiyah HAFID). Not to forget, the Malaysian community in Kyutech, always active in organizing various activities, being a stress reliever. I would also like to appreciate the administrative and support staff, especially Mr. Toshi WAKABAYASHI, Ms. Masako HAYASHI, and Ms. Yoko FUJIWARA who enlivened my life in Japan.

To my best buddies; Associate Professor Dr. Moniza WAHEED, Dr. Ahmad Akira Omar FAROUK, Dr. Keeren SUNDARAJOO, Mr. Nazaruddin RAMLI, Muhammad Said HAKIM, and Aiza JAMALUDDIN, a big thank you for the constant reminders on why I decided to pursue my doctoral degree. Not to forget, Tithiphong Sukheeket and Bhusita Svetthaya for their encouragement for me to further continue my studies.

Special mentions go to my mentors: Professor Dr. Arifin ABDU, Mr. Nazri NOH, and Mr. Aris Fadzilah Bin ABDULLAH.

Finally, to keep the best for the last, I would like to acknowledge my father, Dr. LIM KHONG CHIU, my siblings, Dr. ERIC Lim Teik Chung, DR. FELICIA Lim Chun Min, and ANDY Lim Teik Hong for their enduring support and everlasting love. To my mother, NG YOKE OI, for always being there for me, to praise me during my times of glory, and to comfort me during my times of failure. There are no words to describe my appreciation for her and I hope the completion of this study would serve as a symbol of my appreciation.

LIST OF FIGURES

Fig		Page
1.1	Graphene synthesis based on the 'top-down' and 'bottom-up' approaches	1
1.2	Schematic illustration of (a) single photocatalyst and (b) heterojunction catalyst anchored on graphene sheet.	9
1.3	(a) Photographs of colonies formed by <i>E. coli</i> after remediation with cotton, rGH and Ag/rGH (b) Number of bacterial colonies ($\times 10^3$) formation.	12
2.1	Digital images of the as-prepared graphene hydrogels. (a) rGH, (b) rGH-OA, (c) rGH-MA, (d) rGH-SA, (e) rGH-GA and (f) rGH-AA	18
2.2	SEM images of reduced graphene-based hydrogels. (a) rGH, (b) rGH-OA, (c) rGH-MA, (d) rGH-SA, (e) rGH-GA, (f) rGH-AA	20
2.3	(a) FTIR spectrum, (b) TGA thermogram, (c) XRD spectra and (d) N_2 adsorption-desorption isotherm of the as-prepared graphene hydrogel	22
2.4	(a) Wide spectra and (b) C1s split spectra of the reduced graphene hydrogel	27
2.5	Dispersity of the graphene-based hydrogels in various solvents (left) after sonication for 2 h	30
2.6	Cyclic voltammogram of 1 mM potassium ferricyanide, $[(K_3Fe(CN)_6)]$ with a scan rate of 100 mV/s using GCE modified with the graphene-based hydrogels.	31
3.1	SEM images of freeze-dried (a) GO, (b) rGH, (c) rGH-Mg, (d) rGH-Ca. EDS spectrum with elemental distribution for (e) rGH-Mg and (f) rGH-Ca	43
3.2	(a) XRD, (b) FTIR, (c) Raman spectrum (d) TGA thermogram of GO, rGH, rGH-Mg, and rGH-Ca	44
3.3	(a-c) C 1s split spectra of rGH, rGH-Mg, and rGH-Ca. (d) Mg 2p split spectra of rGH-Mg. (e) Ca 2p split spectra of rGH-Ca. (f) wide spectra of GO, rGH, rGH-Mg, and rGH-Ca	48
3.4	(a) N_2 adsorption-desorption isotherm and (b) BJH pore size distribution of the freeze-dried rGH, rGH-Mg, and rGH-Ca	49
3.5	The adsorption capacity of the rGHs using various initial concentration (20, 50 and 100 mg/L) of MB and RhB	52
3.6	Intraparticle diffusion plot of MB and RhB adsorption onto the hydrogels	53
3.7	FTIR of freeze-dried rGHs before and after adsorption with (a) MB and (b) RhB	57
3.8	Regeneration efficiency after adsorption of (a) MB and (b) RhB after 3 cycles.	59
4.1	SEM images of (a) rGH (b) rGH-OA, (c) rGH-DA and (d) rGH-DDA under $\times 1000$ magnification	66
4.2	ATR-FTIR of rGH, rGH-OA, rGH-DA and rGH-DDA	67
4.3	XPS (a)wide spectra, (b) C1s, and (c) N1s split spectra of the hydrogels	68

4.4	(a) Raman spectra, (b) TGA thermograms, (c) XRD spectra and (d) N ₂ adsorption-desorption isotherm of the alkylamine surface-functionalized hydrogel	70
4.5	Cyclic voltammogram of 5 mM potassium ferricyanide (K ₃ Fe(CN) ₆] using graphene modified glassy carbon electrode (GCE) in the potential range of -1.0V to 1.0V at a scan rate of 100 mV/s	75
4.6	Adsorption capacity of MB and BPA using the modified hydrogels	75
4.7	Pseudo-(a,b) first-order and (c,d) second-order kinetic models for the adsorption of (a) BPA and (b) MB	77
4.8	Regeneration percentage after 3 cycles for the hydrogels after the adsorption of (a) BPA and (b) MB	78
5.1	Photo images of the graphene-based hydrogels: (a) rGH, (b) Ag/rGH (c) Ag/TPP/rGH (d) Ag/TOMPP/rGH (e) Ag/TOBPP/rGH	89
5.2	SEM images of images of interior microstructure of reduced graphene hydrogels: (a) rGH, (b) Ag/rGH (c) Ag/TPP/rGH (d) Ag/TOMPP/rGH (e) Ag/TOBPP/rGH	90
5.3	(a) Raman spectra (b) TGA thermogram (c) ATR-FTIR spectra (d) XRD spectra of the modified hydrogels.	91
5.4	XPS (a) wide (b) Ag 3d (c) N 1s and (d) UV-vis spectra of the modified graphene hydrogels	93
5.5	The average hydrodynamic diameter (AHD) of the modified graphene-based hydrogels	96
5.6	N ₂ adsorption-desorption isotherm of the modified hydrogels	97
5.7	(a) Time-dependent study (b) pseudo-first-order (c) pseudo-second-order kinetic studies for the adsorption of MB at 298 K.	101
5.8	(a) Reusability studies (3 cycles) of the hydrogels on the adsorption of MB, (b) Effect of initial MB concentration for adsorption of Ag/TPP/rGH under dark and light condition	102
6.1	Digital image of the freeze-dried hydrogel. (a) rGH, (b) CNF/rGH, (c) Cu ₂ O/ CNF/rGH, (d) TiO ₂ /CNF/rGH. (e) Cu ₂ O/TiO ₂ /CNF/rGH	111
6.2	SEM images of (a) Cu ₂ O, (b) commercial TiO ₂ , (c) rGH, (d) CNF/rGH, (e) Cu ₂ O/ CNF/rGH, (f) TiO ₂ /CNF/rGH. (g) Cu ₂ O/TiO ₂ /CNF/rGH. EDX mapping of Cu ₂ O/TiO ₂ /CNF/rGH for the element (h) Ti and (i) Cu	112
6.3	(a) XRD and (b) Raman spectra of Cu ₂ O, TiO ₂ , CNF/rGH, Cu ₂ O/CNF/rGH, TiO ₂ /CNF/rGH and Cu ₂ O/TiO ₂ /CNF/rGH.	114
6.4	(a) ATR-FTIR and (b) TGA of the freeze-dried hydrogels	117
6.5	(a) UV-DRS absorption spectra and their respective (b) Tauc plots of the hydrogels.	119
6.6	BET calculated from N ₂ adsorption-desorption isotherm and their corresponding DFT-pore size	121

6.7	XPS spectra of the samples (a) wide region, (b-f) C1s split spectra, (g) Ti 2p split spectra and (h) Cu 2p split spectra of the samples	124
6.8	(a) Adsorption capacity of MO as a function of time and their adsorption kinetics plots (dots) and curve fitted (line) by (b) pseudo-first-order kinetic model and (c) pseudo-second-order kinetic model.	125
6.9	(a,b) Deterioration curve (C/C0) for the photodegradation of MO and their first order kinetics using various hydrogel-based photocatalyst. (c,d) Photodegradation of MO using Cu2O/TiO2/rGH under various pH and their kinetics. (e,f) Photodegradation under various initial concentration MO and their kinetics.	128
6.10	(a) The effect of different scavengers on the photodegradation of MO carried at optimum photocatalytic condition. (b) PL emission spectra of the samples	130
6.11	Schematic of the proposed photodegradation of MO using from the generation of ROS	133
6.12	Repeatability test for photodegradation of MO using Cu ₂ O/TiO ₂ /CNF/rGH	135
6.13	Histogram of total viable count, Log CFU/mL for (a) cells only (b) rGH, (c) CNF/rGH. (d) Cu ₂ O/CNF/rGH, (e) TiO ₂ /CNF/rGH and (f) Cu ₂ O/TiO ₂ /CNF/rGH. Inset: spotting test of E. coli colonies on LB agar under 10-fold cell dilutions.	136
S2.1	(a) FTIR spectrum and (b) XRD spectra of GO	161
S3.1	The absorption spectrum and linear concentration curve of (a) RhB and (b) MB under a varying concentration	162
S3.2	UV-vis spectrum of GO suspension in the presence of MgCl ₂ and CaCl ₂	163
S3.3	Digital image of freeze-dried (a) rGH, (b) rGH-Mg and (c) rGH-Ca	163
S3.4	Pseudo first order (a,b), Pseudo-second order (c,d) and Elovich kinetic model (e,f) of MB and RhB adsorption on the hydrogels	164
S3.5	Digital image of the dye solution before (a) and after for (b) rGH, (c) rGH-Mg and (d) rGH-Ca in the simultaneous adsorption of MB and RhB	165
S4.1	UV-vis spectra of varying concentration of (a) BPA and (b) MB. <i>Inset</i> . Calibration curve of absorbance against concentration	165
S4.2	UV-Vis spectrum of GO	166
S4.3	Digital image of the freeze-dried hydrogel. (a) rGH, (b) rGH-OA, (c) rGH-DA and (d) rGH-DDA	166
S4.4	Pore size distribution of the freeze-dried hydrogels	167
S4.5	FTIR spectrum of the hydrogel after the adsorption of (a) BPA and (b) MB	169
S5.1	General scheme for the synthesis of the porphyrin complexes.	169
S5.2	Structure of (a) TPP (b) TOMPP and (c) TOBPP	170
S5.3	FT-IR spectrum of TPP, TOMPP and TOBPP	170
S5.4	The UV-Vis absorption spectra of TPP, TOMPP and TOBPP in CH ₂ Cl ₂	171

S5.5	Plot of Size distribution in scattering intensity as measured by DLS: (a) rGH, (b) Ag/rGH, (c) Ag/TPP/rGH, (d) Ag/TOMPP/rGH and (e) Ag/TOBPP/rGH	172
S5.6	UV -Vis spectrum of methylene blue at concentration range from 0.01 mg/L to 20 mg/L at room temperature. <i>Inset</i> : Standard curve for the adsorption of MB onto hydrogels	173
S6.1	EDX analysis of the as-prepared Cu ₂ O nanospheres	174
S6.2	(a) UV-DRS absorption spectra and (b) Tauc plots of the TiO ₂ and Cu ₂ O spheres	175
S6.3	FTIR spectrum of the Cu ₂ O/TiO ₂ /CNF/rGH before and after the photocatalytic degradation of MO	175
S5.4	MS spectrum of MO solution using GC-MS after 2 h of irradiation.	176

LIST OF TABLES

Table	Page
1.1 Overview of the structures and main properties of GBM	4
1.2 Recently reported 3D hybrid graphene for the remediation of various pollutants	10
2.1 Water content and density of the reduced graphene-based hydrogel	19
2.2 XRD parameters of the hydrogels	24
2.3 BET Surface area and BJH pore size/volume of the reduced graphene hydrogels	25
2.4 Curve fitting results obtained from the XPS split spectra of C 1s	28
3.1 Properties of the GO colloidal suspension in the presence of MgCl ₂ and CaCl ₂ .	41
3.2 Elemental composition of GO, rGH, rGH-Mg, and rGH-Ca obtained from EDX analysis	42
3.3 Elemental composition, and C 1s binding energy obtained from XPS	47
3.4 BET surface area and textural properties of freeze-dried hydrogels.	51
3.5 Kinetic parameters obtained from the PSO, PSO, and Elovich kinetic model for the adsorption of MB and RhB	53
3.6 Langmuir, Freundlich, and Temkin equilibrium isotherm constant for the adsorption of MB and RhB	55
3.7 Adsorption capacities of MB and RhB onto various hydrogel-based adsorbents	56
4.1 Properties of the GO colloidal suspension	66
4.2 Structural parameters obtained from the XRD spectra	72
4.3 Molecular distance of the alkylamine obtained from computational methods	73
4.4 Adsorption capacities of MB and BPA onto variously reported adsorbents	80
5.1 Diameter and water content of the modified graphene hydrogel	88
5.2 BET surface area, BJH pore size and volume of the freeze-dried graphene-based hydrogels based on the desorption process	98
5.3 Adsorption capacity of various hydrogels towards MB.	103
6.1 The crystallite size and lattice strain for the samples	115
6.2 Atomic percentage derived from the deconvolution of the C1s split spectra.	122
6.3 Kinetic parameters obtained from the PFO and PSO kinetic model for the adsorption of MO	126
6.4 Comparison with recently reported photocatalyst for the degradation of MO	134
S3.1 The parameters of the intraparticle diffusion model by the hydrogel	164
S4.1 Specific surface area and texture properties of the reduced graphene samples obtained using BET and BJH analysis, respectively	166

S4.2	Chemical bonding and atomic percentage obtained from the high-resolution C1s spectra of the hydrogels	167
S4.3	Fitted kinetic parameters for the BPA adsorption onto the hydrogels	168
S4.4	Fitted kinetic parameters for the MB adsorption onto the hydrogels	168
S5.1	FT-IR data of free-base porphyrin complexes.	171
S5.2	The absorption data molar extinction coefficient (ϵ) of all compounds	171
S5.3	Kinetic Parameters for the adsorption of MB at 298 K	173

LIST OF ABBREVIATIONS

AA	Adipic acid
BPA	Bisphenol A
CNF	Cellulose nanofiber
CB	Conduction band
Gr	Graphene
GA	Graphene aerogel
GBM	Graphene-based material
GA	Glutaric acid
GO	Graphene oxide
IPD	Intraparticle diffusion
MA	Malonic acid
MB	Methylene blue
MO	Methyl orange
NP	Nanoparticle
OA	Oxalic acid
rGO	Reduced graphene oxide
rGH	Reduced graphene hydrogel
SA	Succinic acid
ROS	Reactive oxygen species
RhB	Rhodamine B
PFO	Pseudo-first order
PSO	Pseudo-second order
VB	Valence band
3D	Three dimensional

CHAPTER 1

INTRODUCTION AND LITERATURE REVIEW

1.1 Overview of Graphene-based materials

Since the successful isolation of graphene from graphite by Andre Geim and Kostya Novoselov using the mechanical cleavage technique by applying the scotch tape method, ample synthesis techniques have then been reported for the synthesis of graphene-based materials (GBMs) [1]. In short, the synthesis technique can be divided into a top-down or bottom-up approach which is depicted in Fig. 1.1. The production of desired GBMs for their specific applications can be manipulated during the pre-synthesis or post-synthesis step which makes this material interesting to be explored. The term ‘graphene’ has been loosely used in many studies without taking into consideration the number of layers present. Therefore, terms such as ‘graphene flakes’ or ‘graphene sheets’ are often used to address them as graphene. A substantial number of review articles which collated the most recent GBMs synthesis method for their specific applications have been reported. To obtain a comprehensive understanding of the synthesis route of single-layer and multi-layer graphene, we would like to direct the reader to the review by Lee et al. (2017) and Smith et al. [3]. Table 1.1 summarized the overview of GBMs in terms of their chemical structure and main properties.

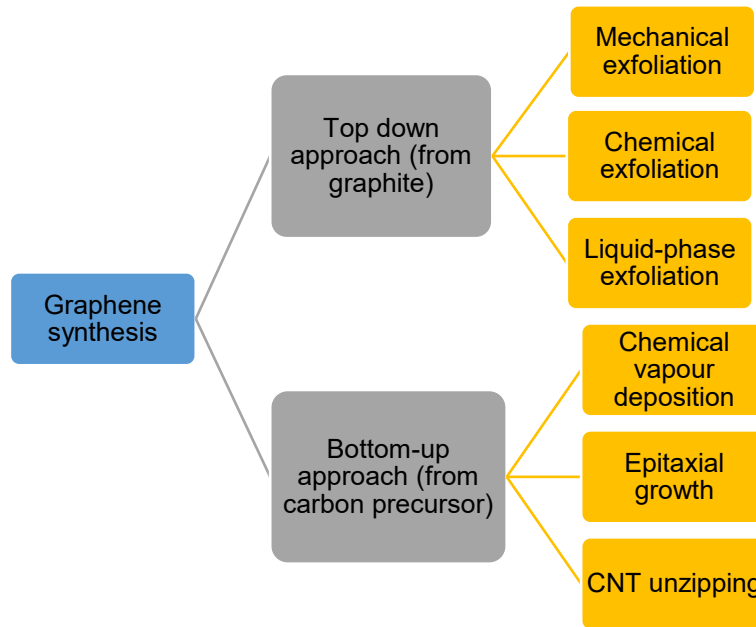


Fig. 1.1 Graphene synthesis based on the ‘top-down’ and ‘bottom-up’ approaches

1.1.1 Graphene (Gr)

Graphene or 'pristine graphene' can be defined as a single layer hexagonally sp^2 hybridized carbon allotrope that exists in a honeycomb crystal lattice [1,4,5]. Graphene is the basic building block of carbon allotropes such as fullerene (0D), carbon nanotubes (1D), and graphite (3D). The preparation of single-layer graphene can be realized via mechanical exfoliation, chemical vapour deposition, and epitaxial growth on silicon carbide (SiC). Often, the process to obtain large scale, single-layer graphene is an arduous task which requires complicated equipment and various post-treatment synthesis. Up to now, the race to produce a high-quality single-layer graphene layer in mass quantity is still ongoing. Chemical vapour deposition (CVD) is still regarded as the most effective strategy to prepare high-quality pristine graphene with the largest production rate [6]. Besides, graphene also can be obtained via ultrasonic treatment in ionic liquids (IL) and surfactants. The setback behind the ultrasonic treatment often leads to the reduced surface area which is not desirable in some applications. Chen et al. [7] succeeded in the exfoliation of graphite to obtain low-defect and stable pristine graphene in urea/glycerol dispersion under mechanical stirring without sonication. In another study, the use of organic salt-assisted exfoliation method in ethanol has been reported for the preparation of high-quality pristine graphene dispersion [8]. Recently, the ultrafast synthesis of pristine graphene can also be achieved at room temperature inside a transmission electron microscope using a gold catalyst [9].

1.1.2 Graphene oxide (GO)

GO is a single-layer hydrophilic derivative of graphene often produced by the exfoliation of graphite. To date, there is no accurate description of GO structure but the consensus is that GO is composed of a collection of six-membered rings connected to the majority of oxygenated groups. Among them, hydroxyl and epoxide constitute the majority, with carboxylic, carbonyl, and phenolic groups present in smaller quantities at the edges of the plane [10]. GO is not a recently found material as it has been known in existence since the 1840s. The presence of aromatic (sp^2) and aliphatic (sp^3) components have predominantly made GO be the starting point for the large-scale preparation of most GBMs. Unlike pristine graphene, GO provides a wide range of chemical interactions for various functionalities to improve its inherent properties. GO is often characterized by a low C/O ratio of less than 3:1 and typically closer to 2:1. Interestingly, GO is reported to have limited electrical and thermal transport due to the oxygen

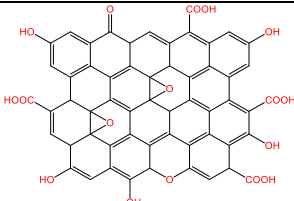
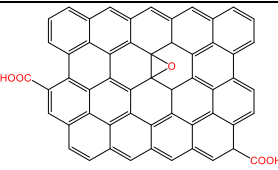
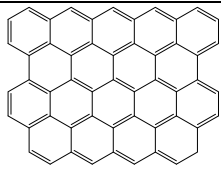
functionalization on the basal plane surface. The interesting properties of GO can be tuned leading to a plethora of applications including water purification, multifunctional gels, and membrane technology in wastewater treatment. GO nanosheets are about 1 nm in thickness with the diameter varying from a few nanometres to hundreds of microns. The desired properties for their specific application are highly dependent on the dimension as well as its size distribution. The Hummers' method was first introduced as a strategy in the preparation of graphitic oxide by the reaction of graphite with KMnO_4 , NaNO_3 , and H_2SO_4 [11]. The method produced explosive exothermic reactions and generate toxic gases such as NO_2 and N_2O_2 which are harmful to the environment. The preparation of GO via elimination of NaNO_3 in the starting mixture has shown to also produce GO with similar chemical structure, thickness, and lateral dimension [12]. There onwards various modified version has been proposed to mitigate the setbacks by altering the mixing ratio of the reactants under various conditions [13–16]. On a positive note, the successful commercialization of GO powder/suspension has reduced the need for researchers to synthesis GO.

1.1.3 Reduced graphene oxide (rGO)

From its name, rGO is the reduced form of GO that retains the salient properties of pristine graphene which possesses good thermal stability, high mechanical strength, and highly conductive. rGO consists of a graphene-like basal plane with structural defect and populated with a smaller number of oxygen-containing functional groups as compared to GO. rGO is often prepared from GO as the fabrication protocol can be scaled up to mass-produce the product. From previous studies, the reduction of GO could be achieved from a plethora of techniques such as thermal, chemical, electrochemical, microwave, photo-assisted, and/or microbial, in which each of them led to significant differences in the properties of the end product. The thermal reduction has been known to produce rGO sheets that closely resemble the properties of graphene [17]. Different protocols have their advantages and disadvantages in terms of their cost incurred, scalability, chemical waste, and energy usage. Nowadays, a few important aspects are considered in the reduction of GO which takes into account the aspect of environmentally friendly, low cost, shorter reaction time, etc. The paramount factor to determine a successful reduction to high-quality rGO can be evaluated by accessing the C/O ratio, surface defects, and improvement in their mechanical strength, conductivity, and optical property as compared to GO. Also, the preparation of three-dimensional rGO in the form of hydrogel, aerogel, films, foam, monolith, and bead has seen its vast usage in various applications especially in

electric/electronics, catalysis, and adsorbents. Among all synthesis methods, hydrothermal treatment has gained ample attraction for its' feasibility in the preparation of three-dimensional (3D) structures while retaining some form of functional groups on the graphene sheet [18–20].

Table 1.1 Overview of the structures and main properties of GBMs [21–29]

	GO	rGO	Gr
Chemical structure			
Synthesis route	Oxidation of graphite	Reduction of GO	CVD, mechanical exfoliation, epitaxial growth
C/O ratio	2.1 – 2.9	6.0 – 13.5	-
Young's modulus (GPa)	380 – 470	600	1000
Electron mobility (cm² V⁻¹ s⁻¹)	insulator	up to 320	10000 – 50000
Conductivity (S m⁻¹)	0.00029	up to 6300	10 ⁴ – 10 ⁵
Thermal conductivity (W m⁻¹ k⁻¹)	72	30 – 2600	1500 – 5800

1.2 Hydrothermal preparation for three-dimensional graphene architecture

In this dissertation, the author will focus on the green synthesis pathways using the hydrothermal method. GO is a single-layer hydrophilic derivative of graphene often produced by exfoliation of graphite containing oxygen-containing functional groups such as carbonyl, hydroxyl, epoxide, and phenolic present at the basal and edges. The presence of aromatic (sp^2) and aliphatic (sp^3) components have predominantly made GO be the starting point for the preparation of 3D macrostructure. For the synthesis of different rGO based materials, this method is usually associated with the 'one-step' synthesis. This protocol is typically performed in a closed environment with an inner vessel made of Teflon to provide high corrosion resistance at temperatures above 100°C under high pressure, and the outer container is made of stainless steel to withstand high pressure and corrosion. The superheated water acts as the reducing agent with high diffusion and dielectric constant which severe the oxygenated functional groups on the GO [30]. Through this technique, GO alone can be partially reduced, but to further improve the degree of reduction, chemical reductants are usually added. The ability to control the reaction process by adjusting the temperature, time of reaction, medium of reaction, pH, and medium concentration allows the production of different rGO morphologies. Attributed to the strong hydrophobic and π - π interactions between the graphene sheets, direct self-assembly of dispersed GO sheets is possible without the use of any crosslinking agents [31,32]. Xu and co-workers, among the pioneers in the synthesis of 3D graphene, studied the formation of hydrothermally prepared 3D rGH by using various GO concentrations at 180°C [33]. The freeze-drying technique is often applied to retain the structure of the hydrogel obtained; in which the dried form is often denoted as 'aerogel'. Other drying techniques such as oven drying and vacuum drying often led to the collapse of the hydrogel structure due to the π - π stacking between the graphene sheets.

1.3 Common remediation method for wastewater

1.3.1 Adsorption

In essence, adsorption is a mass transfer process that is attributed to the transfer of a molecule from a liquid/gas interface to a solid surface due to physical/chemical bonding. Adsorption process is often employed for the remediation of hazardous pollutants due to their high efficiency, cost-efficiency, and easy operation route [34]. To date, the search for low-cost, durable, and high-performance adsorbent has

intensified. The adsorption can occur via the physisorption or chemisorption process. On some occasions, the two processes may occur simultaneously, independent of one another [35]. Various factors are involved in the determination of adsorption capability that includes specific surface area and the textural properties (pore size and pore volume) of the adsorbent. Besides, the functionalities present on the adsorbent are another factor to access the improved adsorption capability. Often in adsorption studies, determining parameters such as temperature, pH, initial concentration of adsorbate, amount of adsorbent, contact time, and stirring speed are studied to obtain a comprehensive view of the adsorbent capability of the particular adsorbent. To explore the feasibility and efficiency of the adsorbent often requires three fundamental study aspects: kinetic, isothermal, and thermodynamic studies. Understanding the adsorption kinetics using various kinetic models such as quasi-first order kinetic model (PFO), quasi-second order kinetic model (PSO), intraparticle diffusion model (IPD), etc are important in determining the adsorption rate and adsorption mechanism. On the other hand, analysis of isotherm data is vital to describe the equilibrium relationship between adsorbent-adsorbate [36]. The qualitative assessment of the adsorption data can be portrayed as a curve of the adsorbed amount on the surface as a function of the concentration or partial pressure of the adsorbate at a constant temperature. Various adsorption isotherm models have been utilized in adsorption studies such as Langmuir, Freundlich, Langmuir-Freundlich, Brunauer-Emmett-Teller, Dublin-Radushkevich, Temkin, Sips etc. Similarly, thermodynamic studies predict the adsorption whether the adsorption is spontaneous by providing information regarding energy changes using the Gibbs free energy equation.

1.3.2 Photocatalysis

Photocatalysis is one of the advanced oxidation processes (AOP) that changes the rate of chemical transformation under the presence of a catalyst that absorbed light to initiate the reaction. To address current energy demand, the development of photocatalysis technologies for environmental remediation has been rampant since the past decade. This eco-friendly technology harnesses solar energy for the degradation of various pollutants in water bodies. On this note, a large number of studies on the photocatalytic degradation by various pollutants have been previously reported for the efficient decomposition/mineralization of phenolic compounds [37–39]. The selection into an efficient photocatalytic system is usually based on the band-energy gap and charge carrier mobility where in essence the

development of an efficient photodegradation catalyst can utilize a wide range of visible light. In this notion, ample studies have utilized wide-bandgap photocatalyst ($E_g > 3\text{eV}$) and visible-light-responsive photocatalysts ($E_g \leq 3\text{eV}$) in the hybrid GBMs system. The fundamental process of photocatalysis is based on the formation of superoxide radicals and hydroxyl radicals from the photocatalyst which was produced from the electron-hole pairs. Besides, electrons and holes may also produce other active species which improves the degradation activity. To name a few, photocatalysts including metal oxides (TiO_2 , Ag_2O , ZnO), metal halides and oxyhalides (AgBr), multi-component oxides, (SrTiO_3 , BiVO_4 , Bi_2WO_6), metal phosphate (Ag_3PO_4), and metal-free materials ($\text{g-C}_3\text{N}_4$, Si) have been explored as a feasible solution. To apply them alone in wastewater treatment which is usually the case, the setbacks may include fast recombination of photogenerated electrons and holes, agglomeration, and regeneration which hinders the photocatalysis process due to the reduction of reactive species generation used for the degradation process. The shift in usage to second/third generation photocatalyst by applying a multi-component photocatalytic system has shown significant improvement in degradation of phenolic compounds by suppressing charge carrier recombination and assist in post-separation problems [40]. Similar to adsorption, the performance of photocatalyst for the degradation also depends on parameters such as pH, light intensity, presence of interfering compounds, and amount of catalyst. The review on photodegradation of BPA in aqueous media using various photocatalysts has been recently reported by Reddy et al. [41].

1.4 Types of pollutants

1.4.1 Synthetic dye molecules

Synthetic dyes are often used in the textile, food, plastic, paper, printing, pharmaceutical, and cosmetic industries. Common water pollutants and harmful to aquatic animals and plants are dyes that have good solubility in water [42]. Studies on the adsorption of cationic or anionic dye molecules such as methylene blue (MB), rhodamine B (RhB), crystal violet (CV), congo red (CR), acid red (AR), malachite green (MG), methyl orange (MO), sunset yellow (SY), basic blue (BB), etc. are extensive. The chemical structure of the dye molecules determines the various colours of the dyes. Cationic dyes contain functional groups that dissociate in an aqueous solution into positively charged ions in which the onium group is the common group. On the other hand, anionic dyes contain negatively charged functional groups such as carboxylic and sulfonic groups. Often, the interaction of the dye molecules with the GBMs occurred via π - π

interactions, electrostatic interaction, and/or hydrophobic interaction. Improvements in the adsorption capacity are often associated with the adsorbents' functionality, surface area, and textural properties.

1.4.2 Heavy metal

Due to the detrimental effect on human health and the marine ecosystems, heavy metal pollution on water bodies from factory discharges (e.g. automotive, painting, mining, etc.) and agricultural run-offs is an environmental concern. The accumulation of heavy metal may occur in the soft tissue of the human body through food, water, or adsorption through our skin. To date, GBMs have been successfully used to adsorb various heavy metal ions such as chromium, mercury, cobalt, arsenic, cadmium, zinc, lead, etc. Given the serious damage caused by their toxic nature, immediate action is needed to rectify this situation. To date, in the field of heavy metal remediation, 3D GBMs have attracted great interest.

1.4.3 Emerging contaminants

The term "emerging pollutants" is used to describe any synthetic or naturally occurring chemical or microorganism with unknown or suspected ecological and human health effects. Many of them are used and released into the environment continuously, even in trace amounts, and some may cause chronic toxicity, endocrine disruption in humans and aquatic wildlife, and the development of bacterial pathogen resistance. The usage of GBMs for the remediation of organic pollutants such as phenolic compounds, polycyclic aromatic hydrocarbon, aromatic amine pesticides, antibiotics, etc from various sources have surged in recent years. Besides the discussed pollutants in the previous section, emerging pollutants are usually toxic and remain stable in the ecosystem which requires complex removal methods.

1.5 3D graphene for wastewater remediation

To date, ample studies have reported on the usage of hybrid 3D graphene for the adsorption and photocatalysis of various pollutants. The altering of the specific surface area and textural properties by introducing modifiers has become a leading strategy to improve the adsorption performance. Besides, the addition of modifiers provides multiple sites of interactions and functionalities on the graphene surface which is desirable for the improvement in their performance. In terms of photocatalysis, the unique properties of the 3D macrostructure allow for the anchoring of various photocatalysts to address the limitation brought by powder-based photocatalysts. Fig. 1.2 summarized the typical photocatalytic process

on a single photocatalyst and heterojunction catalyst. In essence, the adsorption and photocatalysis process may contribute synergistically to the remediation of the pollutants. Often, the poor reusability and regeneration of conventional photocatalysts are not attractive in real-time applications. Specifically, the combination of TiO_2 with other p or n-semiconductor materials with narrow bandgap such as CdS, CuO, Co_3O_4 , CuS, and MoS_2 has been previously explored as a feasible strategy to improve photocatalytic activity. The fabrication of TiO_2 /GBMs hybrid system using a narrow-band gap semiconductor with band potentials matching TiO_2 allows photogenerated carriers from the narrow bandgap semiconductor to be transferred to TiO_2 via the heterojunction interface.

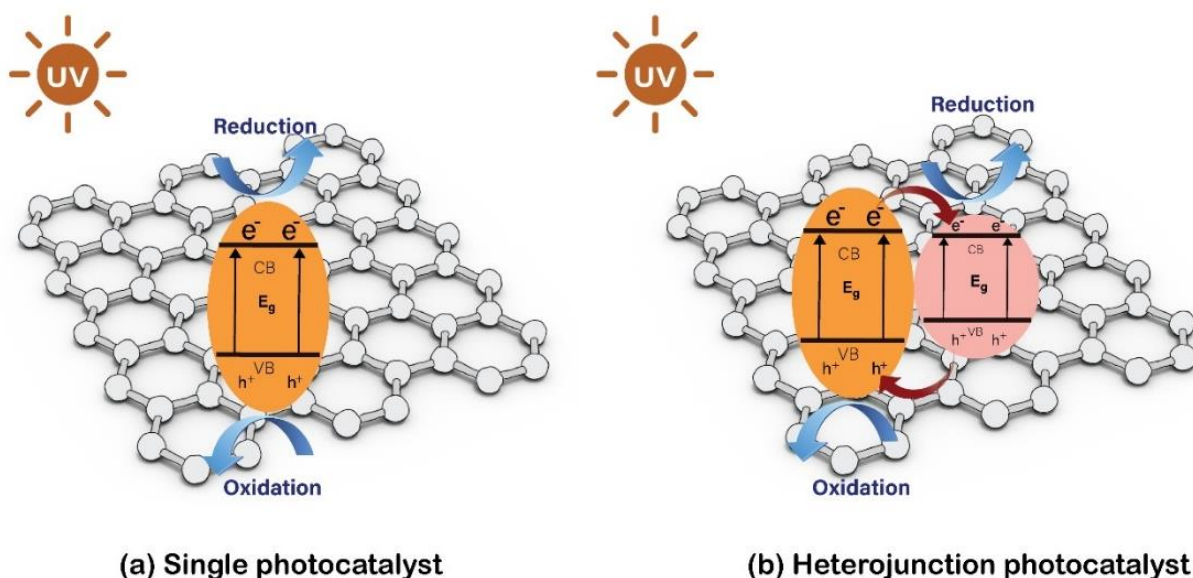


Fig. 1.2. Schematic illustration of (a) single photocatalyst and (b) heterojunction catalyst anchored on a graphene sheet.

The photogenerated electron-hole moves to the surface and interacts with the hydroxyl groups and oxygen where adsorption creates free radicals at the surface of the semiconductor. The synergistic effect of the semiconducting materials with the TiO_2 /GBMs has shown excellent performance in the remediation of various dye molecules. Table 1.2 summarized some of the recently reported usages of hybrid 3D graphene for the remediation of various pollutants. There are still other avenues in improving the salient properties of 3D graphene, but this dissertation will focus on the usage of Cu_2O , cuprous oxide the material of interest.

Table 1.2. Recently reported 3D hybrid graphene for the remediation of various pollutants

No	Photocatalyst	Pollutant	Mode of remediation	Removal efficiency (%)	Ref.
1	Fe ₃ O ₄ @SnO ₂ /Ag-Gr	2,4 dichlorophenol	Adsorption and photocatalysis	78.00	[43]
2	Fe-g-C ₃ N ₄ /rGH	phenol and coking wastewater	Photocatalysis and Fenton	86.90	[44]
3	Ag ₃ PO ₄ /rGH	BPA	Adsorption and photocatalysis	90.00	[45]
4	TiO ₂ /GA	tetracycline, methylene blue and rhodamine B	Adsorption and photocatalysis	43.20, 77.80, and 91.90	[46]
5	BiPO ₄ /GA	phenol, BPA and formaldehyde	Adsorption and photocatalysis	50.67, 96.23, and 26.40	[47]
6	C ₃ N ₄ -MoS ₂ /Gr	ampicillin	PEC	74.60	[48]
7	Bi ₇ O ₉ I ₃ /N-Gr	RhB	Photocatalysis	96.30	[49]
8	rGO/ZnO/Ag	MB	Photocatalysis	99.99	[50]

There is no 'one size fits all' mechanism to characterize the photocatalytic degradation of pollutants as the process often takes a few steps to complete the reaction to form the final product which is often CO₂ and H₂O. The pathways mainly depended on the photocatalyst used for the photodegradation process. The fundamental process of photodegradation is regulated by the electrons in the VB and holes in the CB which are formed from light exposure.

Zhang et al.,[20], applied the hydrothermal method to prepare the Z-scheme 3D g-C₃N₄-ZnO@GA heterojunctions for the adsorption and photocatalysis of various dye molecules under visible light irradiation. In the preparation of their 3D hybrid material, they first synthesized the g-C₃N₄ using heat decomposition from melamine. The ZnO was prepared using Zn(NO₃)₂ as the precursor. Both the photoactive materials were then added into the GO suspension, sonicated and subjected to hydrothermal treatment at 180°C for 24 h. The reduction of GO using ascorbic acid (AA) was first reported by Zhang et al.,[21]. Since then, many studies have reported on a 3D graphene formation using AA as the green reducing agent. Often AA is mixed into the GO suspension and mildly heated without agitation to drive the self-assembly to a graphene-monolith structure. This one-pot method allows for the preparation of various hybrid 3D graphene structure by merely mixing the photocatalytic materials in the GO suspension. Li et al., [22] prepared a TiO₂/rGH using commercially obtained Degussa TiO₂ (P25) as the photoactive material. In their synthetic protocol,

they added an equal volume of PEG 200 and TiO_2 into GO, and subject them to ultrasonication. Following that, they used sodium ascorbate as the self-assembly agent by heating the suspension at 95°C for 60 min to obtain the 3D hybrid material. Recently, the in-situ growth method was reported by Ma et al., [23] to prepare a hybrid 3D BiVO_4/rGH for the photodegradation of tetracycline (TC). The one-step method was initiated by adding $\text{Bi}(\text{NO}_3)_3 \cdot 5\text{H}_2\text{O}$ and various mass fraction of rGH in distilled water, followed by sonication and stirring. Then, NH_4VO_4 and $\text{CO}(\text{NH}_2)_2$ were added respectively and stirred. The suspension was heated at 80°C for 24 h to obtain the 3D photocatalytic material. They posited that the directional migration of BiVO_4 and rGH substantially inhibits photogenerated carriers from recombination, thus increasing the separation efficiency.

1.6 Anti-bacterial disinfection properties of 3D graphene architecture

Hybrid 3D graphene macrostructure has also been reported to be effective anti-bacterial agents. Membrane stress, oxidative stress, and/or wrapping isolation produced the mechanism behind their effective anti-bacterial activity [51]. The general mechanism of the anti-bacterial process involves the degradation of Coenzyme A by the photocatalytic reaction generated by reactive oxygen species (ROS), leading to denaturation of the enzyme that inhibited respiratory activity, causing cell death. Cell death is caused by the disruption of the membrane of the cell wall, which leads to potassium ion leakage and subsequent flow of cellular components such as ribonucleic acid (RNA) and protein. Anti-bacterial activity against gram-positive and gram-negative species of bacteria such as *Escherichia coli*, *Staphylococcus aureus*, *Pseudomonas aeruginosa*, *Streptococcus faecalis*, and *Candida albicans*, etc. are often used as model bacteria to access the antibacterial activity of a certain material. Previous studies have shown that GO possessed greater antibacterial activity as compared to rGO due to their morphological features of having sharp-like edges. In anti-bacterial studies, the aggregation of the GBMs is usually a challenge due to strong inter-planar interactions limiting their surface area and mode of action. Therefore, to enhance anti-bacterial activity, different functionalization and surface modification of GBMs using metal nanoparticles, metal oxides, polymers, antibiotics, etc. have been carried out.

The use of stabilized anti-bacterial metal nanoparticles such as silver (Ag) on GBMs has been extensively investigated. AgNP has been identified as causing direct damage to the bacterial cell membrane. Previous studies have shown that Ag ions bind to the thiol groups in enzymes, and disrupt the bacteria's respiratory

chain leading to cell death. Also, through photocatalytic activation, AgNP can generate ROS to fight against bacteria. The drawbacks of AgNPs, however, include agglomerations, ease to oxidize, recovery complexity, and cytotoxicity. In enhancing the efficiency of bacterial inactivation, hybridization between the AgNPs and GBMs is a possible strategy. The inclusion of graphene-based material in the hybrid system allows the size and morphology of the AgNPs to be systematically controlled and the surface area significantly enhanced, thus facilitating interaction with the bacteria. Besides, the strong interaction of the AgNP and GBMs with electrostatic interaction allows for the easy recovery of nanoparticles that can leech into the environment, causing secondary pollution that is not desirable. As proof of concept, we prepared Ag/rGH to access its anti-bacterial activity towards *Escherichia coli* via the hydrothermal and freeze-dried method. Improvements in the inactivation of bacteria from rGH and AgNP/rGH can be seen from the bacterial plate count in Fig. 1.3(a-b) compared to the cotton sample only (control). The bacterial disinfection results show that almost 100% of *E. coli* inactivation was achieved by AgNP/rGH. The results showed that 3D-based Ag/rGH in wastewater treatment could be a potential remedy for the process of bacterial inactivation.

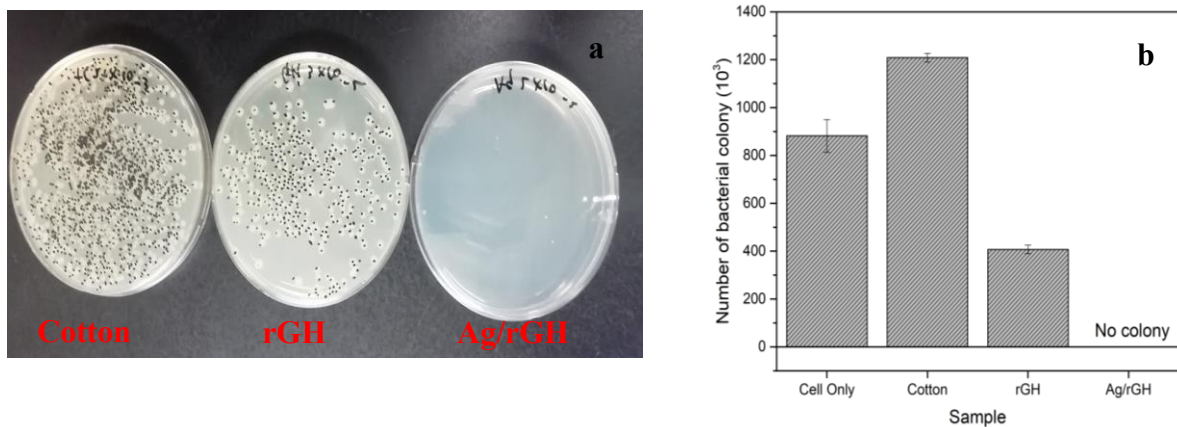


Fig. 1.3. (a) Photographs of colonies formed by *E. coli* after remediation with cotton, rGH and Ag/rGH
(b) Number of bacterial colonies ($\times 10^3$) formation.

1.7 Problem statement and objectives

The remediation of various pollutants using 3D graphene-based is an emerging trend that is gaining wide interest. In this regard, a graphene-based hydrogel/aerogel could be an alternative strategy that can overcome the limitation associated with powder-based adsorbent/photocatalyst. The preparation of 3D hydrogel structure via hydrothermal treatment is mainly attributed to the need to eliminate the usage of chemical reductants which incurred additional cost. In addition, the one-pot synthetic method is a facile and efficient strategy to prepare various functionalized 3D hydrogel with improved properties for usage as adsorbent/photocatalyst. Hence, the objectives of this study are:

The objectives of this study are:

- i. To prepare 3D modified graphene hydrogels via hydrothermal treatment and freeze-drying.
- ii. To characterize the 3D graphene hydrogel in terms of their morphological, structural, optical, and electrochemical properties.
- iii. To evaluate the adsorption capability of the 3D graphene towards selected pollutants.
- iv. To carry out photocatalytic degradation and identify their degradation mechanism on selected pollutants using the 3D graphene.
- v. To access the antibacterial activity of the 3D graphene towards selected bacteria

CHAPTER 2

ACCESSING EFFECTS OF ALIPHATIC DICARBOXYLIC ACID TOWARDS THE PHYSICAL AND CHEMICAL CHANGES IN LOW TEMPERATURE HYDROTHERMALLY REDUCED GRAPHENE HYDROGEL

Abstract

To date, studies pertaining the effect of aliphatic dicarboxylic acids (DCAs) on the properties of hydrothermally reduced graphene hydrogels (rGH) are limited and mainly used as either a reducing agent or cross-linkers. The modification of the properties of the hydrogels by introducing small amount of additive into the mixing composition is important from the point of view of imparting desired properties to the graphene-based hydrogel as intended for their specific applications. In this study, the in-situ preparation of rGH was carried out in the presence of a series of aliphatic DCAs namely oxalic acid (OA), malonic acid (MA), succinic acid (SA), glutaric acid (GA) and adipic acid (AA) in the graphene oxide (GO) reaction mixture via green hydrothermal method and freeze-drying. The as-prepared hydrogels were systematically characterized to probe the changes in their chemical and physical changes. Higher specific surface (SSA) of the hydrogel is obtained for shorter chain length DCAs. The FTIR and XPS results also indicated that shorter chain DCAs exhibited better reducing capability in the removal of oxygen functional groups. The C/O ratio obtained showed decrement with the increase in the chain length of the DCA. On the other hand, good dispersity was found for longer chain DCAs in polar solvent. Overall, this study provided a comprehensive understanding on hydrothermally reduced graphene hydrogels prepared in the presence of dicarboxylic acids.

Keywords: Graphene; hydrogel; hydrothermal; chain length; aliphatic dicarboxylic acid

2.1 Introduction

Graphene is a unique sp^2 carbon material that possessed high surface area, chemical stability, and great electron mobility. However, graphene sheets tend to aggregate due to their π - π interactions which hinders their fullest potential in various applications such as pollution remediations, energy storage, sensor, etc. To solve the inherent problems posed by two-dimensional (2D) graphene structure, researchers have proposed the transformation to a three-dimensional structure that retains the salient properties of graphene making it an attractive strategy for its usage in various applications[52]. Three-dimensional (3D) graphene hydrogel has attracted ample interest due to its highly porous framework, low density, tunable porosity, and easy utilization. Besides, the surface of the graphene sheets in the 3D macrostructure can be exploited for functionalization or anchoring, improving their physiochemical properties. The commonly reported self-assembly process involved the hydrothermal[33,53], and chemical reduction[54] process in the development of 3D macrostructure. The in-situ assembly of reduced graphene hydrogel from graphene oxide (GO) using hydrothermal reduction has shown to bring far superior benefits owing to the elimination of the usage of reducing agents; hence lowering the cost. The process implements the use of overheated supercritical (SC) water to play the role of the reducing agent allowing the catalysis of heterolytic bond cleavage[55]. Besides that, the output from the treatment does not emit harmful end-products, offering the green alternative in comparison to organic solvents. During the hydrothermal treatment, the number of oxygenated functional groups is removed and the self-assembly process occurred from the hydrophobic interaction and π - π interactions between the reduced sheet[56].

The addition of additives in the precursor before the hydrothermal reaction has become a common procedure due to the abundance of oxygen-containing functional groups distributed on GO sheets such as carboxylic (-COOH), epoxides (C-O-C), hydroxyl (-OH), and carbonyl (C=O) groups on their edges and basal plane enabling functionalization with various materials. The high chemical reactivity of the oxygenated groups enables the tuning of the graphene properties[19]. Among them, aliphatic dicarboxylic acids have been used alongside GO precursor either as cross-linkers or reducing agents in the preparation of graphene-based materials. Aliphatic dicarboxylic acids (DCAs) are important water-soluble organic compounds containing two carboxyl functional groups at both ends of their chemical structure. The physical

and chemical characteristics of DCAs presents many applications in different areas such as nanotechnology, polymer, and the pharmaceutical industries.

Previously, Bai et al. prepared few-layer graphene sheets using oxalic acid and NaCl under sonication for transparent conductive film applications[57]. Kumar *et al.* carried out the reduction of GO using various amount ratios of malonic acid: GO and found that the reduction fared better as compared to oxalic acid. They attributed the efficient reduction from the active methylene group that acts as an effective nucleophile[58]. In another study, Amanulla *et al.*, synthesized AuNP/rGO nanocomposite using succinic acid as the reducing agent for calorimetric sensor application[59]. Besides, Al-Hazmi *et al.*, reported on an efficient method to obtain high-quality graphene using the treatment of graphite flakes with glutaric acid using the microwave-assisted solvothermal method, in which the graphite flakes were pushed at an equal distance of the length of the glutaric acid [60]. Previous studies mentioned above have indicated the feasibility of using DCA as reducing agents or cross-linkers between graphene sheets.

However, studies on the usage of DCA in the preparation of hydrothermally reduced graphene hydrogel are limited in the sense that previous studies only applied one kind of DCA in the preparation of graphene-based materials. Also, fundamental studies on the effect of the DCA on the formation of hydrothermally reduced graphene hydrogel are worth exploring especially in terms of their physical and chemical changes. Thus, to develop a better understanding of the relationship between chain length of DCAs and reduced graphene hydrogel formation via hydrothermal process, a series of DCAs consisting of oxalic acid (OA), malonic acid (MA), succinic acid (SA), glutaric acid (GA) and adipic acid (AA) were used in this work. The impact of increasing the carboxylic chain length towards the formation of hydrothermally reduced graphene hydrogel was systematically studied in terms of their morphology, crystallinity, chemical interactions, and dispersion. The findings of this study will bridge the knowledge gap on this subject matter; which is paramount in practical applications involving the preparation of graphene-based hydrogels.

2.2 Materials and Methods

2.2.1 Chemicals

Dispersion of graphene oxide (GO) in water (0.1-2.0 %) was obtained from Nippon Shokubai Co. Ltd (AX-1-FM-W-151). The dicarboxylic acids consisting of oxalic acid (OA), malonic acid (MA), succinic acid (SA), glutaric acid (GA), and adipic acid (AA) were obtained from Wako Pure Chemical Industries Ltd, Japan. Potassium hexacyanoferrate (III) 99% was purchased from Sigma Aldrich. Deionized water (18.25 M Ω .cm) was obtained from a Milli-Direct 16 (Millipore Q, USA). Unless specified otherwise, all the reagents and materials were readily used without additional purification. For the sonication process, a bath sonicator (AS ONE Ultrasonic Cleaner Single Frequency, 3L (MSC-3) 40 kHz, 100W) was used as described below.

2.2.2 Synthesis of reduced graphene hydrogels

GO (30 mL) was first ultrasonicated for 1 hour until reaching a concentration of 2 mg/mL to exfoliate the graphene sheets. 0.01 M of aliphatic DCA was readily added to the aqueous GO dispersion and further sonicated for 0.5 h at room temperature. The solution was then transferred into a modified 100 mL borosilicate glass vial that can withstand high temperature and pressure. The hydrothermal reduction is carried out in a TOMY High-pressure steam sterilizer (LBS-325) at 120°C for 12 hours. The autoclave was then naturally cooled to ambient temperature. The resulting hydrogel was then immersed in deionized water for 24 hours to remove any unreacted materials and was lyophilized at -50°C for 24 hours to remove any moisture content before any characterization is carried out. The obtained hydrogels with the addition of oxalic acid (OA), malonic acid (MA), succinic acid (SA), glutaric acid (GA), and adipic acid (AA) were denoted as rGH-OA, rGH-MA, rGH-SA, rGH-GA, and rGH-AA, respectively to ease identification. The GO suspension without any addition of DCAs is denoted as rGH, acting as the control.

2.2.3 Characterizations

The morphology of the freeze-dried hydrogel surface was accessed using scanning electron microscopy (SEM) on a JEOL 6000 microscope. N₂ adsorption-desorption was carried out on a Surface Area and Pore Size Analyzer (Nova 4200e, Quantachrome Instruments) in which the Brunauer-Emmett-Teller (BET) surface area and Barrete-Joynere-Halenda (BJH) pore size were obtained from the obtained isotherms.

The crystalline structure of the hydrogels was accessed using a Rigaku X-ray diffractometer with Cu K- α radiation at 40kV and 15 mA with a scan rate of 10°/min. The chemical bonding changes were accessed on an Attenuated total reflection-Fourier transform infrared (ATR-FTIR), PerkinElmer Spectrum GX in the range of 4000 to 500 cm^{-1} . X-ray photoelectron spectroscopy (XPS) measurements were performed using Axis Nova (XPS) Surface Analyzer (Kratos Analytical Ltd, Japan). Thermogravimetric analysis (TGA) was performed to analyze thermal stability from room temperature to 550°C at a rate of 2°C/min under the N₂ atmosphere using EXSTAR TG/DTA7000. The electrochemical analyzer Nova 1.1 Autolab potentiostat (PGSTAT204, Metrohm Autolab, Netherlands) connected to an external computer was utilized to carry out the electrochemical measurement. The three-electrode system consisted of a glassy carbon electrode (GCE) as the working electrode, Ag/AgCl/KCl (3M), and platinum as the reference and auxiliary electrode, respectively. The freeze-dried graphene-based hydrogel was first sonicated in DMF to a concentration of 1 mg/mL and the suspension is drop-casted on the GCE surface and allowed to dry before proceeding with electrochemical measurements.

2.3 Results and Discussion

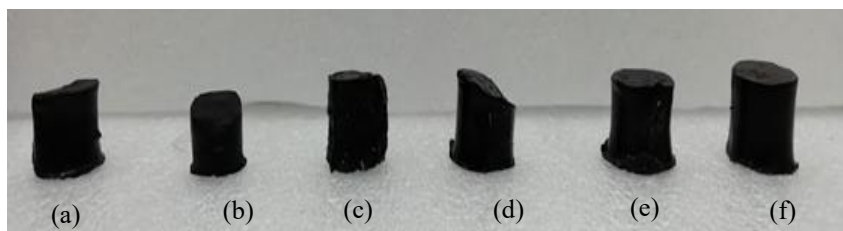


Fig. 2.1. Digital images of the as-prepared graphene hydrogels. (a) rGH, (b) rGH-OA, (c) rGH-MA, (d) rGH-SA, (e) rGH-GA and (f) rGH-AA

Based on Fig. 2.1, the digital images of the hydrogels obtained after hydrothermal treatment for 12 h at 120°C using autoclave showed the formation of almost cylindrical-shaped which is consistent with previously reported studies[31,33]. Two essential factors need to be taken into account for the hydrogel to be formed: hydrothermal temperature and time. The gelation process is due to the strong π - π and hydrophobic interaction of reduced graphene sheets above a critical concentration of the starting GO

suspension[31]. To evaluate the physical changes, the water content of the hydrogels was evaluated in which the results were shown in Table 1 using the following equations:

$$\text{Water content (\%)} = \frac{M_w - M_d}{M_w} \times 100\%$$

M_w represents the mass of the as-prepared hydrogel and M_d denotes the mass after freeze-drying. It can be seen that the water content and diameter of the hydrogel increased with the increase in the chain length of aliphatic DCAs. The water content roughly represents the empty voids and spaces which were consisted of the pores filled with water. Although a similar concentration of GO dispersion was used, the volume obtained were 1.92 cm³, 0.95 cm³, 1.25 cm³, 2.12 cm³, 2.72 cm³ and 3.41 cm³ for rGH, rGH-OA, rGH-MA, rGH-SA, rGH-GA, and rGH-AA, respectively as shown in Table 2.1. Using the volume of rGH as a reference, the volume increased as much as 43.70 % for rGH-AA. Hence, the findings showed that the presence of the DCAs affected the cross-linking network which corresponds to the change in their physical properties in terms of volume and water content.

Table 2.1. Water content and density of the reduced graphene-based hydrogels

Sample	Water content (%)	Volume (cm ³)	Density (g/cm ³)
rGH	99.02	1.92	0.62
rGH-OA	98.06	0.95	1.24
rGH-MA	98.44	1.25	1.59
rGH-SA	99.17	2.12	1.23
rGH-GA	99.20	2.72	1.03
rGH-AA	99.32	3.41	0.64

The SEM images of the freeze-dried hydrogels are depicted in Fig. 2.2 to further probe their surface morphology. The freeze-drying process leads to the removal of the ice crystal from the voids and hence causing the graphene layers to be rearranged and finally leading to the formation of a three-dimensional porous structure[53]. The disordered randomly oriented graphene sheets shown in Fig. 2.2(a) possessed

a wrinkled texture which is consistent with many studies[61,62]. However, in the presence of the aliphatic DCA during hydrothermal treatment, the morphology graphene sheets showed more exfoliated layers and possess a more porous nature as depicted in Fig. 2.2(b-f)[63].

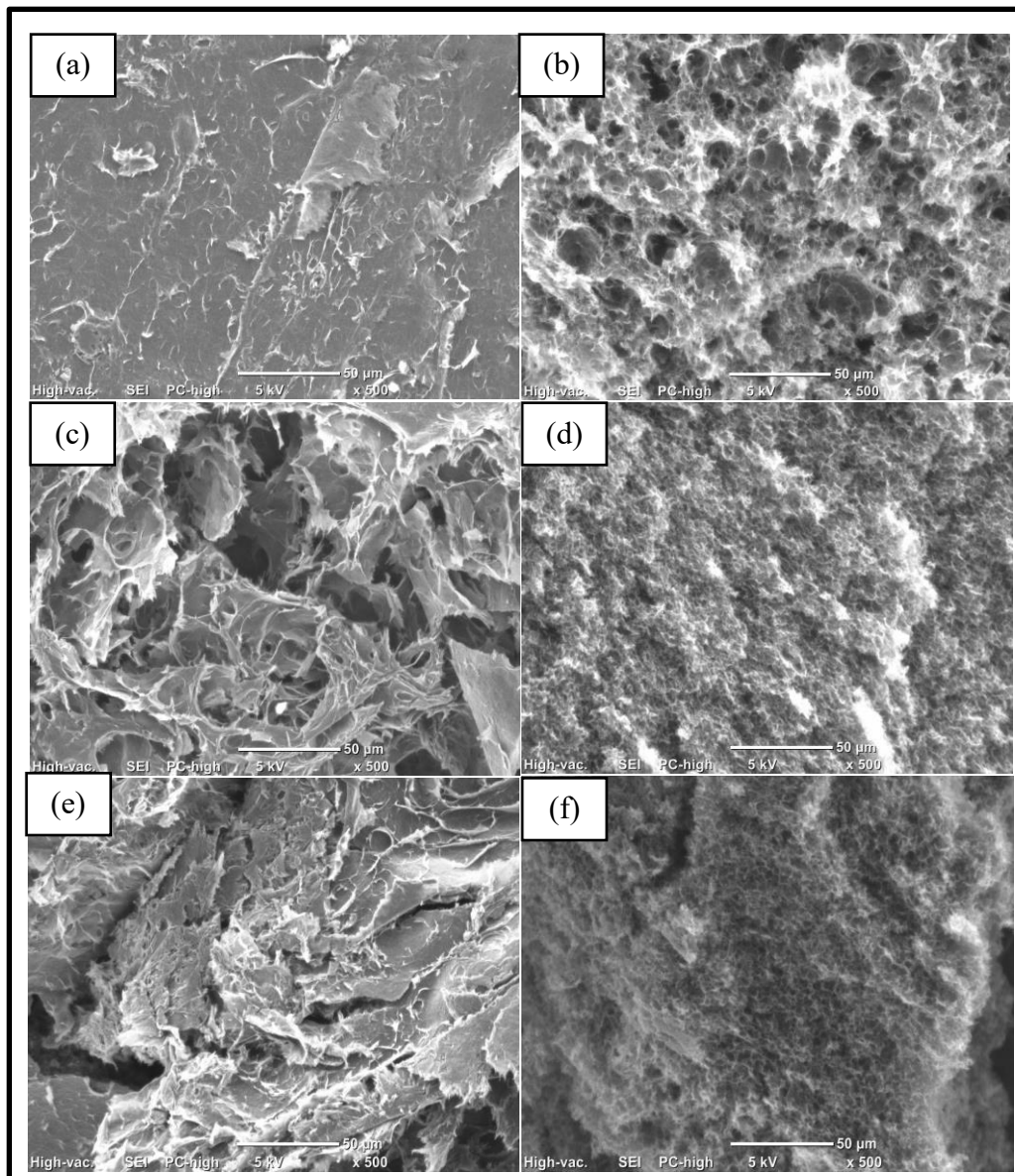


Fig. 2.2. SEM images of reduced graphene-based hydrogels. (a) rGH, (b) rGH-OA, (c) rGH-MA, (c) rGH-SA, (d) rGH-GA, (e) rGH-AA

FTIR provides an overview of the presence of the oxygen-containing functional groups for the freeze-dried hydrogels. The spectrum of GO as shown in Fig. S2.1(a) possessed peaks at $1,080\text{ cm}^{-1}$ correspondings to C-O stretching vibration mode related to the presence of the alkoxy group, $1,280\text{ cm}^{-1}$ attributed to C-O

from the epoxy group, $1,618\text{ cm}^{-1}$ associated with the presence of C = C bond, and $1,750\text{ cm}^{-1}$ assigned to C = O stretching vibration mode in the carboxyl group. The commonly found broad peak at $3,212\text{ cm}^{-1}$ originates from the hydroxyl O-H bond[64]. This spectrum confirms the presence of alkoxy, epoxy, and carboxyl group characteristic to GO. Fig. 2.3(b) depicts the ATR-FTIR spectra of rGH, rGH-OA, rGH-MA, rGH-SA, rGH-GA, and rGH-AA. Four prominent peaks attributed to the C=O, C=C, C-O-C (epoxy) and C-O (alkoxyl) can be observed after the hydrothermal treatment occurring around 1720 cm^{-1} , 1580 cm^{-1} , 1240 cm^{-1} and 1048 cm^{-1} , respectively. The hydrothermal treatment diminished the O-H groups around 3300 cm^{-1} and increased the peak intensity of the C=C around 1580 cm^{-1} which confirmed the restoration of the sp^2 carbon network. The C-O peak in rGH-OA weakened extensively which further proved their reducing capabilities. The increased intensity and shift in the position of the C-O-C peak for cross-linked rGHs can be posited from the low hydrothermal temperature which is not sufficient to sever the strong covalently bonded carbon symmetry at the basal plane. The oxygen groups of the DCA should functionalize on the edge of the graphene plane without causing lattice distortion and defects at the basal plane[65]. In addition, the increase in peak intensity and the shift in the peak position of the C=O may be attributed to the successful surface functionalization of the DCA on the graphene surface via ester formation. This finding showed that the alkoxy group is susceptible to the hydrothermal treatment for short-chain DCA (OA).

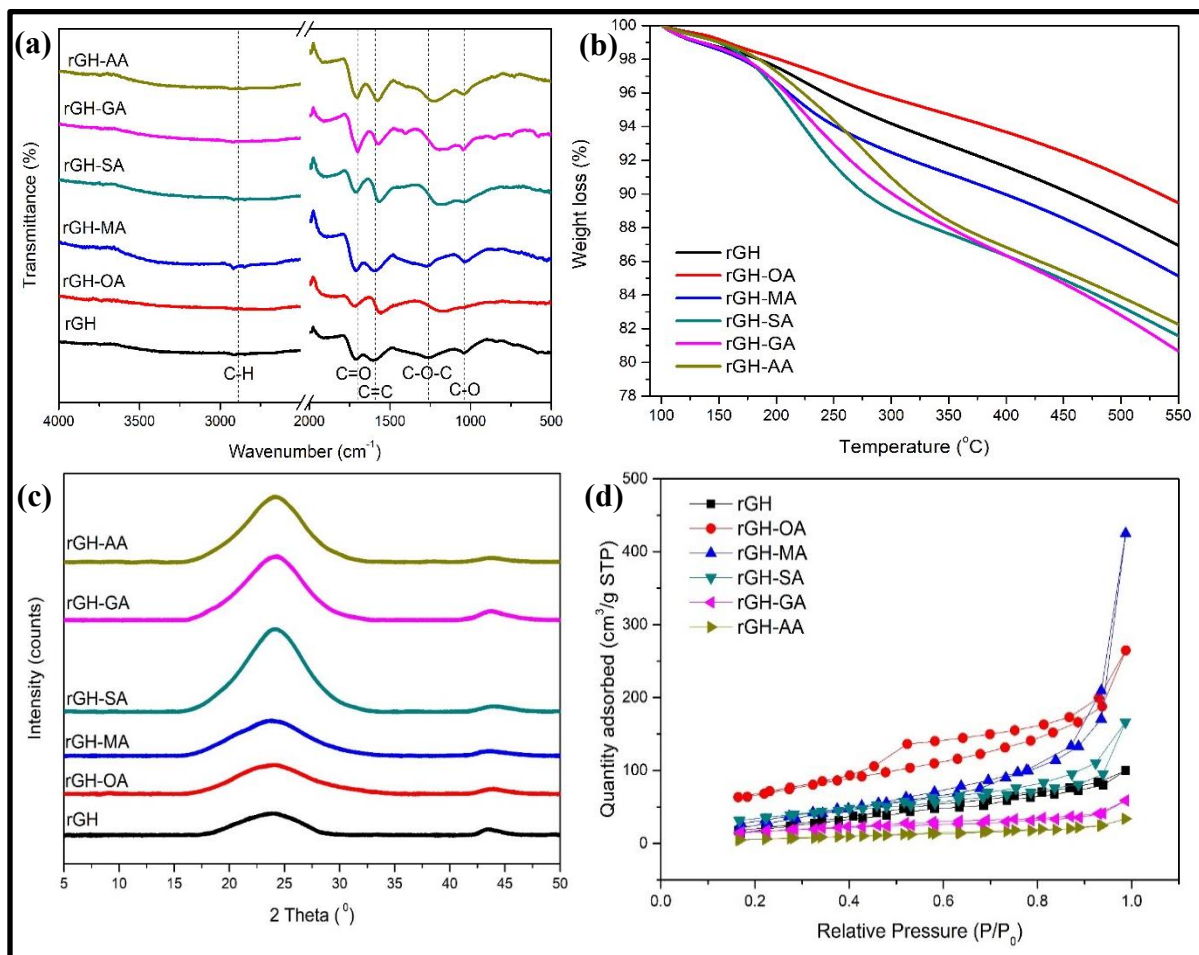


Fig. 2.3. (a) FTIR spectrum, (b) TGA thermogram, (c) XRD spectra and (d) N₂ adsorption-desorption isotherm of the as-prepared graphene hydrogel

Thermogravimetric analysis (TGA) was used to access the thermal stability of the freeze-dried hydrogel. There were three significant stages of mass loss based on the thermograms in Fig. 2.3(b). The mass loss until about 150°C is ascribed to the removal of absorbed water. The second step observed from 150 to 500°C is attributed to the loss of oxygen-containing functional groups on the basal and planar plane which were not removed completely via the hydrothermal treatment [66]. And the third step above 500°C is related to the unstable carbon remaining and pyrolysis of the oxygen functional groups on the graphene sheet to yield carbon monoxide and carbon dioxide [67]. However, it can be seen that rGH-OA exhibited the highest thermal stability which is possible from the restoration of the sp² carbon network due to the reducing capability of OA in the removal of the more oxygen-containing functional groups during hydrothermal treatment. However, on the other hand, longer chain derivatives of the aliphatic DCA (MA onwards) showed

a slight deterioration in their thermal stability. The notable mass loss at about 350°C can be partly ascribed to the pyrolysis of the weakly bonded chemically grafted DCAs as supported by the FTIR results[68]. Hence, the difference in weight loss between the control sample, rGH and the rGH-DCA enables us to predict the functionalization rate of the DCA on the basal plane. The total weight loss difference in comparison to rGH is 1.87%, 5.44%, 6.31%, and 4.75 % for rGH-MA, rGH-SA, rGH-GA and rGH-AA, respectively. This finding further indicates that there is no direct relation between the chain length of DCA and their functionalization rate on the basal plane.

The XRD patterns of the reduced graphene hydrogels are shown in Fig. 2.3(c) to probe its crystalline changes. GO showed the typical wide diffraction peak at $2\theta=10.24^\circ$ corresponding to the (0 0 1) crystal plane as shown in Fig. S2.1(b). The smaller peaks obtained at $2\theta=19.77^\circ$ and 26.36° indicate the presence of abundant oxygen atoms that were not fully intercalated[69]. Well-resolved diffraction peaks observed at 2θ are around 23.8° corresponding to the d-spacing values of 0.373 nm for the rGH. On the other hand, the small diffraction peak at 2θ at 42.98° is related to the (1 0 2) plane of rGO structure. The findings are in agreement with to previously reported study on hydrothermally prepared graphene hydrogels[70]. The diffraction peak intensities of the (002) peak showed higher intensity for a longer chain length of DCA (from SA onwards) in comparison to the short-chain length of DCA. The increased intensity peak at 2θ and no significant changes in the 2θ peak position ($< 1^\circ$) in the presence of increased chain length of aliphatic DCA indicated that the reduced graphene sheets consisted of disorderedly stacked sheets which are in agreement with the results obtained from the morphology in the SEM analysis. Often, the reduction in d-spacing between the graphene sheet indicate reduction occurred by the removal of the remaining oxygen groups. Interestingly, only rGH-MA showed an increase in the d-spacing which may be related to the cross-linking effect of the rGO lamellae by MA. This behaviour can be attributed to the preferential grafting of the oxygen-containing functional group onto GO during the sonication process which played a supporting role like “pillars”, hence leading to the increase in d-spacing of the rGH-MA[71]. It can also be seen that there was no significant pattern of changes in the d-spacing with the increase of the DCA's chain length. The crystallite size of the hydrogels was calculated using the full width at half maximum (FWHM) of the (0 0 2) plane refraction peak, the highest intensity peak using the Debye-Scherrer equation:

$$D = \frac{k\lambda}{\beta \cos \theta}$$

where D is the crystallite size, λ is the wavelength of the X-ray (1.54 \AA), β is the FWHM of the diffraction peak and θ is the diffraction angle. Table 2.2 further summarizes the crystallite size of hydrogel based on the (0 0 2) plane. The crystallite size of rGH-GA and rGH-AA significantly decreased in comparison to rGH which is possible from disruption of graphitic stacked ordering and the creation of more grain boundaries or lateral defects from the introduction of the longer DCAs[72].

Table 2.2. XRD parameters of the hydrogels

Hydrogel	(0 0 2)			(1 0 2)			*Crystallite size (nm)
	2 θ	FWHM ($^{\circ}2\theta$)	d-spacing (\AA)	2 θ	FWHM ($^{\circ}2\theta$)	d-spacing (\AA)	
rGH	23.81	2.50	3.73	42.98	1.54	2.10	3.39
rGH-OA	24.25	1.92	3.67	43.69	3.65	2.07	4.42
rGH-MA	23.66	2.69	3.76	42.94	2.30	2.10	3.15
rGH-SA	23.96	1.50	3.71	43.68	2.99	2.07	5.66
rGH-GA	24.41	4.61	3.63	43.65	2.50	2.07	1.84
rGH-AA	24.06	3.65	3.69	43.66	3.07	2.07	2.33

*The crystallite size is measured from the (0 0 2) diffraction peak position

To elucidate the surface areas and microstructure of the hydrogels, low-temperature nitrogen adsorption-desorption isotherm were carried out as depicted in Fig. 2.3(d). The type IV adsorption-desorption isotherm indicated that significant mesopores are present in the hydrogels with pore diameter between 2- 50 nm. The isotherm of rGH-OA exhibited a significant H3 hysteresis loop which is a typical characteristic of non-rigid aggregates of plat-like possessing open large pores[61,73]. The specific area and textural property of the hydrogels are summarized in Table 2.3 Interestingly, the specific area and pore volume improved until rGH-MA but decreased significantly as the chain length of the aliphatic DCA increased further. The decreased surface area obtained in a longer chain of aliphatic DCA hydrogels can be attributed to the agglomeration/precipitation and partial overlapping of the sheets leading to inaccessible surface added on with the presence of the remaining oxygen functionalities from the longer chain aliphatic DCA which was not completely removed by the hydrothermal treatment[74]. In comparison to the theoretical surface area

of graphene, the significant decrease of the surface area obtained in this study could be largely attributed to hydrothermal and freeze-drying treatment. Often, the stacking of the graphene sheets due to the extensive van der Waals interaction reduces the accessible surface area with regards to their degree of stacking[75]. On this notion, the number of graphene stacking is accessed by applying the scaling law which is described as:

$$N = \frac{2600}{A}$$

where the N is the number of graphene sheets per plate, 2600 is the theoretical surface area of graphene (m^2/g) and A is the experimental BET surface area measured (m^2/g). The graphene stacking number is also summarized in Table 2.3.

Table 2.3. BET Surface area and BJH pore size/volume of the reduced graphene hydrogels

Sample	Specific surface area (m^2/g)	Average pore size (nm)	Total pore volume (m^3/g)	Number of stacking, N
rGH	22.51	1.739	0.132	115
rGH-OA	54.71	1.976	0.357	47
rGH-MA	58.83	1.728	0.655	44
rGH-SA	31.88	1.624	0.217	81
rGH-GA	12.13	1.981	0.069	214
rGH-AA	7.059	1.723	0.048	368

XPS was further performed to access the surface chemical composition of the freeze-dried hydrogels. Fig. 4(a) shows the XPS wide spectra possessing characteristic peaks of C1s and O1s, respectively. The atomic ratio of carbon to oxygen (C/O) was obtained via the atomic concentration (%) for the C1s and O1s peaks. C/O ratios are often analyzed to access the reduction degree of graphene-based materials. However, it is important to note that DCAs alkyl chains are also included into the C content and hence the C/O ratio obtained may not necessarily portray the actual carbon content of the bulk reduced graphene sheet. The C/O ratio should be interpreted with caution. The C/O ratio decreased with the increase of the DCA chain length. It is found that that the presence of short-chain DCAs (OA and MA) during hydrothermal treatment enables the easy restoration of the sp^2 carbon network due to the removal of the oxygen functional groups

on the graphene sheets. The findings obtained also support the result obtained from the FT-IR and TGA for short-chain length DCAs. On contrary, in the case of the longer DCAs chain length, the lower C/O ratio obtained is possible from the surface functionalization of DCAs which hinders the effective removal of oxygen-containing groups during hydrothermal.

Based on Fig. 2.4(b), the deconvolution of C1s spectra corresponds to the C-C/C=C (284.6 eV), C-O (286.4 eV), attributed to the hydroxyl/phenolic and O-C=O (carbonyl and carboxylic) at around 288.7 eV[76]. The curve fitting results of the C1s split spectra was further shown in Table 2.4. Except for rGH-OA, the increase of O-C=O percentage indicates the surface functionalization of the DCAs occurred on the reduced graphene surface. Interestingly, the increase of O-C=O is the greatest for rGH-MA. On the other hand, the decrease of the C-O and O-C=O percentage in rGH-OA further substantiated the reducing capability of OA as supported by the FT-IR and TGA results.

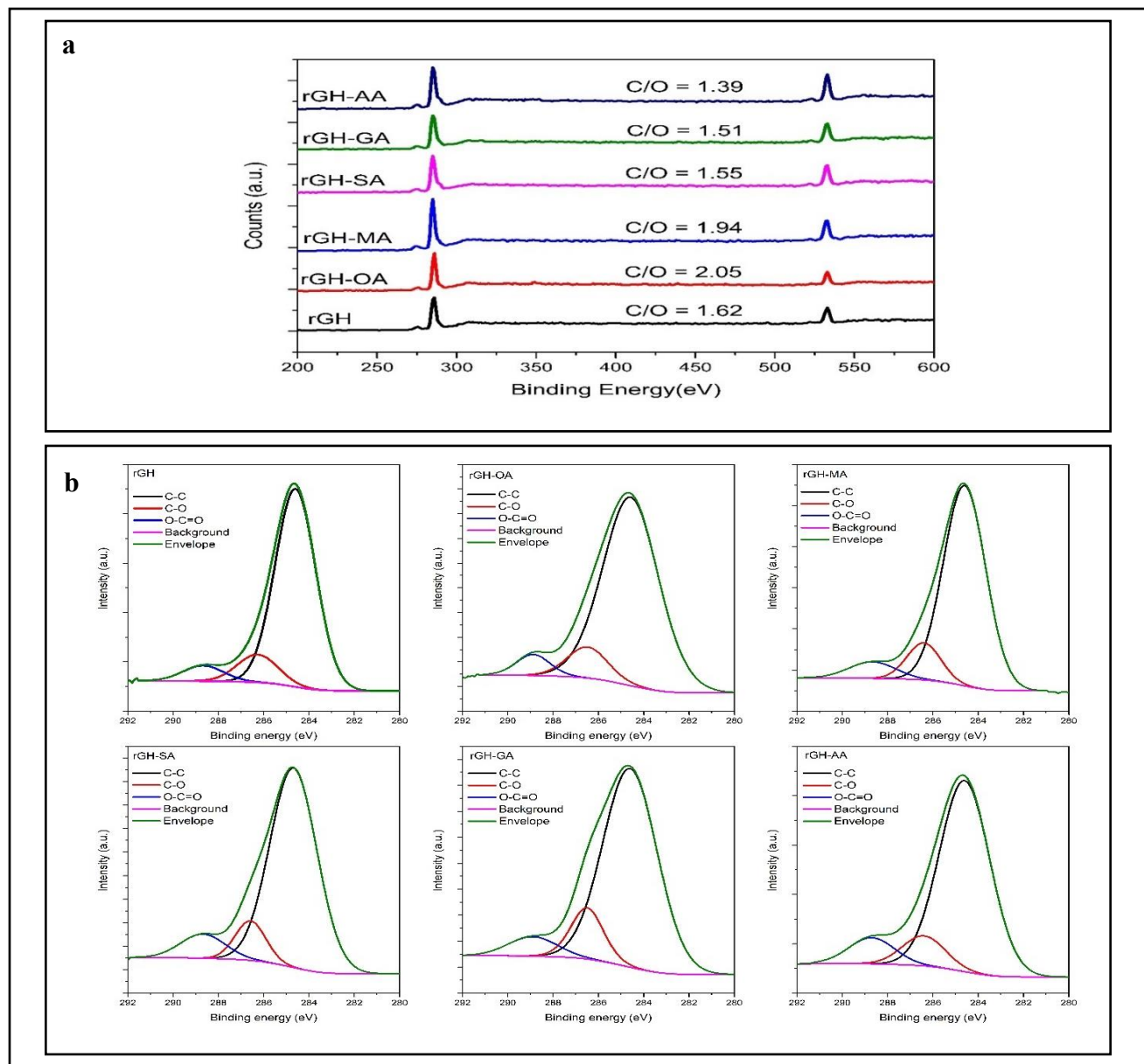


Fig. 2.4. (a) Wide spectra and (b) C1s split spectra of the reduced graphene hydrogel

In addition, the increase in the C-C/C=C also showed the improved restoration of the sp^2 aromatic rings during hydrothermal. In hindsight, the changes in the C-C/C=C are relatively subtle for other DCAs, which can be explained by the small amount of DCAs used in the hydrothermal treatment.

Table 2.4. Curve fitting results obtained from the XPS split spectra of C1s

	Assignments	Binding energy (eV)	Area	Atomic Percentage (%)
rGH	C-C/C=C	284.6	45240.1	82.04
	C-O	286.3	6349.3	11.52
	O-C=O	288.7	3552.0	6.45
rGH-OA	C-C/C=C	284.6	47958.1	84.23
	C-O	286.5	5755.0	10.11
	O-C=O	288.9	3222.7	5.66
rGH-MA	C-C/C=C	284.6	57171.0	80.72
	C-O	286.4	8460.5	11.95
	O-C=O	288.7	5192.1	7.34
rGH-SA	C-C/C=C	284.7	44352.7	80.43
	C-O	286.6	5687.5	10.32
	O-C=O	288.7	5101.3	9.26
rGH-GA	C-C/C=C	284.7	46030.7	80.19
	C-O	286.5	7311.5	12.74
	O-C=O	288.9	4057.1	7.07
rGH-AA	C-C/C=C	284.6	54121.7	79.58
	C-O	286.4	7215.3	10.61
	O-C=O	288.7	6663.5	9.80

Digital photographs as shown in Fig. 2.5 were taken to further assess the dispersion stability of the graphene-based hydrogels in a wide range of solvents such as H₂O, MeOH, EtOH, acetone, CHCl₃, and DMF. The amphiphilic dispersion of the reduced graphene hydrogels depends on their complex structure which includes oxygen-functioning groups, topological defect clusters, and edge/defects on their plane to form stable dispersion[77]. The dispersion stability was investigated by adding 1.0 wt.% of the freeze-dried hydrogel into various organic solvents with a 1:10 weight ratio and sonicated for 2 hours. The final concentration of the suspension was maintained at 0.1 mg/mL. The abundance of oxygen-containing functional groups on GO exhibited good dispersion in various organic solvents as compared to its reduced form[78]. The surface of the reduced graphene after freeze dry becomes hydrophobic due to the deoxygenation process during hydrothermal treatment.[53,79]. The results showed that all of the freeze-dried hydrogels retained excellent solubility in DMF for up to 10 days. In terms of colloidal stability, the Derjaguin-Landau-Verwey- Overbeek (DLVO) theory is fundamental in the study of colloidal properties in polar media which states that the interaction energy is the sum of the van der Waals and electrostatic interactions. Stable dispersion means that the electrostatic interactions are greater in comparison to van der Waals[80]. In DMF, the greater electrostatic repulsive force overcomes the attractive van der Waals forces resulting in the good dispersion attributed to the creation of electric charge on the graphene particle surface[81]. Interestingly, for rGH-AA, the functionalization on the reduced graphene surface also improved the dispersity in low polar solvents such as MeOH and EtOH with low precipitation sedimented at the bottom. rGH-MA also showed improved dispersity in H₂O and EtOH as compared to rGH. Besides, rGH-SA also showed good dispersion stability in non-polar solvents such as CHCl₃ posited from the effective spacers formed which improve exfoliation of the graphene sheet and preventing agglomeration[82].

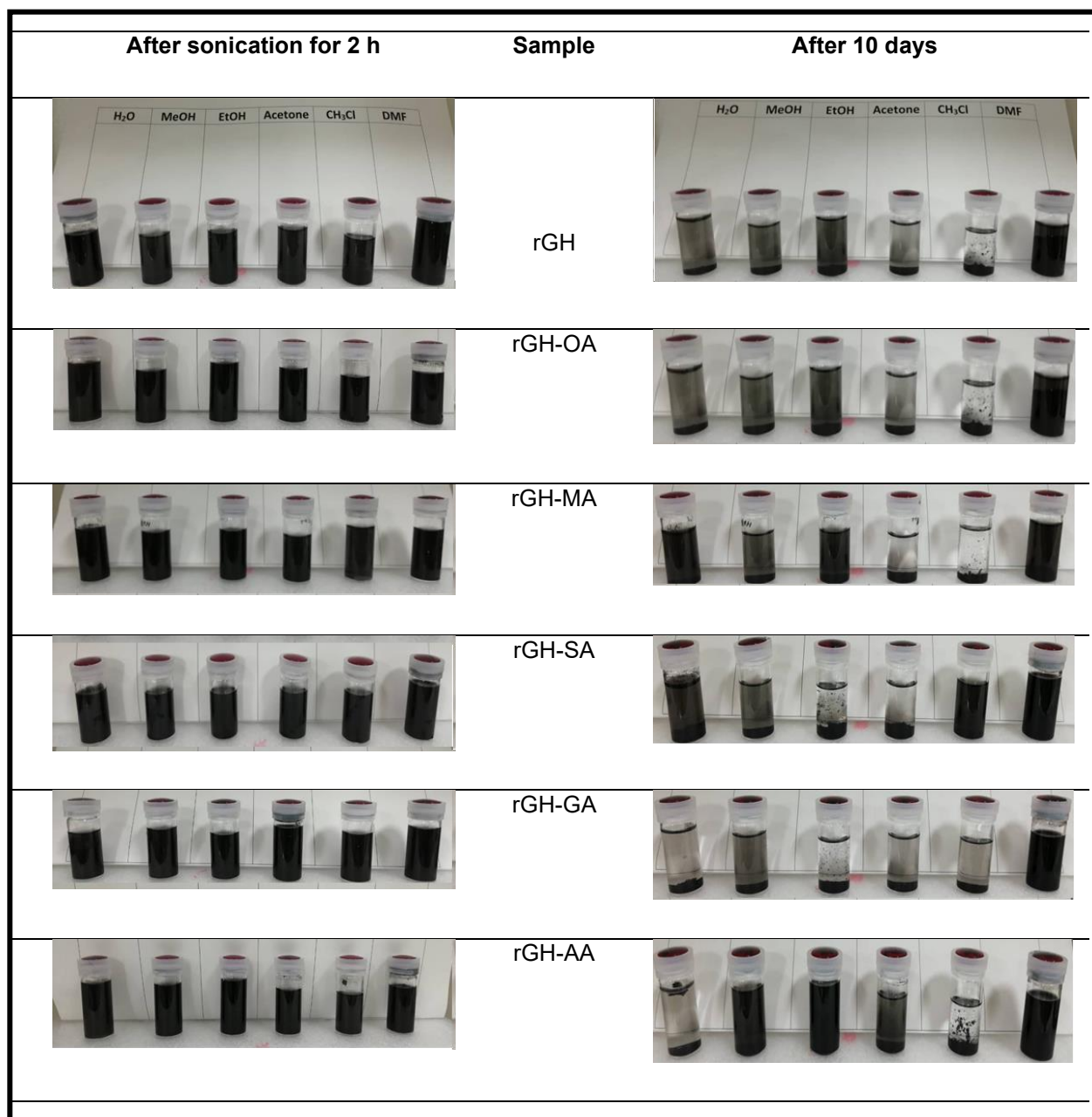


Fig. 2.5. Dispersivity of the graphene-based hydrogels in various solvents (left) after sonication for 2 h (right) after left for 10 days. (a) rGH, (b) rGH-OA, (c) rGH-MA, (d) rGH-SA, (e) rGH-GA, (f) rGH-AA

The determination of the electrochemical properties of the hydrogels was further accessed using cyclic voltammetry. Cyclic voltammetry was carried out on potassium ferricyanide $[(K_3Fe(CN)_6)]$ as the electrochemical probe using the dispersion of modified rGH modified on the glassy carbon electrode (GCE) by the drop-casting method. Fig. 2.6 depicts the almost reversible one-electron transfer cyclic voltammogram for $[(K_3Fe(CN)_6)]$ which is common. The improved voltammetric response (anodic current)

in the presence DCAs as compared to bare rGH can be attributed to the increased charge transport properties and transfer dynamic [83]. Besides, the enhancement in the oxidation current is resulted from the salient properties of reduced graphene such as high specific surface area and excellent conductivity. In contrary to the BET surface area as shown in Table 2.3, the sonication of the freeze-dried graphene hydrogel to suspension form may induce better separation of the graphene sheets which increased their surface area. Interestingly, rGH-MA showed the highest anodic current which corresponds to the highest surface area as obtained from the BET studies. However, the only minimal increase could be observed for the rGH-DCA in comparison to bare rGH. Besides, the slight shifting of the anodic peak to a less negative potential peak can be related to the increase in selectivity of the modified graphene-based electrode which is paramount in research on chiral sensing applications [84]. It is important to understand that various experimental factors such as temperature, pH, salt concentration, amount of modifier, and type of electrolyte may also affect the performance of the modified electrode. It would be interesting to further optimize the working condition which can improve its performance. This finding further showed that graphene-based material prepared in the presence of DCA showed slightly improved electrochemical properties which can be used as a potential modifier for improved performance in sensing applications.

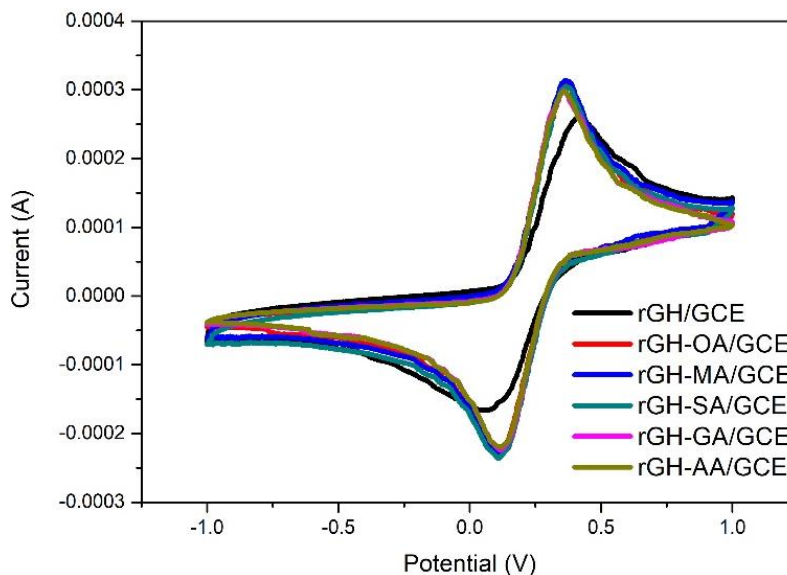


Fig. 2.6. Cyclic voltammogram of 1 mM potassium ferricyanide, $[(K_3Fe(CN)_6)]$ with a scan rate of 100 mV/s using GCE modified with the graphene-based hydrogels.

2.4 Conclusion

In summary, we have successfully prepared various reduced graphene hydrogels in the presence of various chain lengths of aliphatic DCAs possessing different physical and chemical properties. The volume and water content of the hydrogel prepared increased with the increase in the chain length. Improved thermal stability is achieved for shorter chain length DCAs; rGH-OA and rGH-MA. Besides, decreased surface area obtained in longer alkyl chain DCA hydrogels possible from the agglomeration/precipitation and partial overlapping of the sheets leading to the inaccessible surface. FTIR and XPS indicated that reduction or surface grafting of the oxygen-containing functional groups from the DCAs occurred. The surface grafting of some longer chain DCAs such as AA exhibited improved dispersity in low polar solvents. Overall, this study provided a more detailed understanding of hydrothermally reduced graphene hydrogels and its' implications from the addition of DCAs. Hence, this work will be beneficial in the development of novel graphene-based hydrogels for their usage in their intended applications such as biomedical, electronics, wastewater treatment, and sensor applications.

CHAPTER 3

HYDROTHERMALLY REDUCED GRAPHENE HYDROGEL INTERCALATED WITH DIVALENT IONS FOR DYE ADSORPTION STUDIES

Abstract

Fundamental studies involving divalent ion intercalated graphene-based hydrogel are still lacking in terms of their adsorption behavior towards dye pollutants. In this study, we prepared a self-assembled Mg^{2+} and Ca^{2+} intercalated reduced graphene hydrogel using hydrothermal treatment to evaluate the intercalation impact on the adsorption capability towards cationic dyes, methylene blue (MB) and rhodamine B (RhB). The morphological, structural, thermal and textural properties of the divalent ion intercalated reduced graphene hydrogels (rGHs) were studied using Fourier transform infrared spectrometer (FT-IR), thermogravimetric analysis (TGA), Raman spectroscopy, scanning electron microscope-energy dispersive spectroscopy (SEM/EDS), X-ray photoelectron spectroscopy (XPS), Brunauer-Emmett-Teller (BET) surface area analysis, and X-ray diffraction (XRD). The increased adsorption capacity of rGH-Ca and rGH-Mg as compared to rGH towards the dye molecules resulted from the increase in the specific surface area and pore volume due to the Mg^{2+} and Ca^{2+} bridging that formed spaces between the graphene sheets framework. Adsorption kinetics and the equilibrium adsorption isotherm were fitted by a pseudo-second-order (PSO) alongside intraparticle diffusion (IPD) kinetic model and Langmuir isotherm respectively. In addition, the Mg^{2+} and Ca^{2+} intercalated reduced graphene hydrogel showed good regeneration after three cycles of simultaneous adsorption without any structural deformities.

Keywords: graphene hydrogel; hydrothermal; dye adsorption; calcium; magnesium

3.1. Introduction

Water bodies contaminated with dye-containing effluent disposed from various industries such as textile and printing often contribute to massive environmental and health problems[85–88]. Currently, the treatment of dye wastewater includes biological treatment, coagulation, floatation, and adsorption. Due to the low cost, ease of operation, and high performance, adsorption is often preferred for dye removal from waste water. [34,89–91]. For the past years, many significant findings on the remediation of dye wastewater via adsorption have been reported using graphene-based nanomaterials upon comparing to other carbon-based materials such as biochar, activated carbon, etc [92–96]. From the carbon family, graphene possessed a honeycomb crystal lattice composing of hexagonally sp^2 hybridized carbon atom with a thickness of equal to one atom diameter[97]. This two-dimensional (2D) material has gained prominence among researchers due to its unique properties such as possessing high surface area ($2600 \text{ m}^2/\text{g}$), intrinsic electron mobility ($200,000 \text{ cm}^2/\text{Vs}$), Young's Modulus (1 TPa), and high thermal conductivity (5000 W/mK) [61,98,99]. Graphene oxide (GO) is a commonly used precursor in the synthesis of graphene. Until now, the salient properties associated with 2D graphene have not yet been realized due to the fact that they cannot exist in a free state due to aggregation of the sheets from the intrinsic π - π [100].

In wastewater remediation applications, the usage of graphene-based powder complicates the post-recovery process which is not ideal in large-scale applications. The development of three-dimensional (3D) graphene-based architecture such as hydrogels or aerogels has become a promising choice to tackle the aforementioned drawbacks. The 3D reduced graphene hydrogel block morphology explicitly tackles the issue of easy recovery and prevents the release of graphene nanosheets from contributing to secondary contamination.[101]. The intrinsic π - π interactions and van der Waals interactions drive the hydrogel formation between the sheets to achieve macroscopic structural stability[31,102]. 3D graphene framework contains an interconnected porous structure with a large specific surface area making them ideal for wastewater treatment[103,104]. Besides, reduced graphene-based hydrogels can act as a templating material for the inclusion/blending with small molecules, metal/metal oxide nanoparticles, polymer complex, etc which enable the design of novel multi-functional hydrogels with upgraded properties[105,106]. In terms of pollution remediation, reduced graphene hydrogel form π - π interactions with adsorbate molecules containing aromatic rings. Furthermore, remaining oxygenated groups on their surface enable electrostatic,

van der Waals forces, and hydrogen bonding interactions with the pollutants such as small dyes[107]. Previously, ample studies have been conducted using graphene-based hydrogel as promising adsorbent material for wastewater dye remediation[35,108–113]. To date, various approaches were reported in the successful fabrication of reduced graphene-based hydrogels which include hydrothermal treatment[31,114–116], solvothermal method, and chemical vapor deposition (CVD)[117]. Inherently, the hydrothermal process is a preferred alternative as it is a scalable approach that enables the control in the size and properties of the hydrogel from operating parameters such as hydrothermal time and hydrothermal temperature[118]. Also, the process eliminates the usage of reducing agents, which significantly reduced the cost[70]. During the hydrothermal process, superheated water acts as a strong electrolyte with high diffusion and dielectric constant; hence readily catalyzes bond cleavage of oxygen moieties present on the basal planes of the graphene sheets[30].

Previously, Jiang *et al*[119] compared divalent ion (Ca^{2+} , Ni^{2+} , and Co^{2+}) linkage between graphene sheets in a 3D architecture prepared via hydrothermal treatment. They found that the graphene sheet is interconnected via chemical and hydrogen bonds, which are driven by water molecules, divalent ions, and oxygen-functional groups on the reduced graphene sheet. The inclusion of calcium ions is also reported to improve the mechanical performance of alginate/graphene-based hydrogel due to the formation of different microcosmic morphologies within the framework[120,121]. In energy applications, Ca^{2+} forms bridge between graphene sheets; hence creating new electron energy levels and conduction channels [122]. The comparison between alkali metal ions as crosslinkers should be made to reduce the knowledge gap to fully grasp their effect on the physical and chemical properties of the hydrogels synthesized. Taking the unique behavior of reduced graphene hydrogel, we herein describe a simple one-pot synthesis via the hydrothermal treatment of GO in the presence of Mg^{2+} and Ca^{2+} for the preparation of divalent-ion intercalated reduced graphene hydrogels (rGH). The effect of divalent metal ion cross-linking within the 3D macrostructure is accessed for their adsorption behavior towards methylene blue and rhodamine B. The findings of this study will provide useful insights on future works on intercalated reduced graphene hydrogel practical applications in dye wastewater treatment.

3.2. Materials and Methods

3.2.1 Materials, reagents, and equipment

Graphene oxide (GO) dispersion in water (0.1-2.0 %) was used as received from Nippon Shokubai Co., Ltd (AX-1-FM-W-151). Magnesium chloride (MgCl_2), calcium chloride (CaCl_2), methylene blue (MB), rhodamine B (RhB), hydrochloric acid (HCl) was obtained from Wako Pure Chemical Industries Ltd, Japan. Deionized water (18.25 M Ω cm) produced by a Milli-Direct 16 (Millipore Q, USA) was used for the entire experiment. All the reagents and materials were used without further purification unless otherwise specified. For the sonication process, a bath ultrasonicator (AS ONE Ultrasonic Cleaner Single Frequency, 3L (MSC-3) 40 kHz, 100W) was used as described below.

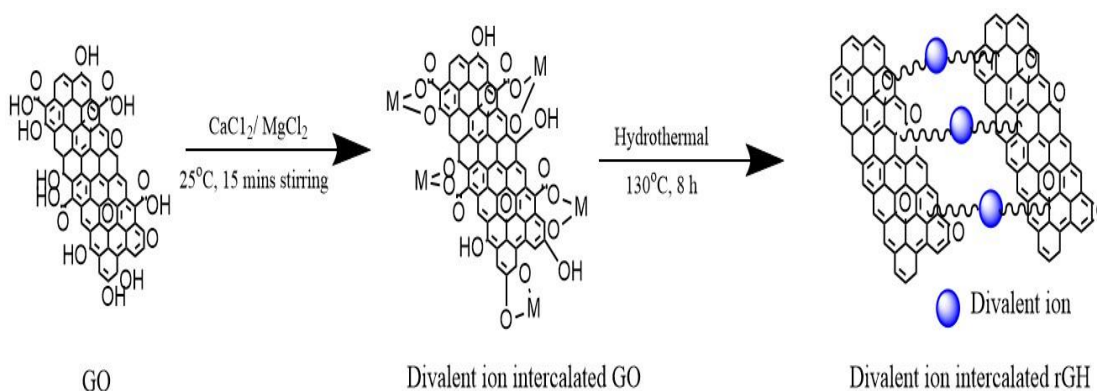
3.2.2. Synthesis of divalent ion intercalated reduced graphene hydrogel

30 mL of GO solution was prepared by the sonication of GO dispersion in deionized water to a concentration of 2 mg/mL for 1.5 hours to exfoliate the graphene sheets. 10 mL of 0.01 M MgCl_2 and CaCl_2 was added into the GO solution, respectively, and stirred for 15 minutes. The solution mixture was then transferred into an 80 mL modified autoclave glass bottle and sealed. The hydrothermal reduction was carried out in a high-pressure steam sterilizer (TOMY LBS-325) at 130°C for 8 hours. The resulting reduced graphene hydrogels (rGH) were then dialyzed in H_2O for 24 h. The obtained rGHs were denoted as rGH-Mg and rGH-Ca to ease identification. The hydrothermal treatment of GO solution (40 mL) without the addition of divalent salt was also carried out and denoted as rGH. The rGH samples were then freeze-dried at -50°C for 24 hours to remove any moisture content without destroying the 3D macrostructure. The freeze-dried rGHs were kept for characterization studies as described below.

3.2.3. Characterizations

The absorption spectrum of the colloidal suspension of individual GO and with the presence of MgCl_2 and CaCl_2 were measured by UV-vis spectrophotometer (Genesys 10s, Thermo Fisher Scientific). The zeta potential and particle size analysis of the colloidal suspension were determined using DelsaMax Pro Beckman Coulter, Inc. The morphology of the freeze-dried hydrogels was accessed using JEOL 6000 microscope scanning electron microscopy (SEM) attached with an energy dispersive X-ray analyzer (EDX)

operated at 10kV accelerating voltage. The crystalline structure was recorded on a Rigaku X-ray diffractometer with Cu K- α radiation at 40kV and 15 mA with a scan rate of 10°/min. FTIR spectroscopy was carried out on a PerkinElmer Spectrum GX. Thermogravimetric analysis (TGA) was performed on an EXSTAR TG/DTA7000 under a continuous N₂ stream. Raman spectroscopy measurements were performed using JASCO NRS-5100 Laser Raman Spectrometer with an excitation wavelength of 532 nm and a 2.5 mW laser power beam. The I_D/I_G ratio was automatically calculated using the Spectra Manager II software pre-installed after performing wavenumber correction and intensity correction. X-ray photoelectron spectroscopy (XPS) was performed on an Axis Nova (XPS) Surface Analyzer with a monochromatized Al K α X-ray source. The XPS spectra were analyzed for their relative atomic percentages of the element species present using the CasaXPS program. The peaks are fitted by Gaussian-Lorentzian (GL) formula fitted with a Shirley background. N₂ adsorption-desorption studies were carried out using a Surface Area and Pore Size Analyzer, Quantachrome Instruments. The surface area and pore size distribution of the rGH samples were calculated using the Brunauer-Emmett-Teller (BET) method via N₂ adsorption-desorption isotherms and the Barrete-Joynere-Halenda (BJH) method, respectively.



Scheme 3.1. The schematic representation of the formation of divalent ion intercalated reduced graphene hydrogel without taking into account the interactions that occurred for the formation of a hydrogel

3.2.4. Adsorption experiments

Analytical grade dyes, cationic MB, and RhB were used as model pollutants for the adsorption experiment at room temperature to probe the adsorption performance of the hydrogels. The as-prepared hydrogels were placed into 20 mg/L, 150 mL dye solution, and agitated until adsorption-desorption equilibrium is achieved. For each experimental run, 2 mL of the dye solution was removed at a specific time interval and centrifuged at 2000 rpm for 5 min to remove suspended particles before residue dye absorbance measurements were taken. From Fig. S3.1, the residual concentration of the MB and RhB were computed from the calibration curve prepared by measuring the absorbance at various concentrations of the dye at 664 and 554 nm, respectively. The adsorption capacity (Q_e) for the hydrogels were calculated using the following equation:

$$Q_e = \frac{(C_0 - C_t)V}{m} \quad (1)$$

where C_0 represents the initial concentration (mg/g), C_t represents the equilibrium concentration at the specific time(mg/g), V is the volume of the dye solution (L) and m is the mass of the adsorbent (mg). Three kinetic models, namely pseudo-first-order (PFO), pseudo-second-order (PSO), and Elovich were used to understand the adsorption kinetics of the MB and RhB adsorption. PFO corresponded to a diffusion-controlled process in a solid-liquid phase. PSO assumed the process is controlled by adsorption reaction at a liquid-solid interface. Elovich model was applied to describe the adsorption in a non-ideal state. The model assumes that the rate of solute adsorption decreases exponentially as the amount of adsorbed solute increases. The models' equation can be described as follows:

The pseudo-first-order (PFO) model:

$$\ln(Q_e - Q_t) = \ln Q_e - \frac{K_1 t}{2.303} \quad (2)$$

The pseudo-second-order (PSO) model:

$$\frac{t}{Q_t} = \frac{1}{K_2 Q_e^2} + \left(\frac{1}{Q_e}\right) t \quad (3)$$

The Elovich model:

$$Q_t = \frac{1}{\beta} \ln \alpha \beta + \frac{1}{\beta} \ln t \quad (4)$$

where Q_e and Q_t are the dye amount adsorbed at equilibrium (mg/g), k represents the time, K_1 (h^{-1}) or K_2 (g/mg.h) refers to the adsorption rate constant, α is the initial adsorption rate (mg/g) and β is the desorption coefficient (mg/g). To further confirm the diffusion mechanism process, the intraparticle diffusion (IPD) model was also applied and can be written as:

$$Q_t = K_p t^{1/2} + C \quad (5)$$

where K_p is the rate constant of the intraparticle diffusion kinetic model, C is the thickness of the boundary layer.

The Langmuir, Freundlich, and Temkin adsorption isotherms were applied in the process to probe the adsorption process by fitting the equilibrium data. The Langmuir model presumes monolayer adsorption onto a homogenous adsorbent surface with the idea that energy change is uniform for all adsorption. On the other hand, the Freundlich model assumes that multilayer adsorption occurs on a heterogeneous surface. On the other hand, the Temkin model assumes that the heat of adsorption decreases linearly instead of logarithmically with the increase in the surface coverage and that adsorption can be characterized by uniform binding energies. The linear form of the equation employed to describe the adsorption isotherm is as follows:

Langmuir isotherm model:

$$\frac{C_e}{Q_e} = \frac{1}{K_L Q_m} + \frac{C_e}{Q_m} \quad (6)$$

Freundlich isotherm model:

$$\ln Q_e = \ln K_F + \frac{1}{n} \ln C_e \quad (7)$$

Temkin isotherm model:

$$Q_e = \frac{RT}{B} \ln K_T + \frac{RT}{B} \ln C_e \quad (8)$$

where C_e is the equilibrium concentration of the dye solution (mg/L). Q_e and Q_m are the adsorption capacity (mg/g) adsorbed on the adsorbent at equilibrium and maximum adsorption capacity (mg/g), respectively.

K_L is the Langmuir binding constant (L/mol), K_F is the Freundlich binding constant (L/mol), K_T is the equilibrium binding constant (L/mol) corresponding to maximum binding energy and $1/n$ is the adsorption intensity. B is related to the heat of adsorption (J/mol), R is the universal gas constant (8.314 J/K. mol) and T is the absolute temperature (K).

3.3 Results and Discussion

Before hydrothermal reaction, the addition of $MgCl_2$ and $CaCl_2$ into the GO suspension led to the intercalation between the divalent atoms and the oxygen-containing functional groups occurring between the basal plane and edges; hence leading to a network of continuous bridging[123,124]. The divalent ions (M^{2+}) may interact with GO sheets via two different binding modes. The strongest binding mode is the M^{2+} ions bound to the carboxylic group at the edges which results in the cross-linking with neighboring sheets. The second, from the creation of C-OH due to the ring-opening epoxide by M^{2+} which facilitates the intercalation of metal ions into the gallery between GO sheets[124]. To probe the interaction with the divalent ions, UV-visible analysis was conducted on the GO suspension which is shown in Fig. S3.2. The UV-Vis spectrum of GO suspension after sonication showed two distinct bands, a maximum at 262 nm attributed to π - π^* transition of the aromatic C-C bonds, and the shoulder peak at 302 nm corresponds to the n - π^* transition of the carbonyl C=O bonds[125]. The decrease in intensity of the shoulder peak and also the slight blue shift could be possible from the intercalation of the divalent ion with the oxygen-containing functional groups. Saha *et al.*,[126] found the blue shifting upon studying the effect of anionic surfactant (SDS) intercalation on GO. From Table 3.1, the addition of the neutral salt solution of $MgCl_2$ and $CaCl_2$ does not bring significant changes to the pH of the GO suspension. To further confirm the intercalation behavior and access the colloidal stability, DLS and zeta potential studies were conducted. The increase in the lateral size of the GO and also the increase in zeta potential value after the inclusion of the divalent ion in the GO suspension indicated that Mg^{2+} and Ca^{2+} showed good affinity towards the oxygen functional groups GO sheets are highly negative charged which is attributed to the ionization of oxygen-containing functional groups present at the basal and planar plane. We posit that the higher particle diameter obtained for rGH-Ca is attributed to the larger ionic size of Ca^{2+} for easier chelation with the oxygenated group of the GO[127]. The higher hydration energy of $MgCl_2$ led to the greater volumetric dimension of its hydrated ion

which may limit their interactions via ionic cross-linking with the negatively charged GO sheets[128]. Zeta potential values below (more negative) than -30 mV are considered ideal to represent sufficient electrostatic repulsion to ensure a stable dispersion[129]. The more positive zeta potential values obtained for the colloidal suspension of GO in the presence of divalent ion occur due to the lower charge density of GO from the interaction with negatively charged functional groups.

Table 3.1. Properties of the GO colloidal suspension in the presence of MgCl₂ and CaCl₂.

Sample	pH	Diameter (nm)	Zeta Potential (mV)
GO	2.70	2015.2	-39.24
GO + MgCl ₂	2.69	4563.3	-36.63
GO + CaCl ₂	2.69	7680.9	-32.37

Fig. S3.3 depicts the hydrogels after the freeze-drying process which showed the retainment of the cylindrical monolith reduced graphene hydrogel in the presence of the Mg²⁺ and Ca²⁺. The surface of the reduced graphene hydrogel after freeze dry becomes hydrophobic[53,79]. From previously reported studies, the freeze-drying process removed water molecules embedded in the pore structure which leads to the collapse of the framework due to π-π interactions between the graphene sheets. It can be seen that the presence of Mg²⁺ and Ca²⁺ introduced in the graphene framework preserved the cylindrical structure of the hydrogel. It is posited that the divalent ion bridged the individual graphene sheets; hence retaining the hydrogel structure.

Fig. 3.1 depicts SEM images of the freeze-dried hydrogels. GO possesses a wrinkled surface topography and a disorderly manner as depicted in Fig. 3.1(a) which can be attributed to the deviation from the sp² planar character of the carbon atom. Based on Fig. 3.1(b-d), the morphology of rGHs depicted a randomly oriented 3D framework after hydrothermal treatment. The reduced graphene nanosheets are of aggregated crumples nanosheets which were similar to previous literature obtained via hydrothermal treatment[30]. The aggregation of reduced graphene sheets is attributed to the increased hydrophobic interactions between individual sheets. The intercalation of the divalent ion may occur electrostatically in which the ion

coordinates with the carboxylic groups; hence forming linkages between the reduced graphene sheets. In the situation in which the carboxylic groups are saturated, electrostatic repulsion between other carboxylic groups is reduced, leaving the system to interact through the $\pi=\pi$ bond network which drives the stacking[130]. The intercalation of Mg^{2+} and Ca^{2+} can be roughly accessed from the atomic elemental composition from the EDX signals assigned to Mg and Ca. Even though the peak signal is relatively low (< 1% atomic percentage), the inclusion of the divalent ion altered the morphology in terms of the introduction of more pore cavities.

Table 3.2. Elemental composition of GO, rGH, rGH-Mg, and rGH-Ca obtained from EDX analysis

Sample	C	O	S	K	Mg	Ca	Total
	(%)	(%)	(%)	(%)	(%)	(%)	(%)
GO	55.99	39.82	3.81	0.38	0.00	0.00	100.00
rGH	75.31	24.69	0.00	0.00	0.00	0.00	100.00
rGH-Mg	76.15	23.28	0.00	0.00	0.57	0.00	100.00
rGH-Ca	76.74	22.49	0.00	0.00	0.00	0.77	100.00

The elemental analysis of the commercial GO as well as the rGHs samples were summarized in Table 3.2. The presence of a trace amount of S and K in the commercial GO sample may be attributed to the residue reactants used during the manufacturing process. The C/O atomic percentage (at. %) of GO, rGH, rGH-Mg, and rGH-Ca is 1.40, 3.05, 3.27, and 3.41, respectively. The slight increase in the C/O ratio indicates that the intercalation of Mg^{2+} and Ca^{2+} further assisted in the removal of the oxygenated functional groups during the hydrothermal treatment. The result of the intercalation of the divalent ion creates C-OH from the to the ring-opening epoxide which can be directly desorbed from the graphene sheet due to Coulomb repulsion derived from the extra charge accumulation[131]. Hence, the rearrangement of aromatic sp^2 carbon resulted in a higher C/O ratio for the divalent ion intercalated hydrogels. The difficulty of Mg^{2+} intercalation in comparison to Ca^{2+} can be attributed to the strong electrostatic forces between the Mg ions and the negatively charged groups on the graphene sheet which induce the intrinsically slow kinetics of ion insertion and diffusion[132].

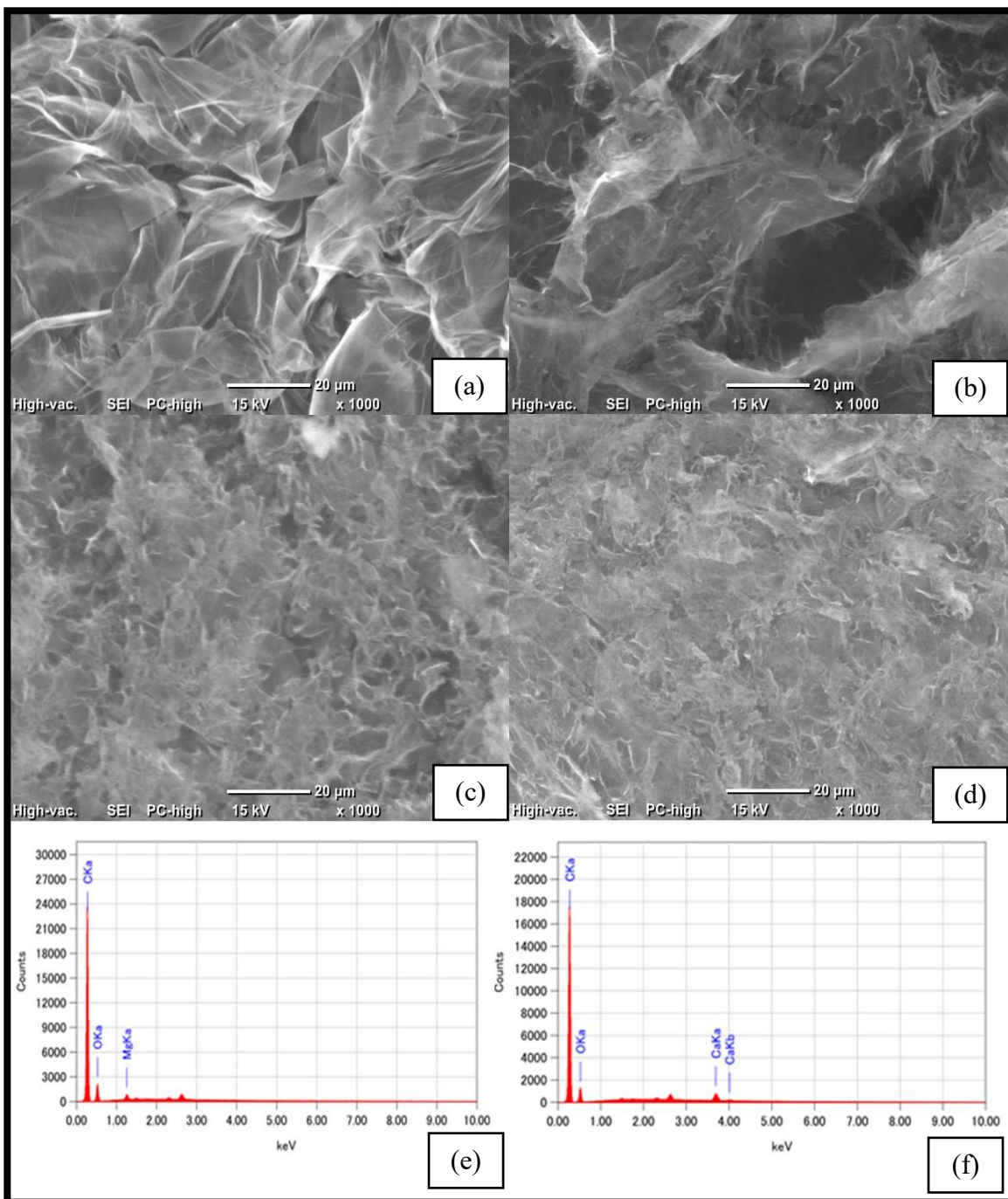


Fig. 3.1. SEM images of freeze-dried (a) GO, (b) rGH, (c) rGH-Mg, (d) rGH-Ca. EDS spectrum with elemental distribution for (e) rGH-Mg and (f) rGH-Ca

The interlayer spacing of GO and the freeze-dried hydrogels were confirmed using powder X-ray diffraction (XRD). From Fig. 3.2(a), the diffractogram of the commercial freeze-dried GO exhibited a sharp peak at 7.25° corresponding to the characteristic carbon peak (001) with a d-spacing of 1.21 nm. The larger

d-spacing obtained from GO upon comparing to other previous reported findings[133] (~0.80 nm) could be attributed to the freeze-drying process that retains the graphene framework. The d-spacing of the most intense peak was calculated by using Bragg's equation which is presented as:

$$n\lambda = 2 d \sin \theta \quad (9)$$

where n is an integer, λ is the X-ray wavelength and θ is the angle between incidence and reflected rays.

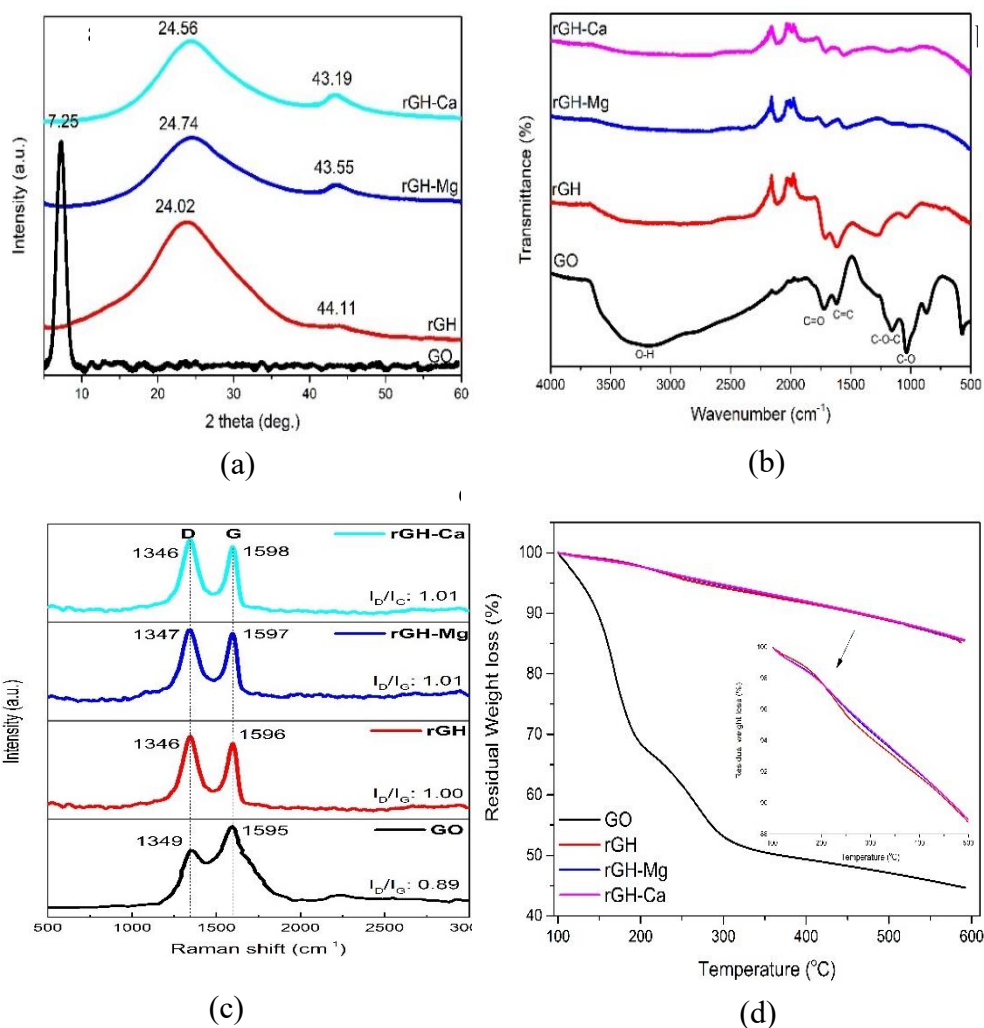


Fig. 3.2. (a) XRD, (b) FTIR, (c) Raman spectrum (d) TGA thermogram of GO, rGH, rGH-Mg, and rGH-Ca

The reduction of GO led to the disappearance of the (0 0 2) peak and appearance of a well-resolved diffraction peak observed at 24.02°, 24.74°, and 23.56° corresponding to d-spacing values of 0.370, 0.360,

0.362 nm for rGH, rGH-Mg, and rGH-Ca, respectively. The finding indicated that GO has been successfully reduced to its' reduced form via hydrothermal treatment. The intercalation of the divalent ion resulted in reduced interlayer spacing in comparison to rGH. The presence of small diffraction peaks, 2θ at ~ 43.0 - 44.0° is related to the (1 0 2) plane of reduced graphene structure. Hence, the inclusion of intercalated Mg^{2+} and Ca^{2+} between the graphene layers led to the decrease in the interlayer spacing making the sheets packed tightly to one another; which signified the intercalation of the divalent ions into the graphene framework.

FTIR provided an overview of the presence of chemical functionalities in the freeze-dried hydrogels. Fig. 3.2(b) depicts the ATR-FTIR spectra of GO, rGH, rGH-Mg, and rGH-Ca. The spectrum of GO with following peaks: $1,080\text{ cm}^{-1}$ corresponded to C-O (alkoxy group), $1,280\text{ cm}^{-1}$ (epoxy group), $1,618\text{ cm}^{-1}$ associated with the presence of C = C (aromatic), and $1,750\text{ cm}^{-1}$ assigned to C = O (carboxyl group) present mostly along the sheet and basal plane. The broad peak at $3,212\text{ cm}^{-1}$ originated from the hydroxyl O-H bond. The hydrothermal reduction of the GO led to the significant weakening of the O-H and C=O peaks and is apparent in the Mg^{2+} and Ca^{2+} intercalated reduced graphene hydrogels. Moreover, the intense weakening of alkoxy groups (1040 cm^{-1}) and the epoxy groups for the divalent ion intercalated samples indicated possible interaction with the groups. The peak at about 1550 cm^{-1} confirmed the restoration of the sp^2 carbon network while the peak at around 1710 cm^{-1} corresponded to vibrations of carbonyl groups. Hence, the intercalation is posited to occur from the interaction of the divalent ion to the carboxylic group which is linked to the neighboring sheet. The intercalation in between the graphene sheets also may occur from the ring-opening epoxide by the divalent ions. A similar result corroborated the study by Park et al.[124], in which the epoxy/ether C-O stretch significantly decreased after exposure to Lewis acidic divalent metal ions leading to the ring-opening of the epoxide.

Raman spectroscopy characterization was carried out to access the intercalation effect of Mg^{2+} and Ca^{2+} towards the defects and disorder within the graphene sheet structure. The Raman spectra of GO, rGH, rGH-Mg, and rGH-Ca are depicted in Fig. 3.2(c). The two characteristics bands of GO located at 1392 and 1596 cm^{-1} were assigned to the D and G band, respectively. The D band is assigned to the breathing mode of k point phonons with A_{1g} symmetry and band attributed to the sp^3 hybridization of carbon; G band on the other hand is the characteristic peak from sp^2 hybridization corresponding to the E_{2g} phonon scattering of

carbon atoms. The weak band present around 2640 cm^{-1} is often associated with the 2D band due to the second-order two phonons with opposite momentum in the highest optical branch adjacent to the K point of the Brillouin zone[134]. After the hydrothermal reaction, the D band peak remained unchanged while the G-band peak of their reduced state red-shifted. The increase in the number of sp^2 atomic domains and also the successful reduction of GO to a reduced state were evident from the redshift in the G band[29]. The intercalation induces a red shift of the G band due to the lower Fermi energy level and shifts the band gap due to the doping effect. The slight shift of the G band of the divalent ion intercalated reduced graphene hydrogel in comparison to rGH also confirms the interaction between graphene and the divalent ion due to charge transfer which has been previously reported[135]. The probing into the order/disorder crystal structures can be observed from the integrated intensity ratio (I_D/I_G) between the D and G bands. The I_D/I_G of GO, rGH, rGH-Mg, and rGH-Ca is 0.89, 1.00, 1.01, and 1.01, respectively. The increase in the ratio indicated the decrease in the average size of sp^2 carbon domains suggesting the easier orientation of the aromatic rings after the removal of the oxygen-containing functional groups. The intercalation of Mg^{2+} and Ca^{2+} induced a higher I_D/I_G ratio in which it is hypothesized that the divalent ions do not introduce defect from their interaction with the epoxy and carboxyl groups as supported by the FTIR result. The lateral dimension size of the sp^2 carbon cluster (L_a) can be calculated using the following equation[136,137].

$$L_a \text{ (nm)} = (2.4 \times 10^{-10})\lambda^4 \frac{1}{I_D/I_G} \quad (10)$$

where λ is the Raman excitation wavelength of the laser (532 nm). Based on the I_D/I_G obtained from Fig. 3.2(c), the calculated L_a values were 21.60, 19.22, 19.03, and 19.03 for GO, rGH, rGH-Mg, and rGH-Ca, respectively. The intercalation of the divalent ions within the hydrogel framework reduced the L_a value suggesting a decrease in the average in-plane crystallite size of the sp^2 carbon.

Thermogravimetric analysis (TGA) was further used to probe the thermal stability of the prepared samples. Fig. 3.2(d) displays the TGA thermograms for GO, rGH, rGH-Mg, and rGH-Ca, respectively. GO showed major weight loss (~30%) between 100 and 200°C which can be attributed to the removal of labile functional groups such as hydroxyl, epoxy, and carbonyl which yielded CO, CO₂, and steam[138]. The reduced state samples exhibited a smooth weight loss curve which can be attributed to the removal of most oxygen functional groups via the hydrothermal process. Between 100-200°C, the weight loss of the divalent ion intercalated samples was slightly higher than that of rGH, suggesting higher moisture content. It can be

inferred that the intercalation of Mg^{2+} and Ca^{2+} increases the hygroscopicity of the hydrogels. Closer inspection from the inset in Fig. 3.2(d) showed that the rGH-Mg and rGH-Ca exhibited slight improvement in their thermal stability between 200-400°C with a lower mass loss reported which can be attributed to the intercalation effect. However, the weight loss of the hydrogel samples remained similar beyond 400°C.

Table 3.3. Elemental composition, and C 1s binding energy obtained from XPS

Sample	Elemental composition (%)				C1s Deconvolution (%)						
	C	O	Mg	Ca	Csp ²	Csp ³	C-O	C=O	O- C-O	C(O)OH	π - π*
rGH	67.92	32.08	0.00	0.00	69.50	9.10	13.18	2.80	3.04	0.60	1.78
rGH-Mg	76.65	22.46	0.89	0.00	71.72	15.77	5.92	1.89	1.48	1.95	1.26
rGH-Ca	73.54	24.47	0.00	1.99	71.89	13.41	6.23	3.76	1.87	1.58	1.27

XPS characterization was further carried out to investigate the elemental composition and also to confirm the successful intercalation of the Mg^{2+} and Ca^{2+} within the reduced graphene framework. The quantified atomic concentration of the functional groups is shown in Table 3.3. Fig. 3(f) depicts the XPS wide spectra of rGH, rGH-Mg, and rGH-Ca. The typical C 1s and O 1s peaks can be observed for all the freeze-dried samples with a trace amount of Mg and Ca from the intercalation with the graphene sheets. Although the Ca 2p and Mg 2p peaks cannot be observed clearly from the wide peak spectrum, the split peaks indicated otherwise. The atomic percentage of Ca is greater than Mg by one-fold which substantiates the notion that Mg^{2+} is difficult to chelate with the oxygenated groups of the graphene sheets. The low content of the divalent ion could be the reason for their weak signal strength. The deconvoluted high-resolution C 1s region of the samples was shown in Fig. 3 (a-c), possessing peak binding energies at around 284.6, 285.4, 286.3, 287.1, 287.9, 289.1, and 290.3 eV assigned to C=C, C-C, C-O, C=O, O-C-O, C(O)OH, and π -π*, respectively. It can be seen that the atomic percentage of alkoxy and epoxy groups significantly decreased which further supports the notion that intercalation occurs via ring-opening epoxide by the divalent ions and also via the alkoxy groups. The findings corroborated the result obtained via FTIR. The increase in the Csp² atomic composition percentage also suggests that the divalent ion-assisted in the rearrangement of the

C=C aromatic structure. Fig. 3.3(d) depicts the fitted Mg 2p core-level spectra deconvoluted to Mg 2p_{1/2} and Mg 2p_{3/2}. The binding energy at 51.4 eV and 48.6 eV correspond to the Mg²⁺ state and Mg⁰, respectively. As for the Ca 2p spectra in Fig. 3.3(e), the deconvolution at 347.9 and 351.4 eV are attributed to the Ca 2p_{3/2} and Ca 2p_{1/2}. The split of 3.5 eV between the two peaks is evident for the presence of Ca²⁺ coordination within the graphene framework[122].

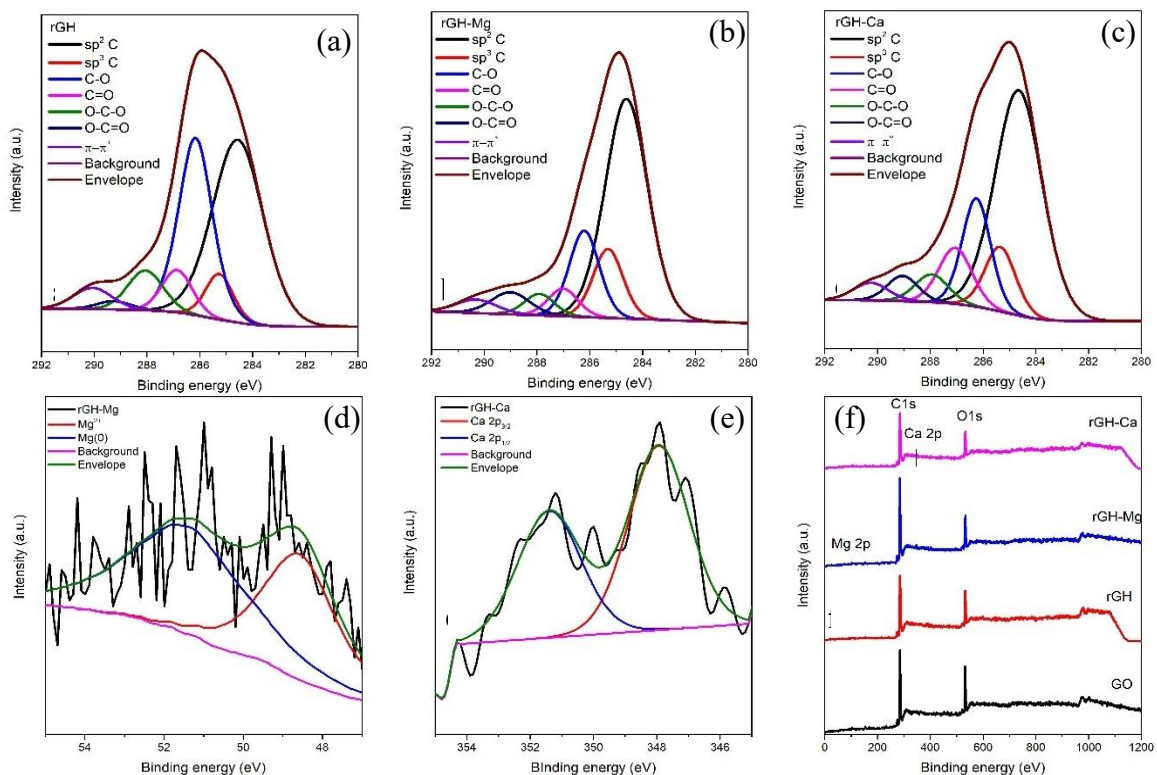
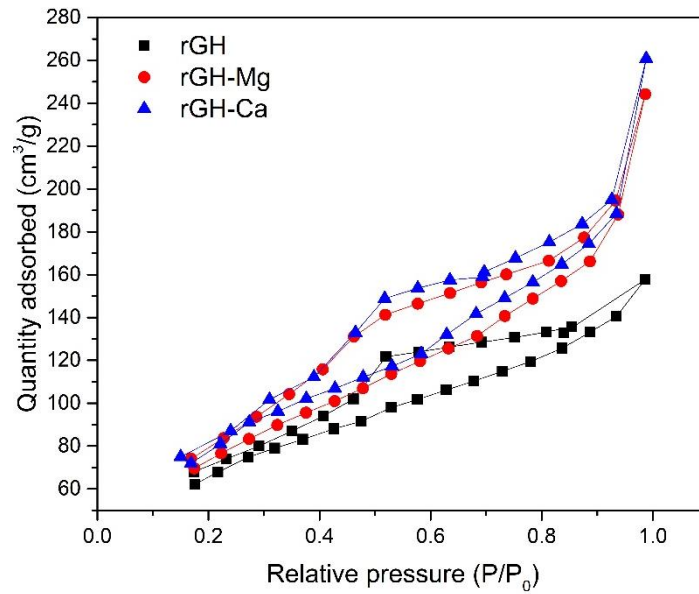
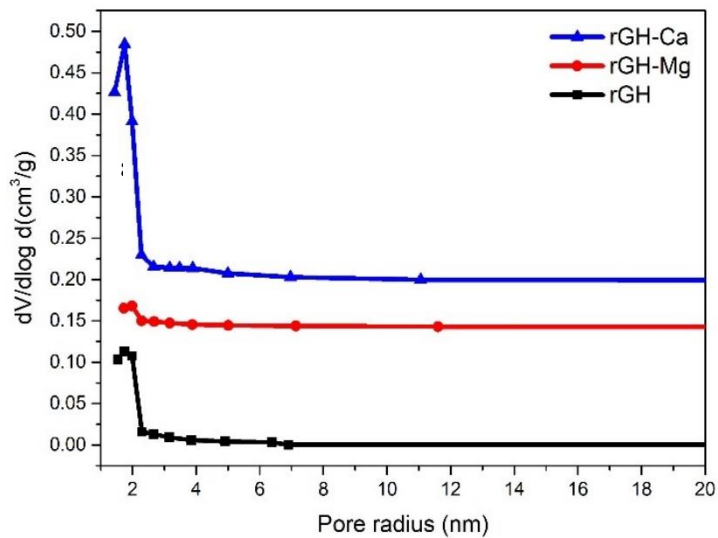


Fig. 3.3. (a-c) C 1s split spectra of rGH, rGH-Mg, and rGH-Ca. (d) Mg 2p split spectra of rGH-Mg. (e) Ca 2p split spectra of rGH-Ca. (f) wide spectra of GO, rGH, rGH-Mg, and rGH-Ca



(a)



(b)

Fig. 3.4. (a) N_2 adsorption-desorption isotherm and (b) BJH pore size distribution of the freeze-dried rGH, rGH-Mg, and rGH-Ca

Fig. 3.4(a) depicts the nitrogen adsorption-desorption isotherm of the freeze-dried rGH, rGH-Mg, and rGH-Ca which exhibited an H3 hysteresis loop with the typical type IV isotherm suggesting the presence of mesopores and slit-like pores. It can be seen that the hysteresis loop closes below 0.4 P/P_0 which is possible from the smaller neck diameter than the critical size on the reduced graphene hydrogel surface

which led to the desorption mechanism occurring from larger pores involving cavitation [139]. From Table 3.4, rGH-Ca was found to exhibit the largest surface area at 63.09 m²/g; followed by rGH-Mg at 50.48 m²/g and rGH at 41.14 m²/g. The increase in the surface area can be attributed to the successful intercalation of the Mg²⁺ and Ca²⁺ that become cross-linkers and also act as spacers between the graphene sheets which create a porous framework. However, the surface area was lower than the theoretical value of exfoliated pristine graphene which is about 2600 m²/g which may be attributed to the varying synthesis/drying process. The significant decrease of the hydrogel's surface area could be attributed to the aggregation of the sheets during GO sonication leading to the coalescing of the reduced graphene sheets after hydrothermal treatment as supported by SEM results. The estimation into the number of stacking of the graphene sheets can be further realized by applying the scaling law which is described as [140,141]:

$$N = 2600 / A \quad (11)$$

where the N is the number of graphene sheets per plate, 2600 is the theoretical surface area of graphene (m²/g) [142] and A is the experimental BET surface area measured (m²/g). It can be seen that the estimated number of graphene sheets present is 63, 47, and 41 for the freeze-dried rGH, rGH-Mg, and rGH-Ca, respectively. Fig. 3.4(b) shows the pore size distribution of the freeze-dried hydrogels with bimodal pore size distribution around 2 nm in radius for the mesopores. Barrett, Joyner, and Halenda (BJH) method were utilized in the calculation of the pore size distributions and volume from the experimental isotherms using the Kelvin model of pore filling as adapted in previous studies[143–145]. The data was readily obtained from the Nova e software program installed on the workstation. It can be observed that the intercalation of the Mg²⁺ and Ca²⁺ between the graphene sheets induced higher pore volume which is posited to occur due to the spacing effect elicited from the divalent ions. The higher pore volume obtained for rGH-Ca can be attributed to the larger ionic size of the Ca²⁺ in comparison to Mg²⁺. The larger surface area and pore volume after divalent ion intercalation should enhance the diffusion of liquid reactants which are beneficial for the dye adsorption process.

Table 3.4. BET surface area and textural properties of freeze-dried hydrogels.

Sample	Specific surface area m²/g	Pore radius Dv(r)	Pore volume cc/g
rGH	41.135	1.741	0.145
rGH-Mg	54.884	1.741	0.265
rGH-Ca	63.088	1.751	0.313

From previous studies, adsorption of dye compounds onto the highly porous graphene-based hydrogels can occur via several interactions which may include π - π interactions, electrostatic interactions, and hydrogen bonding interactions[146,147]. To evaluate the in-situ adsorption capacity of rGH, rGH-Mg, and rGH-Ca towards MB and RhB, the 'wet-hydrogel' sample was used instead of the freeze-dried samples. The wet hydrogel samples were placed in the dye solutions and agitated for 24 h to achieve the adsorption-desorption equilibrium. The water content present in the hydrogel matrix not only acts as supporting media and provides transport nanochannels but also promotes hydrogen bonding to induce the adsorption process[148, 149]. The findings indicated that the inclusion of a small amount of divalent ion in the hydrogel matrix could bring improvement in their adsorption capacities towards MB and RhB. Based on Fig. 3.5, the effect of initial dye concentration on the adsorption capacity of the hydrogels is shown. It can be seen that the amount of dye adsorbed increased with an increase in the initial concentration. The initial dye concentration provided an important driving force to overcome the mass transfer resistance of the dye and the hydrogel. High dye concentrations increase the gradient between the bulk solution and that of the adsorbent, which enhances the driving forces for the diffusion of dye molecules to the adsorbent surface[150]. Hence, the higher adsorption capacity for dye is expected at a higher initial concentration. Generally, the adsorption capacity for MB is higher as compared to the RhB because of the larger size of RhB[151]. The adsorption capacity of the rGH-Ca showed the highest adsorption capacity at a higher initial dye concentration (100 mg/L) for both MB and RhB. The adsorption behavior of RhB corresponds to the surface area of the hydrogel, with rGH-Ca performed the best attributed to their higher surface area in

comparison to rGH and rGH-Mg. As for MB adsorption, rGH-Mg and rGH-Ca possessed almost similar adsorption capacity at lower concentrations (20 and 50 mg/L) of dye concentration. It is posited that at a low concentration of dye solution, π - π interactions play a determining role in the adsorption process for rGH-Mg and rGH-Ca which is supported by the almost similar sp^2 atomic percentage obtained from the XPS result.

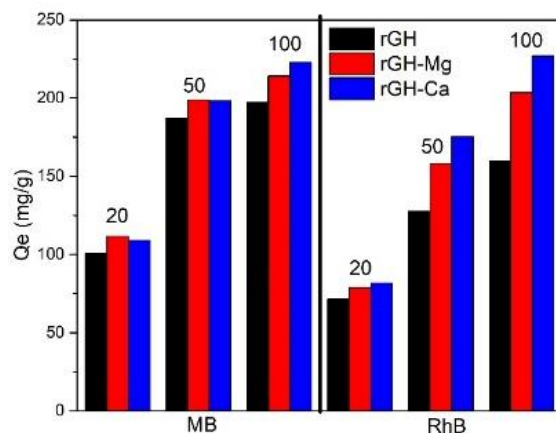


Fig. 3.5. The adsorption capacity of the rGHs using various initial concentration (20, 50 and 100 mg/L) of MB and RhB

Kinetic studies were carried out to understand the mechanism involved during the adsorption process. The linear plots of $\ln(Q_e - Q_t)$ vs t and $\ln(Q_e - Q_t)$ vs t/Q_t corresponding to the PFO and PSO are depicted in Fig. S3.4(a-d). The linear plot of the Elovich model is obtained from the Q_t vs. $\ln t$ as shown in Fig. S3.4(e-f). The lower regression value for the Elovich model proved that this model is not suitable to accurately describe the kinetic process. The kinetic parameters obtained from the models are displayed in Table 3.5. The kinetic data of MB and RhB adsorption using the hydrogels can be accurately described by the PSO model from the better regression coefficient as compared to the PFO and Elovich model. Moreover, the linear plots of t/Q_t versus t indicated good agreement between experimental results and the calculated values. For MB adsorption, the fastest adsorbing hydrogel is rGH followed by rGH-Mg and rGH-Ca. While for RhB adsorption, the rate of adsorption showed that rGH-Mg showed the highest rate followed by rGH and rGH-Ca. Thus, these results revealed that the diffusion of the dye molecules onto the hydrogels is

controlled adsorption, posited to be via chemisorption through binding reaction by sharing/exchange of electrons or covalent forces.

Table 3.5 Kinetic parameters obtained from the PSO, PSO, and Elovich kinetic model for the adsorption of MB and RhB

Sample	Pseudo-First Order			Pseudo-Second Order			Elovich		
	Q_e	K_1	R^2	Q_e	K_2	R^2	α	β	R^2
MB									
rGH	107.61	0.002902	0.96962	123.92	0.000024	0.98502	1.060	0.04440	0.93857
rGH-Mg	123.41	0.002902	0.95907	140.85	0.000018	0.97394	1.087	0.03985	0.91910
rGH-Ca	118.32	0.002695	0.93354	138.89	0.000018	0.97647	1.054	0.04054	0.92249
RhB									
rGH	40.55	0.001914	0.95924	74.68	0.0001242	0.98612	17.846	0.12314	0.74884
rGH-Mg	37.71	0.001794	0.96048	74.35	0.0001496	0.98806	31.446	0.13240	0.73716
rGH-Ca	40.55	0.002096	0.96130	87.26	0.0000981	0.98204	10.678	0.09706	0.75825

From Fig. 3.6, the plot of Q_t versus $t^{1/2}$ confirms the multistage adsorption of the dye molecules on the hydrogels with three slopes obtained. The first linear line indicated the transfer of dye molecules to the external surface posited to occur via strong electrostatic interactions. The second linear line corresponds to the slow adsorption step in which the dye molecules entered the internal porous network of the hydrogels via intraparticle diffusion. The final stage is the final equilibrium step, in which the dye molecules moved slowly from the larger pores to the smaller pores, leading to a retarded adsorption rate[152,153].

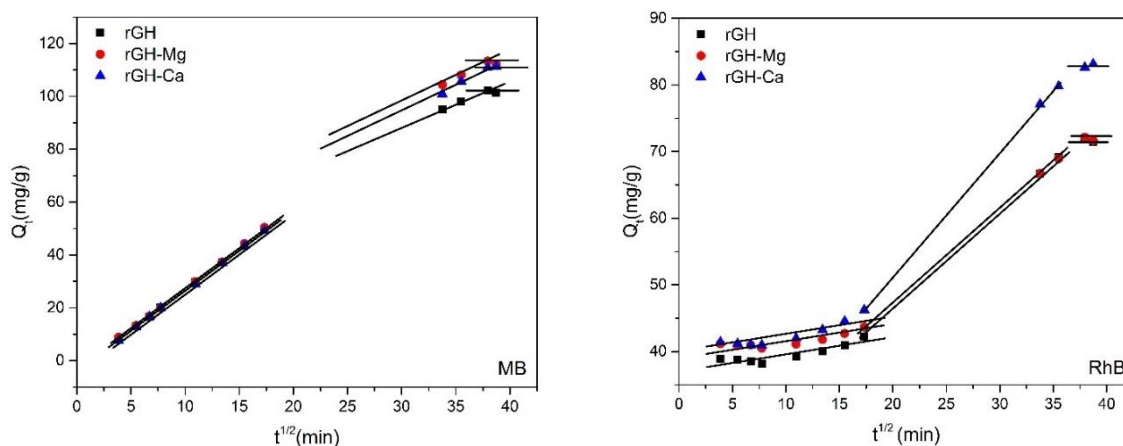


Fig. 3.6. Intraparticle diffusion plot of MB and RhB adsorption onto the hydrogels

From Table S3.4, the negative C value obtained for MB adsorption can be attributed to the combined effects of film diffusion and surface reaction control which has been previously reported[154]. For MB adsorption, $K_1 > K_2$ indicated a faster diffusion process during the initial stage of adsorption. However, as for RhB adsorption, the value of $K_1 > K_2$, indicating that IPD process was faster than the first step. Hence, it is considered that surface adsorption involving PSO and IPD are involved simultaneously in the adsorption of the dye compounds.

The study into the adsorption isotherm provided vital insights into the interaction behavior of the adsorbate and adsorbent. It is important to establish the correlation for the equilibrium curve for the optimization of a dye adsorption system. Table 3.6 summarizes the equilibrium isotherm constant for the adsorption of MB and RhB using the hydrogels. For both the adsorption of MB and RhB, it was found that the experimental data conformed to the Langmuir isotherm model yielding linear correlation coefficients (R_2) closer to unity for rGH, rGH-Mg, and rGH-Ca as compared to Freundlich and Temkin isotherm model. Hence, it can be posited that the adsorption sites on the rGHs were occupied by dye molecules in monolayer form having the same adsorption energy. Further, Langmuir isotherm can be used to access the maximum adsorption capacity (Q_m) of the hydrogels towards MB and RhB. Interestingly, the maximum adsorption capacity for MB followed the following trend: rGH (282.49 mg/g) > rGH-Ca (224.22 mg/g) > rGH-Mg (243.31 mg/g). From XPS measurement, the presence of a higher percentage of oxygenated functionalities on rGH promote interactions with the MB. It is posited that the surface of rGH is surrounded by a higher number of functional groups such as carboxyl, hydroxyl and epoxy groups as the binding sites which drive the adsorption capacity with the cationic dye, MB. However, the interaction between the divalent ion intercalated rGH showed higher K_L values which indicated greater interaction between rGH and MB which is important for the post-treatment process. On the other hand, the RhB adsorption followed the following isotherm model in order: Langmuir > Temkin > Freundlich. The maximum adsorption capacity (Q_m) for RhB followed the following trend: rGH-Ca (299.40 mg/g) > rGH-Mg (260.42 mg/g) > rGH (192.31 mg/g) which showed that the intercalated divalent ion improved the maximum adsorption capacity by almost 35% and 57% for Mg^{2+} and Ca^{2+} , respectively. The affinity between adsorbate and adsorbent was accessed using the dimensionless separation factor, R_L which can be expressed as:

$$R_L = \frac{1}{1 + K_L C_0} \quad (11)$$

where K_L is the calculated Langmuir constant and C_0 is the initial concentration of the dye solution. Often, the R_L ($0 < R_L < 1$) indicate a favorable isotherm, while ($R_L > 1$) is unfavorable and ($R_L = 1$) is linear. The separation factors calculated for all the hydrogel samples indicated that the adsorption of both the cationic dyes is favorable.

Table 3.6. Langmuir, Freundlich, and Temkin equilibrium isotherm constant for the adsorption of MB and RhB

Sample	Langmuir model			Freundlich model			Temkin model		
	Q_m	K_L	R^2	K_F	n	R^2	K_T	B	R^2
MB									
rGH	282.49	0.09056	0.98769	78.40	4.937	0.45218	0.3208	132.33	0.66571
rGH-Mg	224.22	0.29419	0.99999	87.62	4.4905	0.89475	0.5799	111.74	0.55911
rGH-Ca	243.31	0.15498	0.99968	69.66	3.4775	0.88091	0.3039	140.57	0.66571
RhB									
rGH	192.31	0.006157	0.99968	31.05	2.602	0.95183	0.6045	41.72	0.99476
rGH-Mg	260.42	0.049016	0.99999	29.88	2.177	0.95183	0.3370	69.60	0.99187
rGH-Ca	299.40	0.045294	0.99906	29.62	2.026	0.94789	0.3681	73.00	0.99903

In terms of the adsorption performance of the divalent ion intercalated rGH with previously reported adsorbent for MB and RhB, the intercalated divalent rGHs were comparable to that of previously reported adsorbents. Table 3.7 represents some adsorption capacity of some hydrogel-based adsorbents. The differences in their adsorption capacity can be attributed to various factors including the functionalities, textural properties, and experimental conditions. The results showed that the adsorption capacity of divalent ion intercalated rGH prepared using the facile hydrothermal method can be beneficial in the preparation of adsorbents with high structural integrity. It is posited that the adsorption of various noxious pollutants such as heavy metals, emerging contaminants, etc is also possible using the divalent ion intercalated rGHs.

Table 3.7. Adsorption capacities of MB and RhB onto various hydrogel-based adsorbents

Adsorbate	Adsorbent	Kinetic model	Adsorption isotherm	Q_e (mg/g)	Reference
MB	rGH	PSO/IPD	Langmuir	123.92	This work
	rGH-Mg	PSO/IPD	Langmuir	140.85	This work
	rGH-Ca	PSO/IPD	Langmuir	138.89	This work
	Ag/TPP/rGH	PSO	-	130.37	[18]
	P(HEMA-co-DMMa) copolymer	PSO	Langmuir	80.27	[155]
	CS-CNT	PSO	-	21.74	[156]
	P-N-GO	PSO	-	12.71	[157]
	PVA/PCMC/GO/bentonite	PSO	Langmuir	157.50	[158]
	TA-rGH	PSO	Langmuir	348.40	[159]
	PAAm-Agar/Clay@rGO	PSO	Langmuir	189.00	[160]
RhB	GO - cellulose nanowhiskers	PSO	-	122.5	[161]
	rGH	PSO/IPD	Langmuir	74.68	This work
	rGH-Mg	PSO/IPD	Langmuir	74.35	This work
	rGH-Ca	PSO/IPD	Langmuir	87.26	This work
	GO - cellulose nanowhiskers	PSO	-	62	[161]
	rGO/Nd ₂ O ₃	PSO	-	244.50	[162]
	PAAm-Agar/Clay@rGO	PSO	Langmuir	186.40	[160]
	P-N-GO	PSO	-	11.91	[157]
CS-CNT	PSO	-	9.66	[156]	

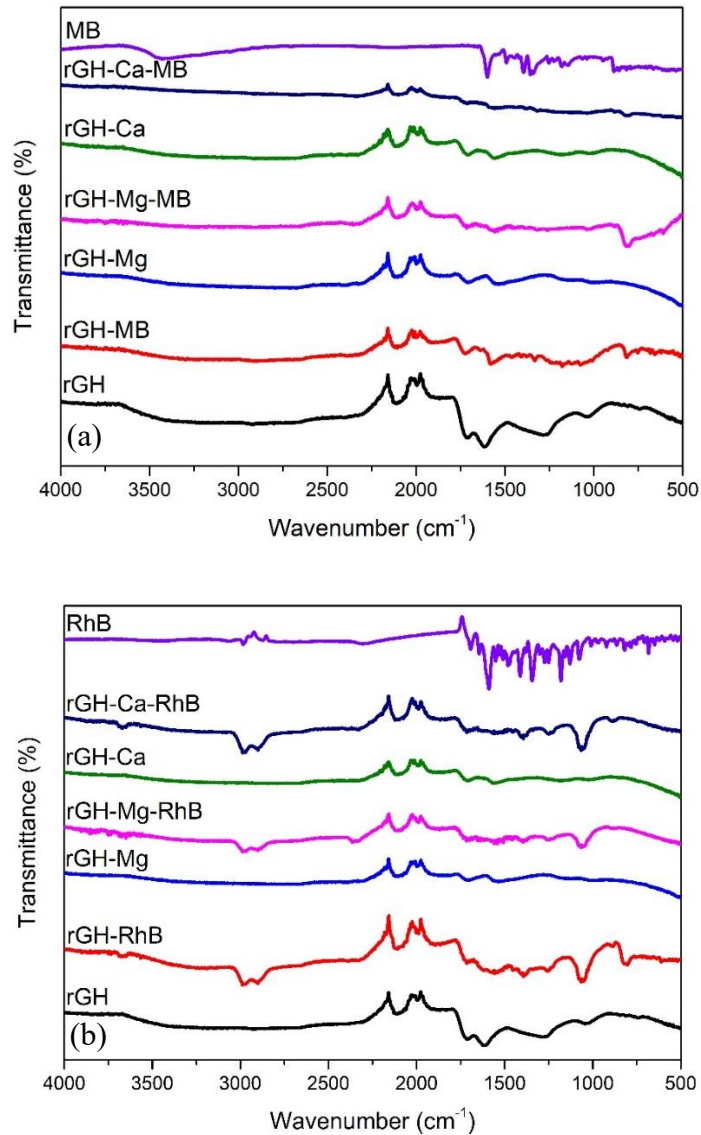


Fig. 3.7. FTIR of freeze-dried rGHs before and after adsorption with (a) MB and (b) RhB

To elucidate the active sites and interaction between the as-prepared reduced graphene hydrogels and the dyes, the hydrogels collected after adsorption for 24 h were freeze-dried and subjected to FTIR analysis. The interaction of the cationic dyes might occur either via physical or chemical bonding such as π - π interactions, hydrogen bonding, and/or via electrostatic interactions. The FTIR before and after the adsorption of MB and RhB was shown in Fig. 3.7(a) and 3.7(b), respectively. For pure MB, peaks appearing at 3430 and 1181 cm^{-1} are attributed to the O-H and C=C skeleton of the aromatic rings, respectively. The spectra ranging from 1600 to 1341 are assigned to the aromatic ring structures of MB[163]. The interaction

with MB shifted the C=O bond ($\sim 1714\text{ cm}^{-1}$) and also almost completely removed the C-OH ($\sim 1250\text{ cm}^{-1}$) and C-O-C (1040 cm^{-1}) suggesting strong electrostatic interactions. On the other hand, the adsorption of the RhB showed new adsorption peaks around $\sim 800\text{ cm}^{-1}$ and $\sim 1390\text{ cm}^{-1}$ indicating chemical interactions with the rGHs. Pure RhB showed typical bands at 2984, 1590, and 1345 cm^{-1} [164]. The peaks appearing around 2987 and 2900 cm^{-1} corresponded to the C-H stretching vibration of the RhB adsorbed on the surface of the hydrogels. The slight introduction of the peak around $\sim 3300\text{ cm}^{-1}$ may be attributed to the hydrogen bonding that occurs with the RhB. Besides, the increase in the intensity of the 1060 cm^{-1} corresponded to the C-O; indicating that the interaction with RhB also is driven by electrostatic interaction.

From the kinetic studies, chemisorption has been posited to be one of the main driving forces that govern the adsorption mechanism of the divalent ion intercalated rGHs; possibly due to the electrostatic interactions. To access the adsorption affinity towards the dye molecules (MB and RhB), simultaneous adsorption studies were conducted by placing the as-prepared hydrogel in an aqueous solution containing an equal concentration of both dye molecules. From visual observation, the rGHs showed greater affinity towards cationic MB dye as compared to the RhB dye as depicted in Fig. S3.5 from the clear change in color (from bluish to pinkish) before and after adsorption. The possible explanation can be attributed to the electrostatic interaction due to the positive charged sulfur and nitrogen in MB structure; hence driving the adsorption process further in addition to the porous structure framework. In addition, the IPD parameters of MB adsorption further corroborated the findings, with MB having higher K_1 values. Similar adsorption affinity behavior has also been previously reported elsewhere [165,166].

Considering the potential practical application and to reduce material cost, the divalent ion intercalated hydrogels should possess excellent recyclability and reusability. The cycling adsorption experiments were performed to access the regeneration efficiency of the as-prepared hydrogels. The results were depicted in Fig. 3.8(a) and (b). After each cycle of adsorption, the hydrogels were dialyzed in dilute HCl for 6 h and washed with H_2O before the regenerated hydrogels were subjected to the next adsorption cycle. It can be seen that the regeneration efficiency decreased each cycle which is due to loss of small graphene fragments during the adsorption/desorption under agitation; hence leading to reduced surface area for interactions. After three(3) cycles of adsorption-desorption, the divalent ion intercalated hydrogels

maintained above 95% of its initial capacity demonstrating good adsorption recyclability for both MB and RhB which is an added value for large scale applications. In comparison, the adsorption capacity obtained for rGH is only about 89.3 and 88.5% for MB and RhB, respectively. Therefore, the divalent ion intercalated hydrogels can be used as an efficient cationic dye adsorbent.

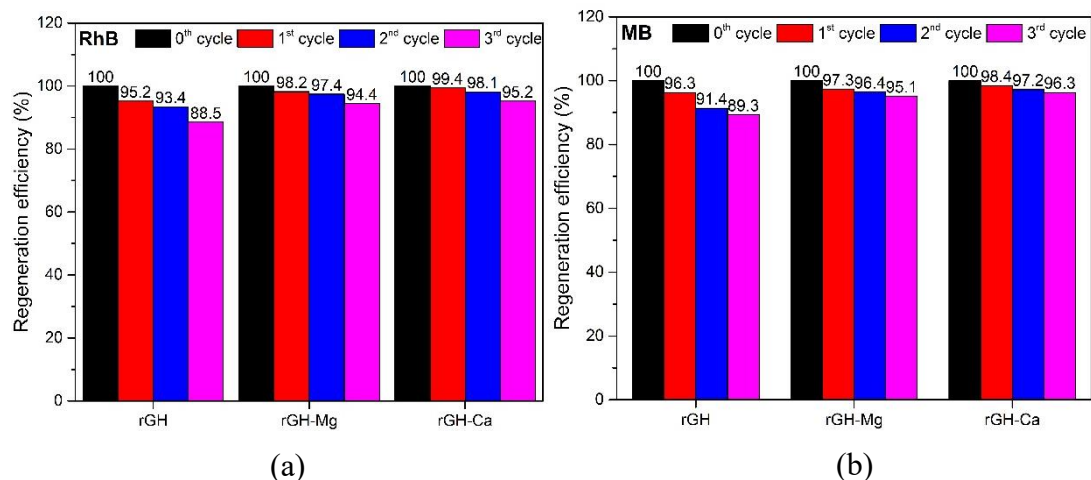


Fig. 3.8. Regeneration efficiency after adsorption of (a) MB and (b) RhB after 3 cycles.

3.4 Conclusion

In the present work, divalent ion intercalated reduced graphene hydrogel was successfully prepared via hydrothermal treatment. The intercalation of Mg^{2+} and Ca^{2+} rGH occurred via the alkoxy and epoxy functional groups showed improved performance towards the adsorption of cationic dyes, MB, and RhB with a higher affinity towards MB. The improvement in their adsorption capacity can be attributed to the increase in their physical attributes such as surface area and pore volume. The adsorption kinetics and the equilibrium adsorption isotherm conformed to a pseudo-second-order (PSO) alongside intraparticle diffusion (IPD) kinetic models and Langmuir isotherm respectively. The interaction between the divalent ion intercalated rGH showed higher K_L values which indicated greater interaction with the dye molecules which is important for the post-treatment process. The regeneration process indicated good recovery and efficiency after three cycles which is an important factor to address the inherent problem with powder-based adsorbents. Thus, the present investigation provided further insight into the application of divalent ion intercalated graphene-based hydrogels as dye adsorbent which is efficient, economical, and environmentally friendly in the treatment of dye wastewater.

CHAPTER 4
DESIGN OF REDUCED GRAPHENE HYDROGEL WITH ALKYLAMINE SURFACE
FUNCTIONALIZATION THROUGH IMMERSION/AGITATION METHOD AND ITS ADSORPTION
MECHANISM

Abstract

To date, existing methods for graphene functionalization entail complex procedures, hence efficient and facile methods are desired. In this study, alkylamine functionalization on reduced graphene hydrogel (rGH) was achieved *via* a facile two-step method involving hydrothermal treatment of graphene oxide (GO) to rGH followed by the immersion/agitation treatment of the rGH in octylamine (OA), decylamine (DA) and dodecylamine (DDA). It was found that the interactions of the alkylamine occurred via the epoxy ring-opening and amidation. To emphasize the advantage of this method, the adsorption kinetics on methylene blue (MB) and bisphenol-A (BPA) was further accessed. Shorter alkyl chain alkylamine (OA & DA) functionalized rGHs showed improvement in their adsorption capacity due to the increase in the specific surface area of the hydrogels. The highest specific surface area was obtained for rGH-DA at 47.80 m²/g followed by rGH-OA (47.37 m²/g), rGH-DDA (42.00 m²/g) and rGH (27.29 m²/g). However, longer chain alkyl chain alkylamine (DDA) functionalized rGHs showed lower adsorption capacity posited from the crowding of long alkyl chain which decreases the π - π interactions between the MB/BPA and the graphene sheets. rGH-DA exhibited the highest adsorption capacity for MB and BPA at 482 and 228 mg/g, respectively. In addition, the alkylamine functionalized hydrogels showed high regeneration behaviour after three cycles of adsorption-desorption: above 85% and 75% for MB and BPA, respectively. This proposed facile functionalization route will open interesting possibilities in the design of novel reduced graphene-based based hydrogels with improved adsorption performance that can bring ample of benefits in wastewater remediation.

Keywords: Graphene; hydrogel; alkylamine; adsorption; methylene blue; bisphenol

4.1 Introduction

The in-situ assembly of reduced graphene hydrogel (rGH) from graphene oxide (GO) via hydrothermal treatment is a versatile strategy to prepare the three-dimensional (3D) graphene macrostructures for various practical applications such as adsorbents, catalysts, sensors and scaffolds [31,32,167]. The properties of rGH can be tuned by adjusting the hydrothermal temperature, hydrothermal time, GO concentration, and pH of the GO suspension. The π - π stacking and hydrophobic interactions between the reduced graphene sheets were responsible for the formation of 3D macrostructures. The hydrothermal treatment possesses advantages of convenience, minimal cost, and produces less harmless by-products. Often, some oxygenated functional groups remained after hydrothermal treatment which opens possibilities for functionalization [168]. The template of the hydrogel enables the inclusion of modifiers such as metal/metal oxide, polymers, porphyrins, etc in the design of novel multi-functional hydrogel. The moderate reactivity at the interface enables systematic control on its surface properties that can be tailored for potential usage in desired applications. The ongoing development of functionalized graphene-based materials mainly focused on the process, which is simple, low cost and does not require a sophisticated pre-synthesis route. Often, the one-pot synthesis of functionalized graphene via hydrothermal treatment is reported. The study into post-treatment functionalization of rGH is worth exploring.

The functionalization of graphene-based materials can occur either via non-covalent or covalent interactions [75,169]. Covalent functionalization diminished the electronic properties of the graphene by altering the sp^2 structure which shifts the Fermi level of graphene from its Dirac point [170]. In comparison, non-covalent functionalization such as π - π interactions, electron donor-acceptor complexes, hydrogen bonding, and van der Waals forces which are usually preferred does not alter the structure and electronic properties and at the same time introducing new chemical groups on the surface[75]. In most situation, non-covalent functionalization improved binding capacity and reactivity which is important in pollution remediation applications[75]. The nitrogen functionalities present in graphene have shown to bring ample benefits. The method to introduce nitrogen has been widely used which usually follows two routes: either via direct synthesis or post-treatment methods. However, the doping after its initial growth usually involves a relatively high energy and chemically active nitrogen source to introduce defect and replacing the carbon with nitrogen[171]. However, the latter is much preferred as it only introduces N at defect and edge on the

surface without sacrificing the inherent salient properties of the graphene. Among the methods are thermal treatment, plasma treatment and N_2H_4 treatment. However, most of the route proposed does not meet the desired point of low cost, fewer post-treatment procedures, and producing harmful-by-products in which may greatly increase production cost on an industrial scale.

Alkylamine is often associated with the production of various biosurfactants for carbon capture applications [172,173]. Alkylamine functionalization using varying chain length on graphene-based material had been previously reported using the gamma-ray irradiation method [174]. However, most of the previous studies involved functionalizing GO which contains various oxygenated functional groups for interactions. Since the nitrogen atom in the amine groups is more nucleophilic than oxygen, the studies showed that amine functionalization improves the dispersity of the graphene oxide in a low polar solvent, and leads to higher mechanical properties and thermal stability[175–177]. The remaining oxygenated functional groups on the reduced graphene hydrogel after hydrothermal treatment opens up an avenue for functionalization with alkylamine.

It has been recognized that water contaminants caused by pollutants such as dye compounds, heavy metals and emerging contaminants posed adverse effects on human health and ecosystems. The design of a novel hydrogel-based adsorbent that is highly efficient remains a significant challenge. Graphene-based hydrogels were explored thoroughly as a promising candidate as adsorbent attributed to their large surface area, abundant pore structure and tailorable surface properties enabling their effective usage in pollution control [178–180]. In terms of practical application, hydrogel-based adsorbent enables easy separation from aqueous media after usage which is more advantageous than most powder-based adsorbents.

In this context, a simple method that is green, economical and practical is proposed to successfully functionalize the reduced graphene hydrogel that can be performed under room temperature without sophisticated equipment. Our proposed approach is a greener method that significantly minimizes and eliminate unnecessary steps and chemical consumption in the preparation of functionalized graphene-based hydrogels. Thus, to develop a better understanding of the relationship between functionalization of alkylamine on the reduced graphene hydrogel, a series of increasing alkyl-chain length of alkylamine consisting of octylamine (OA), decylamine (DA) and dodecylamine (DDA) were used in this work. The

functionalized reduced graphene hydrogels were then systematically investigated for the adsorption of methylene blue (MB) and bisphenol A (BPA). This proposed route will provide a feasible alternative to industries focusing on pollutant remediation and beneficial for future studies on the application of simple surface functionalization method on graphene-based hydrogels.

4.2 Materials and Methods

4.2.1 Materials

Graphene oxide dispersion in water (0.1-2.0 %) was gifted by Nippon Shokubai Co. Ltd (AX-1-FM-W-151). Octylamine (OA), decylamine (DA), dodecylamine (DDA), methylene blue (MB), bisphenol A (BPA), hydrochloric acid (HCl) and ethanol (C₂H₅OH) were obtained from Wako Pure Chemical Industries Ltd, Japan. Deionized water (18.25 MΩ.cm) is obtained from Milli- Direct 16 (Millipore Q, USA) dispenser and used to prepare the aqueous solution. Unless specified otherwise, no further purification is needed for all the reagents and materials used.

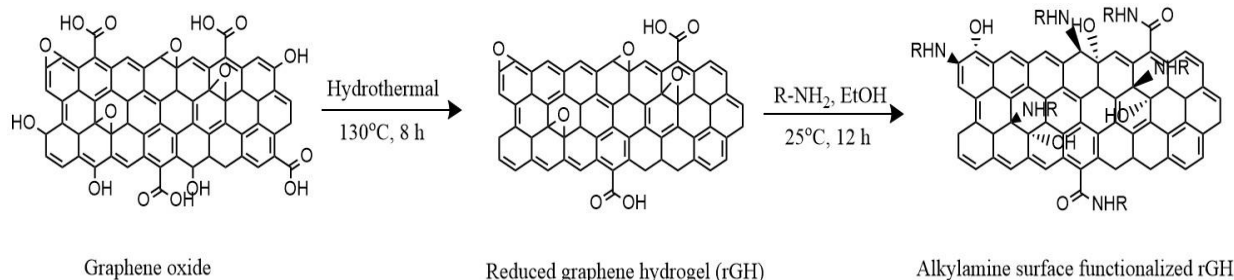
4.2.2 Synthesis of rGH

2.0 mg/mL of GO suspension was prepared by adding 30 mL of deionised water in the commercially obtained 4 g of GO slurry. The suspension was then sonicated for 1 h using a bath ultrasonicator (AS ONE Ultrasonic Cleaner Single Frequency, 3L (MSC-3) 40 kHz, 100W) to exfoliate the GO layers and transferred to a modified borosilicate glass bottle [19,181]. The hydrothermal treatment is carried out at 130°C for 8 hours in a TOMY High-pressure steam sterilizer (LBS-325). The resulting reduced graphene hydrogel obtained was then dialyzed in distilled water for 24 h with occasional changing of the water. The hydrogel is termed rGH to act as the control sample and to ease identification.

4.2.3 Synthesis of alkylamine surface-functionalized rGH

The prepared rGHs were transferred into a solution containing various chain length of 0.01 M alkylamine in EtOH and agitated for 12 h. The hydrogels were then removed and washed with excess EtOH and H₂O to remove unreacted alkylamine before subjected to the evaporation process using an evaporator for 1 hour. The solvent-free surface-functionalized rGHs were then freeze-dried at -50 °C for 24 hours to remove any

moisture content without destroying the 3D macrostructure. The freeze-dried rGHs were kept for characterizations and termed rGH-OA, rGH-DA and rGH-DDA to ease identification. The methodology for the preparation of the alkylamine-functionalized rGH is summarized in Scheme 1.



Scheme 4.1. Suggested general scheme of the synthesis of alkylamine surface-functionalized Rgh using the two-step methods of hydrothermal treatment and immersion/agitation. R is the alkyl chain

4.2.4 Characterizations

The surface morphology of the freeze-dried hydrogels was accessed using JEOL JCM-6000 versatile benchtop scanning electron microscope. FTIR spectra were recorded using Nicolet iS5 spectrophotometer (ThermoFisher Scientific, Japan) in the range of 4000 cm^{-1} to 500 cm^{-1} . The X-ray diffraction (XRD) was performed using a Rigaku X-ray diffractometer with Cu K- α radiation with a scanning range from $5 - 60^\circ$. TGA measurements were taken using EXSTAR TG/DTA7000 under N_2 atmosphere from room temperature to 550°C at a rate of $10^\circ\text{C}/\text{min}$. The XPS measurements were measured using an Axis Nova (XPS) Surface Analyzer with a monochromatized Al K α as the X-ray source. Casa XPS software was used to carry out the fitting of the deconvoluted peaks of C1s, O1s and N1s [182]. The Raman spectra of the hydrogels were recorded on a JASCO NRS-5100 Laser Raman Spectrometer using a 2.5 mW laser power beam. The Brunauer-Emmett-Teller (BET) surface area and Barrett-Joyner-Halenda (BJH) pore size distribution were determined using the Surface Area and Pore Size Analyzer, Quantachrome Instruments. Electrochemical analyzer Nova 1.1 Autolab potentiostat (PGSTAT204, Metrohm Autolab, Netherlands) connected to an external computer was used to carry out electrochemical measurements. The three-electrode system consisted of a glassy carbon electrode (GCE) as the working electrode, Ag/AgCl/KCl (3M) and platinum as the reference and auxiliary electrode, respectively. The freeze-dried reduced graphene hydrogel was

sonicated in DMF to prepare a 1.0 mg/mL of suspension and drop-casted on a glassy carbon electrode (GCE) and allowed to dry before electrochemical measurements were taken.

4.2.5 Adsorption experiment

The model pollutants, MB and BPA were used to access the adsorption behaviour of the hydrogels. The graphene-based hydrogel is placed in the aqueous solution of the pollutants and agitated continuously for 24 h until adsorption equilibrium is achieved. The residue pollutants were measured using a UV-Vis spectrophotometer (Genesys 10s, Thermo Fisher Scientific). The concentration of MB and BPA were obtained using a standard calibration line as depicted in Fig. S4.1(a) and Fig. S4.1 (b), respectively. The adsorption capacity (Q_e) was calculated with the following equation:

$$Q_e = \frac{(C_0 - C_t)V}{m}$$

where C_0 and C_t represent the initial concentration (mg/g) and remaining concentration (mg/g) of the pollutants at time t , V is the volume of the solution (L), and m is the mass of the adsorbents (mg).

4.3 Results and Discussion

Before hydrothermal reaction, the colloidal GO suspension was probed using UV-Vis as shown in Figure S4.2. The UV-Vis spectrum of GO suspension showed two distinct bands, a maximum at 223 nm attributed to π - π^* transition of the aromatic C-C bonds while the shoulder peak at 302 nm corresponds to the n - π^* transition of the carbonyl C=O bonds. The finding is consistent with other previous reports on the optical property of GO suspension [183–185]. DLS and zeta potential studies were also conducted to access the zeta potential and particle size distribution. From Table 4.1, the GO suspension exhibited a zeta potential value of -39.24 mV and a mean lateral diameter of 2015.2 nm. Zeta potential values more negative than -30 mV are considered ideal to represent sufficient electrostatic repulsion to ensure a stable dispersion. GO sheets are highly negative charged which is attributed to the ionization of oxygen-containing functional groups present at the basal and planar plane. As shown in Scheme 1, the alkylamine is posited to react with the remaining epoxy groups and also the carboxylic groups of the reduced graphene hydrogel during the immersion/agitation. Previously, it was reported that the low-temperature hydrothermal route employed does not remove the epoxy groups due to the strong hydrogen bond interaction between the oxygen

molecules [186]. The freeze-dried hydrogels depicted in Fig. S4.3 showed that the alkylamine functionalized hydrogel shrink in size. The possible explanation can be attributed to the evaporation process to remove the EtOH which has led to the partial agglomeration of the graphene sheets.

Table 4.1. Properties of the GO colloidal suspension

Sample	pH	Diameter (nm)	Mobility ($\mu\text{m cm/s V}$)	Zeta Potential (mV)
GO	2.70	2015.2	-2.05	-39.24

SEM images in Fig. 4.1(a-d), showed the morphology of rGH, rGH-OA, rGH-DA and rGH-DDA after freeze-drying. The interconnected 3D thin layer of rGH showed the wrinkles on the graphene sheet indicating self-assembly during the hydrothermal process. The alkylamine surface functionalization lead have led to substantial morphological changes, with more wrinkles formed that can be attributed to the functionalization of varying alkyl length of alkylamines [187]. Besides that, overlapping and coalescing of the sheets is apparent leading to physical cross-linking sites[33]. The reduced graphene nanosheets are more closely packed, forming thick stacked layers structure as alkylamine functionalization occurred. The further agglomeration of reduced graphene sheets is possible from the increased hydrophobic interactions between individual sheets.

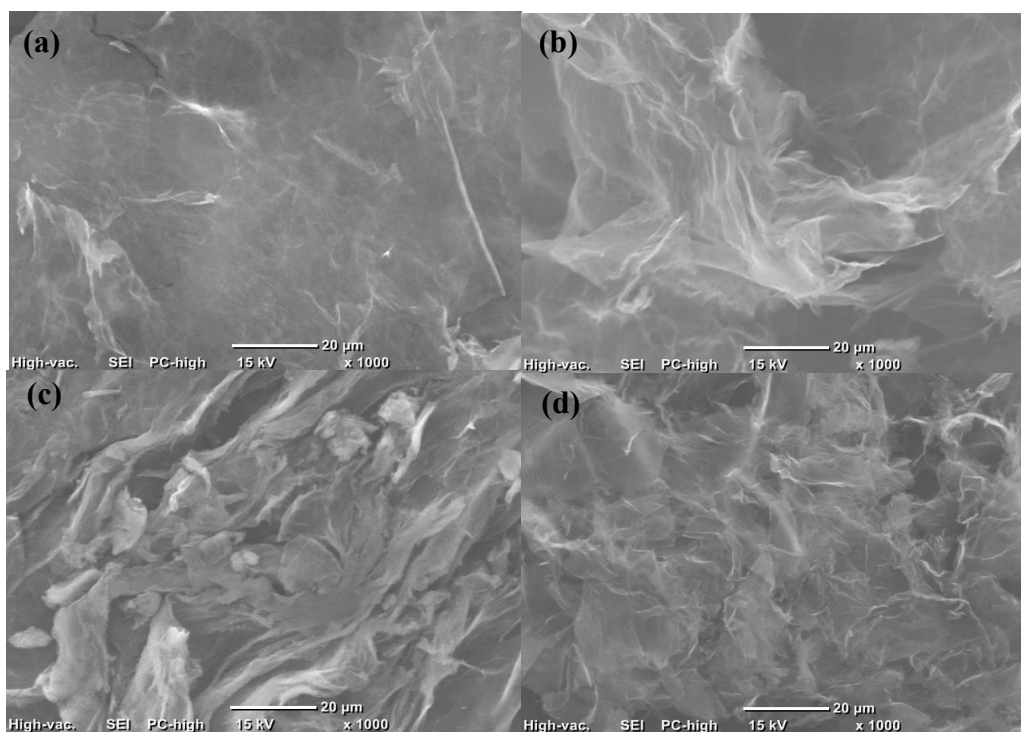


Fig. 4.1. SEM images of (a) rGH (b) rGH-OA, (c) rGH-DA and (d) rGH-DDA under x1000 magnification

ATR-FTIR is carried out to confirm the alkylamine surface functionalization on the reduced graphene surface. Fig. 4.2. shows the FT-IR spectra of rGH, rGH-OA, rGH-DA, and rGH-DDA. For rGH, the peak at 1593 cm^{-1} confirmed the restoration of the sp^2 carbon network while the peak at 1718 cm^{-1} corresponds to the stretching vibrations of the $\text{C}=\text{O}$ of carbonyl or carboxyl groups. The peak at 1046 cm^{-1} corresponds to the $\text{C}-\text{O}-\text{C}$ arranged in an epoxide ring. It is obvious from the decrease in intensity of the epoxide band after successful functionalization of the alkylamine on the rGH indicated that the interaction occurred via the epoxide ring-opening mechanism. In addition, the intensity of amide carbonyl stretch ($\text{C}=\text{O}$) is more apparent for the rGH-OA and rGH-DDA as compared to rGH-DA. Moreover, the asymmetric peaks at 2920 and 2845 cm^{-1} together with a peak about 730 cm^{-1} assigned to the $\text{C}-\text{H}$ stretching vibration showed the absorption band of the alkylamine. The strong peak at 1565 cm^{-1} can be ascribed to the $\text{N}-\text{H}$ deformation band for protonated and/or hydrogen-bonded primary amine [188]. It can also be seen the intensity of the $-\text{CH}_2$ peak assigned at 1465 cm^{-1} increased with the increase of chain length. Hence, this finding showed the successful alkylamine surface functionalization using the simple immersion/agitation method.

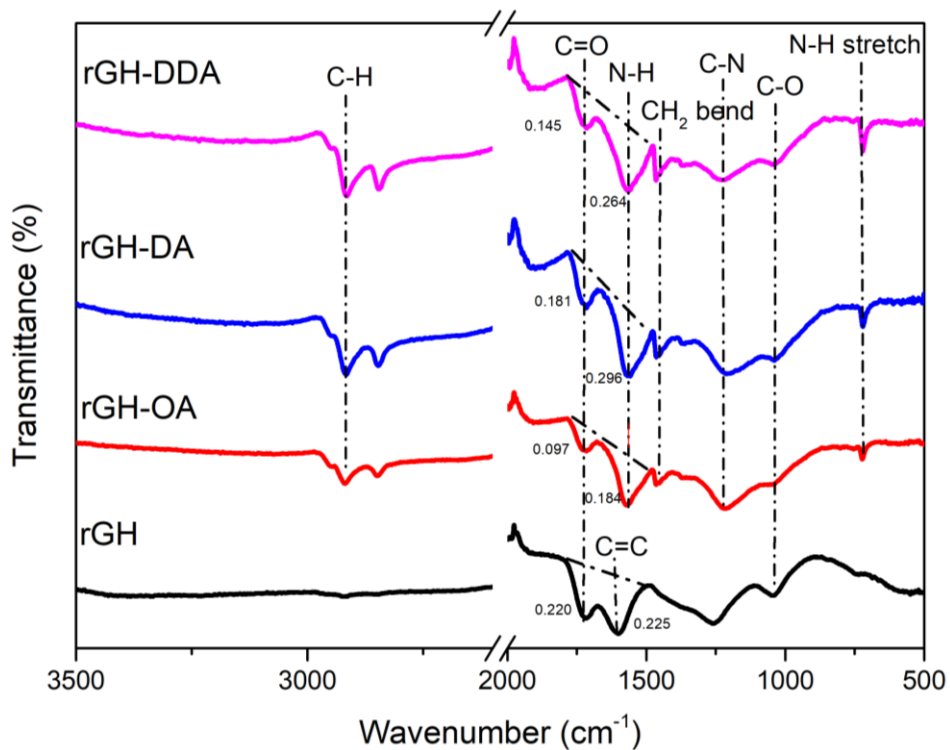


Fig. 4.2. ATR-FTIR of rGH, rGH-OA, rGH-DA and rGH-DDA

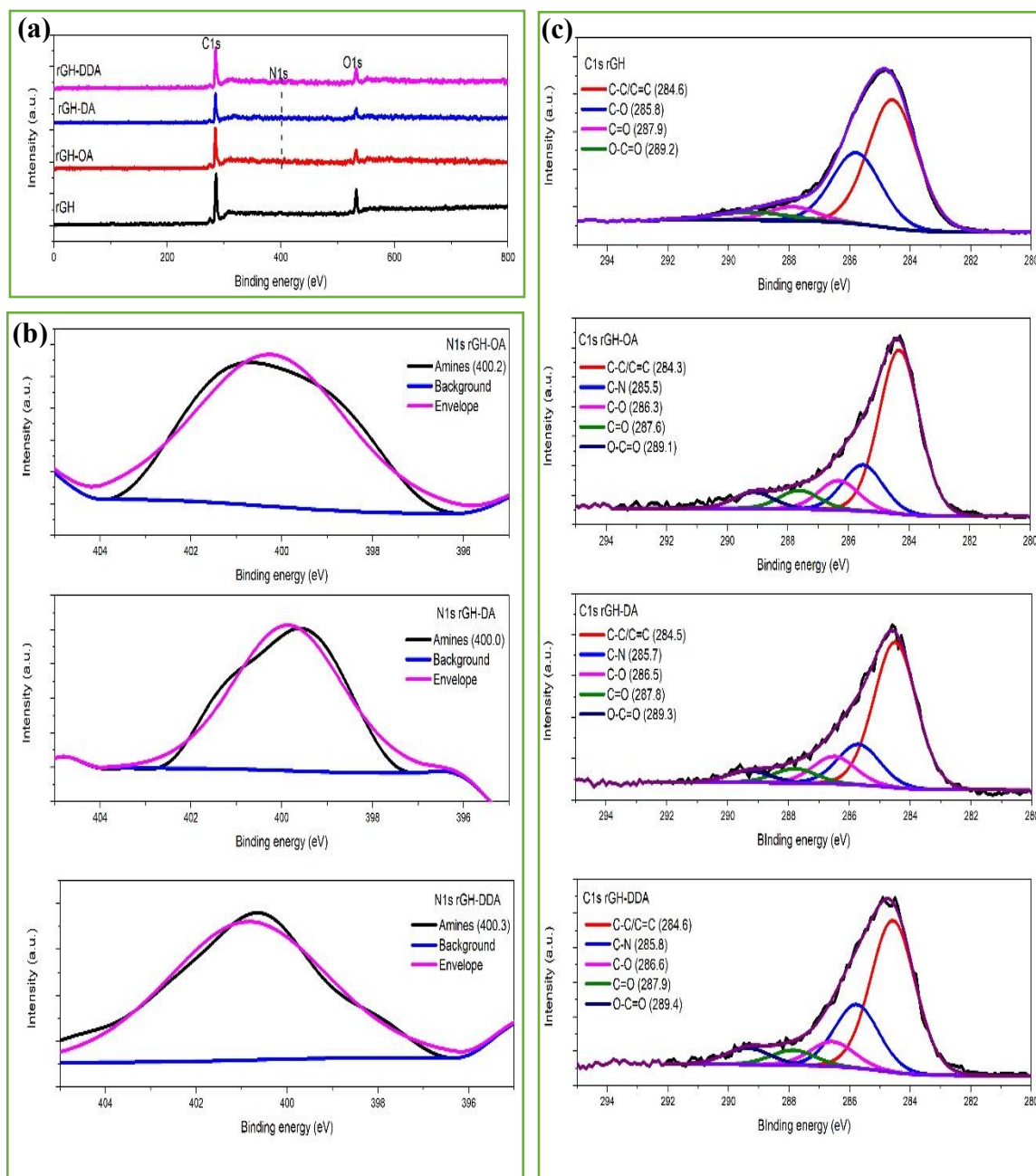


Fig. 4.3. (a) wide spectra, (b) N1s, and (c) C1s split spectra of the hydrogels

XPS characterization was further carried out to ascertain the surface functionalization mechanism of the alkylamines on the graphene surface using the immersion/agitation method. Fig. 4.3(a) depicts the XPS wide spectra of rGH, rGH-OA, rGH-DA, and rGH-DDA. The survey spectra of the rGH showed the typical

C1s and O1s peaks around 284 and 532 eV, respectively. On the other hand, the wide spectra of alkylamine surface-functionalized samples showed the presence of weak N1s peak which is not so apparent possibly due to lower content alkylamine functionalized on the rGH surface. However, the high-resolution N1s spectra from Fig. 4.3(b) demonstrated the clear band positioned at ~400 eV which is attributed to amine functionality. The deconvolution of the N1s spectrum of aminated graphene usually yielded bands attributes to pyridines (398.4 eV), amines (399.8 eV), graphitic nitrogen (401.4 eV), and pyridine N-oxide (403.8 eV) in which amine functionality often appear to be the dominant nitrogen species [189]. However, in our case, the curve fitting does not demonstrate the presence of other nitrogen species besides the dominant amine functionality. The chemical bonding from the high-resolution C1s spectra of the hydrogels was depicted in Fig 4.3(c) and summarized in Table S3. The high-resolution C1s core spectrum of rGH showed the overlapping peaks attributed to C=C/C-C bonds (284.6 eV), C-O bonds in hydroxyl (285.8 eV), C=O (287.7 eV) and O-C=O (289.2 eV). The remaining C-O component can be attributed to the residual ether groups which are considered to be hydrothermally stable, hence limiting the full reduction of the graphene oxide [190]. Upon comparing to the control sample, the C1s spectra of the alkylamine surface-functionalized rGH showed a significant decrease in the C-O functionality relative peak area. One of the reasons could be due to the formation of the C-N bond suggesting that the alkylamine reacts with the remaining epoxy groups on the rGH surface via ring-opening reaction [191]. Besides that, the decrease in oxygen content indicates that oxygen-containing groups on the hydrogel were either eliminated or substituted on the surface of the graphene [23]. Table S2 further summarized the chemical bonding and atomic percentage obtained from the high-resolution C1s spectra of the hydrogels. The findings further corroborated the FTIR results which showed the decrease in the C-O-C peak intensity.

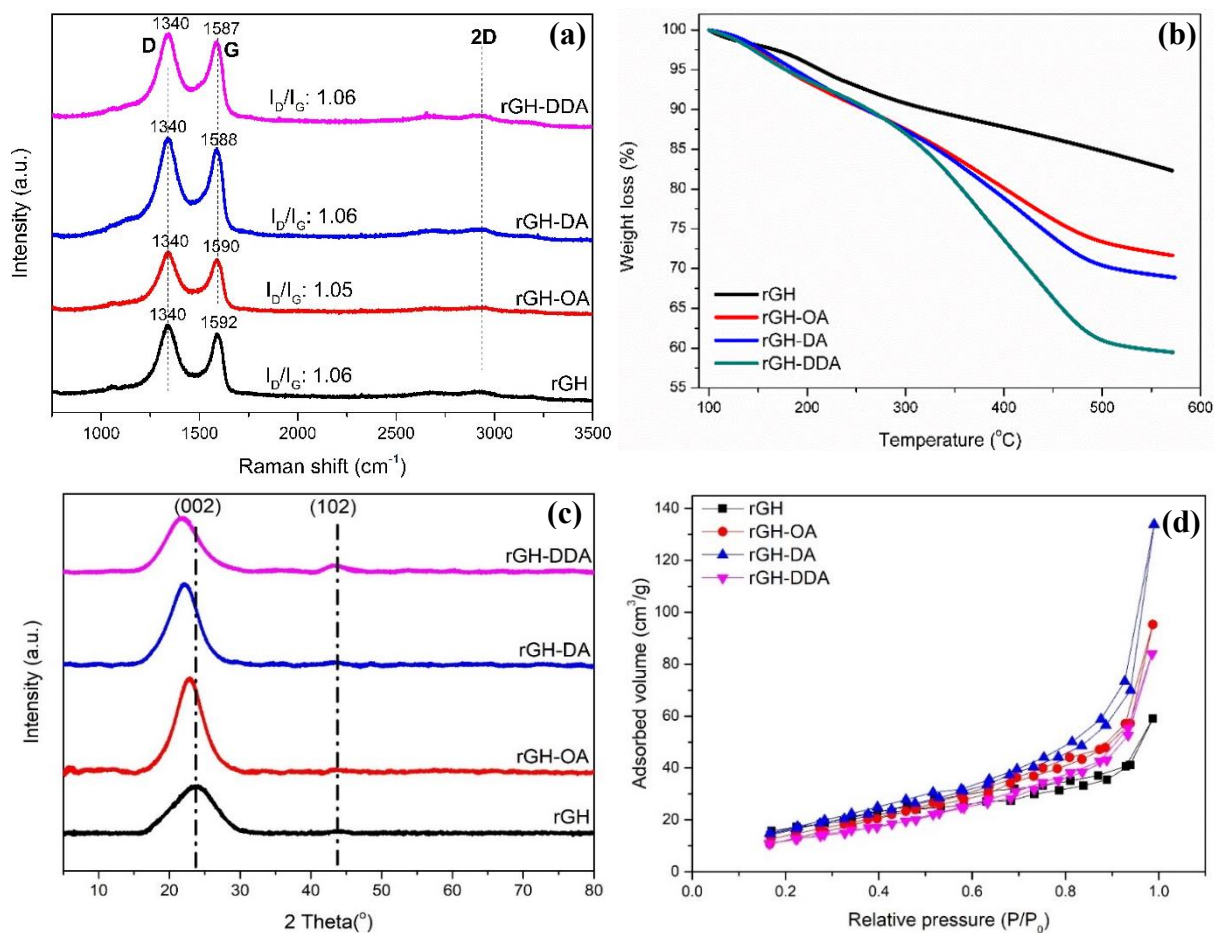


Fig. 4.4. (a) Raman spectra, (b) TGA thermograms, (c) XRD spectra and (d) N₂ adsorption-desorption isotherm of the alkylamine surface-functionalized hydrogel

To access the structural effect of alkylamine functionalization on the rGHs surface, Raman spectroscopy analysis is carried out as depicted in Fig. 4.4(a). This non-destructive tool is commonly used in the characterization of carbon-based materials such as graphene. The three characteristic bands that are found in all the graphene-based hydrogels occurred around 1340, 1590 and 2800 cm⁻¹ correspond to the D, G and 2D bands, respectively. The D-band provides information on the disorder or defect behaviour due to sp³ hybridized carbon formation[192]. On the other hand, the G and 2D bands are related to layer thickness and doping. In addition, the broadened 2D band around 2700 cm⁻¹ that appeared in the spectra is seen as a distinct band of graphene induced by a two-phonon resonant scattering process. The intensity D and G bands are not greatly affected upon comparing to the control sample, rGH. The slight shifting of the G and 2D bands may be attributed to the successful functionalization which has been previously reported due to

the existence of N of the alkylamine [193]. The I_D/I_G ratio can provide insight into the degree of disorder in sp^2 and the presence of defects, impurities, or chirality introduced during functionalization processes [194]. The I_D/I_G ratio of the control sample, rGH and functionalized rGH, remained almost similar indicating that the immersion/agitation method does not introduce structural defect within the graphene. It is posited that the functionalization only can occur with the remaining carboxylic groups and epoxy groups which is in smaller quantity due to the hydrothermal treatment.

To further probe the surface functionalization of alkylamine on the reduced graphene sheets, TGA analysis is carried out. Based on Fig. 4.4(b), rGH displayed better thermal stability due to the removal of most oxygen-containing groups during the hydrothermal route. In the case of rGH-OA, rGH-DA and rGH-DDA, steady weight loss occurred from 100 – 300°C which is ascribed to the decomposition of labile oxygen-containing groups [63]. The significant weight loss that occurred from 300 – 500°C is posited from the pyrolysis of functionalized amines groups from graphene sheets [195]. The difference in weight loss between the control sample, rGH and the alkylamine functionalized graphene hydrogels enables the rough assessment of the alkylamines graft rate. Hence, the percentage of alkylamine grafted on the reduced graphene surface is 10.97%, 13.45%, 22.84% for OA, DA and DDA, respectively. The higher degradation percentage of longer chain alkylamine can be attributed to the fragmentation of free alkylamine that was physically adsorbed on the surface of the reduced graphene hydrogels [196]. Hence, it can be posited that the functionalization rate of the alkylamine is related to the chain length of the alkyl contents in the alkylamine. Contrary to previous reports that showed short alkyl chain length possessed higher thermal stability than longer alkyl chain length, we found that the immersion/agitation method yielded lower thermally stable material. We posit that the longer chain length results in greater hydrophobic interaction that decreases the interaction between alkylamine and rGH. Hence, as a result, lower thermal stability is obtained from the free alkylamines from the physisorption during the immersion/agitation. Besides, the longer alkyl chain length resulted in carbocation and carbon radicals becoming more stable which ease the decomposition process [197].

XRD is further carried out to study the changes in phase and structure of the alkylamine functionalized reduced graphene hydrogel. Based on Fig. 4.4(c), well-resolved diffraction peaks at 23.9° of the rGH corresponds to the (0 0 2) plane while the small diffraction peak at 43.1° is attributed to the (1 0 2) plane of

the reduced graphene structure [198,199]. The diffraction patterns were processed using X'Pert High Score software to access the distance between the graphene layers, known as d-spacing and the FWHM. The Scherrer's equation was applied to the width of the (0 0 2) diffraction peaks for the evaluation of the crystallite size. The structural parameters obtained from the XRD spectra are summarized in Table 4.2.

Table 4.2. Structural parameters obtained from the XRD spectra

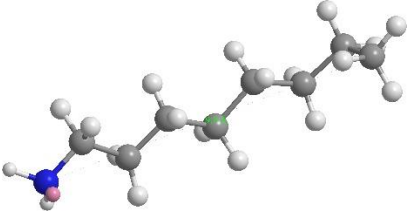
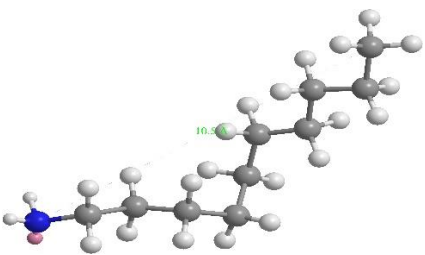
Sample	(001)			(102)		
	2 θ	FWHM (deg)	d-spacing (nm)	2 θ	FWHM (deg)	d-spacing(nm)
rGH	23.85	0.968	0.3728	43.14	1.920	0.2095
rGH-OA	22.81	2.016	0.3895	43.10	2.304	0.2098
rGH-DA	22.06	1.440	0.4025	43.35	2.304	0.2072
rGH-DDA	21.81	2.688	0.4071	43.10	2.688	0.2100

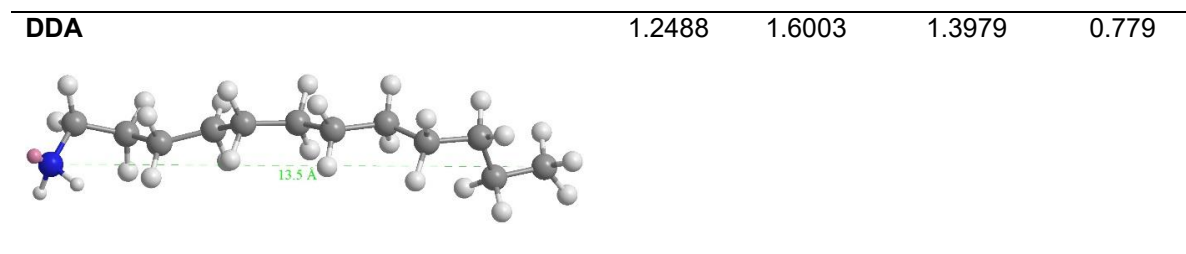
The gradual shifting of the (0 0 2) peak and decreased interlayer distance with the increase of alkylamine chain length can be attributed to the expansion in the interlayer separation caused by the alkyl-groups and the intercalation of amine groups between the graphene layers [200]. The XRD findings also corroborated the findings by Stankovich *et al.* on the modification of GO paper using various chain length of alkylamine suggesting that the intercalation of amines occurred via chemisorption and physisorption [201]. The increased intensity of the (102) peak can be attributed to the crystallization of the grafted amines in the rGO which has been previously reported [202]. Hence, the results obtained indicate that the surface functionalization of alkylamine can be achieved using the immersion/agitation method.

The BET surface area and BJH pore size analysis of the samples were further investigated by N₂ adsorption-desorption to obtain a better understanding of their porous features. Fig. 4.4(d) depicts the isotherm with type IV shape with H3 hysteresis loop suggesting that the hydrogels have a mesoporous structure with non-rigid aggregates pore structure which is slit-shaped and panel-shaped [203]. Based on the pore size distribution in Fig. S4, the pore diameters of the samples lie in the range of 2–100 nm, and the main pore size is about 1.6 – 4.0 nm which is in the mesoporous range. The BET surface and BJH pore size and volume of the hydrogels are summarized in Table S1. The obtained specific surface area (SSA) is 27.288, 47.374, 47.791 and 41.996 m²/g for rGH, rGH-OA, rGH-DA, and rGH-DDA, respectively. The increase in the surface area is posited to be attributed to the physically adsorbed alkylamine into the pores of the rGHs. Besides, the amine groups may have acted as spacers which led to the increase in their inter-

layer spacing. To prove that physisorption may occur, the length of the alkylamines were estimated using computational software. The 2D chemical structure of the alkylamines was first constructed using ChemDrawProfessional 16.0 software, and the optimized geometries were transferred into Chem3D. The distance measurement of the alkylamines was set between the N atom and C atom alkyl chain end group, followed by structure minimization using the MM2 tool to obtain the estimated molecular length of the alkylamines. From Table 3, the average length of the OA, DA and DDA were 0.97 nm, 1.03 nm and 1.40 nm, respectively after molecular dynamics simulations. Their obtained molecular length is significantly smaller as compared to the pore size of the graphene hydrogels, hence enabling physisorption to also occur. The lower values of the specific surface area (SSA) obtained for rGH as compared to previous report findings can be attributed to the freeze-drying techniques [204]. However, the drawback was mitigated upon the functionalization of the alkylamine using the simple immersion/agitation method which has successfully improved the specific surface area and pore volume. This finding further substantiated the XRD results which showed that intercalation of the amines has occurred. The rGH-DA possessed the largest pore volume, which is a positive aspect for usage as an adsorbent which enables the uptake of more pollutants in their pores.

Table 4.3. Molecular distance of the alkylamine obtained from the computational method

Molecular distance	Min(nm)	Max(nm)	Average(nm)	S.D
OA	0.8888	1.0566	0.9731	0.389
				
DA	0.5964	1.3223	1.0265	1.274
				



Cyclic voltammetry (CV) study was further to access the electrocatalytic activities of the prepared graphene-based material and to further confirm the successful surface functionalization. Previously, it was reported that the presence of N could enhance the attraction of ions in graphene layers, hence providing improved current densities [200]. Fig 4.5. depicts the voltammogram of 5 mM of $(K_3Fe(CN)_6)$ using graphene modified glassy carbon electrode (GCE) to investigate the electrochemical properties of functionalized graphene material [205]. The CV performed using $(K_3Fe(CN)_6)$ as the electrochemical probe depicted the cyclic voltammogram with an almost reversible one-electron transfer on the electrode surface[206]. The reaction is considered electrochemically reversible if the heterogeneous electron transfer is rapid upon compared to the mass transfer, diffusion or migration flux of the reactants and products of the electrode reaction [207]. The Randles-Sevcik equation can be used to describe the peak current.

$$i_p = 2.69 \times 10^5 n^3/2 AD^{1/2} v^{1/2} C \quad (2.6)$$

where n is the number of moles of electron transfer in the reaction (Equiv/mole), A is the electrode surface area (cm^2), v is the scan rate (V/s), D is the analyte's diffusion coefficient (cm^2/s) and C is the analyte's concentration (mol/cm). The improvement of the oxidation peak current (I_{pa}) for rGH/GCE over GO/GCE can be attributed to the electron transfer inhibitory effect of GO. The reduction of the GO to rGO improved the specific surface area of the GCE and hence improving the sensitivity towards $(K_3Fe(CN)_6)$ [208]. The improvement in the voltammetric response with the amine-functionalized graphene is due to the different charge transport properties and transfer dynamic [83]. These findings further showed the successful functionalization of the alkylamine which introduced the nitrogen functionality that resulted in higher electrocatalytic activity and conductivity[209]. The greatest enhancement is obtained for rGH-DDA, followed by rGH-OA and rGH-DA. The findings indicate that that the affinity to functionalize on the surface of the rGH does not depend on the chain length of the alkylamine. Additionally, the slight shift of the anodic peak

toward a more negative potential can be attributed to the enhanced selectivity of the functionalized graphene [84]. It is critical to understand that various experimental variables such as temperature, pH, salt concentration, modifier concentration, and type of electrolyte may also affect the modified electrode's performance.

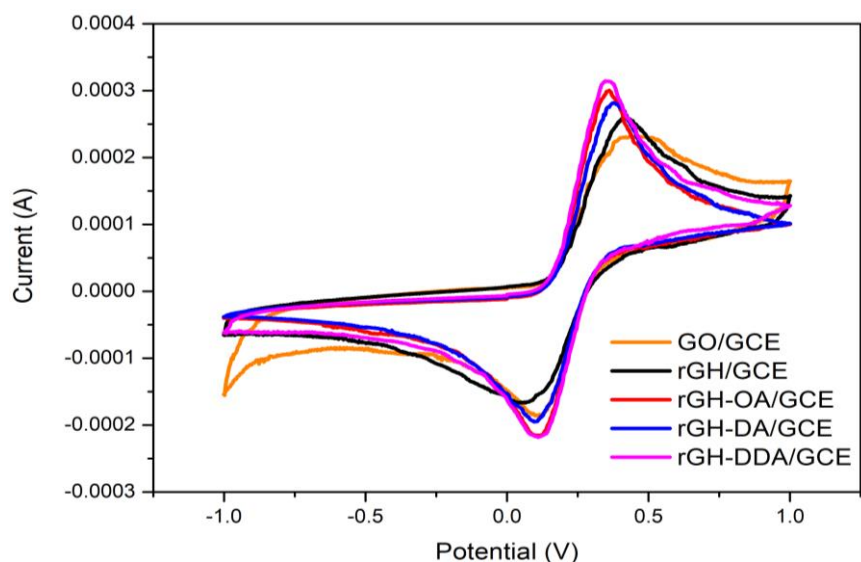


Fig. 4.5. Cyclic voltammogram of 5 mM potassium ferricyanide ($K_3Fe(CN)_6$) using graphene modified glassy carbon electrode (GCE) in the potential range of -1.0V to 1.0V at a scan rate of 100 mV/s

Adsorption properties of the alkylamine surface-functionalized graphene-based hydrogels

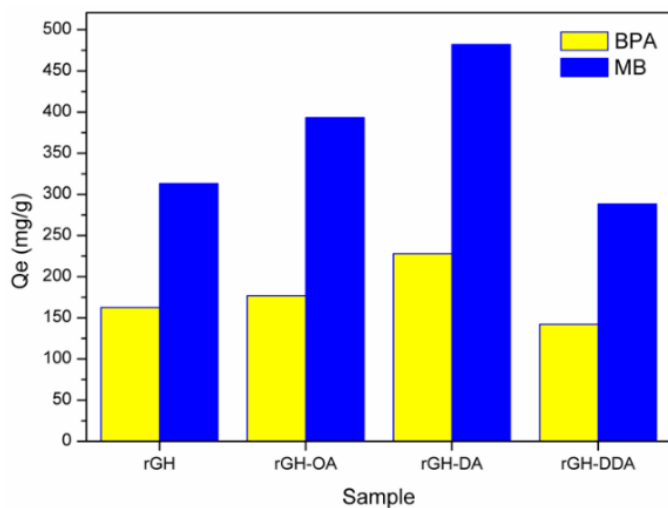


Fig. 4.6. The adsorption capacity of MB and BPA using the modified hydrogels

Attributed to the high porosity and large surface area, the functionalized rGHs were considered as ideal adsorbent for dyes, and organic compounds from water. Inspired by previous studies on the adsorption capabilities of graphene-based hydrogels, two model pollutants; MB and BPA were used to access the adsorption capability of the functionalized rGHs using the immersion/agitation method. From Fig. 4.6., the adsorption capability of both MB and BPA followed the following trend:

$$\text{rGH-DA} > \text{rGH-OA} > \text{rGH} > \text{rGH-DDA}$$

The adsorption capacity of rGH-DA increased to 40.2 % and 53.9% for BPA and MB, respectively, upon comparing to rGH. The enhanced adsorption rate of the pollutants after surface functionalization with OA and DA can be attributed to several factors even though the pore radius obtained from BJH are smaller than rGH. The major contributing factor would be the larger specific surface area which allowed for additional interactions with the adsorbate. Moreover, contributing factors including electrostatic interaction between the negatively charged oxygen/nitrogen functional groups, π - π interactions between the pollutants and the aromatic rings of the graphene-based materials and hydrogen bonding. However, the lower adsorption capacity of the sterically hindered, rGH-DDA compared to rGH can be attributed to the capping effect that may have hindered the π - π interactions with the pollutants which is a significant mode of interaction [210]. The lower adsorption capacity for rGH-DDA maybe also due to the crowding of the long alkyl chain which limits the access of the adsorbate with the active sites to interact via π - π interactions and electrostatic interactions resulting in sluggish reaction [211]. Further, to predict the adsorption rate from MB and BPA, two kinetic models were applied, namely the pseudo-first-order (PFO) and pseudo-second-order (PSO) model. PFO corresponds to a diffusion-controlled process involving solid-liquid phase adsorption; inclined towards physisorption. The PFO kinetic models for the adsorption of BPA and MB are illustrated in Fig. 4.7(a) and (b), respectively.

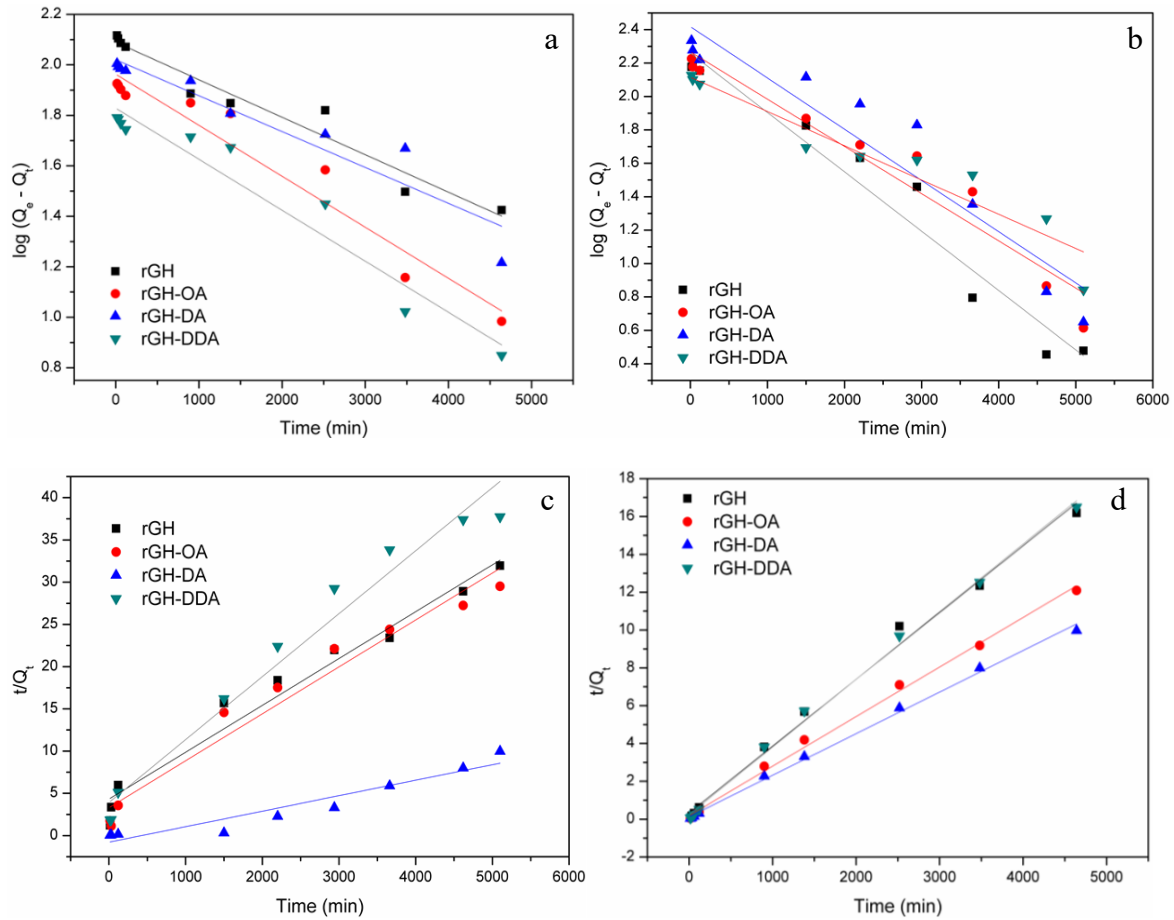


Fig. 4.7. Pseudo-(a,b) first-order and (c,d) second-order kinetic models for the adsorption of (a) BPA and (b) MB

On the other hand, the PSO assumes that adsorption reaction occurring at the liquid/solid interface controls the process, inclined towards chemisorption [212]. The linearized form of the model employed to describe the adsorption are as follows:

The pseudo-first-order model:

$$\ln(Q_e - Q_t) = -k_1 t + \ln(Q_e)$$

The pseudo-second-order model:

$$\frac{t}{Q_t} = \left(\frac{1}{Q_e}\right)t + \frac{1}{Q_e^2 k_2}$$

where Q_e and Q_t are the pollutant amount (mg/g) adsorbed by the hydrogels at equilibrium and the amount adsorbed at a certain time, t respectively. k_1 (h^{-1}) or k_2 (g/mg.h) is the adsorption rate constant. A straight

line is obtained by the fitting of experimental data of t/q_t versus t as shown in Fig. 4.7(c) and 10(d) which enables the determination of q_e and k_2 . All the parameters (K_1 & K_2) and the correlation coefficient (R^2) obtained from the pseudo-models are shown in Table S3 and S4 for the adsorption of MB and BPA, respectively. The adsorption kinetic data for both MB and BPA can be accurately described by the PSO model for all the hydrogel samples as they showed better regression coefficient (R^2), closer to unity; hence conforming to the chemisorption process in which the adsorption occurred through the binding reaction by sharing of electrons or covalent interactions. Interestingly, the rGH-DA showed the lowest adsorption rate (K_2). On the other hand, the adsorption rate for MB increases as the alkyl chain length of the alkylamine is increased.

To elucidate the regeneration properties of the hydrogels, desorption was carried out using ethanol, HCl and deionised water as the desorption agents for the BPA and MB, respectively. The process is conducted by immersing and agitating the used hydrogels for 12 h after one cycle of adsorption is carried out. As depicted in Fig. 8(a) and (b), the hydrogels maintained high adsorption capacity of above 85% and 75% for MB and BPA, respectively after 3 cycles indicating that the hydrogels prepared using the simple immersion/agitation method can be a promising candidate for functionalized adsorbent in wastewater treatment.

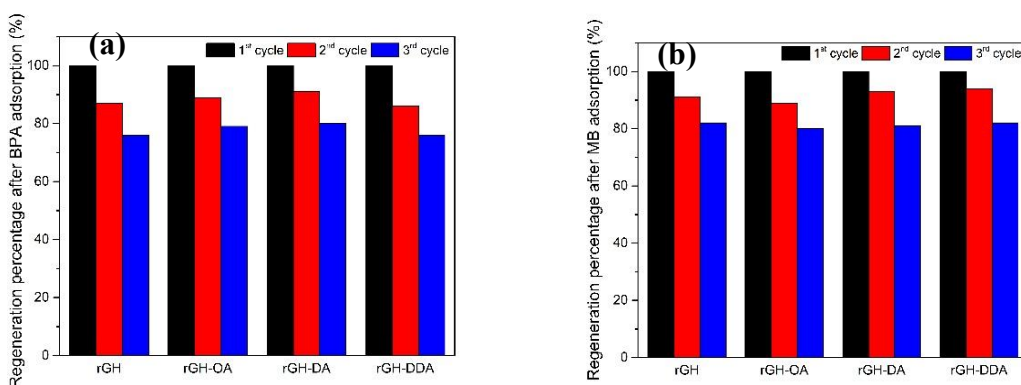


Fig. 4.8. Regeneration percentage after 3 cycles for the hydrogels after the adsorption of (a) BPA and (b) MB

Previously it was found that the interaction with organic pollutants with graphene-based materials often occurred via π - π interactions, electrostatic interactions, van der Waals, and hydrogen bonding[147,213].

In the case of the alkylamine-functionalized rGH, the larger specific surface area allows for more interactions with the pollutant, MB and BPA. FTIR studies are further used to access the interaction between the modified hydrogels and the pollutants as depicted in Fig. S5.1(a) and Fig. S5.2(b). Upon comparing to the FTIR spectra from Fig. 4.2., for MB, new strong peaks appearing at 1140 and 854 cm^{-1} highly suggest that the presence of bending band of N-H and C-N from the MB amide band functional group. Besides that, the appearance of the broad hydroxyl (OH) peak around 3300 cm^{-1} after MB adsorption highly suggests that hydrogen bonding did participate as one of the mechanisms of interaction; but is posited to be the least likely mode of interaction. Moreover, a significant increase in the intensity of C=O (COOH) showed that this functional group participated in the adsorption of MB. While for the BPA, the appearance of hydroxyl peak after BPA adsorption also indicate that hydrogen bonding did participate in BPA adsorption. The new peaks around 400-1800 cm^{-1} with significant intensity can be ascribed to the large amount of BPA adsorbed on the surface of the hydrogels [214]. However, π - π interaction is believed to be the main mechanism of interaction for both pollutants due to the aromatic structure of the pollutants and the graphene-based hydrogels.

In terms of adsorption performance of the as-prepared alkylamine surface-functionalized hydrogel with previously reported adsorbents for MB and BPA, the functionalized hydrogel exhibited good adsorption capabilities. Table 4.4 represents the adsorption capacity of some adsorbents towards MB and BPA. The differences in their adsorption capacity can be attributed to various factors including the functionalities, textural properties and experimental conditions. The results showed that the adsorption capacity of functionalized rGH prepared using the facile immersion/agitation method were comparable to that of previously reported adsorbents and can be a promising future for the remediation of noxious pollutants such as MB and BPA.

Table 4.4. Adsorption capacities of MB and BPA onto variously reported adsorbents

Adsorbate	Adsorbent	Adsorption capacity (mg/g)	Regeneration (%)	Reference
BPA	Thermally reduced graphene oxide	96.20	-	[215]
	Bagasse- β -cyclodextrin polymer	121.00	88.0	[216]
	MWCNTs- Fe_3O_4 - MnO_2	132.90	94.9 – 103.4	[217]
	Zero-valent Fe nanoparticles /chitosan	65.16	65.0	[218]
	Si/ Fe_3O_4 /N1-(3-trimethoxisilylpropyl) diethylenetriamine	182.66	> 95.0%	[219]
	N-doped polydopamine carbon	1351.00	90.0	[220]
	rGH-DA	228.00	>75.0%	This work
MB	Bagasse- β -cyclodextrin polymer	963.00	86.0	[216]
	Alginate/reduced graphene oxide	23.80	82.0	[121]
	Ag/TPP/rGH	130.37	~90.0	[64]
	Alginate/ SiO_2	139.31	-	[221]
	Graphene nanoplatelets	225.00	-	[222]
	Cellulose/GO	480.77	93.0	[223]
	rGH-DA	482.00	>85.0	This work

4.4. Conclusion

In summary, we report on a simple and economical approach in the preparation of functionalized alkylamine rGHs using the immersion/agitation method. The FTIR, BET, XRD, XPS and CV results indicated successful functionalization of alkylamine on the rGHs. The functionalization of the alkylamines occurred via ring-opening with the epoxy groups and amidation at the carboxylic groups. The adsorption studies showed that the specific surface area affects the adsorption capacity for the MB and BPA for short-chain

alkylamine (OA and DA) functionalized rGHs. The functionalization of the longer alkyl chain of the alkylamine (DDA) on rGH limits the π - π interactions with the MB/BPA, reducing their adsorption capability. The adsorption capacity is the highest for rGH-DA on MB and BPA at 482 and 228 mg/g, respectively. The understanding of the relevant adsorption conditions such as pH, initial concentration and temperature are indeed important parameters for a more comprehensive grasp of the adsorption mechanism and isotherm. Often, the multitude of pollutants present in real condition may interfere with the adsorption process. However, we posit that the adsorption test on MB and BPA using the alkylamine-functionalized rGH under ambient conditions without external manipulations should provide a rough assessment of their performance in actual wastewater conditions. In terms of technical operation, the interesting 3D structure of the alkylamine functionalized rGHs not only resolved the post-separation problems but also addressed the inherent problem of regeneration. Importantly, this present study offers an alternative functionalization method using the facile immersion/agitation treatment to prepare functionalized rGHs with promising potential that can be used in large scale industrial-scale application for wastewater treatment.

CHAPTER 5
SYNTHESIS OF SILVER NANOPARTICLES /PORPHYRIN/REDUCED GRAPHENE OXIDE
HYDROGEL AS DYE ADSORBENT FOR WASTEWATER TREATMENT

Abstract

Facile and versatile strategies for the preparation of reduced graphene oxide hydrogel (rGH) are of great interest due to its various applications in pollution adsorption, catalysis, gas sensors and tissue engineering. In this study, the preparation of a novel self-assembled reduced graphene oxide hydrogel modified with silver nanoparticles (AgNPs) and various porphyrin complex using the green hydrothermal approach is reported. The AgNPs were successfully decorated on the reduced graphene sheets via electrostatic interactions. On the other hand, the interaction of porphyrin complex is via chemical and/or physical bonding to the Ag/rGH sheets via esterification and π - π interactions. Based on thermogravimetric analysis and BET analysis, the intercalation of porphyrin complex improved the thermal stability and specific surface area (SSA) of the modified hydrogels. Further characterizations of the modified hydrogel are accomplished using Raman spectroscopy, X-ray diffraction (XRD), X-ray photoelectron spectroscopy (XPS), Fourier transform infrared spectrometer (FT-IR), scanning electron microscope-energy dispersive spectroscopy (SEM/EDS), and UV-Vis spectrophotometry. The adsorption capacity of the modified hydrogels increased with the integration of AgNPs and porphyrin complexes due to the increase of the number of adsorption sites. The Ag/TPP/rGH exhibits the highest adsorption capacity (130.37 mg/g) towards the cationic dye, methylene blue (MB) which is attributed to the additional binding sites from the available unoccupied aromatic structures of the TPP. All prepared hydrogels kinetic reaction conformed to the pseudo-second order model with good stability for removing MB with efficiency above 90%.

Keywords: Reduced graphene oxide hydrogels; silver nanoparticles; porphyrin; hydrothermal

5.1 Introduction

The study into the removal of dye from wastewater has garnered wide attention due to the harmful effects to our environment. Presently, the removal methods can be divided to either chemical, physical or biological methods in which each method possesses its specific advantages and disadvantages[224]. However, the adsorption method has its superiority of simplicity, high efficiency and low cost. The process of adsorption involves the accumulation of the pollutants in the framework of the adsorbent. Most adsorbents are developed to have the ability to be reused without affecting its adsorption capability. Provided that adsorbents play a vital role in the removal of pollutant from wastewater, an investigation into a reusable novel-based adsorbent having high adsorption capability and regenerative properties is needed. Up to now, many kinds of adsorbent have been applied for dye removal studies such as activated carbon (AC)[225–227], biochar (BC) [228,229], graphene (G)[230–232], clays[233–235], etc. Among them, graphene-based adsorbents have shown high performance for dye wastewater removal.

Graphene is a closely packed conjugated and hexagonally sp^2 hybridized carbon allotrope that exists in a honeycomb crystal lattice[97]. The study on this material is ubiquitous and has gained prominence among researchers in the past years since its discovery in 2010. The interesting properties that it possesses such as large specific surface area, high thermal and electrical conductivity, and good mechanical strength has potential to be an integral aspect in various applications[236–238]. The unique sp^2 hybridization facilitates the delocalization of electrons which is a sort after property in various field[239]. On the other hand, the development of three-dimensional network structure composed of graphene, also known as graphene-based hydrogel has shown to be an excellent accessory over traditional polymer hydrogel in pollution adsorption[147,178], catalysis[240,241], gas sensors[242,243] and tissue engineering[244]. The graphene-based hydrogel provides a template that enables it to blend with small molecules or macromolecules in the synthesis of multi-functional hydrogels that improves its salient properties[245]. Up to now, various preparation routes of novel graphene-based hydrogels with improved functionality and sensitivity using a simple process are explored for their usage in desired applications. The sol-gel technique is a commonly used method in the preparation of graphene-based hydrogel as the route involve using aqueous dispersion of graphene oxide (GO) as the starting material and the gelation is either induced from the reduction of GO, addition of linkers or increasing the concentration of GO. Up to date, the most favorable approach taken to

fabricate 3D graphene-based hydrogels is via the hydrothermal treatment[114,246,247] due to its advantages of simplicity, convenience, low cost and less harmful discharge of only carbon dioxide, CO₂ [31]. In order to improve the salient properties of the graphene-based hydrogels, various molecules have been incorporated through physical and chemical cross-linking, which includes polymers[248,249], biomacromolecules (DNA or protein)[250], and metal nanoparticles[251].

The high surface area of GO makes it an ideal substrate for dispersion of metal nanoparticles (MNPs)[252]. In addition, the abundant functional groups on the surfaces of GO can be used as anchoring sites for MNPs which is possible in the development of a functionalized hydrogel matrix during hydrothermal treatment. *Graphene* sheets have shown to be an effective support template for the silver nanoparticles (AgNPs) which were widely reported for water-treatment[66,253] and anti-bacterial applications[254,255]. Previously, it was reported that transition metal doped graphene-based hydrogel can be achieved via the simple hydrothermal route[251]. In terms of dye adsorption capability, the AgNPs have shown promising results which is attributed to their high surface area, and high reactive sites. As compared to other noble catalyst such as gold (Au), platinum (Pt) and palladium (Pd), the low cost and ease of preparation of AgNPs are among the attributing factors for its' extensive usage. The smaller *AgNPs loaded on graphene sheets* have shown to be effective in increasing the adsorption capacity of various dyes molecules which drive the interactions between adsorbent and adsorbate[256]. In addition, the graphene sheets enable the systematic control over the size and morphology of the AgNPs and hence facilitating the interaction with the adsorbate. Moreover, the strong interaction involving electrostatic interaction between the graphene and AgNPs enable the easy recovery process which addresses the inherent problem with MNPs based adsorbent which have recovery issues. AgNPs alone as an adsorbent may leech into the environment, hence causing secondary pollution which is not desirable.

Porphyrins are a class of macrocycles made up of four pyrrole units linked via methine bridges which have been widely used as the building blocks to synthesize porous materials such as metal–organic frameworks (MOFs), covalent organic frameworks (COFs) and conjugated meso- and microporous polymers (CMPs). These macrocyclic molecules have excellent optical, electronic and catalytic properties; thus, the effective integration of porphyrins into AgNPs/rGH sheets may elicit synergistic effects in catalytic applications. Previously, it was reported by Dasler *et al.*, [257] that graphene sheets can be covalently coupled in a

perpendicular orientation via the only one σ -bond to the porphyrin using the one-pot reductive diazotation approach. To our best knowledge, there has been no reported usage of porphyrins-based composite in the preparation of hydrogel for water-treatment purposes. The inclusion of porphyrin on a graphene-based hydrogel matrix has not been previously reported using the hydrothermal method. Hence, we intend to better understand the interaction of the porphyrins on graphene-based hydrogels and understand their capability in cationic dye adsorptions. In this work, we posit that the porphyrin complex is intercalated into the AgNPs/rGH sheets via π - π stacking interactions and covalent bonding following the hydrothermal reduction of GO sheets which provide additional binding sites for better adsorption capabilities of dye molecules. This approach aims to improve the performance of the graphene-based nanocomposite which is worth exploring, and important for future works and other practical applications of better adsorbent in wastewater treatment.

5.2. Materials and Methods

5.2.1 Materials

Graphene oxide dispersion in water (0.1-2.0 %) was kindly supplied by Nippon Shokubai Co., Ltd (AX-1-FM-W-151). Silver nitrate (AgNO_3), methylene blue (MB), tetrahydrofuran (THF), N,N-dimethylformamide (DMF), hydrochloric acid (HCl), propionic acid and ethanol ($\text{C}_2\text{H}_5\text{OH}$) were obtained from Wako Pure Chemical Industries Ltd, Japan. Pyrrole, benzaldehyde, 4-methoxybenzaldehyde, 4-butyloxybenzaldehyde were purchased from Sigma Aldrich. Deionized water (18.25 M Ω .cm) was obtained from a Milli-Direct 16 (Millipore Q, USA) for the entire experiment. Unless specified otherwise, all the reagents and materials were used without further purification.

5.2.2 Synthesis of porphyrin complexes

The free base porphyrins, tetraphenylporphyrin (TPP) was synthesized using the Alder-Longo method[258]. The other free base porphyrins which include tetrakis(4-methoxyphenyl) phenylporphyrin (TOMPP), and tetrakis(4 butyloxyphenyl) phenylporphyrin (TOBPP) were synthesized using the modified Alder-Longo method[259–261]. The step involved heating the aldehyde in propionic acid followed by adding the same amount of pyrrole and refluxed under continuous stirring. After 2 hours, ethanol was added, and the solution was kept in the refrigerator overnight. The purple crystals obtained was then purified and dried under

ambient temperature. The synthesized products; TPP and TOMPP were in range 9 to 36% yield. However, long chain derivative porphyrins, TOBPP produced lower yield than 10%, due to the steric hindrance and the donating group on the para-position of alkyl long chain derivative. Fig. S5.1 depicts the general scheme for the synthesis of the porphyrin complexes while Fig. S5.2 depicts the molecular structure of the porphyrin complexes.

5.2.3 Synthesis of AgNPs/porphyrin/rGH

30 mL of GO solution was initially ultrasonicated in deionized water to a concentration of 2.0 mg/mL for 1 hours in order to exfoliate the GO layers and also to transform the carboxylic acid groups into carboxylate ions. Next, 35 mg (0.01 M) of AgNO_3 was then added to the aqueous dispersion of GO. 50 mg of TPP was dispersed in 5 mL of THF which gave a light red suspension with a concentration of 10 mg/mL. The porphyrin suspension was mixed with graphene suspension and sonicated for 20 minutes. The solution mixture was then transferred into a modified 80 mL Teflon lined autoclave bottle. The hydrothermal reduction was carried out in a Scientific Autoclave (NCC-1701) at 130°C for 8 hours. After the autoclave naturally cooled to room temperature, the resulting hydrogel was dialyzed in distilled water. The experiment was repeated with different porphyrin complexes; which are TOMPP and TOBPP.

5.2.4 Characterizations

The surface morphology and structure of the prepared composite were examined using scanning electron microscopy (SEM) using a JEOL 6000 microscope fitted with energy dispersive X-ray analyzer (EDX) operated at 15kV accelerating voltage. ATR- Fourier transform infrared spectroscopy were carried out using a PerkinElmer Spectrum GX in the range of 4000 cm^{-1} to 500 cm^{-1} . Thermogravimetric analysis (TGA) was performed to analyze the weight ratios using EXSTAR TG/DTA7000 under N_2 atmosphere from room temperature to 550°C at a rate of $10^\circ\text{C}/\text{min}$. The crystalline structure was recorded on a Rigaku X-ray diffractometer with Cu K- α radiation at 40kV and 15 mA with a scan rate of $10^\circ/\text{min}$. Raman spectroscopy were performed using an JASCO NRS-5100 Laser Raman Spectrometer with an excitation wavelength of 532 nm and 2.5 mW laser power beam. X-ray photoelectron spectroscopy (XPS) of the modified hydrogels was performed on Axis Nova (XPS) Surface Analyzer with a monochromatized Al K α X-ray source. The survey spectra were recorded with high-resolution spectra of 80.0 eV. The fitting of the spectra of the

deconvolution peaks of C 1s, O 1s, N 1s and Ag 3d were using Casa XPS software[182]. The N₂ adsorption-desorption were carried out using a Surface Area and Pore Size Analyzer Quantachrome Instruments. The surface area and pore size distribution of the rGH samples were calculated using the Barrete-Joynere-Halenda (BJH) method. The adsorption spectrum was measured by UV-vis spectrophotometer (Genesys 10s, Thermo Fisher Scientific) using wavelength ranging from 200 – 400 nm. The hydrogel was sonicated in DMF to a concentration of 0.1 mg/mL before UV measurements.

5.2.5 Adsorption experiments

Analytical grade dye, MB was used as the model pollutant and the adsorption behaviour of the as prepared hydrogel is prepared. MB was first dissolved in deionized water to prepare a solution with an initial concentration of 1 g/L. Subsequently, dilution was carried out to the desired concentration. The as-prepared hydrogel cylinder was placed in a solution containing MB (150 mL, 20 mg/L) and the mixture was agitated for 24 hours under normal light condition until adsorption equilibrium is achieved at room temperature. The GH was then removed at different time interval, and the residue dye solution were analysed. The adsorption capacity (Q_e) were calculated with the following equation:

$$Q_e = \frac{(C_0 - C_e)V}{m}$$

where C_0 represents the initial concentration (mg/g), C_e represents the equilibrium concentration (mg/g), V is the volume of the solution and w is the mass of the adsorbents (mg).

5.3. Results and Discussion

Almost cylindrical shaped reduced graphene hydrogels were formed as depicted in Fig. 5.1 after hydrothermal treatment for 8 h at 130°C. The cylindrical shape is consistent with many studies reported in which was posited to be due to the strong π - π and hydrogen bonding above a critical concentration of the starting GO suspension. From the naked eye view, the decoration of AgNPs on the surface is apparent for samples (b)-(e) due to the presence of shiny-like coating on the surface of the cylinder hydrogel. The water content of the samples was evaluated using the following equation:

$$\text{Water content} = \frac{M_W - M_D}{M_W} \times 100 \%$$

where M_w represents the mass of the as-produced rGH and M_d denotes the mass after freeze-drying. Based on Table 1, although the same volume and the same concentration of GO dispersion were used to prepare each sample, the volume of the hydrogel produced were 0.94 cm³, 1.85 cm³, 1.81 cm³, 2.41 cm³, and 1.94 cm³ for rGH, Ag/rGH, Ag/TPP/rGH, Ag/TOMPP/rGH and Ag/TOBPP/rGH, respectively. Fig. 5.2. illustrates the SEM images of horizontally cut cross sections of the modified graphene-based hydrogels. Based on Fig. 5.2(a), the morphology of the rGH clearly depicts randomly oriented 3D framework while the wrinkles that can be seen are attributed to the deviation from the sp² planar character expected for graphene monolayer. The surface of the reduced graphene after freeze dry becomes hydrophobic[53,79]. The agglomeration of sheets is possible from the increased hydrophobic interactions between individual sheets due to the hydrothermal reduction.

Table 5.1. Diameter and water content of the modified graphene hydrogel

Sample	Water content (%)	Volume (cm ³)	Density (mg/cm ³)
rGH	98.6	0.94	23.8
Ag/rGH	98.9	1.85	13.3
Ag/TPP/rGH	99.1	1.81	11.7
Ag/TOMPP/rGH	98.7	2.41	11.9
Ag/TOBPP/rGH	99.2	1.94	9.43

Based on Fig. 5.2(b-e), the partial overlapping and coalescing of graphene nanosheets were accompanied with the successful decoration of the AgNPs randomly oriented on the framework. From Table 2, the elemental composition analysis from EDS confirms the presence of AgNPs that may interact electrostatically in which they coordinate with carboxylic groups with possibility of linking to the graphene sheets. When the carboxylic groups are saturated, the electrostatic repulsion between other carboxylic groups are reduced, leaving the system to interact through the π - π bond.

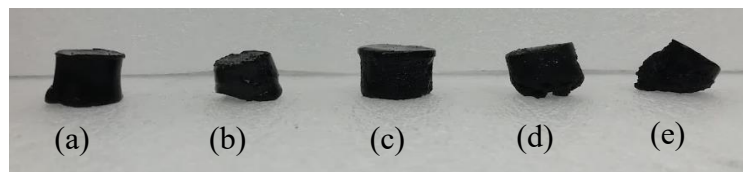


Fig. 5.1. Photo images of the graphene-based hydrogels: (a) rGH, (b) Ag/rGH (c) Ag/TPP/rGH (d) Ag/TOMPP/rGH (e) Ag/TOBPP/rGH

The porphyrin complex deposited on graphene sheets leads to a distinct thickness which is posited to be interacting via strong π - π and hydrophobic interaction which also preserved the structure of the graphene[262]. Hence, this finding may suggest that the strong coalescent of the single layer graphene sheets is driven from the addition of porphyrin complexes which is known to be an electron rich organic molecules bearing bulky aromatic substituents[263].

The Raman spectroscopy enables the study on the geometric structure of the reduced graphene hydrogel samples. In short, the evaluation of disorder of the sp^2 hybridized structure is possible using this technique. Fig. 5.3(a) depicts the Raman spectra of the modified hydrogel samples. The three characteristics bands of graphene-based materials in Raman spectra includes the G band ($\sim 1580\text{ cm}^{-1}$) attributed from in-plane vibration due to the first order scattering of the E_{2g} phonons of the sp^2 hybridized carbon atom, D band ($\sim 1350\text{ cm}^{-1}$) which is due to the breathing mode of k-point phonos of A_{1g} symmetry of the defects involving the sp^3 hybridized carbon bonds such as hydroxyl and/or epoxide bonds, and the 2D bands of single layer graphene sheets located at $\sim 2690\text{ cm}^{-1}$. In comparison to rGH, the Raman spectrum of Ag/rGH indicated that the D and G band shifted to 1342 cm^{-1} and 1593 cm^{-1} , respectively. The almost unchanged I_D/I_G ratio suggests that the AgNPs does not introduce defect on the rGH surface but merely decorate the surface of the graphene sheet.

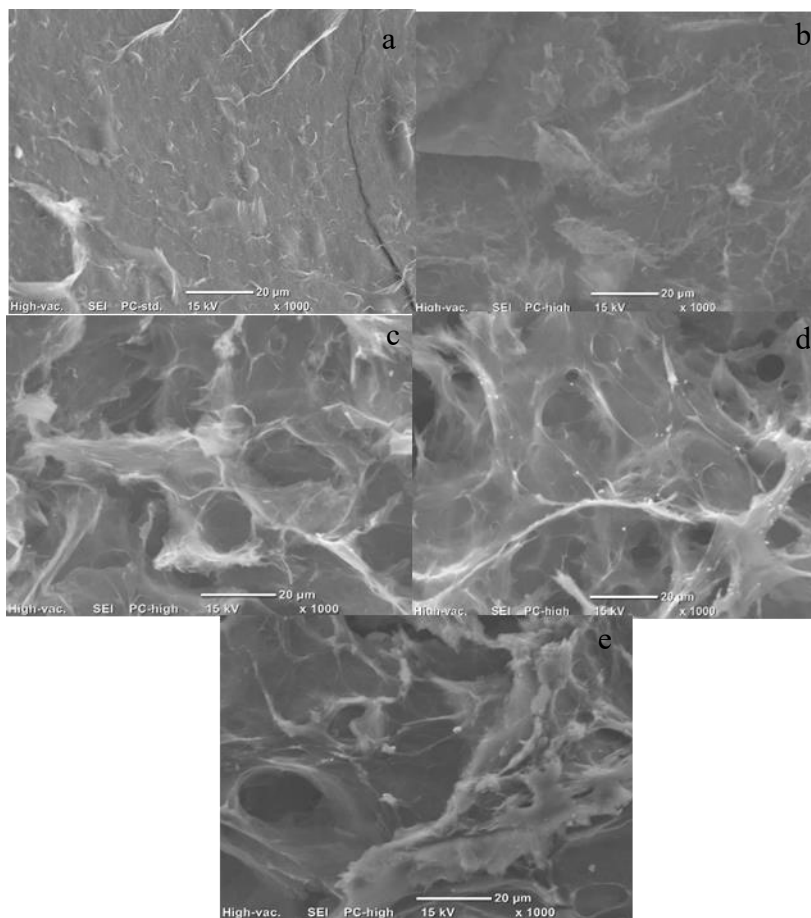


Fig. 5.2. SEM images of images of interior microstructure of reduced graphene hydrogels: (a) rGH, (b) Ag/rGH (c) Ag/TPP/rGH (d) Ag/TOMPP/rGH (e) Ag/TOBPP/rGH

Furthermore, the new Raman peak appearing at 1102 cm^{-1} also indicated that AgNPs were anchored on the graphene sheets via chemical interaction[264]. On the other hand, the I_D/I_G ratio of the porphyrin modified hydrogels are 1.08, 1.04 and 1.10 for TPP, TOMPP and TOBPP, respectively. After functionalization process, the D peak gets slightly stronger and broader due to the higher level of disorder in the samples containing TPP and TOBPP. The findings indicate that the size of the sp^2 domain decreases as the rGO sheet is broken into fragments during the incorporation of porphyrins and the conversion of sp^2 to sp^3 basal carbon atoms due to covalent binding of the porphyrin added[257]. Moreover, new spectroscopic features at about ($820, 997, 1079, 1479, 1526\text{ cm}^{-1}$) can be detected and ascribed to the free base porphyrins. The slight changes in the D-band intensity in the spectra after the incorporation of porphyrins indicated a successful covalent functionalization.

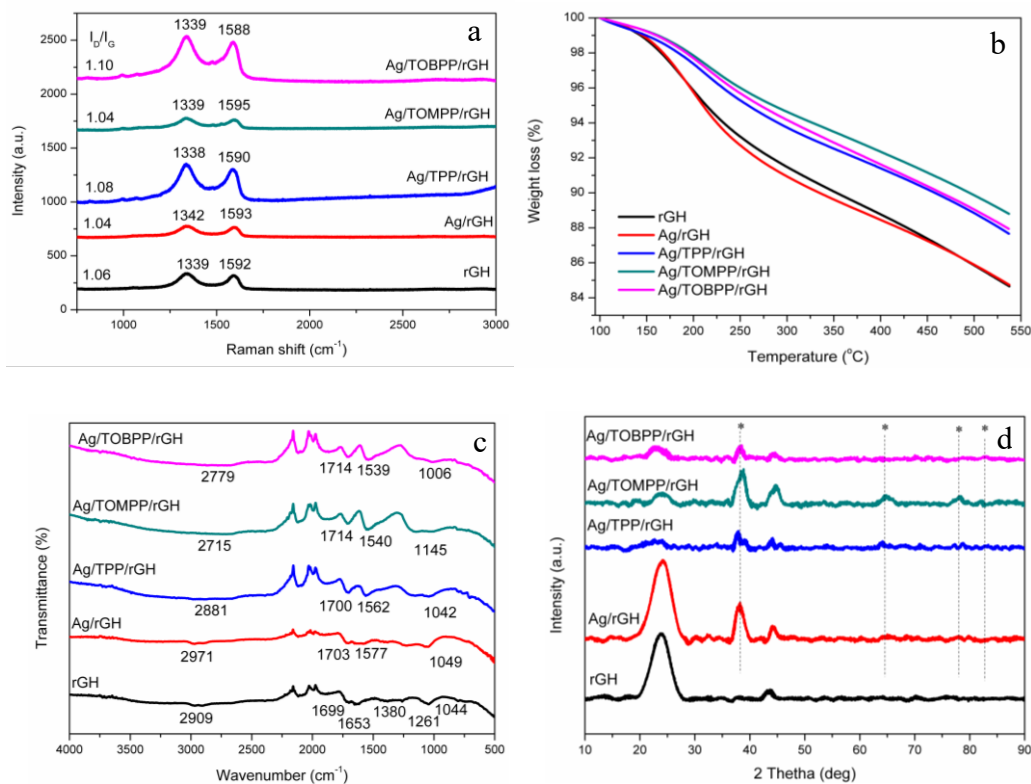


Fig. 5.3. (a) Raman spectra (b) TGA thermogram (c) ATR-FTIR spectra (d) XRD spectra of the modified hydrogels.

Thermogravimetric analysis (TGA) was further used to access the thermal stability of the modified graphene hydrogels. Based on Fig. 5.3(b), the thermal decomposition of the samples takes place in two primary decomposition stages. The first fraction of steady mass loss below 150 °C is attributed to the evaporation of absorbed water. The significant mass loss above 150°C is resulted from the pyrolysis of labile oxygen containing functional groups especially the hydroxyl and epoxy groups on the rGH[61,63]. The decoration of AgNPs on the graphene sheets did not adversely affect the graphene sheets' robustness as almost similar degradation curve could be observed. However, with the presence of porphyrin, they showed higher thermal stability with a lower mass loss at 12.3%, 11.2% and 12.8 % for Ag/TPP/rGH, Ag/TOMPP/rGH and Ag/TOBPP/rGH, respectively below 550°C as compared to rGH and Ag/rGH. The TGA analysis behavior of the three porphyrins is relatively similar. The second degradation fraction is mainly due to the decomposition of porphyrin. The results indicate that porphyrin complex is intercalated in the graphene sheets which increases its' thermal stability. This is supported by the

presence of small amount of N as shown in the XPS elemental analysis. Hence, this result suggests the improved thermal stability of the prepared reduced graphene sample with the presence of porphyrin complex.

FTIR provides an overview of the functional groups present in the hydrogel samples. Fig. S5.3 and Table S5.1 shows the absorption spectra at various wavenumber of the porphyrins. The free base porphyrin complexes exhibited the characteristic peak of N-H stretching and N-H bending vibration in range from 3310-3320 cm^{-1} , and 965-967 cm^{-1} , respectively. The signal peak of C-H stretching (long chain) and C-N stretching in porphyrin ring were showed in the range from 2830-2940 cm^{-1} and 1210-1250 cm^{-1} , respectively. When the number of carbon atom in long chain were increased, the frequency of both signals is found to be slightly decreased due to the electronic effect of long chain substituent. However, the signal peak including C=C stretching in phenyl and C-H bending in porphyrin of all synthesized porphyrin complexes displayed a small peak shift in IR spectra upon comparing to TPP. On the other hand, Fig. 5.3(c) depicts the ATR-FTIR spectra of rGH, Ag/rGH, Ag/TPP/rGH, Ag/TOMPP/rGH and Ag/TOBPP/rGH samples. The spectrum of rGH with following peaks: 1,044 cm^{-1} corresponding to C-O stretching vibration mode related to the presence of the alkoxy group, 1,261 cm^{-1} attributed to C-O from the epoxy group, 1,380 cm^{-1} attributed to carboxylic O-H deformation formation, 1,653 cm^{-1} associated with the presence of C = C bond, and 1,699 cm^{-1} assigned to C = O stretching vibration mode in carboxyl group. For the spectrum of the Ag/rGH, most of the absorption bands are weakened leaving mainly the absorption at 1703 cm^{-1} (C=O), 1577 cm^{-1} (C-OH bending vibrations) and 1049 cm^{-1} (C-OH bending vibrations). The peak at 1653 cm^{-1} in the rGH shifted to a lower frequency at 1577 cm^{-1} in the Ag/rGH. The FTIR results demonstrate that Ag⁺ contributes to the further reduction of GO to reduced graphene and strong interaction may exist between silver nanoparticles and the remaining surface hydroxyl groups. The increase in the intensity of the carbonyl and the peak at about 1500 - 1600 cm^{-1} confirmed the restoration of the sp² carbon network while the peak at around 1700 cm^{-1} corresponds to vibrations of carbonyl groups. The bands in the region 2700-2900 cm^{-1} , maybe attributed to the C-H stretching vibrations of the aromatic rings of the porphyrin, further confirming its existence on graphene sheet. Moreover, the disappearance of the peak at 1380 cm^{-1} also clearly indicates that the porphyrin molecules

are covalently bonded to the reduced graphene sheets via carboxylic acid linkage. These changes clearly indicate a strong interaction between Ag/rGH and the porphyrin complex.

XRD study was further carried out to evaluate the crystalline structures of the prepared modified hydrogels. The XRD patterns of the samples are depicted in Fig. 5.3(d). The XRD spectra of GO which is not shown show a sharp peak at around 10.24° and 19.77° . After reduction of GO, the (0 0 2) peak of GO gradually disappears and well-resolved diffraction peaks observed at 2θ are 23.74° , 24.60° and 23.82° . As for the Ag/rGH, the fingerprint diffraction pattern of Ag observed at 38.1° confirms the formation of high purity crystalline Ag in the composites. Besides that, prominent patterns at 38.1° , 44.31° , 64.51° , and 77.51° which are assigned to the (1 1 1), (2 0 0), (2 2 0), and (3 1 1) crystallographic planes of face-centered cubic AgNPs, respectively. The inclusion of the porphyrin complex leads to a significant decrease in the intensity of the reduced graphene oxide peak located in the 23° - 24° range possibly due to the interaction with the porphyrin complexes which leads to the structural changes of the graphene sheets. However, the prominent patterns assigned to the (1 1 1), (2 0 0), (2 2 0) and (3 1 1) crystallographic planes of face-centered cubic AgNPs remains.

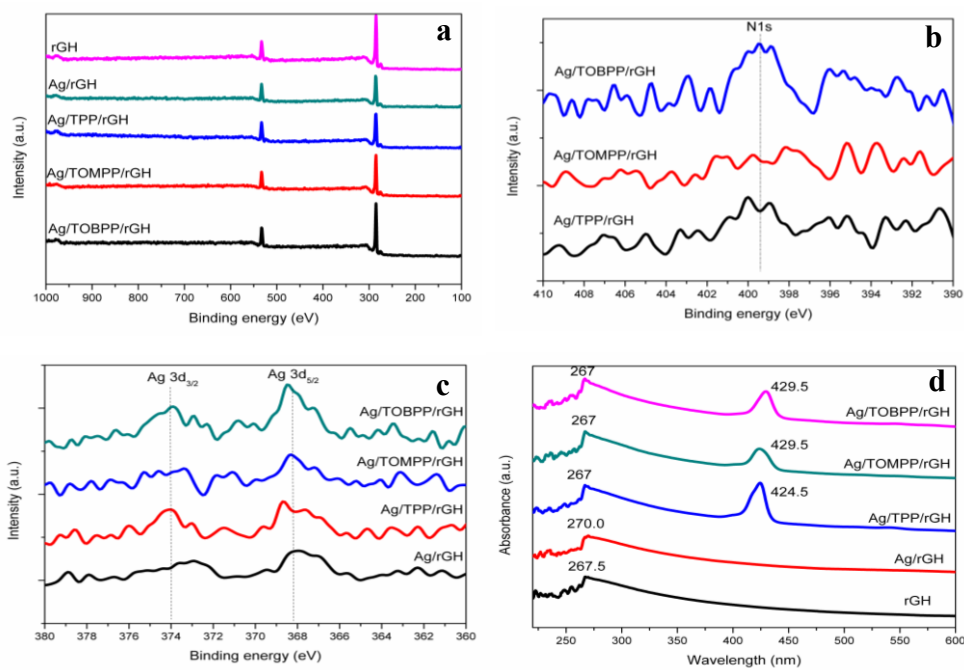


Fig. 5.4. XPS (a) wide (b) Ag 3d (c) N 1s and (d) UV-vis spectra of the modified graphene hydrogels

XPS characterization was carried out to quantify the chemical nature of the functional groups present in the prepared modified graphene-based hydrogels. Fig. 5.4(a) depicts the wide scan XPS spectra of the hydrogels. The obvious peaks at around 280-295 eV and 525-540 eV are attributed to the C1s and O1s, respectively in which contributed to the graphene. The atomic ratio of carbon to oxygen (C/O) was then obtained from the respective area under the C1s and O1s peak. The C/O ratio of Ag/rGH sample decreased to 1.63 from 2.39 (rGH) which showed that the electrostatic interaction of the Ag ions with the carboxylate groups of the graphene sheets hinders the reducing process. However, the inclusion of porphyrin complexes in the starting material somewhat improves the reducing capability during hydrothermal process. The C/O ratio obtained are 1.68, 2.01 and 2.14 for the TPP, TOMPP and TOBPP, respectively. Based on Fig. 5.4(b), the Ag 3d_{5/2} component which occurred at 368.3 eV is characteristic of metallic Ag (0) oxidation state. The findings indicated that AgNPs are decorated on the surface of the modified hydrogels. However, both Ag 3d_{3/2} and Ag 3d_{5/2} shifted slightly towards higher energy level, suggesting the interaction between graphene and AgNPs leads to a decrease in the electron density of Ag atoms, probably due to the conjugation between the d-orbit of Ag atom and π -bond of graphene[265]. The results showed that the content of AgNPs could be controlled by introducing porphyrins as it can be seen that the strong intensity of the Ag 3d_{5/2} of the hydrogels containing TPP, TOMPP and TOBPP samples. On the other hand, the successful interaction of the porphyrin complexes with the graphene sheets can be proven from the N1s spectra of the XPS in Fig. 5.4(c) in which from the presence of N1s peak attributed from the N-H bending and stretching of the porphyrins complex. The interaction is posited via the π - π interactions which preserved the structure of the porphyrin complexes. Based on Fig. S5.4., characteristics bands of the free base porphyrins consisted of a strong absorption band (Soret band) at 417-422 nm and four weak adsorptions band (Q band) around 500-700 nm due to the $\pi \rightarrow \pi^*$ electronic transitions which is recorded in dichloromethane at room temperature. This finding is in agreement with previous studies on the absorption behavior of free-base porphyrin of TPP[266,267]. The intense Soret band assigned to the S₀→S₂ transition is found in a shorter wavelength while the Q bands assigned to the S₀→S₁ transitions, appear in longer-wavelength[260]. The Soret band and Q band of the *para*-substituted porphyrin, TOMPP and TOBPP exhibited a slight red shifting when compared with TPP. The absorption data and molar extinction coefficient (ϵ) of all synthesized porphyrins

are summarized in Table. S5.2. Typically, the optical absorption spectra of GO (not shown) will produce two peaks; one around 230 nm which is due to $\pi-\pi^*$ transitions of the aromatic carbon bond and a small shoulder peak around 300 nm attributed to the $n-\pi^*$ of the carbonyl bonds[268]. Based on Fig. 5.4(c), the UV-visible spectra of rGH showed a characteristic peak at 267.5 nm assigned to the $\pi-\pi^*$ transition that designates that the conjugation remains stored and the majority of oxygen moieties are eliminated from the GO after hydrothermal treatment. As for the Ag/rGH, weak or almost close to no plasmonic band which is expected to be observed for AgNPs at around 420 nm. However, this can be explained by the low concentration of AgNO_3 that lead to the formation of fewer nanoparticles on the surface of the graphene sheets[269]. However, the red-shifting for the $\pi-\pi^*$ transition for the Ag/rGH sample is possible due to the presence of the small amount of AgNPs on the sheet. Based on Fig. S5.4, the characteristics band of the free base porphyrins consisted of a strong absorption band (Soret band) at 417-422 nm and four weak adsorptions band (Q band) around 500-700 nm due to the $\pi\rightarrow\pi^*$ electronic transitions. Hence, for the Ag/TPP/rGH, Ag/TOMPP/rGH and Ag/TOBPP/rGH, slight blue-shifting to 267 nm of the $\pi-\pi^*$ transition band can be observed and the typical absorption band attributed to porphyrins complex which have red-shifted can be seen at 424.5 nm, 429.5 nm and 429.5 nm. The overlapping bands of the Q band and AgNPs plasmonic band leads to a single peak around the region.

Although DLS techniques do not represent the real particle size of graphene-based materials, this technique allows for rough assumption in the measurement of translational diffusion constant of spherical particles[270,271]. In this study, the graphene-based hydrogel suspension in DMF is assumed to be in spherical shape. The average hydrodynamic diameter (AHD) of the hydrogel samples is measured using DLS and depicted in Fig. 5.5

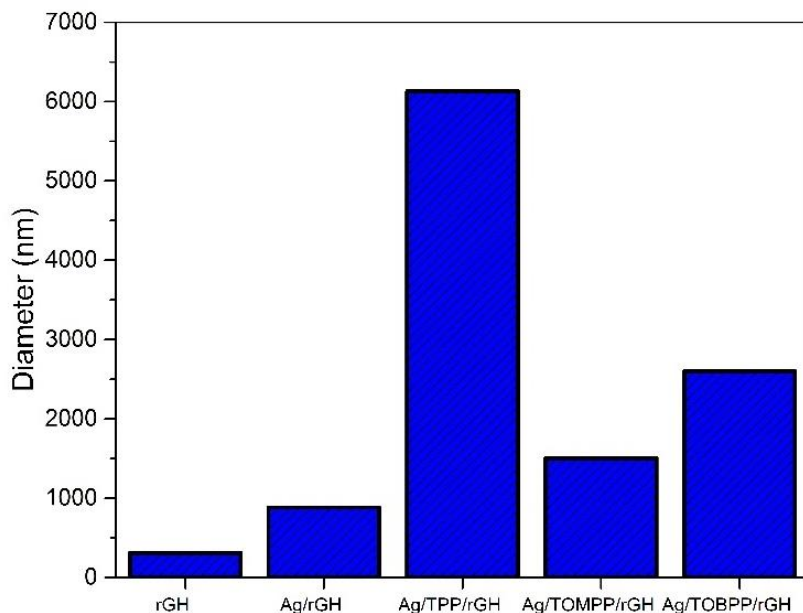


Fig. 5.5. The average hydrodynamic diameter (AHD) of the modified graphene-based hydrogels

The diameter obtained is 308.4, 881.9, 6131.6, 1505.0, 2600.4 nm for rGH, Ag/rGH, Ag/TPP/rGH, Ag/TOMPP/rGH and Ag/TOBPP/rGH, respectively. The increase in the diameter of Ag/rGH as compared to rGH suggesting interactions between rGH and AgNPs. Based on Fig. S5.5., the size distribution of the graphene sheets is narrow and concentrated around 100-500 nm range. However, Ag/rGH solution exhibits two different particle size distributions, which showed that some AgNPs were coated on carrier surface and the remaining part remained in the form of discrete particles at microparticles level (<100nm). In For the case of porphyrins in the hydrogel system, they significantly increase the AHD. Moreover, similar size distribution could be seen for sample Ag/TPP/rGH, and Ag/TOMPP/rGH which showed two distinct particle size distributions similar to Ag/rGH. However, as for Ag/TOBPP/rGH, only one particle size distribution could be seen which is concentrated around 1000 nm. The underlying reason is that the AgNPs may have fully bounded to the graphene/TOBPP sheets.

The zeta potential measurements on the modified graphene-based hydrogels is carried out to access the dispersion stability of the modified hydrogel. Zeta potential is the charge that is present at the interface between a solid surface and the liquid phase which is an important parameter. The double layer around the colloid affects the electrostatic interaction between the graphene sheets. The obtained average zeta potentials are 0.57 mV, 0.71 mV, -0.04 mV, -0.69 mV and -0.84 mV for rGH, Ag/rGH,

Ag/TPP/rGH, Ag/TOMPP/rGH and Ag/TOBPP/rGH, respectively. It was previously reported that Zeta potential experiments showed rGH to be positively charged in DMF[272]. It can be seen that the zeta potential increased after the decoration of AgNPs on the surface of the graphene which can be attributed to the viscosity of the suspension in DMF which leads to the increase in electrophoretic mobility[273]. The zeta potential showed a negative charge with the presence of porphyrin complex and interestingly, more negative value is obtained as the chain length is increased from TPP to TOBPP. The significant increase in the negative zeta potential value can be attributed to the cage effect in DMF caused by negatively charged porphyrin complexes with the chain length

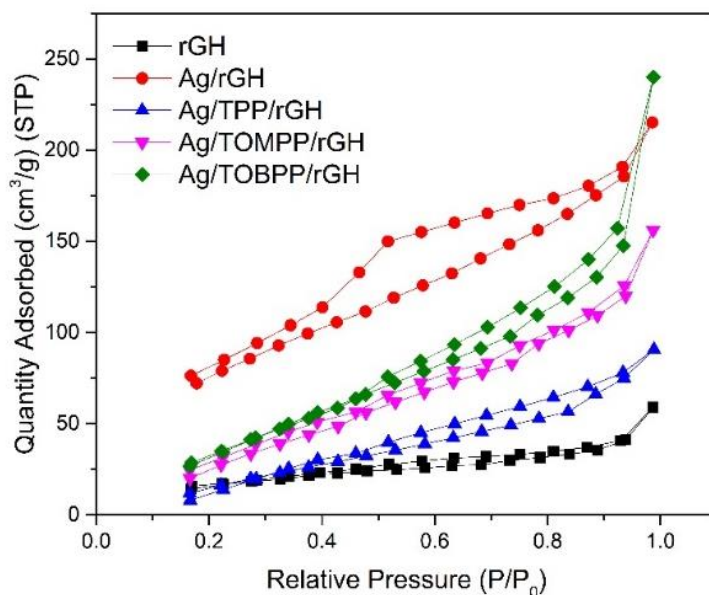


Fig. 5.6. N₂ adsorption-desorption isotherm of the modified hydrogels

In order to elucidate the surface areas and microstructure of the hydrogels, low-temperature N₂ adsorption-desorption isotherm were carried out. Fig. 5.6. shows the N₂ adsorption-desorption isotherm of the freeze-dried hydrogels in which the curves can be characterized by the Type 2 isotherm with hysteresis loops reflecting that micropores or mesopores exist in the hydrogels. This finding conforms to the formation of a mesoporous structure that has connected or non-connected ink-bottle pores or cavities. Table 2 depicts the BET SSAs of rGH, Ag/rGH, Ag/TPP/rGH, Ag/TOMPP/rGH and Ag/TOBPP/rGH were measured at 27.288, 163.721, 68.328, 100.782 and 138.441 m²/g respectively. The significant increase in the surface area but decrease the pore size with the decoration of AgNPs

can be attributed to the thermal reduction of the functional groups attached to the graphene sheets[274]. The low specific surface area obtained as compared to previous studies of graphene-based hydrogels is mainly due to the freeze-drying procedure which leads to the restacking of individual hydrophobic graphene sheets due to strong π - π interaction with the porphyrin complex [182,204].

Table 5.2. BET surface area, BJH pore size and volume of the freeze-dried graphene-based hydrogels based on desorption process

Sample	BET Surface area (m ² /g)	Pore size (nm)	Pore volume (cm ³ /g)
rGH	27.288	1.981	0.069
Ag/rGH	163.721	1.741	0.237
Ag/TPP/rGH	68.328	1.977	0.128
Ag/TOMPP/rGH	100.782	1.973	0.213
Ag/TOBPP/rGH	138.441	1.975	0.354

The dye adsorption capacity of the as-prepared graphene-based hydrogels was investigated by direct adsorption in aqueous MB solutions under normal light condition. The in-situ adsorption of the 'wet' hydrogel could demonstrate real adsorption process instead of freeze-dried samples[275]. The absorbance wavelength of MB occurred around 664 nm recorded at various time-interval and the final concentration of the residue dye MB after immersion is obtained from the standard curve plotted which is depicted in Fig. S5.6. The standard curve was obtained by plotting the maximum absorbance obtained for the MB samples at various concentrations. The coefficient correlation (R^2) obtained at 0.99704 by plotting the absorbance versus the prepared concentration was satisfactory. The primary adsorption kinetic curves of the prepared hydrogels are shown in Fig. 5.7(a) in which the hydrogels demonstrated steady adsorption until reaches equilibrium after 24 h for the MB.

The adsorption capacity obtained are 75.67, 100.76, 130.37, 103.24 and 125.76 mg/g for rGH, Ag/rGH, Ag/TPP/rGH, Ag/TOMPP/rGH and Ag/TOBPP/rGH, respectively. The decoration of AgNPs onto the rGH

has shown to improve the adsorption capacity by 33.2% which can be attributed to increase in its specific surface area and smaller pore size as shown in the BET results. The AgNPs increases the number active sites on the surface of the rGH which increases the uptake of MB[256]. On the other hand, the inclusion of porphyrin complexes on the Ag/rGH improved the adsorption capacity by 130.27%, 36.43% and 66.20% for Ag/TPP/rGH, Ag/TOMPP/rGH and Ag/TOBPP/rGH, respectively when compared to rGH alone. The availability of additional binding sites for MB due to the 'free' aromatic structures exhibited by TPP may be the possible reason why it possessed the highest adsorption capacity. The shifting of the S-band of the porphyrin complexes as obtained from the UV-vis may confirm the π - π interaction of the Ag/rGH and the porphyrin complexes.

The primary adsorption kinetic experiments of the as-prepared composite hydrogels from 0 to 2000 min are shown in Fig. 5.7(a). It can be seen that the adsorption of the MB increases rapidly in initial adsorption times (about 600 min) before reaching equilibrium. The time-dependent study of the MB adsorption demonstrates the improved performance of AgNPs and porphyrins modified rGH as compared to rGH itself. This is compounded to the fact that the incorporation of AgNPs and porphyrin onto the porous rGH create more active sites for the MB interaction, hence increasing the sorption capacity and making the sorption process to occur much faster. Besides, the larger specific surface area and pore volume of the modified hydrogels contributed to the excellent adsorption capacity as compared to control sample, rGH. It is interesting to note that there is no correlation between the adsorption capability to the surface area of the hydrogels to its' the textural properties. Hence, we posit that the adsorption behaviour of MB on the hydrogels is affected by the combination of both. Even though Ag/rGH possessed the highest specific surface area, however, the pore structure is one factor that affects the mass diffusion in the adsorbent resulting in low adsorption capacity as compared to the porphyrin complexes modified graphene hydrogels. However, the high specific surface area affects adsorption selectivity in which they provide multiple adsorption driving forces between the adsorbent and adsorbates[276]. From BET results, it can be seen that the integration of the porphyrin complexes significantly improved the specific surface area (SSA) of the hydrogels.

In adsorption experiment, the kinetic studies provide important insight on the mechanism involved especially involving the adsorption rate and adsorption equilibrium time. The adsorption kinetics of the

hydrogels for MB adsorption are presented in Fig. 5.7(b-c). The adsorption kinetics of the MB adsorption on the hydrogels were investigated using two classical kinetic models namely pseudo first-order (PFO) and pseudo second-order (PSO) kinetic model. The PFO corresponds to a diffusion-controlled process involving solid-liquid phase adsorption while the latter assumes the process is controlled by adsorption reaction at a liquid-solid interface in the adsorbent. The linearized form of the model employed to describe the adsorption are as follows:

The pseudo first-order model:

$$\ln(Q_e - Q_t) = -k_1 t + \ln(Q_e)$$

The pseudo second-order model:

$$\frac{t}{Q_t} = \left(\frac{1}{Q_e}\right)t + \frac{1}{Q_e^2 k_2}$$

where Q_e and Q_t are the MB amount (mg/g) adsorbed on the adsorbent at equilibrium, t represents the time, and k_1 (h^{-1}) or k_2 (g/mg.h) is the adsorption rate constant. All the parameters (K_1 & K_2) and the correlation coefficient (R^2) obtained from the kinetic models are summarized in Table S6. According to our findings, the adsorption kinetic data of MB on the hydrogels can be accurately fitted to the PSO model for all the hydrogel samples as they showed better regression coefficient conforming to the chemisorption process. Thus, these results revealed that the diffusion is not rate control process but a controlled adsorption through the binding reaction by sharing of electrons or covalent interactions. In addition, the calculated adsorption capacity values are closer to the experimental values for the PSO model upon comparing to the PFO model.

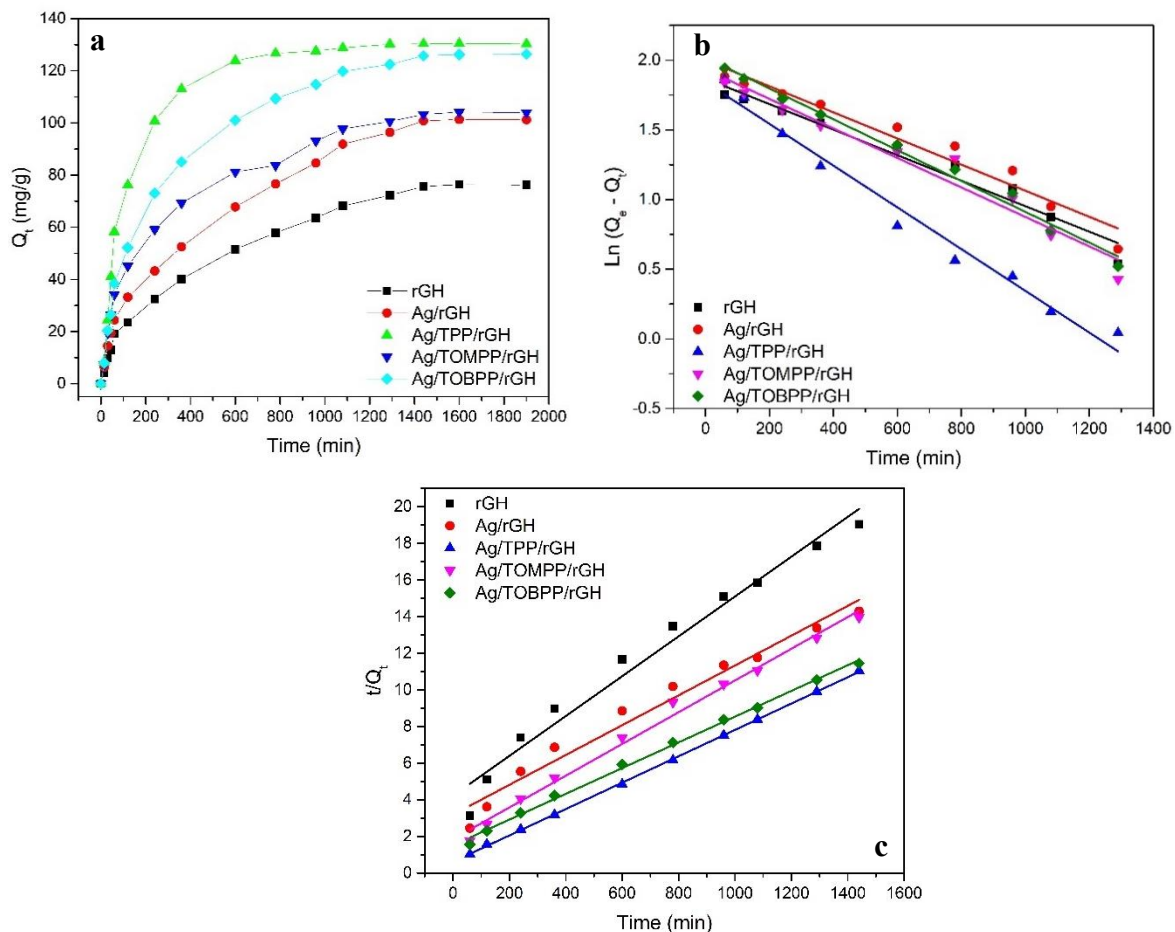


Fig. 5.7. (a) Time-dependent study (b) pseudo-first-order (c) pseudo-second-order kinetic studies for the adsorption of MB at 298 K.

To determine the reusability of the modified hydrogels, consecutive adsorption and desorption was carried out for three cycles using the same hydrogel under the same adsorption conditions. After MB adsorption for every cycle, the hydrogel was removed and shaken in a solution of 0.5 M HCl for 5 hours. Subsequently, the hydrogel is rinsed and washed with deionized water. The adsorption capability remained high after three cycles. As depicted in Fig. 5.8(a), the adsorption-desorption cycles maintain above 90% of the original MB adsorption capacity. Hence, the as-prepared hydrogels possessed stable adsorption behavior towards cationic dye, MB.

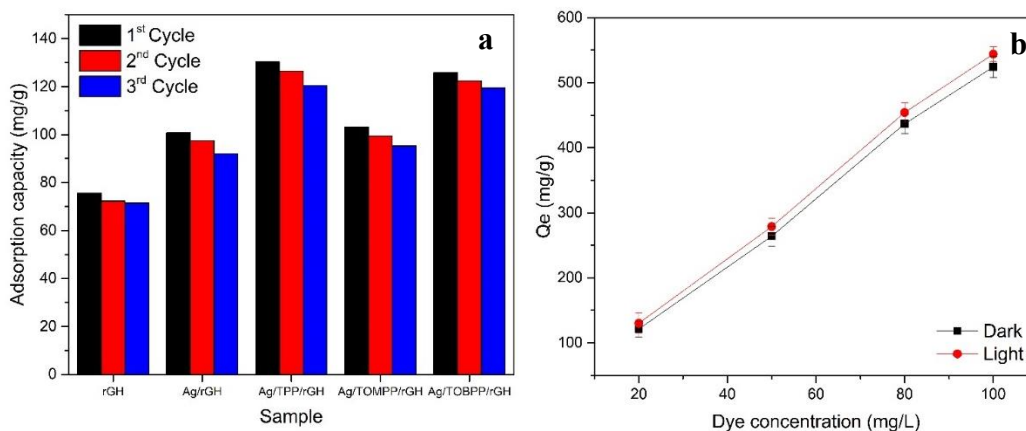


Fig. 5.8. (a) Reusability studies (3 cycles) of the hydrogels on the adsorption of MB, (b) Effect of initial MB concentration for adsorption of Ag/TPP/rGH under dark and light condition

Provided that Ag/TPP/rGH showed the best performance towards MB adsorption, we further carried out MB adsorption at different initial dye concentration (20, 50, 80, and 100 mg/L) under light avoidance and normal light condition to elucidate the photocatalytic behavior of the decorated AgNPs and free base porphyrins on the reduced graphene sheets. From Fig. 8(b), it can be seen that the unit adsorption increased as the concentration increased from 20 mg/L to 100 mg/L due to the increase in mass transfer driving force resulting in higher MB adsorption for both dark and light condition[277]. It is important to note that under both conditions, the MB uptake does not significantly change which can be attributed to the weak intensity of the fluorescent light irradiation under normal light condition which does not induce photodegradation process involving the transfer of electron to the conduction band for the MB degradation. The possible aggregation of the free base porphyrins on the reduced graphene sheets may also be the possible reason which inhibit its photocatalytic efficiency and hence limiting the recombination of photo-induced electron hole pair for the degradation of MB to occur[278].

It is also worth to compare the prepared hydrogel-based adsorbent with some other reported adsorbents prepared for MB adsorption. Table 3 represents the adsorption capacity for some adsorbents. The results showed that the Ag/TPP/rGH hydrogel matrix prepared using the facile hydrothermal has high adsorption capacity towards MB and may have ample of potential for the removal of other dye compounds. The differences on the adsorption capacity can be attributed to the experimental condition and the synthesized

end-product such as functional groups present, and textural properties (pore size and volume) of the matrix system.

Table 5.3. Adsorption capacity of various hydrogels towards MB.

Adsorbent	Cationic organic dye	Adsorption capacity (mg/g)	References
Graphene/Ag ₃ PO ₄	MB	83.75	[224]
GO/chitosan	MB	3.50	[275]
rGO/chitosan	MB	3.44	
Starch/humic acid hydrogel	MB	110	[279]
N,N- dimethylacrylamide and 2-hydroxyethyl methacrylate copolymer (p (HEMA- co-DMAa))	MB	80.27	[155]
RGO/PEI/Ag	MB	~33.00	[280]
Alginate/SiO ₂	MB	139.31	[221]
Ag/TPP/rGH	MB	130.37	This work

Real wastewater samples containing dye molecules, numerous organic and inorganic compounds often possess high electrolyte concentration which often result in complex adsorption mechanism and various interactions with the adsorbent. The presence of salts such as K⁺, Na⁺, Ca²⁺ etc often lead to changes in ionic strength which in turn control the positive charge on the adsorbent surface, making the adsorbent susceptible to certain kind of adsorbate. The increase in the positive charge on the adsorbent surface can

drive electrostatic attraction between the adsorbent-adsorbate. Previous study has shown that graphene-based adsorbent exhibited a better adsorption selectivity towards dye as compared to heavy metal ions in their simultaneous adsorption process. In the presence of higher concentration of cationic dye, the adsorption of heavy metal becomes weaker[281]. For real-wastewater applications, it is posited that the presence of ample free aromatic structure in Ag/TPP/rGH enables the interaction with dye molecules via π - π interactions, alongside other interactions such as electrostatic interactions and hydrogen bonding. In addition, the three-dimensional hydrogel structure of Ag/TPP/rGH addresses the current challenges in practical wastewater applications which includes aggregation and low regeneration properties.

5.4. Conclusion

In this work, we had successfully prepared and characterized a modified graphene-based hydrogel using AgNPs and porphyrin complexes. The decoration of AgNPs and the inclusion of free base porphyrin on the surface of the graphene hydrogel can be confirmed from the various characterization conducted. There were no significant changes to the thermal stability as shown in the TG studies with the decoration of AgNPs but improved with the inclusion of free base porphyrins. The interaction of the AgNPs with the negatively charged functional groups of the graphene sheets is posited to be via electrostatic interactions which is confirmed by FTIR with the disappearing of the carboxylic O-H band. The presence of the porphyrin brings significant structural changes which was proven by XRD with the decrease in the (0 0 2) peak of the graphene sheets indicating successful interaction with the graphene sheets using the hydrothermal treatment. The Raman spectra suggested that the features of the reduced graphene sheets were affected with the inclusion of TPP and TOBPP. The strong π - π interactions of the porphyrin complexes especially Ag/TPP/rGH has shown the best performance for the adsorption of cationic dye, MB. The adsorption capacity of Ag/TPP/rGH reached 130.37 mg/g as compared to the control sample, rGH which is posited to be from the presence of additional binding sites for the MB due to its availability of unoccupied aromatic structures. The kinetic reaction of all hydrogels conformed to the pseudo second order kinetic model with a good stability of up to 90%. Thus, the present investigation provides further insight into the application of a novel graphene-based hydrogels which uses AgNPs and porphyrin complexes as dye adsorbent which is efficient, economical and environmentally friendly for the treatment of dye wastewater.

CHAPTER 6

CU₂O/TIO₂ DECORATED ON CELLULOSE NANOFIBER/REDUCED GRAPHENE HYDROGEL FOR ENHANCED PHOTOCATALYTIC ACTIVITY AND ITS ANTIBACTERIAL APPLICATIONS

Abstract

Photocatalysis has gained attention as a viable wastewater remediation technique. However, the difficulty of recovering powder-based photocatalyst has often become a major limitation for their on-site practical application. Herein, we report on the successful in-situ preparation of a novel three-dimensional (3D) photocatalyst consisting of Cu₂O/TiO₂ loaded on a cellulose nanofiber (CNF)/reduced graphene hydrogel (rGH) via facile low-temperature hydrothermal treatment and freeze-drying. The 3D hydrogel not only provides a template for the anchoring of Cu₂O and TiO₂ but also provides an efficient electron transport pathway for enhanced photocatalytic activity. The results showed that the Cu₂O and TiO₂ were uniformly loaded onto the aerogel framework resulting in the composites with large surface area, hence exposing more active sites. As compared to bare CNF/rGH, Cu₂O/CNF/rGH and TiO₂/CNF/rGH, the Cu₂O/TiO₂/CNF/rGH showed improved photocatalytic activity under UV-irradiation for Methyl orange (MO) degradation. MO degradation pathway is proposed based on GC-MS analysis. The enhanced photoactivity can be attributed to the charge transfer and electron-hole separation from the synergistic effect of Cu₂O/TiO₂ anchored on CNF/rGH. In terms of their anti-bacterial activity towards *Staphylococcus aureus* and *Escherichia coli*, the synergistic effect of the Cu₂O/TiO₂ anchored on the CNF/rGH framework showed excellent activity towards the bacteria.

Keywords: photocatalysis; graphene hydrogel; hydrothermal; cellulose nanofiber; wastewater treatment

6.1 Introduction

To date, concerted efforts are being made to develop novel nanomaterials for advanced oxidation processes (AOP) to address the issue of water security. In comparison to conventional water treatment technologies such as adsorption, precipitation and filtration, AOP combined with these conventional methods are garnering pace to address water pollution in a greener perspective. The most common water pollutants are organic dyes and pigments, often discharged in wastewater which posed environmental concerns. Contaminant degradation applying the photocatalytic process is still developing. Photocatalysis is a technology that is not only environmentally friendly but also leads to no secondary pollution especially in the efficient degradation of a variety of pollutants in aqueous conditions. The degradation of pollutants is attributed to the generation of reactive oxygen species (ROS). Carbon-based materials such as graphene, activated carbon, carbon nanotubes (CNT), fullerenes etc have shown promising results due to their ability to combine with different heterojunctions materials for increased photo efficiency [282–284]. Specifically, graphene and its derivatives have been a versatile tool in the design of multi-functional materials.

The design of a novel photocatalyst that is facile, highly efficient and possessing good stability remains a significant challenge. Recently, three-dimensional (3D) graphene macrostructure such as hydrogel is exploited as a new class of photocatalytic material attributed to their photo-assisted applications in wastewater treatments. The template provided by the graphene-based hydrogel enables the blending of additives or modifiers to further improve the functionalities and salient properties that are beneficial in pollution control applications[285,286]. In addition, the template enables the orientation of photoactive materials to prepare a hybrid 3D macrostructure. In short, to better improve photocatalytic performance, a material with high surface-to-volume ratios is highly sort after. The utilization of natural biomass such as cellulose, a polysaccharide in water-treatment technologies has also gained more attention due to its biodegradability, biocompatibility, high sorption capacity, relatively high thermal stability and non-toxicity properties [287,288]. Their abundant hydroxyl groups enable the functionalization process to occur, opening endless opportunities for the design of various functional materials. Previously, it has been reported that cellulose fibres assisted in the dispersion of metal oxide nanoparticles and control the nucleate precipitation [289]. The disadvantage of utilizing porous cellulose is that it may sacrifice the photocatalytic activity to a certain extent owing to their non-conductive matrix [290]. Double network (DN) hydrogel has

been a forefront in the preparation of hydrogel with excellent properties such as high mechanical strength and surface area due to the interpenetrating and cross-linked polymer networks [291–293]. DN hydrogels consisting of CNF/graphene have shown rather interesting results based on previous literature. The preparation of homogenous dispersion of GO and CNF can be easily achieved via ultrasonication which drives the interaction between the oxygen-functional containing groups of the GO and the hydroxyl groups in cellulose via hydrogen bonding. Previously, it was found that the reduced GO are surrounded by dense conformal nanocellulose network which drives the improvement in their water-transport properties [294]. Hence it is expected that the combination of graphene-cellulose hydrogel will bring immense improvement to their salient properties.

Metal oxide-based nanoparticles have received ample attention in their use for textile and dye remediation due to their optical properties and biocompatibility [295–304]. Titania, TiO_2 is the most commonly used photocatalytic material which has been used due to its stability, low cost and non-toxicity. The photocatalytic performance of TiO_2 is supported with ample studies focusing on their efficiency in degrading various kinds of pollutants [305–308]. However, the setback from TiO_2 in practical application is their high bandgap energy ($E_g=3.2$ eV) which only allows absorption of light in the UV range. Additionally, the rapid recombination of photogenerated electron-hole pairs leads to low quantum efficiency. To overcome the limitations, researchers have coupled a variety of semiconductors, metals, and non-metals with TiO_2 . The strategy of coupling not only allowed for the absorption in the visible light range but also reduce charge carrier recombination due to Schottky barrier formation at the interface. The introduction of a co-catalyst among the simplest ways to enhance solar-to-chemical energy conversion of their large bandgap [309]. The incorporation of Cu_2O has been able to address the limitation by using TiO_2 as the photoactive material alone. Cuprous oxide (Cu_2O) has been known as visible light-responsive photocatalysts with a bandgap of 2.0-2.3 eV[310]. As a p-type semiconductor with a narrow bandgap, making it competitive with other UV light response catalysts such as TiO_2 and ZnO . The synthesis of various shapes and sizes of Cu_2O have been reported elsewhere. Unfortunately, the large surface area and high surface energy of Cu_2O posed aggregation problems similar to TiO_2 . In wastewater purification, Cu_2O photocatalyst has demonstrated high efficiency, non-toxicity and stability. In addition to that Cu_2O also possess good antibacterial properties which is an added value. To address the notion, significant effort has been expended in the design and

preparation of 3D support material to prevent catalyst aggregation; hence improving their photocatalytic efficiency in practical applications. The preparation of TiO₂/rGO, Cu₂O/rGO and Cu₂O/TiO₂/rGO based composite were previously reported for their effective usage in photocatalytic degradation of pollutants. Nyugen *et al.*, prepared a Cu₂O quantum dot/rGO/TiO₂ using the hydrothermal method exhibiting excellent photocatalytic efficiency for several dye compounds degradation [311]. Yang *et al.*, prepared TiO₂/graphene/Cu₂O/ using chemical vapour deposition, followed by electrochemical deposition of Cu₂O on TiO₂ nanotubes for the photoelectrocatalytic oxidation of bisphenol A (BPA) [312]. However, previous studies did not emphasize the preservation of the 3D macrostructure which is paramount in the easy recovery of the catalyst.

In this work, we take advantage of high surface-to-volume ratios of the graphene-based hydrogel as the electron-conducting material to orientate the TiO₂ and Cu₂O using hydrothermal treatment. The graphene sheets with high surface area to volume would prevent photoactive materials from aggregating, thereby promoting electron transfer and improving photocatalytic activity. The incorporation of CNF in the graphene network is posited to improve the synergistic properties of the graphene hydrogel which seems to be a plausible route. Using a one-pot synthesis route, the in-situ formation of the Cu₂O/TiO₂/CNF/rGH can be realized for the remediation of textile dyes effluent using the synergistic adsorption and photocatalysis effect alongside their excellent disinfection properties towards microorganisms. This work is expected to extend the scope of green synthesis of functional 3D graphene materials for photocatalysis applications.

6.2 Materials and Methods

6.2.1 Materials

Commercial ST-01 TiO₂ powder with anatase crystal structure was purchased from Ishihara Sangyo, Japan (surface area: 300 m²/g with particle size: 7 nm). GO (AX-1-FM-W-151) was obtained in-kind from Nippon Shokubai Co., Ltd delivered in water dispersion form (0.1-2.0 %). Commercial cellulose nanofiber (CNF) (BINFi-s WFO-10005) was purchased from Sugino Machine Limited, Japan. Copper sulfate pentahydrate (CuSO₄ · 5H₂O), D (+)-Glucose (C₆H₁₂O₆), sodium hydroxide (NaOH) and methyl orange (MO) were obtained from Wako Pure Chemical Industries Ltd, Japan and used as received.

6.2.2 Preparation of Cu₂O spheres

The Cu₂O were synthesized according to the previously reported method with slight modifications [313]. Briefly, 2.5 g of CuSO₄ was first dissolved in deionised water and 1 g/mL of NaOH was added into the copper precursor solution under vigorous stirring at 70°C. 20 mL of glucose solution is then added drop by drop into the suspension and the heating is continued for 30 minutes which yielded an apparent maroon colour suspension. The reduction and particle growth process were assisted under continuous magnetic stirring. The Cu₂O were collected via centrifugation at 4500 rpm for 15 mins and washed thoroughly with deionised water and absolute ethanol. The resultant maroon coloured Cu₂O was then dried at 70°C in the oven for 24 h to ensure removal of moisture content.

6.2.3 Preparation of Cu₂O/TiO₂/CNF/rGH

As reported in our previous studies, 4 g of GO was dissolved in 30 mL deionised water and sonicated for 1.5 hours to exfoliate the GO sheets [18,19,181]. Separately, 5 g of the commercial CNF is weighed and dissolved in 20 mg/mL NaOH solution under stirring at 5°C; followed by 30 minutes of sonication. 10 mL of the CNF suspension is then added to the GO suspension and sonicated for another 30 minutes. Typically, 43.0 mg and 24.0 mg of the as-obtained Cu₂O and commercial TiO₂ powder were added into the suspension, stirred vigorously alongside the CNF/GO suspension until a homogenous suspension is obtained. The hydrothermal reaction is conducted at 132°C for 8 h. The obtained hydrogel is then dialyzed in deionised water for 24 h. Next, the hydrogel is freeze-dried at -50°C for 24 h to obtain the Cu₂O/TiO₂/CNF/rGH. As a reference, Cu₂O/CNF/rGH and TiO₂/CNF/rGH were prepared using a similar protocol but without the addition of TiO₂, and Cu₂O, respectively. Graphene hydrogel was prepared likewise in the absence of both TiO₂, and Cu₂O in only GO suspension. The freeze-dried hydrogels were kept for characterization studies as described below.

6.2.4 Characterization

The morphology of the freeze-dried hydrogels was accessed on a JCM-6000 Versatile Benchtop Scanning Electron Microscope, JEOL Ltd, Japan fitted with an energy dispersive X-ray analyzer (EDX). Raman spectroscopy was performed using a JASCO NRS-5100 Laser Raman Spectrometer with an excitation wavelength of 532 nm and a 4.7 mW laser power beam. The X-ray diffraction (XRD) patterns were obtained

on a benchtop (MiniFlex 600, Rigaku, Japan) diffractometer with Cu K- α radiation at 40kV and 15 mA, analyzed by X'Pert Highscore Plus software. The FTIR spectrum was acquired using a Nicolet iS5 spectrophotometer (ThermoFisher Scientific, Japan) from 4000 cm^{-1} to 500 cm^{-1} . Thermogravimetric analysis (TGA) was performed on an EXSTAR TG/DTA7000 to analyse the residual weight loss of the samples under N_2 atmosphere from 25°C to 550°C at a rate of 2°C/min. The chemical binding states of the hydrogels were obtained on an X-ray photoelectron spectrometer Axis Nova Surface Analyzer with a monochromatized Al K α X-ray source and pass energy of 80 eV. The fitting of the deconvoluted peaks was carried out using Casa XPS software¹⁵. The ultraviolet-visible light diffuse reflectance spectroscopy (UV-DRS) spectra were obtained on a Shimadzu UV-2600 spectrometer equipped with a diffuse reflectance attachment. The photoluminescence (PL) spectroscopy was measured on an FP-8500 spectrofluorometer (JASCO Corporation, Japan). The surface area and pore size distribution were accessed using a Surface Area and Pore Size Analyzer (Nova 4200e, Quantachrome Instruments). The intermediates and reaction products of the MO photodegradation were analysed on a benchtop Shimadzu GC-MSQP2010 SE. The measurement conditions were as follows, 30 °C to 250 °C (10 °C/ min), 5 min in hold at 250 °C, and the vaporization chamber is set to 280 °C. The pathway of MO degradation is proposed based on GC-MS findings and previously published articles.

6.2.5 Adsorption and photocatalytic degradation of methyl orange

The photocatalytic degradation of methyl orange (MO) was accomplished via a vertical radiation method. The photocatalytic activity of the hydrogel was accessed using a light source of Xe lamp (200W), Eye Cure Light Spot: UP200G. The photocatalytic evaluations were conducted at room temperature. In this experiment, the as-prepared freeze-dried hydrogel was added to 50 mL, 20 mg/L of MO dye solution and shaken in dark condition for 180 min to obtain the adsorption-desorption equilibrium. After several intervals, 1 ml of the solution is extracted and centrifuged. The photodegradation ability was determined by measuring the residue concentration on a Genesys 50 UV-Vis spectrophotometer, Thermo Fisher Scientific based on the absorption maximum of 465 nm. The photocatalytic degradation efficiency was calculated using the following equation:

$$\text{Degradation efficiency(\%)} = \frac{C_0 - C}{C_0} \times 100\% \quad (1)$$

where C_0 is the initial concentration of MO and C is the concentration at time, t . To access the regeneration and reusability of the photocatalyst, the photocatalyst was retrieved and washed with ethanol and distilled water, freeze-dried before being used for the next cycle.

6.2.6 Antibacterial activity assessment

The antibacterial activity of the hybrid 3D hydrogel was tested against *Staphylococcus aureus* ATCC 6538P and *Escherichia coli* 0517:H7, respectively. A single bacteria colony was grown aerobically in 10 mL of Luria Bertani (LB) broth and incubated overnight at 37 °C. Then, 200 μ L of the culture was added into 20 mL of fresh LB broth and incubated at 37 °C until OD_{600} reached 0.5. Subsequently, 1 mL of the culture is harvested via centrifugation at 13,000 rpm for 1 minute. To remove any residual growth medium constituents, the cells pellet was washed four times and diluted to 1:50 using phosphate-buffer saline (PBS; 50 mM sodium phosphate [pH 7.5]-150 mM NaCl). The as-prepared freeze-dried hydrogels were immersed in PBS containing 10^6 CFU/mL cells in a sterilised conical flask and incubated for 2 hours at room temperature under shaking at 200 rpm. A series of 10-fold cell dilutions were carried out to be drop-casted onto LB agar plates. The spot test method is used to access the cell growth inhibition and the quantification of the bacterial colonies was carried out using ImageJ software. After overnight incubation at 37 °C, the culture plates were then photographed. To ensure the reliability of the software, manual counting was also conducted. The test was repeated three times and each time three culture plates were used to seed each concentration of bacteria.

6.3 Results and Discussion

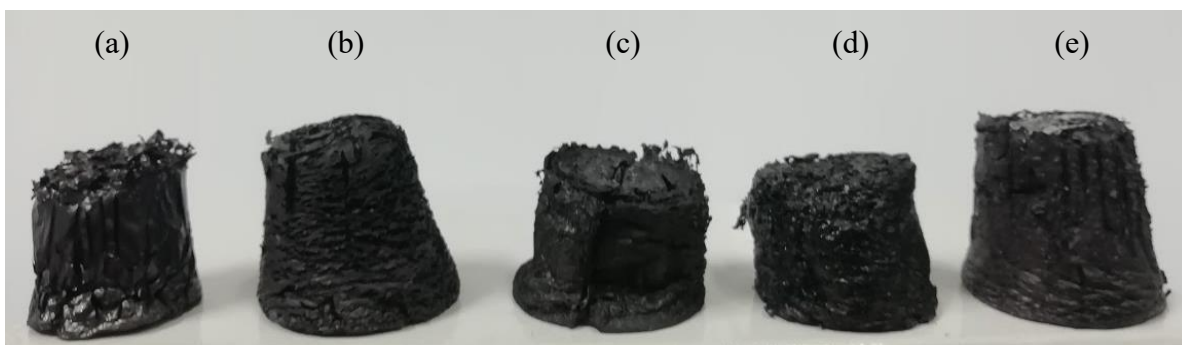


Fig. 6.1. Digital image of the freeze-dried hydrogel. (a) rGH, (b) CNF/rGH, (c) Cu_2O / CNF/rGH, (d) TiO_2 /CNF/rGH. (e) Cu_2O/TiO_2 /CNF/rGH

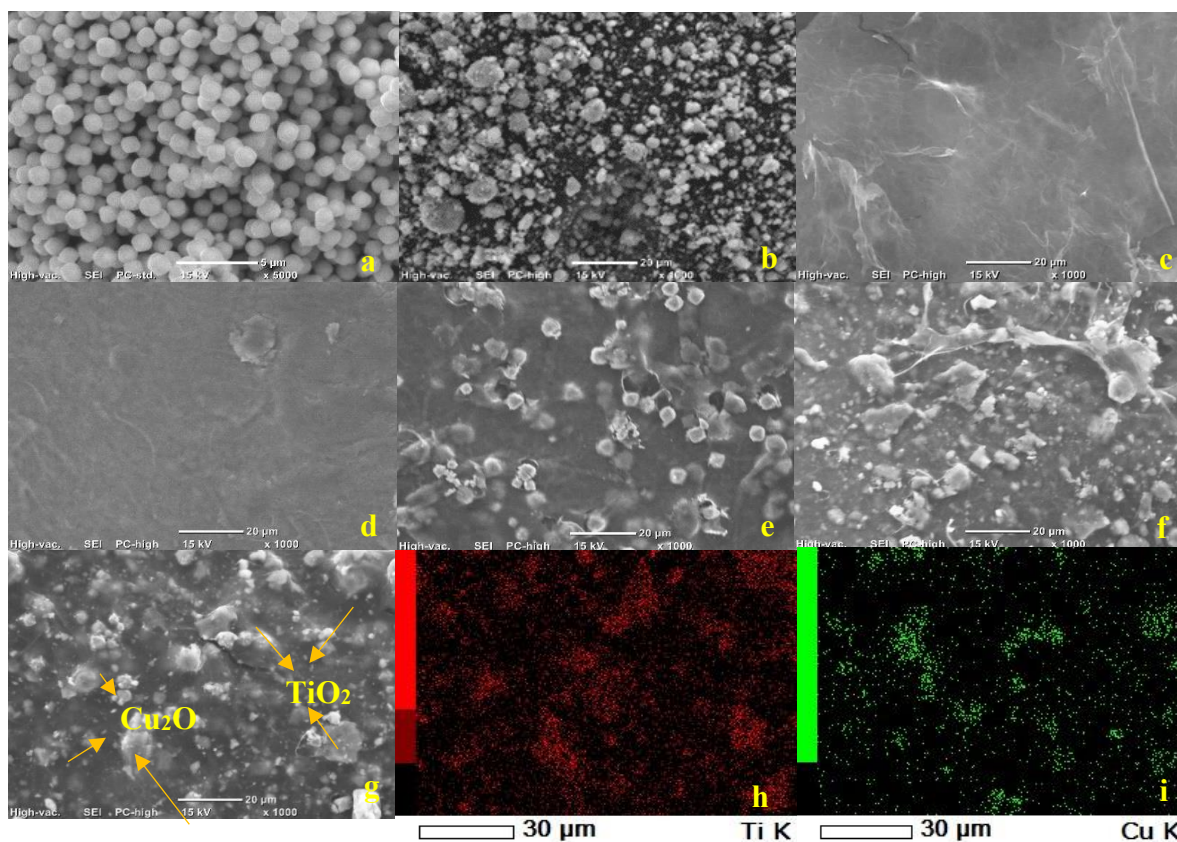


Fig. 6.2. SEM images of (a) Cu₂O, (b) commercial TiO₂, (c) rGH, (d) CNF/rGH, (e) Cu₂O/ CNF/rGH, (f) TiO₂/CNF/rGH. (g) Cu₂O/TiO₂/CNF/rGH. EDX mapping of Cu₂O/TiO₂/CNF/rGH for the element (h) Ti and (i) Cu

The preparation of the aerogels was achieved via the hydrothermal and freeze-drying process and their digital photographs of the freeze-dried hydrogels are illustrated in Fig. 6.1. The CNF incorporated double-network graphene hydrogel expanded in volume due to the increase in the crosslink density in the hydrogel network. The double network structure enables the successful anchoring of the Cu₂O and TiO₂ without affecting the hydrogel structure. From a naked-eye view, it can be seen that the surface freeze-dried rGH appears to be flaky upon comparing to the cellulose incorporated hydrogels. SEM measurements were taken to access the morphology of the nanocomposites. The formation of Cu₂O microspheres has been previously reported using glucose as the reducing agent [135,314]. Based on Fig. 6.2a, the formation of Cu₂O spheres is apparent with an average diameter of 1232 nm. EDX results in Fig. S6.1 further support the formation of Cu₂O which indicated the presence of only copper and oxygen elements; with almost pure

Cu₂O with no Cu or CuO impurities. Based on Fig. 6.2b, the morphology of the commercial anatase TiO₂ showed the typical behaviour of agglomeration. The particle size ranges from 900 nm to 1300 nm with an average diameter of 1100 nm. Fig. 6.2c showed the typical morphology of rGH of a randomly oriented 3D framework consisting of thin large flakes with wrinkles after hydrothermal treatment and freeze-drying. The increased hydrophobic interactions between individual sheets led to the agglomeration of reduced graphene sheets. In the case of CNF/rGH, the surface appears to be compacted possible from the protective layer of CNF on the graphene sheet as shown in Fig. 6.2d. The TiO₂ and Cu₂O appeared to be uniformly distributed on the three-dimensional CNF/graphene network which effectively prevents the accumulation of the graphene lamellae as illustrated in Fig. 6.2e - f, respectively. As for Cu₂O/TiO₂/CNF/rGH, the distribution of the photoactive materials on the graphene sheets can be further confirmed from the EDX mapping analysis of titanium and copper elements as depicted in Fig 2(g-i). The findings corroborated the notion that the TiO₂ and Cu₂O were successfully anchored on the CNF/graphene sheets using the low-temperature hydrothermal treatment. There is also no significant changes in the particle size of Cu₂O/TiO₂ after orientation on the CNF/rGH template.

To identify the successful anchoring of the photocatalyst on the CNF/rGH template, XRD measurements were carried out to probe their crystallographic structure as depicted in Fig. 6.3(a). The diffraction peaks for the spherical Cu₂O matched well with the Cu₂O standard data (JCPDS:05-0667). The Scherrer's equation was applied in the estimation of the crystalline size which is represented as

$$D = \frac{K \lambda}{\beta_{hkl} \cos \theta} \quad (2)$$

where D is the size of crystalline domains; λ is the X-ray wavelength with the value of 1.5418 Å; β_{hkl} is the broadening of occurring at half maximum intensity (FWHM) in radians and θ is the Bragg angle.

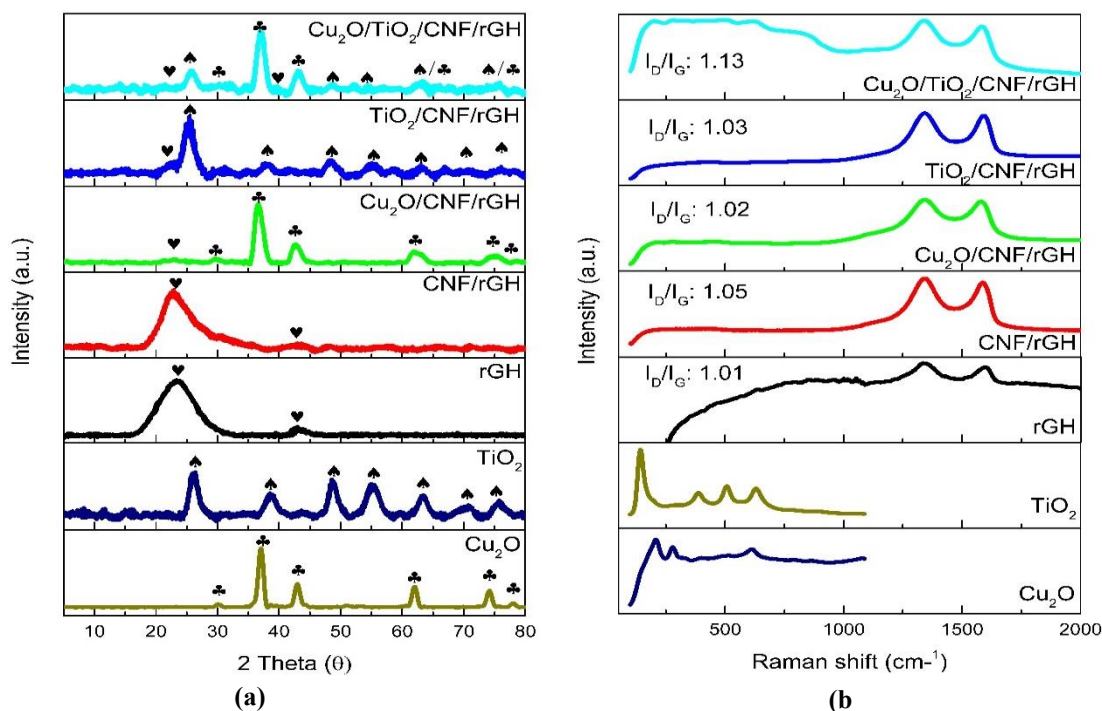


Fig. 6.3. (a) XRD and (b) Raman spectra of Cu₂O, TiO₂, CNF/rGH, Cu₂O/CNF/rGH, TiO₂/CNF/rGH and Cu₂O/TiO₂/CNF/rGH.

The crystallite size of the synthesized Cu₂O is calculated from the (111) and was found to be 6.5 nm. The high crystallinity of the obtained Cu₂O obtained indicated the successful green preparation of Cu₂O using glucose as the reducing agent. The commercially obtained TiO₂ showed peaks ascribed to the (101), (004), (200), (211), (002), (301) and (215) plane which corresponds to the anatase phase possessing an average crystallite size of 8 nm [315]. In our previous study, the commercial CNF, a cellulose type 1 structure exhibited diffraction peaks around $2\theta = 16.5^\circ$, 23.5° , and 35.0° corresponding to (110), (200) and (040) planes [316]. The diffraction pattern of rGH showed a well-resolved peak at around 24.1° and 43.1° ascribed to the (002) and (102) crystal structure. The inclusion of CNF onto the rGH also showed a typical diffraction pattern form of rGH provided that the higher graphitic content in comparison to CNF. However, it is also possible that the (110) peak of the cellulose overlapped with the (002) of the graphene. Besides, the weak broad peak around 16.8° can be derived from the CNF. As for Cu₂O/CNF/rGH and TiO₂/CNF/rGH, the peaks attributed to Cu₂O and TiO₂ were still observable indicating no changes in their crystalline structures. However, it is can be observed that the peak associated with the CNF/rGH around $2\theta = 23^\circ$ was significantly weakened from the inclusion of TiO₂. The probable reason can be due to the obstruction by the TiO₂ (101)

peak and the destruction of regular graphene stacks [317]. The reduction in peak intensity for some TiO₂ crystal planes after inclusion on the CNF/rGH can be ascribed to the presence of Ti³⁺ defect during hydrothermal treatment [318]. Similar behaviour also can be observed in Cu₂O/CNF/rGH, which can be attributed to the saturation of the Cu₂O nanosphere on the graphene sheet. The diffraction pattern of Cu₂O/TiO₂/CNF/rGH showed the strong intensity and the slight peak shifting of the TiO₂ (101) and Cu₂O (110, 111 and 200) plane supported the notion of successful incorporation of the photoactive materials on the CNF/rGH sheet. The broadening of the peaks after the anchoring is in relation to the presence of nano-sized crystallites and the lattice strains [319]. TiO₂ and Cu₂O crystal planes remained with reduced intensity at a higher diffraction angle (>50°) which is possible from the overlapping of the two photoactive materials, supported by the EDX result. Table 1 summarizes the crystallite size and lattice strain of the samples. The crystallite size of the bare Cu₂O and TiO₂ showed a slight reduction after the anchoring on the CNF/rGH template which can be attributed to the loading of the reduced graphene oxide sheets [320]. The anchoring of both Cu₂O/TiO₂ did not yield significant shifting to their Bragg angle which can be ascribed to the homogenous contribution on the template [321]. Table 1 summarized the crystallite size and lattice strain of the samples.

Table 1. The crystallite size and lattice strain for the samples

Sample	2θ (°)	hkl	FWHM (2θ)	Interplanar d-spacing, (Å)	Crystallite size, nm	Lattice strain (%)
TiO ₂	26.07	101	1.942	3.41240	4.2 ± 0.52	3.660
Cu ₂ O	37.11	111	1.344	2.42073	6.3 ± 0.37	1.747
rGH	23.83	002	1.288	3.73142	6.3 ± 0.92	2.663
CNF/rGH	22.54	200/002	3.264	3.94183	2.5 ± 0.45	7.147
TiO ₂ /CNF/rGH	25.33	101	2.496	3.51314	3.3 ± 0.87	4.846
Cu ₂ O/CNF/rGH	36.34	111	1.440	2.46998	5.8 ± 0.72	1.914
Cu ₂ O/TiO ₂ /CNF/rGH	25.97	101 (TiO ₂)	1.920	3.42824	4.3 ± 0.33	3.633
	37.15	111 (Cu ₂ O)	1.824	2.45912	4.6 ± 0.97	2.414

Fig. 6.3(b). shows the Raman spectra to access the defects on the CNF/rGH from the inclusion of the photoactive materials. The as-prepared Cu_2O nanospheres showed strong Raman peaks at 208 cm^{-1} , 278 cm^{-1} , 398 cm^{-1} , 515 cm^{-1} and 613 cm^{-1} confirming the successful preparation using glucose as the reducing agent. An almost similar Raman pattern for Cu_2O peaks has been previously reported [322]. The four characteristic Raman active modes at 143 cm^{-1} , 386 cm^{-1} , 507 cm^{-1} and 630 cm^{-1} corresponds to the E_g , B_{1g} , A_{1g} and E_g symmetry of the commercial TiO_2 , respectively confirming their anatase structure [323]. The Raman spectra of the freeze-dried hydrogels showed two bands around 1340 cm^{-1} (D-band) and 1590 cm^{-1} (G-band), common in most graphitic materials. The D-band is attributed to the sp^3 carbon atoms which are related to the irregular defects in the graphite layer. On the other hand, the G-band is attributed to the in-plane vibration of the sp^2 carbon atoms and is a doubly degenerate phonon mode (E_{2g} symmetry) at the Brillouin zone centre, corresponding to carbon symmetry and crystallization [324]. The inclusion of CNF in the graphene framework shifted the D band from 1340 to 1345 cm^{-1} and the G-band from 1597 to 1587 cm^{-1} which is possible from the introduction of oxygenated functional groups before the hydrothermal treatment. For the $\text{Cu}_2\text{O}/\text{TiO}_2/\text{CNF}/\text{rGH}$ spectra, the weak peaks appearing below 600 cm^{-1} is attributed to the active modes of both Cu_2O and TiO_2 . Previously it was reported that the peaks around 513 and 627 cm^{-1} can be attributed to the overlapping Raman vibration mode of the crystalline Cu_2O and TiO_2 [325]. The I_D/I_G ratio roughly estimates the graphene clusters and defects in the disordered carbon framework [326]. The I_D/I_G ratio of CNF/rGH is 1.05, which is higher than rGH alone indicating a higher defect introduced in the graphene framework. We speculated that the various oxygenated groups present of the CNF may have formed interactions with the side groups of the graphene; possibly via hydrogen bonding which hinders the rearrangement of the sp^2 aromatic structure. The same behaviour has been previously reported which explained that small graphitic domains were formed, which lead to more lattice fringes formation on the oxidative exfoliation of graphite and during subsequent GO reduction [327]. The decoration of the individual TiO_2 and Cu_2O on the CNF/rGH slightly reduced the I_D/I_G ratio. Interestingly, the I_D/I_G ratio of $\text{Cu}_2\text{O}/\text{TiO}_2/\text{CNF}/\text{rGH}$ (1.13) was the highest indicating that the coupling effect of Cu_2O and TiO_2 increases the defect due to the strong chemical bonding with the graphene sheets as compared to $\text{Cu}_2\text{O}/\text{CNF}/\text{rGH}$ (1.02) and $\text{TiO}_2/\text{CNF}/\text{rGH}$ (1.03).

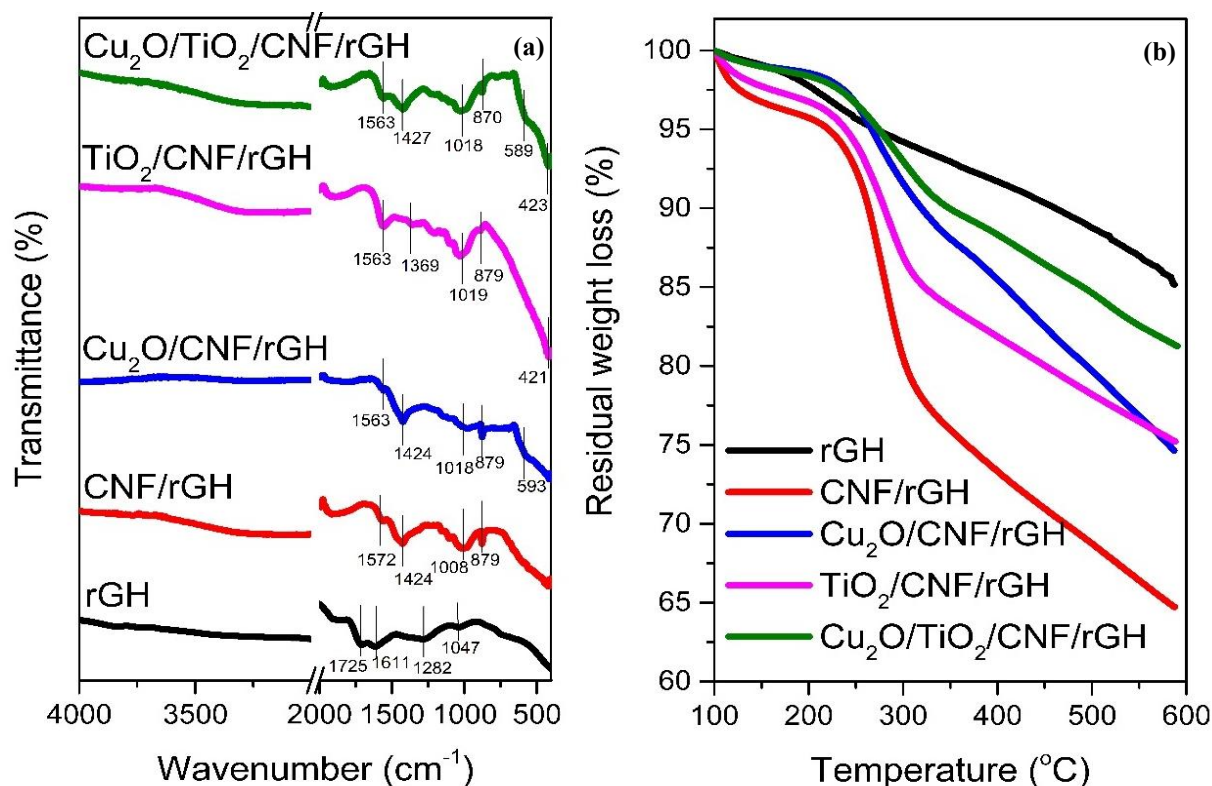


Fig. 6.4. (a) ATR-FTIR and (b) TGA of the freeze-dried hydrogels

FTIR is used to access the chemical interactions between the photoactive materials and the reduced graphene sheets. The FTIR spectrum is depicted in Fig. 6.4(a). The typical spectrum of rGH revealed peaks at $1,047\text{ cm}^{-1}$ corresponding to the C-O stretching vibration mode due to the presence of the alkoxy group, $1,282\text{ cm}^{-1}$ corresponding to the C-O stretching vibration mode associated with the epoxy group, $1,611\text{ cm}^{-1}$ corresponding to the presence of the C = C bond, and $1,725\text{ cm}^{-1}$ corresponding to the C = O stretching vibration mode associated with the carboxyl group present primarily at the sheet's edges and basal plane. The inclusion of CNF into rGH shifted the C=C peaks to 1425 cm^{-1} , and C-O peak to 1008 cm^{-1} . The peak occurring around 1008 cm^{-1} may also be attributed to the C-O-C pyranose ring skeletal vibrations [328]. Also, the presence of CNF can be ascertained from the characteristic peaks present at 1572 cm^{-1} and 879 cm^{-1} which is contributed from the C=O of the CNF and the C₁-H deformation vibrations, respectively [329,330]. Interestingly, the C=O attributed to the reduced graphene could not be observed which is possible from the surrounding cellulose network on the graphene sheet. The presence of Cu_2O and TiO_2 on the CNF/rGH is confirmed from the shoulder peak attributed to Cu-O and Ti-O-Ti vibrations around

589 cm^{-1} and 421 cm^{-1} , respectively [331]. In the case of $\text{TiO}_2/\text{CNF}/\text{rGH}$, the C=C peaks around 1425 cm^{-1} may have overlapped with the Ti–O–C vibrations which occurred between 1400 – 1600 cm^{-1} , hence blue shifting the peaks to 1369 cm^{-1} [332]. For the $\text{Cu}_2\text{O}/\text{TiO}_2/\text{CNF}/\text{rGH}$, the slight shifting of the Cu–O and Ti–O–Ti suggest the successful formation of the $\text{Cu}_2\text{O}/\text{TiO}_2/\text{CNF}/\text{rGH}$.

The thermal stability of the aerogels was accessed by thermogravimetric (TGA) analysis under N_2 atmosphere and their related thermograms are illustrated in Fig. 6.4(b). rGH was the most thermally stable with minimal weight loss residue in the range of 100°C to 600°C, indicating the successful reduction and the removal of most oxygenated containing groups via the hydrothermal treatment. Between 200°C to 300°C, significant weight loss is attributed to the decomposition of labile oxygen-containing functional groups. The steady weight loss beyond 300°C can be ascribed to the decomposition of more stable oxygen-containing groups to carbon monoxide (CO) and carbon dioxide (CO_2) [333–335]. As expected, the cellulose incorporated into the graphene network exhibited lower thermal stability. The CNF/rGH, $\text{Cu}_2\text{O}/\text{CNF}/\text{rGH}$, $\text{TiO}_2/\text{CNF}/\text{rGH}$ and $\text{Cu}_2\text{O}/\text{TiO}_2/\text{CNF}/\text{rGH}$ thermograms exhibited almost similar behaviour with prominent weight loss observed between 250°C to 300°C which is from the thermal decomposition of the pyranose rings in the cellulose skeleton, and the oxygenated containing groups from the rGH [336]. The improved degradation process of the metal oxide incorporated on the CNF/rGH can be ascribed to the barrier effect of the TiO_2 and Cu_2O to the cellulose fibres combustion gas and decomposition products [337]. From the total mass loss obtained from the thermogram, we could also roughly ascertain the grafting/anchoring density of the Cu_2O and TiO_2 photocatalyst on the CNF/rGH by evaluating the difference in the residual weight loss after 600°C. Hence, the content of Cu_2O and TiO_2 anchored on the CNF/rGH was found to be 9.92 wt % and 10.49 wt %, respectively. As expected, the final residue weight loss of $\text{Cu}_2\text{O}/\text{TiO}_2/\text{CNF}/\text{rGH}$ is the least in comparison to $\text{Cu}_2\text{O}/\text{CNF}/\text{rGH}$ and $\text{TiO}_2/\text{CNF}/\text{rGH}$ which is expected from the increased barrier action which retards heat permeation and escape of degradation products [338].

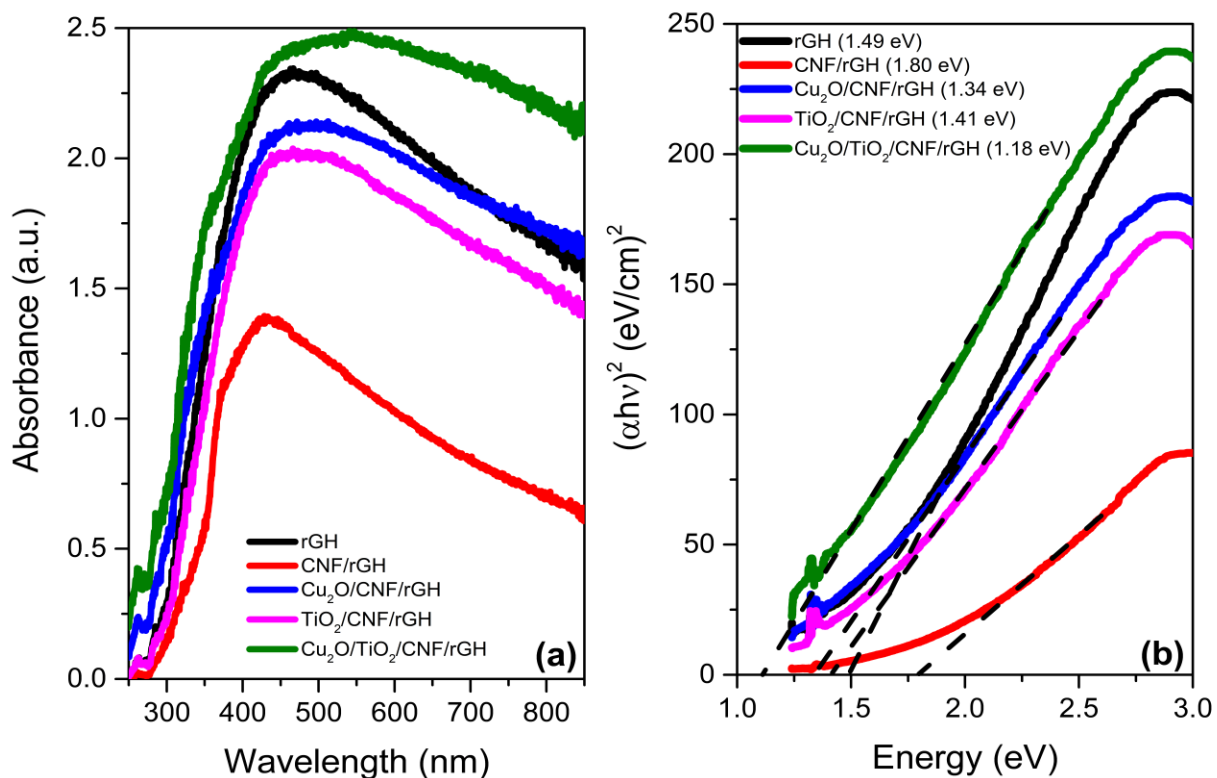


Fig. 6.5. (a) UV-DRS absorption spectra and their respective (b) Tauc plots of the hydrogels.

The intrinsic absorption edge of the commercial TiO₂ is recorded around 330 nm with a bandgap of 3.03 eV indicating a greater absorption edge at the ultraviolet region and no observed absorption in the visible light region above 390 nm. Cu₂O showed an absorption edge around 454 nm with a bandgap of 1.49 eV indicating the absorption at visible light range as illustrated in Fig. S6.2(a) and (b). UV-DRS was applied to further access the optical properties of rGH, CNF/rGH, Cu₂O/CNF/rGH, TiO₂/CNF/rGH and Cu₂O/TiO₂/CNF/rGH; their respective spectra shown in Fig. 6.5(a). All of the hydrogel samples displayed an almost similar light absorption range mostly in the UV region. The absorption of the Cu₂O/TiO₂/CNF/rGH possessed the highest absorbance intensity at the highest wavelength (>500 nm) suggesting the synergistic contribution to the TiO₂ and Cu₂O. Based on Fig. 5(b), the successive Tauc plot depicting the plot of $[\alpha h\nu]^2$ as a function of energy photon based on Kubelka-Munk function was constructed to obtain the estimated band-gap energies (E_g). The band gaps were 1.49 eV, 1.80 eV, 1.34 eV, 1.41 eV, and 1.18 eV, corresponding to rGH, CNF/rGH, Cu₂O/CNF/rGH, TiO₂/CNF/rGH and Cu₂O/TiO₂/CNF/rGH, respectively. The inclusion of CNF in the rGH framework significantly increases the energy bandgap to 1.80 eV which is

attributed to the inherent high band-gap of the cellulose materials [339]. The optical band gap decreased for the photoactive decorated samples which can be explained by the charge transfer between the photoactive materials and the CNF/rGH resulting in a lower energy transition. The inclusion of the TiO₂ and Cu₂O on the CNF/rGH further reduced the bandgap by 25.6% and 21.7%, respectively attributed to their high electron mobility properties in comparison to bare CNF/rGH. For TiO₂/CNF/rGH, the reduction of the bandgap can be attributed to the formation of Ti-O-C which has been previously reported [340]. As for the Cu₂O/CNF/rGH, the introduction of Cu₂O onto CNF/rGH further enables absorption under visible light. This result showed that the interfacial interaction between the presence of both the TiO₂/Cu₂O with the CNF/rGH induced synergistic bandgap narrowing. The bandgap reduction of up to 34.4% indicated effective charge transfer and the formation of new energy levels between the two photoactive materials suggesting the formation of p-n heterojunction from the close contact of both the TiO₂ and Cu₂O [341].

Brunauer-Emmett-Teller (BET) analysis was carried out to access the surface area and textural properties of the freeze-dried hydrogels. From Fig. 6.6, the N₂ adsorption-desorption isotherm and the pore size distribution (PSD) indicated that bare rGH exhibited type III isotherm exhibited a H3 hysteresis loop around 0.5 Pa and rapid increase in the high relative pressure indicating that the aerogels consist of mesoporous-like material with slit-like pores. The specific surface area obtained is 42.05 m²/g, 0.58 m²/g, 0.67 m²/g, 9.35 m²/g and 16.22 m²/g for rGH, CNF/rGH, Cu₂O/CNF/rGH, TiO₂/CNF/rGH and Cu₂O/TiO₂/CNF/rGH, respectively. Interestingly, the inclusion of CNF into the graphene framework yielded isotherms of type IV (IUPAC classification) which illustrated a drop of the adsorbed volume at low relative pressure. Similar isotherm patterns were observed for only cellulose materials [342,343]. This finding further corroborated the findings of a cellulose network surrounding the graphene framework. In comparison to bare rGH, the inclusion of CNF reduced the specific surface area resulting from the coalescence of fibrils by ice formation [344] which is supported by the SEM findings in which a densely packed orientation is observed. The partial blocking of the mesoporous channel by the cellulose material making them inaccessible, hence creating a significant decrease of the cumulated surface area and noticeable difference in the pore size distribution [74]. However, the deposition of Cu₂O and TiO₂ nanoparticles slightly increased the specific surface area and pore volume which is ascribed to the filling of the nanoparticles in the CNF/graphene. The Cu₂O/TiO₂/CNF/rGH showed higher specific surface area due to the spacers created by the photoactive

materials that increase the nanogaps and suppresses the stacking of CNF/rGH sheets [345]. The PSD of the hydrogels were analysed using the DFT method. The half pore size distribution analysis indicated that the pore diameter of the rGH was mainly in the range of 1 to 2 nm. As for CNF/rGH, a wider half pore size is observed at around 6 nm. There was a steep increase in the isotherm at higher relative pressure for TiO₂/CNF/rGH and Cu₂O/TiO₂/CNF/rGH as indicating that the pores were larger.

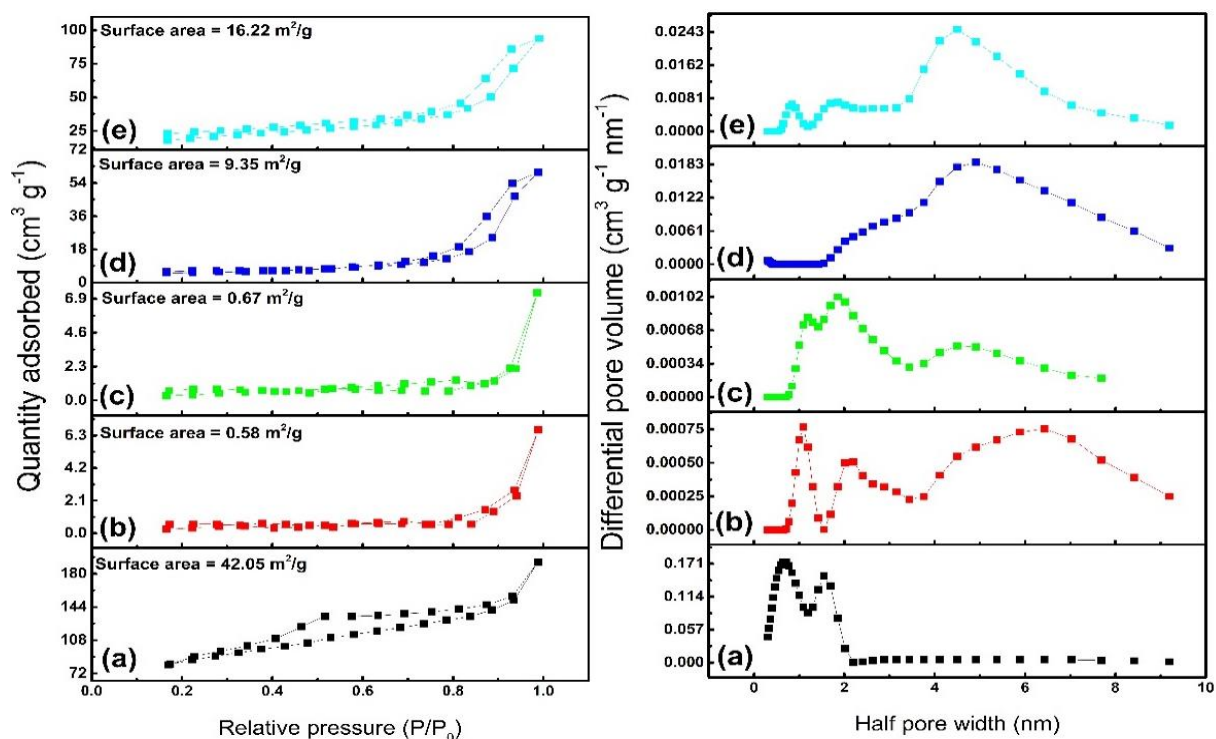


Fig. 6.6. BET calculated from N₂ adsorption-desorption isotherm and their corresponding DFT-pore size distribution of (a) rGH, (b) CNF/rGH, (c) Cu₂O/CNF/rGH, (d) TiO₂/CNF/rGH and (e) Cu₂O/TiO₂/CNF/rGH

XPS is further performed to study the chemical binding states of the samples. The wide spectrum of the samples shown in Fig. 6.7(a) depicts the presence of carbon (C), oxygen (O), copper (Cu) and titanium (Ti) indicating the successful orientation of the photoactive materials on the CNF/rGH. Fig. 7(b-f) showed that C1s split peaks of rGH, CNF/rGH, Cu₂O/CNF/rGH, TiO₂/CNF/rGH and Cu₂O/TiO₂/CNF/rGH which can be resolved to five types of carbon assigned to C=C (284.3 eV), C-C (285.2 eV), C-O (286.4 eV), C=O (287.6 eV) and O-C=O (288.9 eV). The high-resolution spectra peaks were analysed using the Voigt function with a Shirley background. Attributed to the chemical structure of CNF which contains large polar oxygenated groups, the expected increase in the C-C reveals the functionalization of the CNF and graphene sheets

after the hydrothermal reaction as shown in Table 6.2. In comparison to CNF/rGH, the atomic percentage of C=O in TiO₂/CNF/rGH reduced significantly showing that the carboxylic group has the priority to interact with the TiO₂ during the hydrothermal reaction. We posit that the addition of CNF dispersion in NaOH further exfoliate the GO which increases the edge area of the GO causing the content of C=O and COOH to increase due to functionalization with the CNF [346]. For Cu₂O/TiO₂/CNF/rGH, the significant reduction in the C=C and increased C-C atomic percentage indicated that the photoactive materials were able to orientate to the oxygenated groups which hinder the aromatic sp² rearrangement during hydrothermal treatment. We posit that the orientation of the Cu₂O occurred via the esterification (carboxylic linkage) while the TiO₂ via the epoxide and carbonyl linkages. The significant increase in the carboxylic percentage (O-C=O) for the Cu₂O/TiO₂/CNF/rGH may indicate that the electrostatic interaction is hampered.

Table 6.2. Atomic percentage derived from the deconvolution of the C1s split spectra.

Sample	Concentration of C1s Functional Groups (%)					
	C=C	C-C	C-O	C=O	O-C=O	π-π*
rGH	80.40	8.36	5.56	1.59	4.09	0.00
CNF/rGH	53.47	18.53	13.34	9.12	3.87	1.69
Cu ₂ O/CNF/rGH	45.80	21.95	17.88	9.44	2.68	2.25
TiO ₂ /CNF/rGH	49.87	22.09	15.40	6.32	3.50	2.80
Cu ₂ O/TiO ₂ /CNF/rGH	44.67	22.87	15.86	9.76	4.11	2.74

Fig 6.7(g) depicts the Ti 2p split spectra of commercial TiO₂, TiO₂/CNF/rGH and Cu₂O/TiO₂/CNF/rGH contributed from the spin orbit-splitting of the Ti 2p_{3/2} and Ti 2p_{1/2} which has been previously reported elsewhere [347]. The Ti_{2p} core level spectra showed two distinct characteristic peaks at 464.3 and 458.8 eV attributed to Ti 2p_{1/2} and Ti 2p_{3/2}, respectively. It can be observed in TiO₂ that a set of weaker peaks occurring around 461.2 eV can be attributed to the formation of O vacancies and Ti³⁺ sites in TiO₂ lattice [348]. However, no changes in the crystallinity of TiO₂ after hydrothermal treatment for Cu₂O/TiO₂/CNF/rGH as the spin-orbit splitting energy of 5.6 eV confirms the presence of Ti⁴⁺ species. Fig 6.7(h) illustrates the

high-resolution XPS spectra of the Cu 2p present in the synthesized Cu₂O revealing the binding energy at 932.3 eV and 952.7 eV corresponding to the Cu 2p_{3/2} and Cu 2p_{1/2}, respectively. The findings are in good agreement with previously published studies for Cu₂O [349]. The peak for Cu 2p_{3/2} can be further deconvoluted into two peaks, the main peak at 932.4 eV and 934.5 eV which is attributed to the Cu⁺ of Cu₂O and Cu²⁺ of CuO, respectively. The XRD result above further substantiated the formation of Cu₂O. The presence of Cu²⁺, also from the presence of satellite peak can be attributed to the mild oxidation of Cu₂O during the drying process which has been previously reported in a previous study [325]. The shifting of the Cu 2p_{3/2} to 932.9 eV and 935.1 eV for Cu₂O/CNF/rGH and Cu₂O/TiO₂/CNF/rGH can be observed. Theoretically, XPS can only detect components within the upper 5 nm thickness of the surface. The surface of the Cu₂O/TiO₂/CNF/rGH may be saturated with the NPS which caused shifting to higher binding energy suggesting that the surface of the copper changes its electronic state during the hydrothermal treatment.

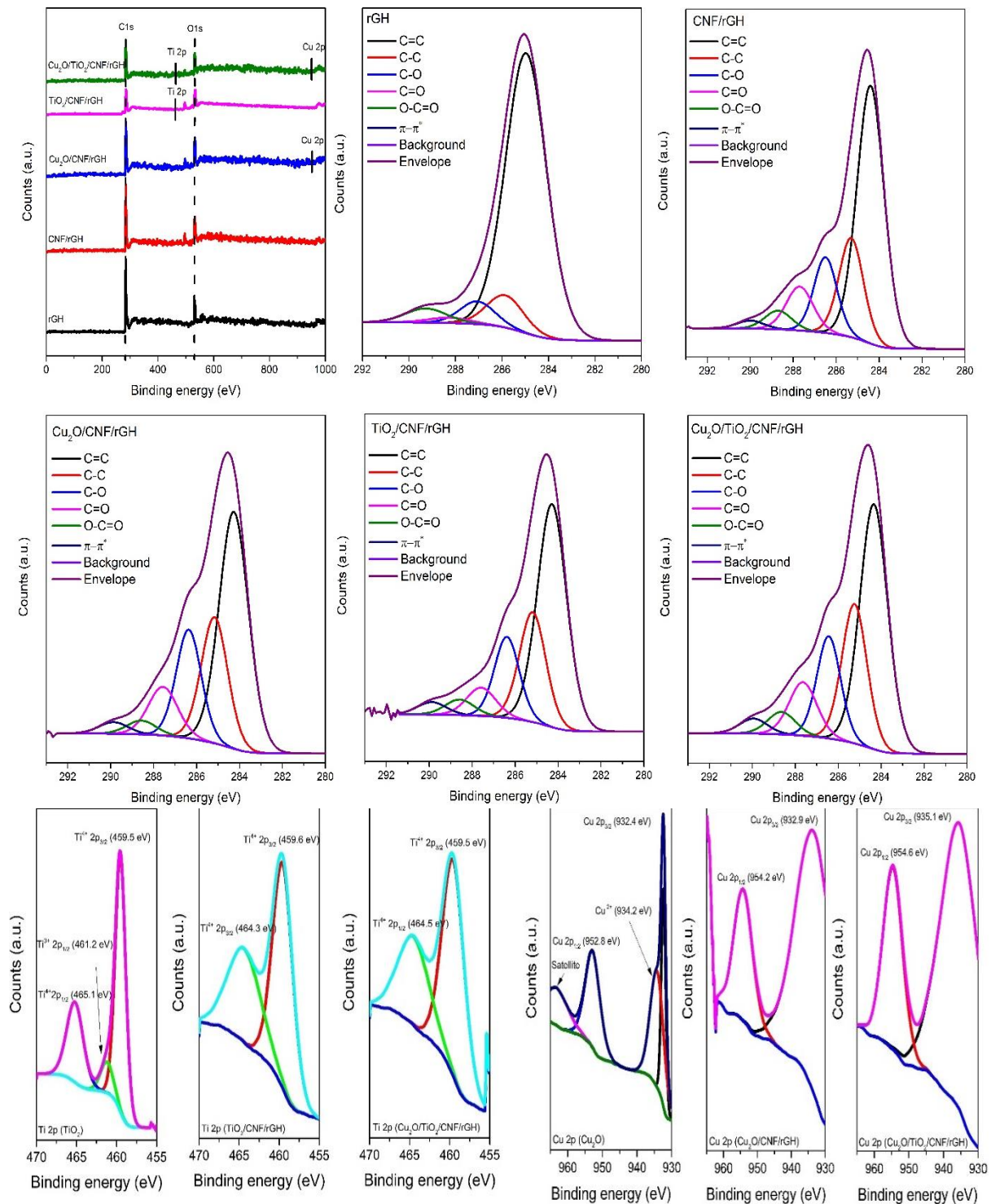


Fig. 6.7. XPS spectra of the samples (a) wide region, (b-f) C1s split spectra, (g) Ti 2p split spectra and (h) Cu 2p split spectra of the samples

MO adsorption and photocatalytic degradation

The photocatalytic efficiency is dependent on the dye molecule's adsorption on the hydrogel and also on the photocatalyst's electron transfer. Provided the porous nature of the graphene-based hydrogel, adsorption is expected to play a significant role. The adsorption study was conducted in the dark which is portrayed in Fig. 8(a).

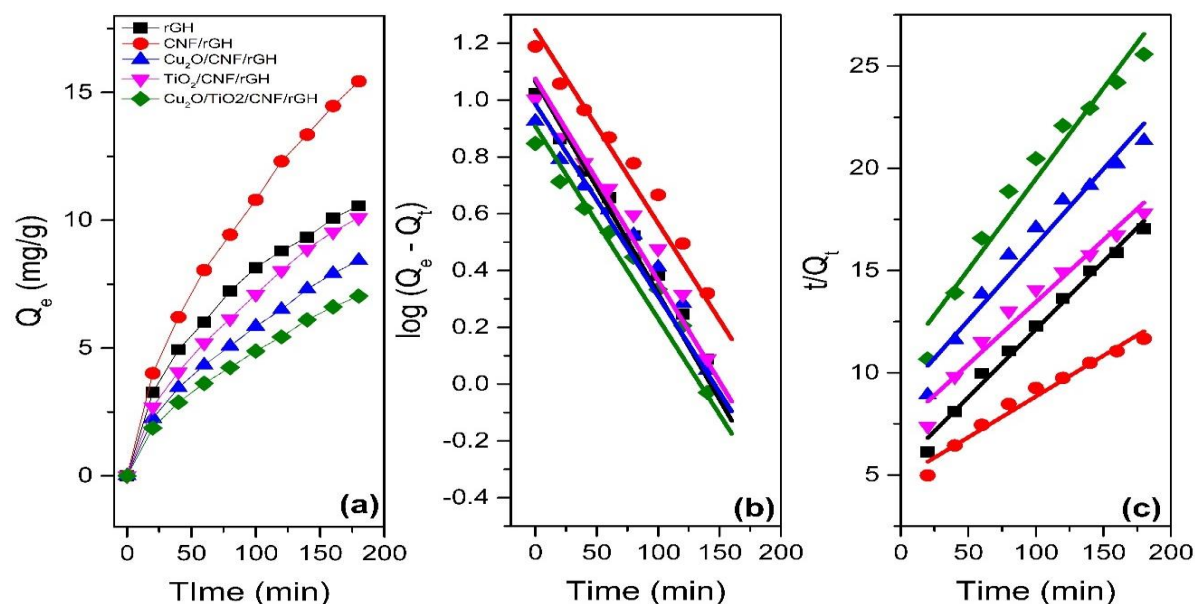


Fig. 6.8. (a) Adsorption capacity of MO as a function of time and their adsorption kinetics plots (dots) and curve fitted (line) by (b) pseudo-first-order kinetic model and (c) pseudo-second-order kinetic model.

The relationship between the adsorption behaviour of the photocatalyst and the contact time was studied by immersing the freeze-dried hydrogels in 20 mg/L of MO for 3 h under shaking. The adsorption performance of CNF/rGH was the best followed by rGH, TiO₂/CNF/rGH, Cu₂O/CNF/rGH and Cu₂O/TiO₂/CNF/rGH. It can be seen that CNF/rGH exhibited nearly 2.5 times the adsorption capacity than Cu₂O/TiO₂/CNF/rGH. This result demonstrated that the synergy between the reduced graphene sheets and CNF provided a multitude of interaction sites with the MO. Contrary to their specific surface area obtained, it can be seen that physisorption play a minimal role in the adsorption of MO as CNF/rGH exhibited the largest surface area. The significant dye-binding ability of the CNF/rGH can be attributed to the physicochemical properties of its surface. Therefore, it can be inferred that the presence of ion-exchanging groups contributed to greater binding affinity than the surface area does. We posit that π - π interactions between the CNF/rGH and the aromatic rings of the MO may contribute to their enhanced

adsorption capabilities. Interestingly, reduced adsorption capacity with the decoration of TiO₂ and Cu₂O on the CNF/rGH. The possible explanation for this behaviour could be attributed to the orientation of the metal oxide nanoparticle which filled the porous structure of the framework hindering the interaction of the anionic dye with the CNF/rGH. The decreased specific surface area attributed to the excess incorporation of metal oxide nanoparticles has been previously reported which contributes to lower adsorption capability [350]. To elucidate the adsorption mechanism, the pseudo-first-order (PFO) and pseudo-second-order (PSO) kinetic models were applied. The linearized form of the equation can be expressed as:

The pseudo-first-order (PFO) model:

$$\ln (Q_e - Q_t) = \ln Q_e - \frac{K_1 t}{2.303} \quad (3)$$

The pseudo-second-order (PSO) model:

$$\frac{t}{Q_t} = \frac{1}{K_2 Q_e^2} + \left(\frac{1}{Q_e}\right) t \quad (4)$$

Fig. 8(b) and 8(c) further depict the experimental data evaluated from the linearized form of the equations and the adsorption parameters are shown in Table 3. The PSO kinetic model showed a better fit in comparison to PFO suggesting that chemisorption played a more significant role than physisorption during the adsorption process. The adsorption capacity of CNF/rGH reached 25.05 mg/g with the lowest K₂ value of 0.0003287 min g/mg while Cu₂O/TiO₂/CNF/rGH exhibiting the lowest adsorption capacity with the highest K₂ value of 0.0007407 min g/mg.

Table 6.3. Kinetic parameters obtained from the PFO and PSO kinetic model for the adsorption of MO

Sample	Pseudo-First Order			Pseudo-Second Order		
	Q _e	K ₁	R ²	Q _e	K ₂	R ²
rGH	11.66	0.0172034	0.95161	15.07	0.0008027	0.98808
CNF/rGH	17.68	0.0156834	0.94361	25.05	0.0003287	0.96983
Cu ₂ O/ CNF/rGH	9.69	0.0155913	0.92692	13.50	0.0006194	0.95452
TiO ₂ /CNF/rGH	11.90	0.0163513	0.93032	16.44	0.0005016	0.96113
Cu ₂ O/TiO ₂ /CNF/rGH	8.09	0.0155913	0.92692	11.28	0.0007407	0.95452

Further investigation of the photocatalytic performance of the as-prepared photocatalysts was conducted using UV irradiation under various conditions. Fig. 9(a) depicts the deterioration curve of the C/C_0 along with the irradiation time of MO using the various photocatalysts. The C/C_0 values after irradiation for 120 min in the presence of rGH, $\text{Cu}_2\text{O}/\text{rGH}$, TiO_2/rGH , $\text{Cu}_2\text{O}/\text{TiO}_2/\text{rGH}$ were found to be 0.47905, 0.23814, 0.21432, 0.27053 and 0.14379, respectively. The blank test showed the slight self-photodegradation of the MO of about 17% after 120 minutes of UV irradiation attributed to the dye self-sensitization. After 120 minutes of UV irradiation, the removal efficiency of MO by $\text{Cu}_2\text{O}/\text{TiO}_2/\text{CNF}/\text{rGH}$ reached up to 85.62%. The degradation rate of rGH, rGH/CNF, $\text{Cu}_2\text{O}/\text{CNF}/\text{rGH}$, and $\text{TiO}_2/\text{CNF}/\text{rGH}$ are 42.09 %, 76.19 %, 78.57% and 72.95%, respectively. The higher photocatalytic activity of $\text{Cu}_2\text{O}/\text{TiO}_2/\text{CNF}/\text{rGH}$ can be attributed to the synergistic effect of TiO_2 and Cu_2O on reduced graphene sheets as the photoactive materials promote the MO photocatalytic degradation due to the ease of electron transfer. Besides, the larger surface area of $\text{Cu}_2\text{O}/\text{TiO}_2/\text{CNF}/\text{rGH}$ also contributed to the ability to capture more incident light and transmit photogenerated electrons, hence promoting charge separation. The photocatalytic activity of $\text{TiO}_2/\text{CNF}/\text{rGH}$ is slightly lower in comparison to CNF/rGH which can be attributed to the highly concentrated CNF/rGO sheets which blocked the active sites of the TiO_2 . The results obtained during MO photodegradation were further fit to Langmuir-Hinselwood pseudo-first-order kinetics as shown in Figure 7c. The formula can be expressed as follows:

$$\ln\left(\frac{C_t}{C_0}\right) = -K_{app}t + b \quad (5)$$

The slope of $\ln(C/C_0)$ versus irradiation time was used to calculate the pseudo-first-order rate constant, K (min^{-1}). C_0 and C are the initial and final concentrations of MB, respectively, at a given time, t . The degradation kinetic constant, K was calculated to be $0.001598 \text{ min}^{-1}$ for the $\text{Cu}_2\text{O}/\text{TiO}_2/\text{CNF}/\text{rGH}$.

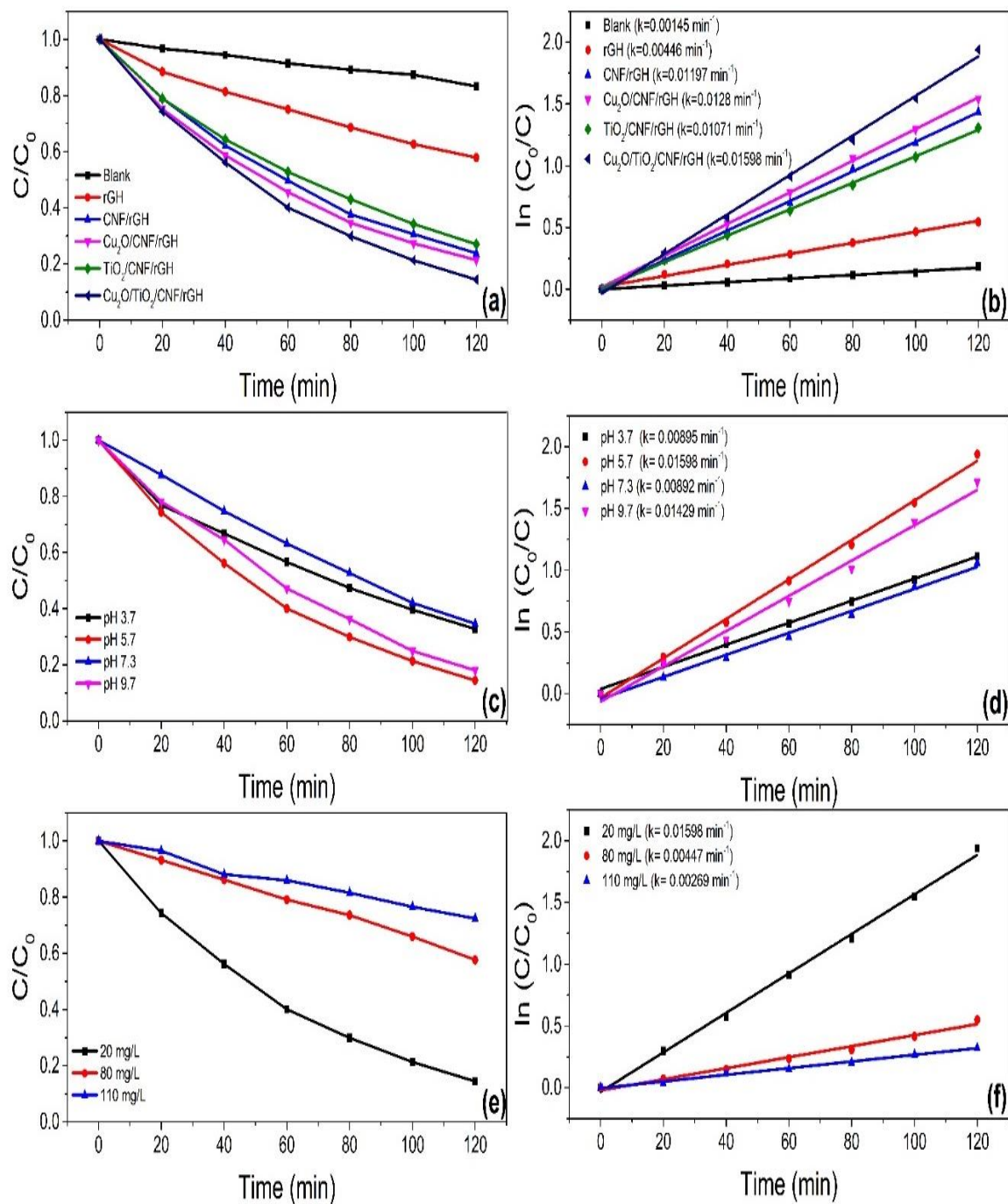


Fig. 6.9. (a,b) Deterioration curve (C/C_0) for the photodegradation of MO and their first order kinetics using various hydrogel-based photocatalysts. (c,d) Photodegradation of MO using $\text{Cu}_2\text{O}/\text{TiO}_2/\text{CNF}/\text{rGH}$ under various pH and their kinetics. (e,f) Photodegradation under various MO initial concentrations and their kinetics.

pH plays a pertinent role during the photodegradation of MO. Fig. 6.9 (c,d) depicts the effect of pH on MO photodegradation and its degradation kinetics. It can be observed that the photocatalytic degradation efficiency of MO decreased with the change of pH to acidic or alkaline. Previously, photocatalytic degradation of MO under highly acidic conditions was found to be unfavourable due to the increasing H^+ and Cl^- concentrations that collapse the interface regions, allowing the attractive van der Waals forces to overcome charge repulsion. On the other hand, the abundance of negatively charged OH^- will result in the repulsion between the photocatalyst and MO dye that decreases the absorption on the catalyst surface leading to lower photodegradation efficiency. At pH 7.3, the $Cu_2O/TiO_2/CNF/rGH$ performed best in the photodegradation of MO with a kinetic constant of 0.01429 min^{-1} . Fig. 6.9 (e,f) illustrates the photodegradation efficiency of $Cu_2O/TiO_2/CNF/rGH$ for varying initial MO initial concentration (20, 80 and 110 mg/L). The results showed that the photodegradation efficiency was 78.6%, 53.1% and 32.2%, respectively. The underlying reason behind the decreased photocatalytic activity can be attributed to the covering of the active sites on the catalyst surface by the MO which hinders the capturing of light. Additionally, at high dye concentrations, the dye molecules may absorb a significant amount of light. Hence, the optimal condition for degradation of MO occurred using 20 mg/L. From the linear fit of the data in Fig 9 (b,d,e), it is clear that the MO photodegradation follows the first-order-kinetic model. The linear regression coefficients (R_2) were close to unity (0.912-0.995). Fig. S6.3 further showed the FTIR spectrum of the freeze-dried $Cu_2O/TiO_2/CNF/rGH$ before and after the photocatalysis test. The presence of weak to no presence of MO functional groups after the photocatalysis process proved that the degradation is mainly attributed to photocatalysis instead of adsorption. Interestingly, the peak around $\sim 1400 \text{ cm}^{-1}$ significantly weakened in which we posit from the structural change of the cellulose network under UV irradiation.

Radical trapping experiment

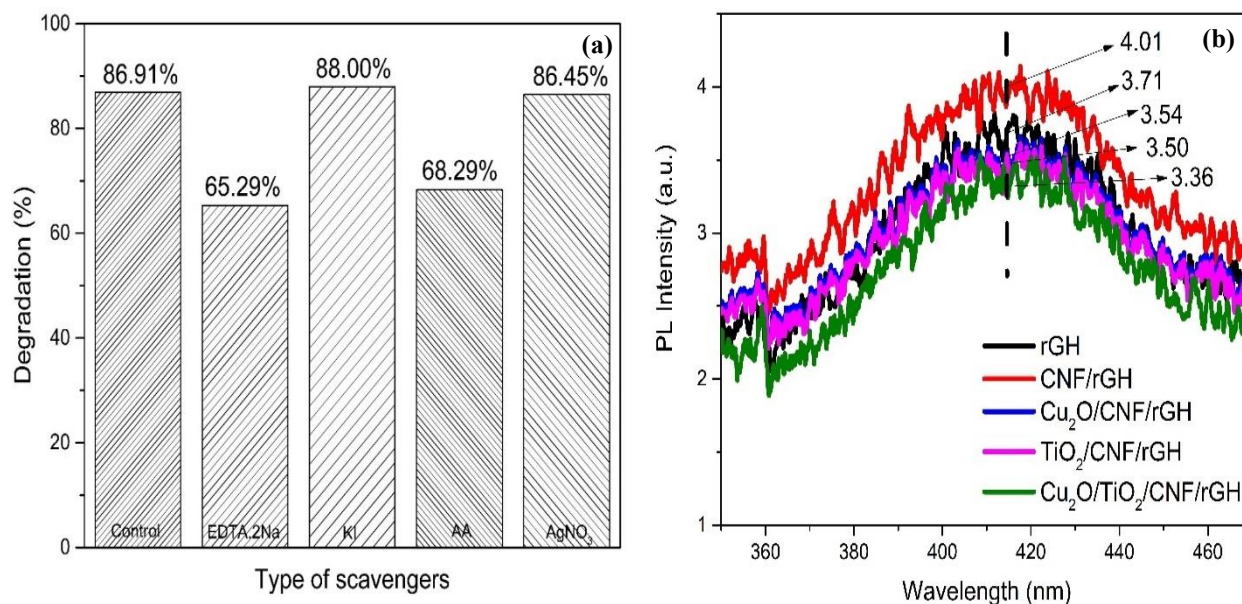


Fig. 6.10. (a) The effect of different scavengers on the photodegradation of MO carried at optimum photocatalytic condition. (b) PL emission spectra of the samples

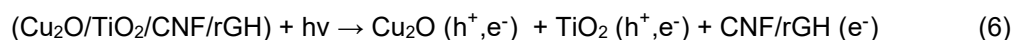
The identification of the reactive species involved in the photocatalytic degradation of MO by Cu₂O/TiO₂/CNF/rGH was accessed using the radical trapping experiment. The radical capture experiments were carried out using various radical scavengers (10 mM) such as potassium iodide (KI), ethylenediaminetetraacetic acid disodium salt (EDTA.2Na), ascorbic acid (AA) and silver nitrate (AgNO₃) acting as the hydroxyl radicals ($\cdot\text{OH}$), holes (h^+), superoxide anion ($\cdot\text{O}_2^-$) and electron (e^-) scavengers, respectively [351]. The obtained results were depicted in Fig. 6.10. The role of scavenger addition to the MO solution could inhibit catalytic efficiency by trapping specific active species. The addition of KI and AgNO₃ does not cause significant changes in the photocatalytic degradation of MO upon comparing to the control sample. The degradation of MO was significantly inhibited from the addition of EDTA.2Na and AA to capture h^+ and $\cdot\text{O}_2^-$, respectively indicating that holes and superoxide anions played vital roles in the photocatalytic activity. h^+ is the dominant oxidative species and directly reacts with the adsorbed MO. Our findings showed that $\cdot\text{O}_2^-$ radicals were generated during the UV irradiation which played a major role in MO degradation. AA can react with superoxide radicals in acidic conditions to produce ascorbate free

radicals ($\text{HA}\cdot$) The recombination of electrons and holes was hindered with the addition of EDTA as a scavenger to capture holes [352]. As a result, more electrons migrated to the photocatalyst's surface and reacted with O_2 to form $\cdot\text{O}_2^-$, enhancing MO degradation. The photoluminescence (PL) measurements were further carried out to access the transfer of electron and charge-carrier trapping as shown in Fig. 6.10 (b). Although the intensity obtained are almost similar but the slight improvement showed that the anchoring of the photocatalyst led to reduced recombination of photogenerated charge carriers [353]. As expected, the inclusion of both the photoactive materials on the CNF/rGH possessed the lowest PL intensity, suggesting the formation of the p-n heterojunction. In addition, the CNF/graphene sheet acted as an effective charge carrier hindering the direct recombination of electron-hole pairs.

Proposed mechanism of photodegradation

The proposed mechanism of the $\text{Cu}_2\text{O}/\text{TiO}_2/\text{CNF}/\text{rGH}$ is predicted according to the radical trapping experiment. Numerous factors could account for the enhanced photocatalytic activity of the $\text{Cu}_2\text{O}/\text{TiO}_2/\text{CNF}/\text{rGH}$ from the addition of Cu_2O and TiO_2 to the CNF/rGO sheets. Cu_2O 's conduction band (CB) and valence band (VB) are theoretically larger than those of TiO_2 (3.03 eV). Upon UV irradiation, electrons were excited in the valence band to the conduction band, forming electron-hole pairs. Additionally, excited electrons could recombine with holes via direct recombination and surface combination, reducing their photocatalytic efficiency. P-N heterojunctions can form when p-type Cu_2O and n-type TiO_2 come into close contact. Since the conduction band of Cu_2O is more negative than that of TiO_2 , an inner electric field may exist, resulting in electron transfer from Cu_2O to TiO_2 [354]. Cu_2O and TiO_2 irradiated with UV light, in which charge separation then occurs, will both be excited and generate electron-hole pair which react with H_2O yielding radicals such as hydroxyl and superoxide radicals that play a role in the mineralization of the MO. The photogenerated electrons will be transferred to the TiO_2 conduction band and the photogenerated holes will move to the valence band of the Cu_2O . Besides, the electrons may also be transferred to the graphene sheet which interacts with atmospheric oxygen leading to the formation of oxygen superoxide radical anions. Owing to the synergistic effect of the graphene sheet, recombination of the hole and electron is hindered in TiO_2 and Cu_2O , further lengthening the charge-carrier lifetime, thus improving the charge separation [355,356]. In addition, the CNF/rGH sheet enables better adsorption of the MO due to the π - π interactions, which greatly enhanced the photocatalytic reactions. These h^+ and $\cdot\text{O}_2^-$ degrade the MO into

oxidized products. The photocatalytic degradation of MO can hence be represented in the following equation as follows:



The intermediate of the degradation of MO by $\text{Cu}_2\text{O}/\text{TiO}_2/\text{CNF}/\text{rGH}$ was analysed by GC-MS mass spectrometry and the degradation pathway is proposed. Based on Fig. S6.4, the chromatogram depicted the formation of several degradation products which is identified from the mass spectrum values and the fragmentation pattern. The pattern is corresponding to the low molecular mass aromatic compound after the photodegradation process for 120 min. Some intermediates could not be identified due to various reasons such as the instability of their derivatives and analytical limitations. The first step in the photodegradation involved the splitting of the MO to sodium-4-diazenylbenzenesulfonate ($m/z=207$) and 4-(dimethylamino)phenol ($m/z=137$). The removal of methyl radical from the 4-diazenylbenzenesulfonate undergoes cyclization to produce 4-cyclohexanone lactone cation ($m/z=190$). The C–N bonds in the dimethylamino group and between the aromatic ring and the azo bond are easily broken, implying that they may be easily broken down during the photodegradation process [357]. The aniline generated a peak at m/z 94 in the form of protonated $[\text{M} + \text{H}]^+$ after desulfonation of the sodium 4-diazenylbenzenesulfonate. Further oxidative reactions resulted in ring-opening and formation of short linear aliphatic carboxylic acids, inorganic ions, CO_2 and H_2O [358,359]. The probable degradation pathway is depicted in Fig. 6.11.

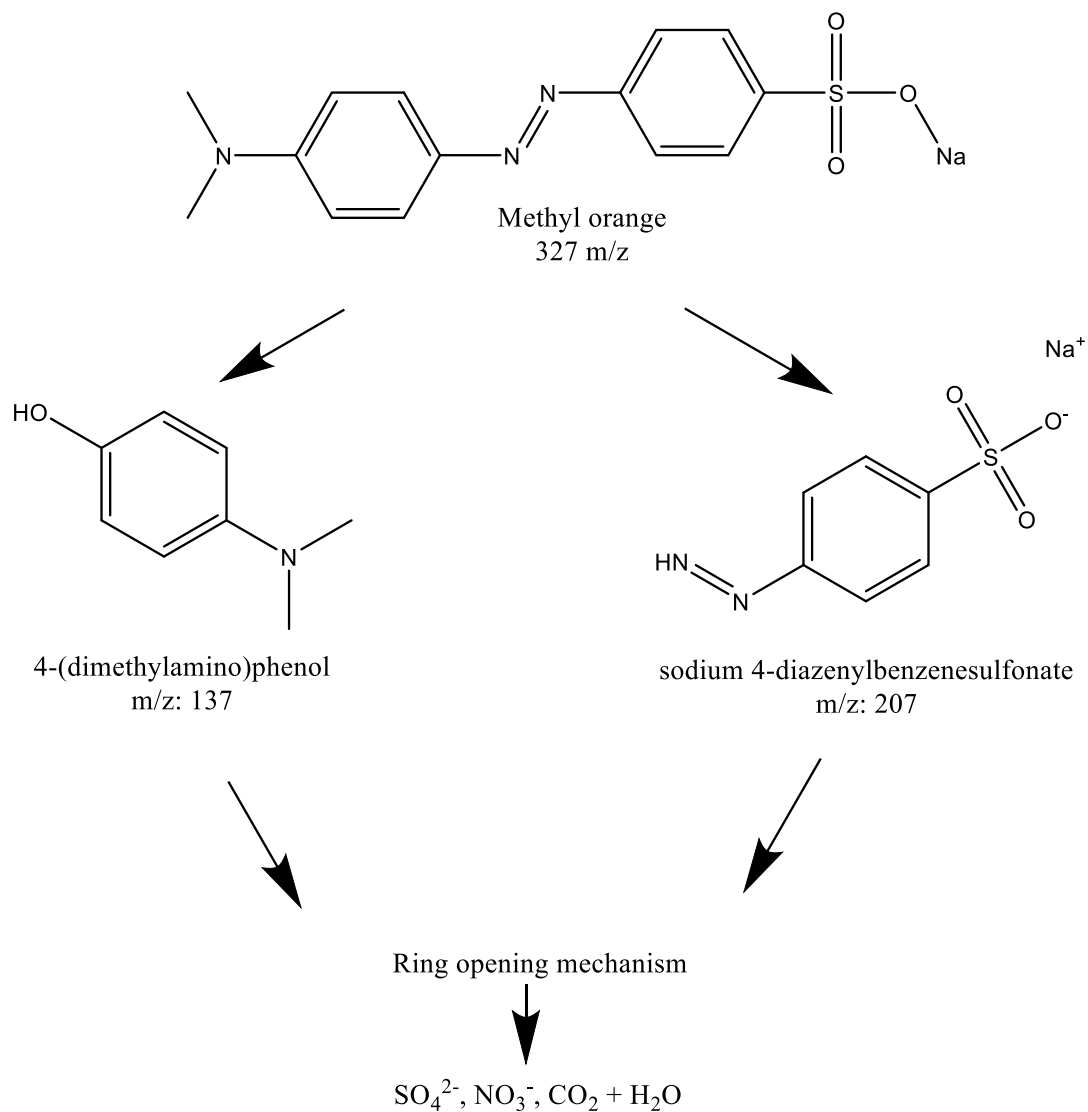


Fig. 6.11. Proposed degradation pathway for MO using $\text{Cu}_2\text{O}/\text{TiO}_2/\text{CNF}/\text{Rgh}$

Stability and reusability

The stability and reusability of the $\text{Cu}_2\text{O}/\text{TiO}_2/\text{CNF}/\text{rGH}$ are further evaluated under optimized photodegradation conditions. The reusability of the composite is an essential aspect for the reduction in the operational cost of the photocatalyst. To access the photodegradation behaviour, three consecutive runs were performed as shown in Fig.6.12. After each run, the composite is thoroughly washed with deionized

water and ethanol, filtered and dried before a fresh MO solution was used in successive runs. The photodegradation rate for the four runs were 85.0%, 84.34%, 81.42 %, and 79.5% after 120 min of irradiation time indicating that the photocatalyst is mostly stable under UV irradiation. The decreased in the photodegradation efficiency can be attributed to the depletion of the composite during the washing process. In addition, the decreased efficiency can be ascribed to the partial loss of the Cu₂O/TiO₂ resulting from the strong oxidation condition. However, it is important to note that the easy recovery of the hydrogel sample is an added value that reduced the cost and operational procedure. From Table 4, Cu₂O/TiO₂/CNF/rGH exhibited remarkable efficiency in the photodegradation of MO in comparison to previously reported 3D based photocatalyst. It is paramount to understand that experimental conditions were varied in each of the tests which differently affect the photocatalytic degradation. However, it should provide a general idea of this kind of work. The facile preparation method and good reusability of our modified hydrogel are expected to perform well in wastewater treatment.

Table 6.4. Comparison with recently reported photocatalyst for the degradation of MO

No	Photocatalyst	Time (min)	Dye concentration (mg/L)	volume, (%)	Degradation (%)	References
1	Sb ₂ Se ₃ /β-In ₂ Se ₃	180	80 mL (10 mg/L)		78.00	[360]
2	Ag/RP	20	50 mL (50 mg/L)		100.00	[361]
3	Ag/AgCl	65	50 mL (20 mg/L)		92.20	[362]
4	Ag/TiO ₂	120	100 mL (7.5 mg/L)		65.40	[363]
5	Ag/TiO ₂ /biochar	60	40 mL (20 mg/L)		85.38	[364]
6	ZnO/GO	120	100 mL (5-25 mg/L)		95.00	[365]
7	Cu ₂ O/TiO ₂ /CNF/rGH	120	50 mL (20 mg/L)		85.62	This work

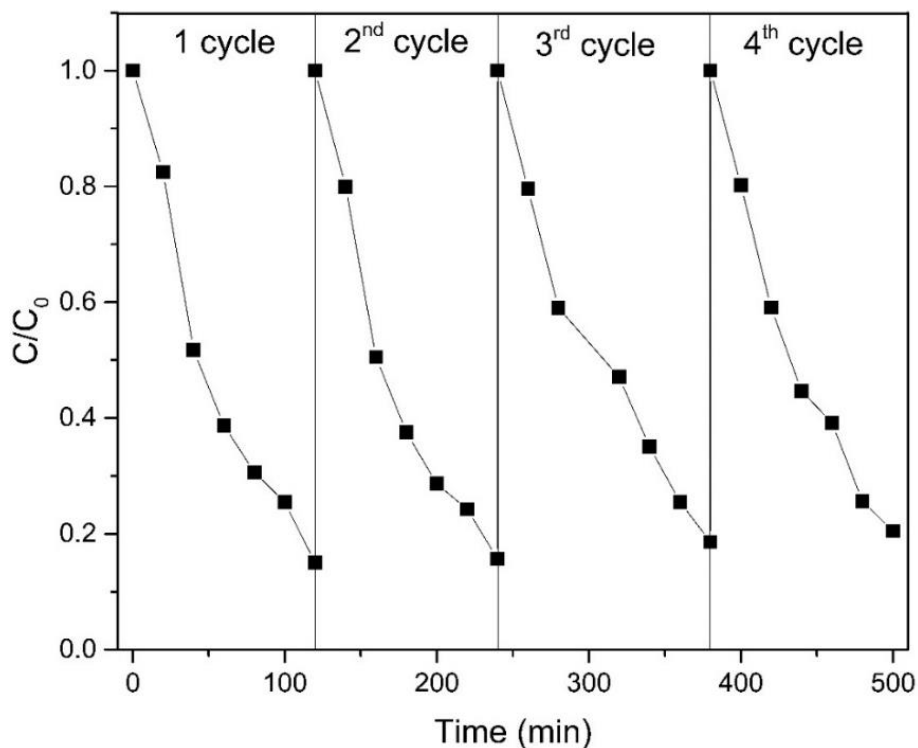


Fig. 6.12. Repeatability test for photodegradation of MO using Cu₂O/TiO₂/CNF/rGH

Antibacterial assessment of Cu₂O/TiO₂/CNF/rGH

In wastewater treatment, a material exhibiting antibacterial properties is an added value as contamination of water sources is common due to domestic discharge. In real applications, microorganism contamination can hinder the photocatalytic efficiency of the catalyst, hence material exhibiting antibacterial properties can significantly address the inherent problem. To access the performance of the hydrogels in bacterial disinfection, the hydrogels were immersed/agitated in a saline solution containing *S. aureus* or *E. coli* under dark conditions. Fig. 6.13 illustrates the total viable count and spotting test experiments (inset). It can be seen that total inhibition of bacteria is achieved for Cu₂O/CNF/rGH, TiO₂/CNF/rGH and Cu₂O/TiO₂/CNF/rGH, indicating the excellent antibacterial properties exhibited by TiO₂ and Cu₂O which has been extensively covered in previous literature [366,367]. Briefly, bacteria inhibition by metal oxides usually occurs via releasing metal ions and reactive oxygen species (ROS) generation. The morphology, size, and crystal nature of the nanoparticles also play a significant role in the bacterial inhibition process. In general, graphene hydrogel-oriented nanoparticles possessing high volume surface area to volume facilitate contact with the bacteria to enable easy entry into the bacterial cell wall to cause cell damage [368]. The result

obtained showed that Cu₂O/TiO₂/CNF/rGH possessed excellent antibacterial properties for both Gram-negative and Gram-positive bacteria alongside Cu₂O /CNF/rGH and TiO₂/CNF/rGH, which is an added value in wastewater treatment. As for the blank sample, rGH and CNF/rGH, the serial dilution at 10³ yielded well-delineated colonies in an acceptable range. It can be seen that the inclusion of CNF improved the antibacterial properties as much as 1-fold in comparison to rGH. The observations were confirmed in a repeat trial in which 10 µL of bacterial cultures were used for the spot testing. To conclude the observations, the orientation of Cu₂O/TiO₂ on CNF/rGH possessed favourable antibacterial activity for future application in real-time conditions. However, to obtain a more comprehensive antibacterial effect, various factors need to be taken into consideration such as the dimension of the particles anchored on the template and the ratio of TiO₂ to Cu₂O on the template.

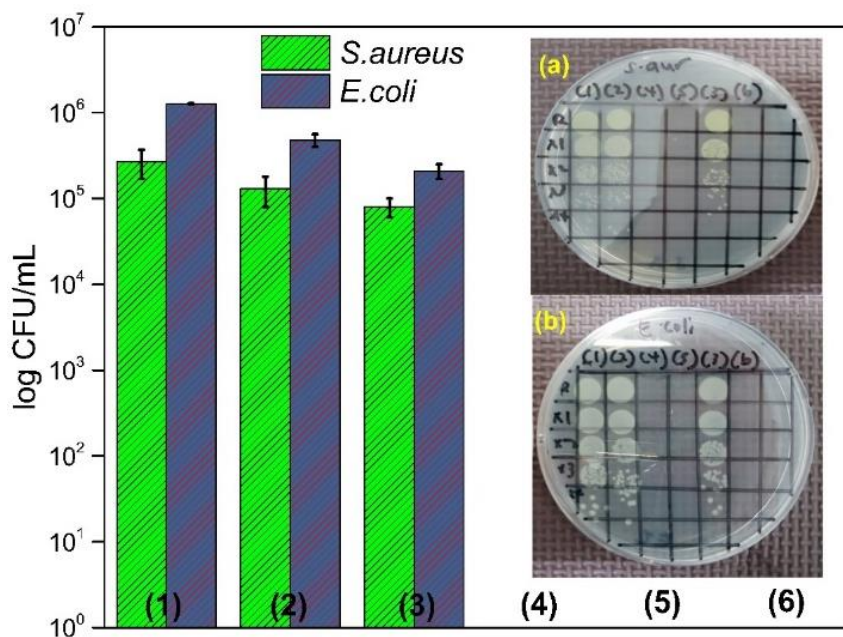


Fig. 6.13. Histogram of the total viable count of (a) *S. aureus* and (b) *E. coli*. Log CFU/mL for (1) cells only (2) rGH, (3) CNF/rGH. (4) Cu₂O/CNF/rGH, (5) TiO₂/CNF/rGH and (5) Cu₂O/TiO₂/CNF/rGH. *Inset:* spotting test of bacterial colonies on LB agar under 10-fold cell dilutions.

6.4 Conclusion

The Cu₂O/TiO₂/CNF/rGH was successfully prepared via an in-situ facile one-pot hydrothermal synthesis and freeze-drying. The morphology, crystallinity, specific surface area, thermal stability and optical

properties were characterized by SEM, XRD, Raman, BET, XPS, FTIR, TGA and UV-DRS. $\text{Cu}_2\text{O}/\text{TiO}_2/\text{CNF}/\text{rGO}$ exhibited higher photocatalytic activity towards the degradation of MO under UV irradiation in comparison to commercial CNF/rGH, $\text{Cu}_2\text{O}/\text{CNF}/\text{rGH}$, and $\text{TiO}_2/\text{CNF}/\text{rGH}$. The synergistic effect of TiO_2 , Cu_2O , CNF and rGO promoted the photodegradation activity due to the improved electron transfer process. The removal efficiency of the $\text{Cu}_2\text{O}/\text{TiO}_2/\text{CNF}/\text{rGH}$ was 85.62% of MO within 120 min under normal pH. The photocatalyst exhibited high reusability and regeneration percentage even after three cycles. The MO photodegradation was shown to be mainly affected by the superoxide radical and hole formation. In addition, the $\text{Cu}_2\text{O}/\text{TiO}_2/\text{CNF}/\text{rGH}$ exhibited strong antibacterial activity towards *S. aureus* and *E. coli*. The versatility of the proposed 3D photocatalyst prepared using the facile hydrothermal method opens ample avenues for extensive usage in wastewater treatment applications.

CHAPTER 7

CONCLUSION AND RECOMMENDATIONS

7.1 Conclusion

Without a doubt, 3D graphene hydrogel/aerogel has a promising future due to its unique characteristics and features that can provide ample research and development opportunities that are not exclusive only to water-remediation applications. In this study, the preparation of 3D graphene hydrogels via the hydrothermal treatment is achieved by satisfying three main criteria: the concentration of GO as the starting material, hydrothermal time, and hydrothermal temperature. Besides, this study has successfully shown that the hydrothermal treatment is a feasible yet simple approach in the functionalization of various modifiers such as divalent metal ions, metal/metal oxide nanoparticles, and porphyrins complexes. It was found that the interaction between the graphene sheets and the modifiers may be either via covalent or non-covalent interactions. Various dimensions of graphene hydrogels can be obtained which can be tuned accordingly based on their intended applications. The study into the structural, optical, morphology, electrochemical, and electrical properties of the modified graphene hydrogel using a plethora of techniques such as XRD, XPS, FTIR, TGA, Raman, SEM, UV-Vis, UV-DRS, and PL instruments has been carried out, where it was seen fit. However, it is important to understand that the 'one-step' protocol is only applicable to modifiers that can withstand the hydrothermal time and temperature (<120 °C). In our study, the functionalization of the alkylamine on the reduced graphene hydrogel surface can only be achieved using a 'two-step protocol to preserve the alkylamine from degradation. The functionalization is succeeded using the simple immersion and agitation method which improved their functionalities for the adsorption of MB and BPA.

Provided that various reported adsorbent/photocatalyst is powder-based, which significantly does not offer the advantage of reusability as they are prone to lose during the remediation process. The development of the hybrid 3D graphene hydrogel inherently offers the advantage of simple recovery and reusability; significantly reduce the operational cost in real-time application. The adsorption capability of the modified 3D graphene hydrogel was accessed via adsorption kinetics and isotherm; in which most of them satisfy

the pseudo-second-order and Langmuir isotherm. Besides, the regenerative percentage for the modified hydrogels often achieved above 85 %. In the photocatalytic degradation of MO, the hybrid 3D Cu₂O/TiO₂ on CNF/rGH showed excellent photodegradation efficiency of up 80% after four successive cycles. The successful anchoring of the photoactive materials on the 3D graphene hydrogel via the hydrothermal treatment enables for more novel hybrid photocatalyst to be prepared in the future. Our study found that the degradation mechanism was mostly initiated by the hole (h⁺) and superoxide anions. Finally, in terms of the antibacterial inactivation on *E. coli*, the prepared hybrid 3D graphene hydrogel also exhibited excellent activity. Results from this study may open up new possibilities in the application of antimicrobial 3D graphene structure in various applications. Further studies are needed in the long run to enhance 3D GBMs with multi-functionalities with outstanding adsorptive and photocatalysis ability.

7.2 Recommendation for future studies

This study may not have covered the broad aspect of synthesis and the applications of modified 3D graphene hydrogel in wastewater remediation, but is hoped to provide a general idea to new entrants and experienced researchers intending to apply them as the material of interest in wastewater related remediation. Hence, the recommendations for future studies to further improve our existing study are as follows:

7.2.1 Pre-synthesis/Characterizations

- (a) In our study, the 3D graphene hydrogel was prepared using low temperature (<132°C) hydrothermal temperature due to instrumental limitations. It will be more inclusive to also compare the functionalization rate at higher hydrothermal temperatures.
- (b) The morphological evaluation of the modified 3D graphene can also be achieved using TEM-SAED and AFM to obtain a more comprehensive evaluation of the the modified graphene sheet.

7.2.2 Adsorption and photocatalysis

- (a) Molecular dynamic simulations and DFT computational methods can be applied to correlate with the experimental results obtained.

- (b) Most studies have been conducted under laboratory conditions using a synthesis solution containing the desired pollutants that do not reflect the full potential of GBMs. Other contaminants may be present in natural or man-made bodies of water that may compete with the intended target contaminants. Therefore, to evaluate the practicality and performance of the GBMs comprehensively, a real-analysis study should be conducted.
- (c) It can be seen that the photocatalytic study only focused on a single dye molecule as the model pollutant. Simultaneous remediation of various pollutants could further provide a more comprehensive assessment in terms of their performance.

7.2.3 Antibacterial applications

- (a) The long-term toxicity effect of the hybrid 3D graphene on aquatic organisms for use in water-remediation applications must also be understood. Further tests such as in vivo toxicity tests can be conducted to obtain a more comprehensive effect of the hybrid 3D graphene material.
- (b) In this study, only Gram-negative bacteria, *E.coli* is applied for the antibacterial evaluation. The evaluation of more bacteria models can be conducted as the structure of Gram-negative and Gram-positive bacteria is significantly different which may give varying results.
- (c) The antibacterial mechanism of action can be studied to determine their action. In the study, we only hypothesize the morphology of the graphene sheet possessing a sharp edge that is responsible for its antibacterial properties.
- (d) Photocatalytic disinfection test can be further carried to also access the 3D hybrid $\text{Cu}_2\text{O}/\text{TiO}_2/\text{CNF}/\text{rGH}$ antibacterial properties.

REFERENCES

- [1] A.K. Geim, Graphene: Status and Prospects, *Science* (80-.). 324 (2009) 1530–1534. <https://doi.org/10.1126/science.1158877>.
- [2] H.C. Lee, W.W. Liu, S.P. Chai, A.R. Mohamed, A. Aziz, C.S. Khe, N.M.S. Hidayah, U. Hashim, Review of the synthesis, transfer, characterization and growth mechanisms of single and multilayer graphene, *RSC Adv.* 7 (2017) 15644–15693. <https://doi.org/10.1039/C7RA00392G>.
- [3] A.T. Smith, A. Marie, S. Zeng, B. Liu, L. Sun, Synthesis, properties, and applications of graphene oxide/ reduced graphene oxide and their nanocomposites, *Nano Mater. Sci.* 1 (2019) 31–47. <https://doi.org/10.1016/j.nanoms.2019.02.004>.
- [4] M.J. Allen, V.C. Tung, R.B. Kaner, Honeycomb carbon: A review of graphene, *Chem. Rev.* 110 (2010) 132–145. <https://doi.org/10.1021/cr900070d>.
- [5] Y. Zhu, S. Murali, W. Cai, X. Li, J.W. Suk, J.R. Potts, R.S. Ruoff, Graphene and Graphene Oxide: Synthesis, Properties, and Applications, *Adv. Mater.* 22 (2010) 3906–3924. <https://doi.org/10.1002/adma.201001068>.
- [6] P. Machac, S. Cichon, L. Lapcak, L. Fekete, Graphene prepared by chemical vapour deposition process, *Graphene Technol.* 5 (2020) 9–17. <https://doi.org/10.1007/s41127-019-00029-6>.
- [7] J. Chen, W. Shi, Z. Gao, T. Wang, S. Wang, L. Dong, Q. Yang, C. Xiong, Facile preparation of pristine graphene using urea/glycerol as efficient stripping agents, *Nano Res.* 11 (2018) 820–830. <https://doi.org/10.1007/s12274-017-1691-3>.
- [8] B. Hou, H. Liu, S. Qi, Y. Zhu, B. Zhou, X. Jiang, L. Zhu, Preparation of pristine graphene in ethanol assisted by organic salts for nonenzymatic detection of hydrogen peroxide, *J. Colloid Interface Sci.* 510 (2018) 103–110. <https://doi.org/10.1016/j.jcis.2017.09.052>.
- [9] I.G. Gonzalez-Martinez, A. Bachmatiuk, T. Gemming, B. Trzebicka, Z. Liu, M.H. Rummeli, Rapid synthesis of pristine graphene inside a transmission electron microscope using gold as catalyst, *Commun. Chem.* 2 (2019) 1–8. <https://doi.org/10.1038/s42004-019-0134-3>.
- [10] H. Grajek, J. Jonik, Z. Witkiewicz, T. Wawer, M. Purchała, Applications of Graphene and Its Derivatives in Chemical Analysis, *Crit. Rev. Anal. Chem.* 50 (2020) 445–471. <https://doi.org/10.1080/10408347.2019.1653165>.
- [11] W.S. Hummers, R.E. Offeman, Preparation of Graphitic Oxide, *J. Am. Chem. Soc.* 80 (1958) 1339–1339. <https://doi.org/10.1021/ja01539a017>.
- [12] J. Chen, B. Yao, C. Li, G. Shi, An improved Hummers method for eco-friendly synthesis of graphene oxide, *Carbon N. Y.* 64 (2013) 225–229. <https://doi.org/10.1016/j.carbon.2013.07.055>.
- [13] R. Ikram, B.M. Jan, W. Ahmad, An overview of industrial scalable production of graphene oxide and analytical approaches for synthesis and characterization, *J. Mater. Res. Technol.* 9 (2020) 11587–11610. <https://doi.org/10.1016/j.jmrt.2020.08.050>.
- [14] Y. Hou, S. Lv, L. Liu, X. Liu, High-quality preparation of graphene oxide via the Hummers' method: Understanding the roles of the intercalator, oxidant, and graphite particle size, *Ceram. Int.* 46 (2020) 2392–2402. <https://doi.org/10.1016/j.ceramint.2019.09.231>.
- [15] R. Muzyka, M. Kwoka, Ł. Smędowski, N. Díez, G. Gryglewicz, Oxidation of graphite by different modified Hummers methods, *New Carbon Mater.* 32 (2017) 15–20. [https://doi.org/10.1016/S1872-5805\(17\)60102-1](https://doi.org/10.1016/S1872-5805(17)60102-1).
- [16] N. Yadav, B. Lochab, A comparative study of graphene oxide: Hummers, intermediate and improved method, *FlatChem.* 13 (2019) 40–49. <https://doi.org/10.1016/j.flatc.2019.02.001>.
- [17] V. Agarwal, P.B. Zetterlund, Strategies for reduction of graphene oxide – A comprehensive review, *Chem. Eng. J.* 405 (2021) 127018. <https://doi.org/10.1016/j.cej.2020.127018>.
- [18] A.L.T. Zheng, T. Phromsatiit, S. Boonyuen, Y. Andou, Synthesis of silver nanoparticles /porphyrin/reduced graphene oxide hydrogel as dye adsorbent for wastewater treatment, *FlatChem.* (2020) 100174. <https://doi.org/10.1016/j.flatc.2020.100174>.
- [19] A.L.T. Zheng, S. Boonyuen, T. Ohno, Y. Andou, Hydrothermally Reduced Graphene Hydrogel Intercalated with Divalent Ions for Dye Adsorption Studies, *Processes.* 9 (2021) 169. <https://doi.org/10.3390/pr9010169>.
- [20] I. Ibrahim, T. Tsubota, M.A. Hassan, Y. Andou, Surface Functionalization of Biochar from Oil Palm Empty Fruit Bunch through Hydrothermal Process, *Processes.* 9 (2021) 149. <https://doi.org/10.3390/pr9010149>.

- [21] M. Ahn, R. Liu, C. Lee, W. Lee, Designing Carbon/Oxygen Ratios of Graphene Oxide Membranes for Proton Exchange Membrane Fuel Cells, *J. Nanomater.* 2019 (2019) 1–9. <https://doi.org/10.1155/2019/6464713>.
- [22] M.P. Araújo, O.S.G.P. Soares, A.J.S. Fernandes, M.F.R. Pereira, C. Freire, Tuning the surface chemistry of graphene flakes: new strategies for selective oxidation, *RSC Adv.* 7 (2017) 14290–14301. <https://doi.org/10.1039/C6RA28868E>.
- [23] L. Liu, J. Zhang, J. Zhao, F. Liu, Mechanical properties of graphene oxides, *Nanoscale.* 4 (2012) 5910. <https://doi.org/10.1039/c2nr31164j>.
- [24] C. Fang, J. Zhang, X. Chen, G.J. Weng, Calculating the Electrical Conductivity of Graphene Nanoplatelet Polymer Composites by a Monte Carlo Method, *Nanomaterials.* 10 (2020) 1129. <https://doi.org/10.3390/nano10061129>.
- [25] Y. Wang, Y. Chen, S.D. Lacey, L. Xu, H. Xie, T. Li, V.A. Danner, L. Hu, Reduced graphene oxide film with record-high conductivity and mobility, *Mater. Today.* 21 (2018) 186–192. <https://doi.org/10.1016/j.mattod.2017.10.008>.
- [26] Y. Zeng, T. Li, Y. Yao, T. Li, L. Hu, A. Marconnet, Thermally Conductive Reduced Graphene Oxide Thin Films for Extreme Temperature Sensors, *Adv. Funct. Mater.* (2019) 1901388. <https://doi.org/10.1002/adfm.201901388>.
- [27] X. Mu, X. Wu, T. Zhang, D.B. Go, T. Luo, Thermal Transport in Graphene Oxide – From Ballistic Extreme to Amorphous Limit, *Sci. Rep.* 4 (2015) 3909. <https://doi.org/10.1038/srep03909>.
- [28] J. Chen, L. Li, Thermal Conductivity of Graphene Oxide: A Molecular Dynamics Study, *JETP Lett.* 112 (2020) 117–121. <https://doi.org/10.1134/S0021364020140015>.
- [29] A. Radoń, P. Włodarczyk, D. Łukowiec, Structure, temperature and frequency dependent electrical conductivity of oxidized and reduced electrochemically exfoliated graphite, *Phys. E Low-Dimensional Syst. Nanostructures.* 99 (2018) 82–90. <https://doi.org/10.1016/j.physe.2018.01.025>.
- [30] N. Díez, A. Tiwak, S. Gryglewicz, B. Grzyb, G. Gryglewicz, Enhanced reduction of graphene oxide by high-pressure hydrothermal treatment, *RSC Adv.* 5 (2015) 81831–81837. <https://doi.org/10.1039/c5ra14461b>.
- [31] K. Hu, X. Xie, T. Szkopek, M. Cerruti, Understanding hydrothermally reduced graphene oxide hydrogels: from reaction products to hydrogel properties, *Chem. Mater.* 28 (2016) 1756–1768. <https://doi.org/10.1021/acs.chemmater.5b04713>.
- [32] K. Hu, X. Xie, M. Cerruti, T. Szkopek, Controlling the shell formation in hydrothermally reduced graphene hydrogel, *Langmuir.* 31 (2015) 5545–5549. <https://doi.org/10.1021/acs.langmuir.5b00508>.
- [33] Y. Xu, K. Sheng, C. Li, G. Shi, Self-assembled graphene hydrogel, *ACS Nano.* 4 (2010) 4324–4330. <https://doi.org/10.1021/nn101187z>.
- [34] M. Nageeb, Adsorption Technique for the Removal of Organic Pollutants from Water and Wastewater, in: *Org. Pollut. - Monit. Risk Treat., InTech*, 2013. <https://doi.org/10.5772/54048>.
- [35] Z. Chang, Y. Chen, S. Tang, J. Yang, Y. Chen, S. Chen, P. Li, Z. Yang, Construction of chitosan/polyacrylate/graphene oxide composite physical hydrogel by semi-dissolution/acidification/sol-gel transition method and its simultaneous cationic and anionic dye adsorption properties, *Carbohydr. Polym.* 229 (2020) 115431. <https://doi.org/10.1016/j.carbpol.2019.115431>.
- [36] M. Belhachemi, F. Addoun, Comparative adsorption isotherms and modeling of methylene blue onto activated carbons, *Appl. Water Sci.* 1 (2011) 111–117. <https://doi.org/10.1007/s13201-011-0014-1>.
- [37] A. Nickheslat, M.M. Amin, H. Izanloo, A. Fatehizadeh, S.M. Mousavi, Phenol Photocatalytic Degradation by Advanced Oxidation Process under Ultraviolet Radiation Using Titanium Dioxide, *J. Environ. Public Health.* 2013 (2013) 1–9. <https://doi.org/10.1155/2013/815310>.
- [38] S. Ahmed, M.G. Rasul, W.N. Martens, R. Brown, M.A. Hashib, Heterogeneous photocatalytic degradation of phenols in wastewater: A review on current status and developments, *Desalination.* 261 (2010) 3–18. <https://doi.org/10.1016/j.desal.2010.04.062>.
- [39] P. Chowdhury, S. Nag, A.K. Ray, Degradation of Phenolic Compounds Through UV and Visible-Light-Driven Photocatalysis: Technical and Economic Aspects, in: *Phenolic Compd. - Nat. Sources, Importance Appl., InTech*, 2017. <https://doi.org/10.5772/66134>.
- [40] H. Anwer, A. Mahmood, J. Lee, K. Kim, J. Park, A.C.K. Yip, Photocatalysts for degradation of dyes in industrial effluents: Opportunities and challenges, *Nano Res.* 12 (2019) 955–972.
- [41] P.V.L. Reddy, K. Kim, B. Kavitha, V. Kumar, N. Raza, S. Kalagara, Photocatalytic degradation of

- bisphenol A in aqueous media: a review, *J. Environ. Manage.* 213 (2018) 189–205. <https://doi.org/10.1016/j.jenvman.2018.02.059>.
- [42] G.Z. Kyzas, M. Kostoglou, Green adsorbents for wastewaters: A critical review, *Materials (Basel)*. 7 (2014) 333–364. <https://doi.org/10.3390/ma7010333>.
- [43] A. Rezaei, M.R. Rezaei, M.H. Sayadi, 3D network structure graphene hydrogel-Fe₃O₄@SnO₂/Ag via an adsorption/photocatalysis synergy for removal of 2,4 dichlorophenol, *J. Taiwan Inst. Chem. Eng.* (2021). <https://doi.org/10.1016/j.jtice.2021.03.048>.
- [44] J. Hu, P. Zhang, J. Cui, W. An, L. Liu, Y. Liang, Q. Yang, H. Yang, W. Cui, High-efficiency removal of phenol and coking wastewater via photocatalysis-Fenton synergy over a Fe-g-C₃N₄ graphene hydrogel 3D structure, *J. Ind. Eng. Chem.* 84 (2020) 305–314. <https://doi.org/10.1016/j.jiec.2020.01.012>.
- [45] C. Mu, Y. Zhang, W. Cui, Y. Liang, Y. Zhu, Removal of bisphenol A over a separation free 3D Ag₃PO₄-graphene hydrogel via an adsorption-photocatalysis synergy, *Appl. Catal. B Environ.* 212 (2017) 41–49. <https://doi.org/10.1016/j.apcatb.2017.04.018>.
- [46] T. Xiong, Y. Ye, B. Luo, L. Shen, D. Wang, M. Fan, Z. Gong, Facile fabrication of 3D TiO₂-graphene aerogel composite with enhanced adsorption and solar light-driven photocatalytic activity, *Ceram. Int.* 47 (2021) 14290–14300. <https://doi.org/10.1016/j.ceramint.2021.02.011>.
- [47] W. Yang, S. Tang, Z. Wei, X. Chen, C. Ma, J. Duan, R. Tan, Separate-free BiPO₄/graphene aerogel with 3D network structure for efficient photocatalytic mineralization by adsorption enrichment and photocatalytic degradation, *Chem. Eng. J.* (2021) 129720. <https://doi.org/10.1016/j.cej.2021.129720>.
- [48] W. Yang, Y. Wang, Enhanced electron and mass transfer flow-through cell with C₃N₄-MoS₂ supported on three-dimensional graphene photoanode for the removal of antibiotic and antibacterial potencies in ampicillin wastewater, *Appl. Catal. B Environ.* 282 (2021) 119574. <https://doi.org/10.1016/j.apcatb.2020.119574>.
- [49] J. Yin, D. Gao, X. Zhu, X. Liu, H. Li, One-pot synthesis of 3D porous Bi₇O₉I₃/N-doped graphene aerogel with enhanced photocatalytic activity for organic dye degradation in wastewater, *Ceram. Int.* (2021). <https://doi.org/10.1016/j.ceramint.2021.03.293>.
- [50] S. Banumathi, J. Uma, A. Ravi, B. Balraj, C. Siva, P. Ilanchezhian, G. Mohan Kumar, Rapid sun-light driven photocatalytic functions of 3D rGO/ZnO/Ag heterostructures via improved charge transfer kinetics, *J. Mater. Res. Technol.* 10 (2021) 1301–1309. <https://doi.org/10.1016/j.jmrt.2020.12.062>.
- [51] H.M. Hegab, A. Elmekawy, L. Zou, D. Mulcahy, C.P. Saint, M. Ginic-Markovic, The controversial antibacterial activity of graphene-based materials, *Carbon N. Y.* 105 (2016) 362–376. <https://doi.org/10.1016/j.carbon.2016.04.046>.
- [52] X. Huang, Z. Yin, S. Wu, X. Qi, Q. He, Q. Zhang, Q. Yan, F. Boey, H. Zhang, Graphene-based materials: Synthesis, characterization, properties, and applications, *Small*. 7 (2011) 1876–1902. <https://doi.org/10.1002/sml.201002009>.
- [53] D. Zhao, L. Yu, D. Liu, Ultralight graphene/carbon nanotubes aerogels with compressibility and oil absorption properties, *Materials (Basel)*. 11 (2018) 1–11. <https://doi.org/10.3390/ma11040641>.
- [54] Z. Sui, X. Zhang, Y. Lei, Y. Luo, Easy and green synthesis of reduced graphite oxide-based hydrogels, *Carbon N. Y.* 49 (2011) 4314–4321. <https://doi.org/10.1016/j.carbon.2011.06.006>.
- [55] S. Pei, H.-M. Cheng, The reduction of graphene oxide, *Carbon N. Y.* 50 (2012) 3210–3228. <https://doi.org/10.1016/j.carbon.2011.11.010>.
- [56] G. Gorgolis, C. Galiotis, Graphene aerogels: A review, *2D Mater.* 4 (2017) 1–22. <https://doi.org/10.1088/2053-1583/aa7883>.
- [57] M. Bai, W. Wu, L. Liu, J. Chen, X. Ma, Y. Meng, NaCl and oxalic acid-assisted solvothermal exfoliation of edge-oxidized graphite to produce organic graphene dispersion for transparent conductive film application, *J. Nanoparticle Res.* 21 (2019) 145. <https://doi.org/10.1007/s11051-019-4574-6>.
- [58] A. Kumar, M. Khandelwal, A novel synthesis of ultra thin graphene sheets for energy storage applications using malonic acid as a reducing agent, *J. Mater. Chem. A*. 2 (2014) 20345–20357. <https://doi.org/10.1039/b000000x>.
- [59] B. Amanulla, S. Palanisamy, S.-M. Chen, T.-W. Chiu, V. Velusamy, J.M. Hall, T.-W. Chen, S.K. Ramaraj, Selective Colorimetric Detection of Nitrite in Water using Chitosan Stabilized Gold Nanoparticles Decorated Reduced Graphene oxide, *Sci. Rep.* 7 (2017) 14182.

- <https://doi.org/10.1038/s41598-017-14584-6>.
- [60] F.S. Al-Hazmi, G.H. Al-Harbi, G.W. Beall, A.A. Al-Ghamdi, A.Y. Obaid, W.E. Mahmoud, One pot synthesis of graphene based on microwave assisted solvothermal technique, *Synth. Met.* 200 (2015) 54–57. <https://doi.org/10.1016/j.synthmet.2014.12.028>.
- [61] Y. Cheng, S. Zhou, P. Hu, G. Zhao, Y. Li, X. Zhang, W. Han, Enhanced mechanical, thermal, and electric properties of graphene aerogels via supercritical ethanol drying and high-temperature thermal reduction, *Sci. Rep.* 7 (2017) 1–11. <https://doi.org/10.1038/s41598-017-01601-x>.
- [62] M.A. Worsley, P.J. Pauzauskie, T.Y. Olson, J. Biener, J.H. Satcher, T.F. Baumann, Synthesis of graphene aerogel with high electrical conductivity, *J. Am. Chem. Soc.* 132 (2010) 14067–14069. <https://doi.org/10.1021/ja1072299>.
- [63] K.K.H. De Silva, H.H. Huang, M. Yoshimura, Progress of reduction of graphene oxide by ascorbic acid, *Appl. Surf. Sci.* 447 (2018) 338–346. <https://doi.org/10.1016/j.apsusc.2018.03.243>.
- [64] A.L.T. Zheng, T. Phromsatit, S. Boonyuen, Y. Andou, Synthesis of silver nanoparticles /porphyrin/reduced graphene oxide hydrogel as dye adsorbent for wastewater treatment, *FlatChem.* (2020) 100174. <https://doi.org/10.1016/j.flatc.2020.100174>.
- [65] B. Gupta, N. Kumar, K. Panda, V. Kanan, S. Joshi, I. Visoly-Fisher, Role of oxygen functional groups in reduced graphene oxide for lubrication, *Sci. Rep.* 7 (2017) 45030. <https://doi.org/10.1038/srep45030>.
- [66] T. Jiao, H. Guo, Q. Zhang, Q. Peng, Y. Tang, X. Yan, B. Li, Reduced graphene oxide-based silver nanoparticle-containing composite hydrogel as highly efficient dye catalysts for wastewater treatment, *Sci. Rep.* 5 (2015) 11873. <https://doi.org/10.1038/srep11873>.
- [67] V. Loryuenyong, K. Totepvimarn, P. Eimburanaprat, W. Boonchompoo, A. Buasri, Preparation and characterization of reduced graphene oxide sheets via water-based exfoliation and reduction methods, *Adv. Mater. Sci. Eng.* 2013 (2013) 1–5. <https://doi.org/10.1155/2013/923403>.
- [68] X. Xia, X. Zhang, S. Yi, H. Chen, H. Liu, Supercapacitance properties of porous carbon from chemical blending of phenolic resin and aliphatic dicarboxylic acids, *J. Mater. Res.* 31 (2016) 1665–1673. <https://doi.org/10.1557/jmr.2016.183>.
- [69] M.C. Hsiao, S.H. Liao, M.Y. Yen, P.I. Liu, N.W. Pu, C.A. Wang, C.C.M. Ma, Preparation of covalently functionalized graphene using residual oxygen-containing functional groups, *ACS Appl. Mater. Interfaces.* 2 (2010) 3092–3099. <https://doi.org/10.1021/am100597d>.
- [70] H.H. Huang, K.K.H. De Silva, G.R.A. Kumara, M. Yoshimura, Structural evolution of hydrothermally derived reduced graphene oxide, *Sci. Rep.* 8 (2018) 2–10. <https://doi.org/10.1038/s41598-018-25194-1>.
- [71] D. Hou, K. Li, R. Ma, Q. Liu, Influence of order degree of coaly graphite on its structure change during preparation of graphene oxide, *J. Mater.* 6 (2020) 628–641. <https://doi.org/10.1016/j.jmat.2020.04.009>.
- [72] R. Sharma, N. Chadha, P. Saini, Determination of defect density, crystallite size and number of graphene layers in graphene analogues using X-ray diffraction and Raman spectroscopy, *Indian J. Pure Appl. Phys.* 55 (2017) 625–629.
- [73] S. Chowdhury, R. Balasubramanian, Holey graphene frameworks for highly selective post-combustion carbon capture, *Sci. Rep.* 6 (2016) 1–10. <https://doi.org/10.1038/srep21537>.
- [74] B.D. Ossonon, D. Bélanger, Synthesis and characterization of sulfophenyl-functionalized reduced graphene oxide sheets, *RSC Adv.* 7 (2017) 27224–27234. <https://doi.org/10.1039/c6ra28311j>.
- [75] V. Georgakilas, J.N. Tiwari, K.C. Kemp, J.A. Perman, A.B. Bourlinos, K.S. Kim, R. Zboril, Noncovalent Functionalization of Graphene and Graphene Oxide for Energy Materials, Biosensing, Catalytic, and Biomedical Applications, *Chem. Rev.* 116 (2016) 5464–5519. <https://doi.org/10.1021/acs.chemrev.5b00620>.
- [76] Y. Hu, X. Xie, C. Sun, J. Kou, Assembling reduced graphene oxide hydrogel with controlled porous structures using cationic and anionic surfactants, *Nanotechnology.* 30 (2019) 505602. <https://doi.org/10.1088/1361-6528/ab432d>.
- [77] M.Y. Song, Y.S. Yun, N.R. Kim, H.J. Jin, Dispersion stability of chemically reduced graphene oxide nanoribbons in organic solvents, *RSC Adv.* 6 (2016) 19389–19393. <https://doi.org/10.1039/c5ra23801c>.
- [78] D. Konios, M.M. Stylianakis, E. Stratakis, E. Kymakis, Dispersion behaviour of graphene oxide and reduced graphene oxide, *J. Colloid Interface Sci.* 430 (2014) 108–112. <https://doi.org/10.1016/j.jcis.2014.05.033>.

- [79] Y. Luo, S. Jiang, Q. Xiao, C. Chen, B. Li, Highly reusable and superhydrophobic spongy graphene aerogels for efficient oil/water separation, *Sci. Rep.* 7 (2017) 1–10. <https://doi.org/10.1038/s41598-017-07583-0>.
- [80] M.M. Gudarzi, Colloidal Stability of Graphene Oxide: Aggregation in Two Dimensions, *Langmuir*. 32 (2016) 5058–5068. <https://doi.org/10.1021/acs.langmuir.6b01012>.
- [81] B. Nazari, Z. Ranjbar, R.R. Hashjin, A. Rezvani Moghaddam, G. Momen, B. Ranjbar, Dispersing graphene in aqueous media: Investigating the effect of different surfactants, *Colloids Surfaces A Physicochem. Eng. Asp.* 582 (2019) 123870. <https://doi.org/10.1016/j.colsurfa.2019.123870>.
- [82] J.-P. Tessonnier, M.A. Barteau, Dispersion of Alkyl-Chain-Functionalized Reduced Graphene Oxide Sheets in Nonpolar Solvents, *Langmuir*. 28 (2012) 6691–6697. <https://doi.org/10.1021/la2051614>.
- [83] R. Fuentes Pineda, J. Troughton, M. Planells, I. Sanchez-Molina Santos, F. Muhith, G.S. Nichol, S. Haque, T. Watson, N. Robertson, Effect of alkyl chain length on the properties of triphenylamine-based hole transport materials and their performance in perovskite solar cells, *Phys. Chem. Chem. Phys.* 20 (2018) 1252–1260. <https://doi.org/10.1039/c7cp07682g>.
- [84] R. Mohd Zawawi, A.L.T. Zheng, Zinc oxide/Vancomycin-based Electrochemical Chiral Sensor for the Recognition of Penicillamine Enantiomers, *Int. J. Electrochem. Sci.* (2020) 3255–3267. <https://doi.org/10.20964/2020.04.39>.
- [85] M. Berradi, R. Hsissou, M. Khudhair, M. Assouag, O. Cherkaoui, A. El Bachiri, A. El Harfi, Textile finishing dyes and their impact on aquatic environs, *Heliyon*. 5 (2019) e02711. <https://doi.org/10.1016/j.heliyon.2019.e02711>.
- [86] D.A. Yaseen, M. Scholz, Textile dye wastewater characteristics and constituents of synthetic effluents: a critical review, *Int. J. Environ. Sci. Technol.* 16 (2019) 1193–1226. <https://doi.org/10.1007/s13762-018-2130-z>.
- [87] B. Lellis, C.Z. Fávaro-Polonio, J.A. Pamphile, J.C. Polonio, Effects of textile dyes on health and the environment and bioremediation potential of living organisms, *Biotechnol. Res. Innov.* 3 (2019) 275–290. <https://doi.org/10.1016/j.biori.2019.09.001>.
- [88] Z. Wang, M. Xue, K. Huang, Z. Liu, Textile Dyeing Wastewater Treatment, in: *Adv. Treat. Text. Effl., InTech*, 2011. <https://doi.org/10.5772/22670>.
- [89] G. Crini, E. Lichtfouse, L.D. Wilson, N. Morin-Crini, Conventional and non-conventional adsorbents for wastewater treatment, *Environ. Chem. Lett.* 17 (2019) 195–213. <https://doi.org/10.1007/s10311-018-0786-8>.
- [90] V.K. Gupta, Suhas, Application of low-cost adsorbents for dye removal – A review, *J. Environ. Manage.* 90 (2009) 2313–2342. <https://doi.org/10.1016/j.jenvman.2008.11.017>.
- [91] S. De Gisi, G. Lofrano, M. Grassi, M. Notarnicola, Characteristics and adsorption capacities of low-cost sorbents for wastewater treatment: A review, *Sustain. Mater. Technol.* 9 (2016) 10–40. <https://doi.org/10.1016/j.susmat.2016.06.002>.
- [92] Z. Bano, S.A. Mazari, R.M.Y. Saeed, M.A. Majeed, M. Xia, A.Q. Memon, R. Abro, F. Wang, Water decontamination by 3D graphene based materials: A review, *J. Water Process Eng.* 36 (2020) 101404. <https://doi.org/10.1016/j.jwpe.2020.101404>.
- [93] N. Baig, Ihsanullah, M. Sajid, T.A. Saleh, Graphene-based adsorbents for the removal of toxic organic pollutants: A review, *J. Environ. Manage.* 244 (2019) 370–382. <https://doi.org/10.1016/j.jenvman.2019.05.047>.
- [94] G.Z. Kyzas, E.A. Deliyanni, D.N. Bikiaris, A.C. Mitropoulos, Graphene composites as dye adsorbents: Review, *Chem. Eng. Res. Des.* 129 (2018) 75–88. <https://doi.org/10.1016/j.cherd.2017.11.006>.
- [95] I. Khurana, A. Saxena, Bharti, J.M. Khurana, P.K. Rai, Removal of Dyes Using Graphene-Based Composites: a Review, *Water, Air, Soil Pollut.* 228 (2017) 180. <https://doi.org/10.1007/s11270-017-3361-1>.
- [96] B.Y.Z. Hiew, L.Y. Lee, X.J. Lee, S. Thangalazhy-Gopakumar, S. Gan, S.S. Lim, G.-T. Pan, T.C.-K. Yang, W.S. Chiu, P.S. Khiew, Review on synthesis of 3D graphene-based configurations and their adsorption performance for hazardous water pollutants, *Process Saf. Environ. Prot.* 116 (2018) 262–286. <https://doi.org/10.1016/j.psep.2018.02.010>.
- [97] M. Allen, Honeycomb carbon - A study of graphene, *J. Am. Chem. Soc.* (2009) 184. <https://doi.org/10.1021/cr900070d>.
- [98] U.K. Sur, Graphene: A Rising Star on the Horizon of Materials Science, *Int. J. Electrochem.* 2012 (2012) 1–12. <https://doi.org/10.1155/2012/237689>.

- [99] X.J. Lee, B.Y.Z. Hiew, K.C. Lai, L.Y. Lee, S. Gan, S. Thangalazhy-Gopakumar, S. Rigby, Review on graphene and its derivatives: Synthesis methods and potential industrial implementation, *J. Taiwan Inst. Chem. Eng.* 98 (2019) 163–180. <https://doi.org/10.1016/j.jtice.2018.10.028>.
- [100] J.C. Meyer, A.K. Geim, M.I. Katsnelson, K.S. Novoselov, T.J. Booth, S. Roth, The structure of suspended graphene sheets, *Nature*. 446 (2007) 60–63. <https://doi.org/10.1038/nature05545>.
- [101] F. Zhang, Y.-H. Li, J.-Y. Li, Z.-R. Tang, Y.-J. Xu, 3D graphene-based gel photocatalysts for environmental pollutants degradation, *Environ. Pollut.* 253 (2019) 365–376. <https://doi.org/10.1016/j.envpol.2019.06.089>.
- [102] K. Hu, X. Xie, M. Cerruti, T. Szkopek, Controlling the shell formation in hydrothermally reduced graphene hydrogel, *Langmuir*. 31 (2015) 5545–5549. <https://doi.org/10.1021/acs.langmuir.5b00508>.
- [103] F. Liu, S. Chung, G. Oh, T.S. Seo, Three-Dimensional Graphene Oxide Nanostructure for Fast and Efficient Water-Soluble Dye Removal, *ACS Appl. Mater. Interfaces*. 4 (2012) 922–927. <https://doi.org/10.1021/am201590z>.
- [104] K.C. Lai, L.Y. Lee, B.Y.Z. Hiew, S. Thangalazhy-Gopakumar, S. Gan, Environmental application of three-dimensional graphene materials as adsorbents for dyes and heavy metals: Review on ice-templating method and adsorption mechanisms, *J. Environ. Sci.* 79 (2019) 174–199. <https://doi.org/10.1016/j.jes.2018.11.023>.
- [105] J. Yi, G. Choe, J. Park, J.Y. Lee, Graphene oxide-incorporated hydrogels for biomedical applications, *Polym. J.* 52 (2020) 823–837. <https://doi.org/10.1038/s41428-020-0350-9>.
- [106] H. Lu, S. Zhang, L. Guo, W. Li, Applications of graphene-based composite hydrogels: a review, *RSC Adv.* 7 (2017) 51008–51020. <https://doi.org/10.1039/C7RA09634H>.
- [107] T.J.M. Fraga, M.N. Carvalho, M.G. Ghislandi, M.A. da Motta Sobrinho, Functionalized graphene-based materials as innovative adsorbents of organic pollutants: a concise overview, *Brazilian J. Chem. Eng.* 36 (2019) 1–31. <https://doi.org/10.1590/0104-6632.20190361s20180283>.
- [108] Q. Peng, L. Zhang, X. Yan, Q. Zhang, J. Zhou, T. Jiao, H. Zhao, Preparation and adsorption capacity evaluation of graphene oxide-chitosan composite hydrogels, *Sci. China Mater.* 58 (2015) 811–818. <https://doi.org/10.1007/s40843-015-0090-x>.
- [109] C.Y. Tang, P. Yu, L.S. Tang, Q.Y. Wang, R.Y. Bao, Z.Y. Liu, M.B. Yang, W. Yang, Tannic acid functionalized graphene hydrogel for organic dye adsorption, *Ecotoxicol. Environ. Saf.* 165 (2018) 299–306. <https://doi.org/10.1016/j.ecoenv.2018.09.009>.
- [110] H. Guo, T. Jiao, Q. Zhang, W. Guo, Q. Peng, X. Yan, Preparation of Graphene Oxide-Based Hydrogels as Efficient Dye Adsorbents for Wastewater Treatment, *Nanoscale Res. Lett.* 10 (2015) 0–9. <https://doi.org/10.1186/s11671-015-0931-2>.
- [111] H. Mittal, A. Al Aili, P.P. Morajkar, S.M. Alhassan, Graphene oxide crosslinked hydrogel nanocomposites of xanthan gum for the adsorption of crystal violet dye, *J. Mol. Liq.* 323 (2021) 115034. <https://doi.org/10.1016/j.molliq.2020.115034>.
- [112] N. Sarkar, G. Sahoo, S.K. Swain, Graphene quantum dot decorated magnetic graphene oxide filled polyvinyl alcohol hybrid hydrogel for removal of dye pollutants, *J. Mol. Liq.* 302 (2020) 112591. <https://doi.org/10.1016/j.molliq.2020.112591>.
- [113] J. Xu, P. Du, W. Bi, G. Yao, S. Li, H. Liu, Graphene oxide aerogels co-functionalized with polydopamine and polyethylenimine for the adsorption of anionic dyes and organic solvents, *Chem. Eng. Res. Des.* 154 (2020) 192–202. <https://doi.org/10.1016/j.cherd.2019.12.014>.
- [114] S. Ghosh, P. Kar, N. Bhandary, S. Basu, T. Maiyalagan, S. Sardar, S.K. Pal, Reduced graphene oxide supported hierarchical flower like manganese oxide as efficient electrocatalysts toward reduction and evolution of oxygen, *Int. J. Hydrogen Energy*. 42 (2017) 4111–4122. <https://doi.org/10.1016/j.ijhydene.2016.12.008>.
- [115] T. Jiao, Y. Liu, Y. Wu, Q. Zhang, X. Yan, F. Gao, A.J.P. Bauer, J. Liu, T. Zeng, B. Li, Facile and Scalable Preparation of Graphene Oxide-Based Magnetic Hybrids for Fast and Highly Efficient Removal of Organic Dyes, *Sci. Rep.* 5 (2015). <https://doi.org/10.1038/srep12451>.
- [116] N.W. Pu, C.Y. Chen, H.X. Qiu, Y.M. Liu, C.H. Song, M.H. Lin, M. Der Ger, Hydrothermal synthesis of N-doped graphene/Fe₂O₃ nanocomposite for supercapacitors, *Int. J. Electrochem. Sci.* 13 (2018) 6812–6823. <https://doi.org/10.20964/2018.07.16>.
- [117] Y.H. Kwon, S. Kumar, J. Bae, Y. Seo, CVD-graphene for low equivalent series resistance in rGO/CVD-graphene/Ni-based supercapacitors, *Nanotechnology*. 29 (2018). <https://doi.org/10.1088/1361-6528/aab236>.

- [118] A.N. Fouda, A. Salem, F. El-Tantawy, H. Salem, E.S.M. Duraia, Hydrothermal synthesis of high quality graphene nanosheets anchored by uniform and well distributed silicon nanoparticles, *Superlattices Microstruct.* 124 (2018) 240–247. <https://doi.org/10.1016/j.spmi.2018.08.025>.
- [119] X. Jiang, Y. Ma, J. Li, Q. Fan, W. Huang, Self-Assembly of Reduced Graphene Oxide into Three-Dimensional Architecture by Divalent Ion Linkage, *J. Phys. Chem. C.* 114 (2010) 22462–22465. <https://doi.org/10.1021/jp108081g>.
- [120] J. Fan, Z. Shi, M. Lian, H. Li, J. Yin, Mechanically strong graphene oxide/sodium alginate/polyacrylamide nanocomposite hydrogel with improved dye adsorption capacity, *J. Mater. Chem. A.* 1 (2013) 7433–7443. <https://doi.org/10.1039/c3ta10639j>.
- [121] D. Xiao, M. He, Y. Liu, L. Xiong, Q. Zhang, L. Wei, Strong alginate/reduced graphene oxide composite hydrogels with enhanced dye adsorption performance, *Polym. Bull.* (2020). <https://doi.org/10.1007/s00289-020-03105-7>.
- [122] T. E. Z. Ma, S. Yang, Y. Li, D. Ma, Z. Xing, Y. Li, Enhanced electrical conductivity of TiO₂/graphene: The role of introducing Ca²⁺, *J. Alloys Compd.* 827 (2020) 154280. <https://doi.org/10.1016/j.jallcom.2020.154280>.
- [123] Á. Serrano-Aroca, S. Deb, Synthesis of irregular graphene oxide tubes using green chemistry and their potential use as reinforcement materials for biomedical applications, *PLoS One.* 12 (2017) 1–14. <https://doi.org/10.1371/journal.pone.0185235>.
- [124] S. Park, K.S. Lee, G. Bozoklu, W. Cai, S.B.T. Nguyen, R.S. Ruoff, Graphene oxide papers modified by divalent ions - Enhancing mechanical properties via chemical cross-linking, *ACS Nano.* 2 (2008) 572–578. <https://doi.org/10.1021/nn700349a>.
- [125] T. Zhang, G.-Y. Zhu, C.-H. Yu, Y. Xie, M.-Y. Xia, B.-Y. Lu, X. Fei, Q. Peng, The UV absorption of graphene oxide is size-dependent: possible calibration pitfalls, *Microchim. Acta.* 186 (2019) 207. <https://doi.org/10.1007/s00604-019-3329-5>.
- [126] P. Saha, D.K. Pyne, S. Ghosh, S. Banerjee, S. Das, S. Ghosh, P. Dutta, A. Halder, Effect of an anionic surfactant (SDS) on the photoluminescence of graphene oxide (GO) in acidic and alkaline medium, *RSC Adv.* 8 (2018) 584–595. <https://doi.org/10.1039/C7RA12024A>.
- [127] A. Mautner, T. Kobkeathawin, F. Mayer, C. Plessl, S. Gorgieva, V. Kokol, A. Bismarck, Rapid Water Softening with TEMPO-Oxidized/Phosphorylated Nanopapers, *Nanomaterials.* 9 (2019) 136. <https://doi.org/10.3390/nano9020136>.
- [128] G. Feng, C.-W. Liu, Z. Zeng, G.-L. Hou, H.-G. Xu, W.-J. Zheng, Initial hydration processes of magnesium chloride: size-selected anion photoelectron spectroscopy and ab initio calculations, *Phys. Chem. Chem. Phys.* 19 (2017) 15562–15569. <https://doi.org/10.1039/C7CP02965A>.
- [129] R.J. Hunter, Electrokinetics and the zeta potential, in: *Found. Colloid Sci.* 2, 2001: pp. 376–377.
- [130] R.L.D. Whitby, Chemical control of graphene architecture: Tailoring shape and properties, *ACS Nano.* 8 (2014) 9733–9754. <https://doi.org/10.1021/nn504544h>.
- [131] M. Jin, N. Jiao, C.X. Zhang, H.P. Xiao, K.W. Zhang, L.Z. Sun, Reduction mechanism of hydroxyl group from graphene oxide with and without –NH₂ agent, *Phys. B Condens. Matter.* 477 (2015) 70–74. <https://doi.org/10.1016/j.physb.2015.08.021>.
- [132] Z. Zhao-Karger, M. Fichtner, Beyond Intercalation Chemistry for Rechargeable Mg Batteries: A Short Review and Perspective, *Front. Chem.* 6 (2019). <https://doi.org/10.3389/fchem.2018.00656>.
- [133] M. Ikram, A. Raza, M. Imran, A. Ul-Hamid, A. Shahbaz, S. Ali, Hydrothermal synthesis of silver decorated reduced graphene oxide (rGO) nanoflakes with effective photocatalytic activity for wastewater treatment, *Nanoscale Res. Lett.* 15 (2020) 0–10. <https://doi.org/10.1186/s11671-020-03323-y>.
- [134] G. Bharath, S. Anwer, R. V. Mangalaraja, E. Alhseinat, F. Banat, N. Ponpandian, Sunlight-Induced photochemical synthesis of Au nanodots on α-Fe₂O₃@Reduced graphene oxide nanocomposite and their enhanced heterogeneous catalytic properties, *Sci. Rep.* 8 (2018) 1–14. <https://doi.org/10.1038/s41598-018-24066-y>.
- [135] T. E. Z. Ma, S. Yang, Y. Li, D. Ma, Z. Xing, Y. Li, Enhanced electrical conductivity of TiO₂/graphene: The role of introducing Ca²⁺, *J. Alloys Compd.* 827 (2020) 154280. <https://doi.org/10.1016/j.jallcom.2020.154280>.
- [136] S. Wang, Y. Dong, C. He, Y. Gao, N. Jia, Z. Chen, W. Song, The role of sp²/sp³ hybrid carbon regulation in the nonlinear optical properties of graphene oxide materials, *RSC Adv.* 7 (2017) 53643–53652. <https://doi.org/10.1039/c7ra10505c>.
- [137] W. Peng, G. Han, Y. Huang, Y. Cao, S. Song, Insight the effect of crystallinity of natural graphite on

- the electrochemical performance of reduced graphene oxide, *Results Phys.* 11 (2018) 131–137. <https://doi.org/10.1016/j.rinp.2018.08.055>.
- [138] P. Cui, J. Lee, E. Hwang, H. Lee, One-pot reduction of graphene oxide at subzero temperatures, *Chem. Commun.* 47 (2011) 12370–12372. <https://doi.org/10.1039/c1cc15569e>.
- [139] M. Thommes, K. Kaneko, A. V. Neimark, J.P. Olivier, F. Rodriguez-Reinoso, J. Rouquerol, K.S.W. Sing, Physisorption of gases, with special reference to the evaluation of surface area and pore size distribution (IUPAC Technical Report), *Pure Appl. Chem.* 87 (2015) 1051–1069. <https://doi.org/10.1515/pac-2014-1117>.
- [140] F. Guo, M. Creighton, Y. Chen, R. Hurt, I. Külaots, Porous structures in stacked, crumpled and pillared graphene-based 3D materials, *Carbon N. Y.* 66 (2014) 476–484. <https://doi.org/10.1016/j.carbon.2013.09.024>.
- [141] C. Wang, J. Zhou, F. Du, Synthesis of Highly Reduced Graphene Oxide for Supercapacitor, *J. Nanomater.* 2016 (2016) 1–7. <https://doi.org/10.1155/2016/4840301>.
- [142] S. Gadipelli, Z.X. Guo, Graphene-based materials: Synthesis and gas sorption, storage and separation, *Prog. Mater. Sci.* 69 (2015) 1–60. <https://doi.org/10.1016/j.pmatsci.2014.10.004>.
- [143] H. Ren, X. Shi, J. Zhu, Y. Zhang, Y. Bi, L. Zhang, Facile synthesis of N-doped graphene aerogel and its application for organic solvent adsorption, *J. Mater. Sci.* 51 (2016) 6419–6427. <https://doi.org/10.1007/s10853-016-9939-y>.
- [144] H. Cheng, H. Xue, G. Zhao, C. Hong, X. Zhang, Preparation, characterization, and properties of graphene-based composite aerogels via in situ polymerization and three-dimensional self-assembly from graphene oxide solution, *RSC Adv.* 6 (2016) 78538–78547. <https://doi.org/10.1039/C6RA08823F>.
- [145] L. Ren, K.N. Hui, K.S. Hui, Y. Liu, X. Qi, J. Zhong, Y. Du, J. Yang, 3D hierarchical porous graphene aerogel with tunable meso-pores on graphene nanosheets for high-performance energy storage, *Sci. Rep.* 5 (2015) 14229. <https://doi.org/10.1038/srep14229>.
- [146] Y. Yang, S. Song, Z. Zhao, Graphene oxide (GO)/polyacrylamide (PAM) composite hydrogels as efficient cationic dye adsorbents, *Colloids Surfaces A Physicochem. Eng. Asp.* 513 (2017) 315–324. <https://doi.org/10.1016/j.colsurfa.2016.10.060>.
- [147] N. Baig, Ihsanullah, M. Sajid, T.A. Saleh, Graphene-based adsorbents for the removal of toxic organic pollutants: a review, *J. Environ. Manage.* 244 (2019) 370–382. <https://doi.org/10.1016/j.jenvman.2019.05.047>.
- [148] Y. Sun, F. Yu, C. Li, X. Dai, J. Ma, Nano -/ Micro - confined Water in Graphene Hydrogel as Superadsorbents for Water Purification, *Nano-Micro Lett.* (2020). <https://doi.org/10.1007/s40820-019-0336-3>.
- [149] F. Yu, Y. Sun, M. Yang, J. Ma, Adsorption mechanism and effect of moisture contents on ciprofloxacin removal by three-dimensional porous graphene hydrogel, *J. Hazard. Mater.* 374 (2019) 195–202. <https://doi.org/10.1016/j.jhazmat.2019.04.021>.
- [150] A. Özer, G. Dursun, Removal of methylene blue from aqueous solution by dehydrated wheat bran carbon, *J. Hazard. Mater.* 146 (2007) 262–269. <https://doi.org/10.1016/j.jhazmat.2006.12.016>.
- [151] D. Jiang, R. Deng, G. Li, G. Zheng, H. Guo, Constructing an ultra-adsorbent based on the porous organic molecules of noria for the highly efficient adsorption of cationic dyes, *RSC Adv.* 10 (2020) 6185–6191. <https://doi.org/10.1039/C9RA08490H>.
- [152] S. Thakur, O. Arotiba, Synthesis, characterization and adsorption studies of an acrylic acid-grafted sodium alginate-based TiO₂ hydrogel nanocomposite, *Adsorpt. Sci. Technol.* 36 (2018) 458–477. <https://doi.org/10.1177/0263617417700636>.
- [153] C. Cheng, Z. Liu, X. Li, B. Su, T. Zhou, C. Zhao, Graphene oxide interpenetrated polymeric composite hydrogels as highly effective adsorbents for water treatment, *RSC Adv.* 4 (2014) 42346–42357. <https://doi.org/10.1039/C4RA07114J>.
- [154] W. Rudzinski, W. Plazinski, Kinetics of Solute Adsorption at Solid/Solution Interfaces: On the Special Features of the Initial Adsorption Kinetics, *Langmuir.* 24 (2008) 6738–6744. <https://doi.org/10.1021/la800743a>.
- [155] A.R. Hernandez-Martínez, J.A. Lujan-Montelongo, C. Silva-Cuevas, J.D. Mota-Morales, M. Cortez-Valadez, Á. de J. Ruíz-Baltazar, M. Cruz, J. Herrera-Ordóñez, Swelling and methylene blue adsorption of poly(N,N-dimethylacrylamide-co-2-hydroxyethyl methacrylate) hydrogel, *React. Funct. Polym.* 122 (2018) 75–84. <https://doi.org/10.1016/j.reactfunctpolym.2017.11.008>.
- [156] R. Wang, X. Zhang, J. Zhu, J. Bai, L. Gao, S. Liu, T. Jiao, Facile preparation of self-assembled

- chitosan-based composite hydrogels with enhanced adsorption performances, *Colloids Surfaces A Physicochem. Eng. Asp.* 598 (2020) 124860. <https://doi.org/10.1016/j.colsurfa.2020.124860>.
- [157] R. Wang, Q. Yu, Y. He, J. Bai, T. Jiao, L. Zhang, Z. Bai, J. Zhou, Q. Peng, Self-assembled polyelectrolyte-based composite hydrogels with enhanced stretchable and adsorption performances, *J. Mol. Liq.* 294 (2019) 111576. <https://doi.org/10.1016/j.molliq.2019.111576>.
- [158] H. Dai, Y. Huang, H. Huang, Eco-friendly polyvinyl alcohol/carboxymethyl cellulose hydrogels reinforced with graphene oxide and bentonite for enhanced adsorption of methylene blue, *Carbohydr. Polym.* 185 (2018) 1–11. <https://doi.org/10.1016/j.carbpol.2017.12.073>.
- [159] C. Tang, P. Yu, L. Tang, Q. Wang, R. Bao, Z. Liu, Tannic acid functionalized graphene hydrogel for organic dye adsorption, *Ecotoxicol. Environ. Saf.* 165 (2018) 299–306. <https://doi.org/10.1016/j.ecoenv.2018.09.009>.
- [160] N. Sarkar, G. Sahoo, S.K. Swain, Nanoclay sandwiched reduced graphene oxide filled macroporous polyacrylamide-agar hybrid hydrogel as an adsorbent for dye decontamination, *Nano-Structures and Nano-Objects.* 23 (2020) 100507. <https://doi.org/10.1016/j.nanoso.2020.100507>.
- [161] K. Soleimani, A.D.D. Tehrani, M. Adeli, Bioconjugated graphene oxide hydrogel as an effective adsorbent for cationic dyes removal, *Ecotoxicol. Environ. Saf.* 147 (2018) 34–42. <https://doi.org/10.1016/j.ecoenv.2017.08.021>.
- [162] Y. Zhang, K. Li, J. Liao, Facile synthesis of reduced-graphene-oxide/rare-earth-metal-oxide aerogels as a highly efficient adsorbent for Rhodamine-B, *Appl. Surf. Sci.* 504 (2020) 144377. <https://doi.org/10.1016/j.apsusc.2019.144377>.
- [163] A.C. Pradhan, A. Paul, G.R. Rao, Sol-gel-cum-hydrothermal synthesis of mesoporous Co-Fe@Al₂O₃-MCM-41 for methylene blue remediation, *J. Chem. Sci.* 129 (2017) 381–395. <https://doi.org/10.1007/s12039-017-1230-5>.
- [164] H. Belhanafi, A. Bakhti, N. Benderdouche, Study of interactions between rhodamine B and a beidellite-rich clay fraction, *Clay Miner.* 55 (2020) 194–202. <https://doi.org/10.1180/clm.2020.25>.
- [165] O.S. Bayomie, H. Kandeel, T. Shoeib, H. Yang, N. Youssef, M.M.H. El-Sayed, Novel approach for effective removal of methylene blue dye from water using fava bean peel waste, *Sci. Rep.* 10 (2020) 7824. <https://doi.org/10.1038/s41598-020-64727-5>.
- [166] M. Saghanejhad Tehrani, R. Zare-Dorabei, Highly efficient simultaneous ultrasonic-assisted adsorption of methylene blue and rhodamine B onto metal organic framework MIL-68(Al): central composite design optimization, *RSC Adv.* 6 (2016) 27416–27425. <https://doi.org/10.1039/C5RA28052D>.
- [167] Y. Xu, K. Sheng, C. Li, G. Shi, Self-Assembled Graphene Hydrogel via a One-Step Hydrothermal Process, *ACS Nano.* 4 (2010) 4324–4330. <https://doi.org/10.1021/nn101187z>.
- [168] R. Mohd Firdaus, N. Berrada, A. Desforges, A.R. Mohamed, B. Vigolo, From 2D Graphene Nanosheets to 3D Graphene-based Macrostructures, *Chem. – An Asian J.* 15 (2020) 2902–2924. <https://doi.org/10.1002/asia.202000747>.
- [169] X. Ji, Y. Xu, W. Zhang, L. Cui, J. Liu, Review of functionalization, structure and properties of graphene/polymer composite fibers, *Compos. Part A Appl. Sci. Manuf.* 87 (2016) 29–45. <https://doi.org/10.1016/j.compositesa.2016.04.011>.
- [170] G.L.C. Paulus, Q.H. Wang, M.S. Strano, Covalent electron transfer chemistry of graphene with diazonium salts, *Acc. Chem. Res.* 46 (2013) 160–170. <https://doi.org/10.1021/ar300119z>.
- [171] T. Granzier-Nakajima, K. Fujisawa, V. Anil, M. Terrones, Y.T. Yeh, Controlling nitrogen doping in graphene with atomic precision: Synthesis and characterization, *Nanomaterials.* 9 (2019) 1–18. <https://doi.org/10.3390/nano9030425>.
- [172] A. Uma Maheswari, K. Palanivelu, Alkyl amine and vegetable oil mixture—a viable candidate for CO₂ capture and utilization, *Environ. Sci. Pollut. Res.* 24 (2017) 5733–5745. <https://doi.org/10.1007/s11356-016-8306-5>.
- [173] N. Belman, J.N. Israelachvili, Y. Li, C.R. Safinya, J. Bernstein, Y. Golan, Reaction of Alkylamine Surfactants with Carbon Dioxide: Relevance to Nanocrystal Synthesis, *Nano Lett.* 9 (2009) 2088–2093. <https://doi.org/10.1021/nl900534m>.
- [174] N.A. Daud, B.W. Chieng, N.A. Ibrahim, Z.A. Talib, E.N. Muhamad, Z.Z. Abidin, Functionalizing graphene oxide with alkylamine by gamma-ray irradiation method, *Nanomaterials.* 7 (2017). <https://doi.org/10.3390/nano7060135>.
- [175] S.P. Zhang, H.O. Song, Supramolecular graphene oxide-alkylamine hybrid materials: Variation of dispersibility and improvement of thermal stability, *New J. Chem.* 36 (2012) 1733–1738.

- <https://doi.org/10.1039/c2nj40214a>.
- [176] J. Jang, V.H. Pham, B. Rajagopalan, S.H. Hur, J.S. Chung, Effects of the alkylamine functionalization of graphene oxide on the properties of polystyrene nanocomposites, *Nanoscale Res. Lett.* 9 (2014) 1–6. <https://doi.org/10.1186/1556-276X-9-265>.
- [177] X. Yang, T. Mei, J. Yang, C. Zhang, M. Lv, X. Wang, Synthesis and characterization of alkylamine-functionalized graphene for polyolefin-based nanocomposites, *Appl. Surf. Sci.* 305 (2014) 725–731. <https://doi.org/10.1016/j.apsusc.2014.03.184>.
- [178] N. Yousefi, X. Lu, M. Elimelech, N. Tufenkji, Environmental performance of graphene-based 3D macrostructures, *Nat. Nanotechnol.* 14 (2019) 107–119. <https://doi.org/10.1038/s41565-018-0325-6>.
- [179] M.A. Riaz, G. McKay, J. Saleem, 3D graphene-based nanostructured materials as sorbents for cleaning oil spills and for the removal of dyes and miscellaneous pollutants present in water, *Environ. Sci. Pollut. Res.* 24 (2017) 27731–27745. <https://doi.org/10.1007/s11356-017-0606-x>.
- [180] H. Wang, C. Wang, S. Liu, L. Chen, S. Yang, Superhydrophobic and superoleophilic graphene aerogel for adsorption of oil pollutants from water, *RSC Adv.* 9 (2019) 8569–8574. <https://doi.org/10.1039/c9ra00279k>.
- [181] A.L.T. Zheng, S. Boonyuen, T. Ohno, Y. Andou, Accessing effects of aliphatic dicarboxylic acid towards the physical and chemical changes in low temperature hydrothermally reduced graphene hydrogel, *J. Porous Mater.* (2021). <https://doi.org/10.1007/s10934-021-01072-6>.
- [182] H. Banda, D. Aradilla, A. Benayad, Y. Chenavier, B. Daffos, L. Dubois, F. Duclairoir, One-step synthesis of highly reduced graphene hydrogels for high power supercapacitor applications, *J. Power Sources.* 360 (2017) 538–547. <https://doi.org/10.1016/j.jpowsour.2017.06.033>.
- [183] M.K. Rabchinskii, A.T. Dideikin, D.A. Kirilenko, M. V Baidakova, V. V Shnitov, F. Roth, S. V Konyakhin, N.A. Besedina, S.I. Pavlov, R.A. Kuricyn, N.M. Lebedeva, P.N. Brunkov, A.Y. Vul', Facile reduction of graphene oxide suspensions and films using glass wafers, *Sci. Rep.* 8 (2018) 14154. <https://doi.org/10.1038/s41598-018-32488-x>.
- [184] M.M. Viana, M.C.F.S. Lima, J.C. Forsythe, V.S. Gangoli, M. Cho, Y. Cheng, G.G. Silva, M.S. Wong, V. Caliman, Facile graphene oxide preparation by microwave-assisted acid method, *J. Braz. Chem. Soc.* 26 (2015) 978–984. <https://doi.org/10.5935/0103-5053.20150061>.
- [185] S. Wang, Y. Zhang, H.-L. Ma, Q. Zhang, W. Xu, J. Peng, J. Li, Z.-Z. Yu, M. Zhai, Ionic-liquid-assisted facile synthesis of silver nanoparticle-reduced graphene oxide hybrids by gamma irradiation, *Carbon N. Y.* 55 (2013) 245–252. <https://doi.org/10.1016/j.carbon.2012.12.033>.
- [186] H.P. Mungse, O.P. Khatri, Chemically functionalized reduced graphene oxide as a novel material for reduction of friction and wear, *J. Phys. Chem. C.* 118 (2014) 14394–14402. <https://doi.org/10.1021/jp5033614>.
- [187] S. Bai, X. Shen, G. Zhu, A. Yuan, J. Zhang, Z. Ji, D. Qiu, The influence of wrinkling in reduced graphene oxide on their adsorption and catalytic properties, *Carbon N. Y.* 60 (2013) 157–168. <https://doi.org/10.1016/j.carbon.2013.04.009>.
- [188] E.J. Park, B.C. Park, Y.J. Kim, A. Canlier, T.S. Hwang, Elimination and Substitution Compete During Amination of Poly(vinyl chloride) with Ehtylenediamine: XPS Analysis and Approach of Active Site Index, *Macromol. Res.* 26 (2018) 913–923. <https://doi.org/10.1007/s13233-018-6123-z>.
- [189] M.K. Rabchinskii, S.A. Ryzhkov, D.A. Kirilenko, N. V. Ulin, M. V. Baidakova, V. V. Shnitov, S.I. Pavlov, R.G. Chumakov, D.Y. Stolyarova, N.A. Besedina, A. V. Shvidchenko, D. V. Potorochin, F. Roth, D.A. Smirnov, M. V. Gudkov, M. Brzhezinskaya, O.I. Lebedev, V.P. Melnikov, P.N. Brunkov, From graphene oxide towards aminated graphene: facile synthesis, its structure and electronic properties, *Sci. Rep.* 10 (2020) 6902. <https://doi.org/10.1038/s41598-020-63935-3>.
- [190] K.C. Wasalathilake, D.G.D. Galpaya, G.A. Ayoko, C. Yan, Understanding the structure-property relationships in hydrothermally reduced graphene oxide hydrogels, *Carbon N. Y.* 137 (2018) 282–290. <https://doi.org/10.1016/j.carbon.2018.05.036>.
- [191] A. Yang, J. Li, C. Zhang, W. Zhang, N. Ma, One-step amine modification of graphene oxide to get a green trifunctional metal-free catalyst, *Appl. Surf. Sci.* 346 (2015) 443–450. <https://doi.org/10.1016/j.apsusc.2015.04.033>.
- [192] A. Merlen, J.G. Buijnsters, C. Pardanaud, A guide to and review of the use of multiwavelength Raman spectroscopy for characterizing defective aromatic carbon solids: From graphene to amorphous carbons, 2017. <https://doi.org/10.3390/coatings7100153>.
- [193] G. Wu, X. Tang, M. Meyyappan, K.W.C. Lai, Doping effects of surface functionalization on graphene

- with aromatic molecule and organic solvents, *Appl. Surf. Sci.* 425 (2017) 713–721. <https://doi.org/10.1016/j.apsusc.2017.07.048>.
- [194] T.J.M. Fraga, M.A. da Motta Sobrinho, M.N. Carvalho, M.G. Ghislandi, State of the art: synthesis and characterization of functionalized graphene nanomaterials, *Nano Express*. 1 (2020) 022002. <https://doi.org/10.1088/2632-959X/abb921>.
- [195] H. Liu, C. Liu, S. Peng, B. Pan, C. Lu, Effect of polyethyleneimine modified graphene on the mechanical and water vapor barrier properties of methyl cellulose composite films, *Carbohydr. Polym.* 182 (2018) 52–60. <https://doi.org/10.1016/j.carbpol.2017.11.008>.
- [196] A.M. Shanmugharaj, J.H. Yoon, W.J. Yang, S.H. Ryu, Synthesis, characterization, and surface wettability properties of amine functionalized graphene oxide films with varying amine chain lengths, *J. Colloid Interface Sci.* 401 (2013) 148–154. <https://doi.org/10.1016/j.jcis.2013.02.054>.
- [197] Y. Cao, T. Mu, Comprehensive investigation on the thermal stability of 66 ionic liquids by thermogravimetric analysis, *Ind. Eng. Chem. Res.* 53 (2014) 8651–8664. <https://doi.org/10.1021/ie5009597>.
- [198] B.A. Aragaw, Reduced graphene oxide-intercalated graphene oxide nano-hybrid for enhanced photoelectrochemical water reduction, *J. Nanostructure Chem.* 10 (2020) 9–18. <https://doi.org/10.1007/s40097-019-00324-x>.
- [199] R. Muzyka, S. Drewniak, T. Pustelny, M. Chrubasik, G. Gryglewicz, Characterization of Graphite Oxide and Reduced Graphene Oxide Obtained from Different Graphite Precursors and Oxidized by Different Methods Using Raman Spectroscopy, *Materials (Basel)*. 11 (2018) 1050. <https://doi.org/10.3390/ma11071050>.
- [200] C.C. Caliman, A.F. Mesquita, D.F. Cipriano, J.C.C. Freitas, A.A.C. Cotta, W.A.A. Macedo, A.O. Porto, One-pot synthesis of amine-functionalized graphene oxide by microwave-assisted reactions: An outstanding alternative for supporting materials in supercapacitors, *RSC Adv.* 8 (2018) 6136–6145. <https://doi.org/10.1039/c7ra13514a>.
- [201] S. Stankovich, D.A. Dikin, O.C. Compton, G.H.B. Dommett, R.S. Ruoff, S.T. Nguyen, Systematic post-assembly modification of graphene oxide paper with primary alkylamines, *Chem. Mater.* 22 (2010) 4153–4157. <https://doi.org/10.1021/cm100454g>.
- [202] B. Dehghanzad, M.K. Razavi Aghjeh, O. Rafeie, A. Tavakoli, A. Jameie Oskooie, Synthesis and characterization of graphene and functionalized graphene via chemical and thermal treatment methods, *RSC Adv.* 6 (2016) 3578–3585. <https://doi.org/10.1039/C5RA19954A>.
- [203] Z. AlOthman, A Review: Fundamental Aspects of Silicate Mesoporous Materials, *Materials (Basel)*. 5 (2012) 2874–2902. <https://doi.org/10.3390/ma5122874>.
- [204] A. Alazmi, O. El Tall, S. Rasul, M.N. Hedhili, S.P. Patole, P.M.F.J. Costa, A process to enhance the specific surface area and capacitance of hydrothermally reduced graphene, *Nanoscale*. 8 (2016) 17782–17787. <https://doi.org/10.1039/c6nr04426c>.
- [205] A.L.T. Zheng, Y. Andou, R.M. Zawawi, Voltammetric Determination of Dopamine Mediated By Nanoparticle WO₃/MWCNT Modified Glassy Carbon Electrode, *Int. J. Appl. Chem.* 13 (2017) 899–912.
- [206] A.L.T. Zheng, Y. Andou, R.M. Zawawi, Effects of deposition parameters on the electrochemical behaviour of ZnO thin film, *J. Adv. Chem. Sci.* 3 (2017) 521–524.
- [207] H.H. Girault, *Analytical and Physical Electrochemistry*, EPFL Press, 2005.
- [208] L. Zheng, H. Zheng, W. Chu, Electrochemical Behavior of Glassy Carbon Electrode Modified by Layer-by-layer Self-assembly of Functional Graphene, *IOP Conf. Ser. Earth Environ. Sci.* 170 (2018). <https://doi.org/10.1088/1755-1315/170/2/022163>.
- [209] D. Usachov, O. Vilkov, A. Grüneis, D. Haberer, A. Fedorov, V.K. Adamchuk, A.B. Preobrajenski, P. Dudin, A. Barinov, M. Oehzelt, C. Laubschat, D. V. Vyalikh, Nitrogen-doped graphene: Efficient growth, structure, and electronic properties, *Nano Lett.* 11 (2011) 5401–5407. <https://doi.org/10.1021/nl2031037>.
- [210] J. Wu, H. Yang, Synthesis and Electrocatalytic Oxygen Reduction Properties of Truncated Octahedral Pt₃Ni Nanoparticles, *Nano Res.* 4 (2011) 72–82. <https://doi.org/10.1007/s12274-010-0049-x>.
- [211] F. Wang, W. Ueda, Preparation, characterization and catalytic performance of Mo–V–O oxide layers linked by alkylamines, *Chem. Commun.* (2009) 1079. <https://doi.org/10.1039/b817118a>.
- [212] J.P. Simonin, On the comparison of pseudo-first order and pseudo-second order rate laws in the modeling of adsorption kinetics, *Chem. Eng. J.* 300 (2016) 254–263.

- <https://doi.org/10.1016/j.cej.2016.04.079>.
- [213] J. Wang, J. Zhang, L. Han, J. Wang, L. Zhu, H. Zeng, Graphene-based materials for adsorptive removal of pollutants from water and underlying interaction mechanism, *Adv. Colloid Interface Sci.* 289 (2021) 102360. <https://doi.org/10.1016/j.cis.2021.102360>.
- [214] J. Xu, L. Wang, Y. Zhu, Decontamination of bisphenol A from aqueous solution by graphene adsorption, *Langmuir*. 28 (2012) 8418–8425. <https://doi.org/10.1021/la301476p>.
- [215] J. Kwon, B. Lee, Bisphenol A adsorption using reduced graphene oxide prepared by physical and chemical reduction methods, *Chem. Eng. Res. Des.* 104 (2015) 519–529. <https://doi.org/10.1016/j.cherd.2015.09.007>.
- [216] F.M. Mpatani, A.A. Aryee, A.N. Kani, Q. Guo, E. Dovi, L. Qu, Z. Li, R. Han, Uptake of micropollutant-bisphenol A, methylene blue and neutral red onto a novel bagasse- β -cyclodextrin polymer by adsorption process, *Chemosphere*. 259 (2020) 127439. <https://doi.org/10.1016/j.chemosphere.2020.127439>.
- [217] X. Guo, Y. Huang, W. Yu, X. Yu, X. Han, H. Zhai, Multi-walled carbon nanotubes modified with iron oxide and manganese dioxide (MWCNTs-Fe₃O₄-MnO₂) as a novel adsorbent for the determination of BPA, *Microchem. J.* 157 (2020) 104867. <https://doi.org/10.1016/j.microc.2020.104867>.
- [218] M.H. Dehghani, R.R. Karri, M. Alimohammadi, S. Nazmara, A. Zarei, Z. Saeedi, Insights into endocrine-disrupting Bisphenol-A adsorption from pharmaceutical effluent by chitosan immobilized nanoscale zero-valent iron nanoparticles, *J. Mol. Liq.* 311 (2020) 113317. <https://doi.org/10.1016/j.molliq.2020.113317>.
- [219] S. Kittappa, M. Jang, M. Ramalingam, S. Ibrahim, Amine functionalized magnetic nano-composite materials for the removal of selected endocrine disrupting compounds and its mechanism study, *J. Environ. Chem. Eng.* 8 (2020) 103839. <https://doi.org/10.1016/j.jece.2020.103839>.
- [220] Z. Sun, L. Zhao, C. Liu, Y. Zhen, J. Ma, Fast adsorption of BPA with high capacity based on Π - Π electron donor-acceptor and hydrophobicity mechanism using an in-situ sp² C dominant N-doped carbon, *Chem. Eng. J.* 381 (2020) 122510. <https://doi.org/10.1016/j.cej.2019.122510>.
- [221] C.O. Panão, E.L.S. Campos, H.H.C. Lima, A.W. Rinaldi, M.K. Lima-Tenório, E.T. Tenório-Neto, M.R. Guilherme, T. Asefa, A.F. Rubira, Ultra-absorbent hybrid hydrogel based on alginate and SiO₂ microspheres: a high-water-content system for removal of methylene blue, *J. Mol. Liq.* 276 (2019) 204–213. <https://doi.org/10.1016/j.molliq.2018.11.157>.
- [222] R.M. Firdaus, N.I.M. Rosli, J. Ghanbaja, B. Vigolo, A.R. Mohamed, Enhanced adsorption of methylene blue on chemically modified graphene nanoplatelets thanks to favorable interactions, *J. Nanoparticle Res.* 21 (2019). <https://doi.org/10.1007/s11051-019-4701-4>.
- [223] L. Chen, Y. Li, S. Hu, J. Sun, Q. Du, X. Yang, Q. Ji, Z. Wang, D. Wang, Y. Xia, Removal of methylene blue from water by cellulose/graphene oxide fibres, *J. Exp. Nanosci.* 11 (2016) 1156–1170. <https://doi.org/10.1080/17458080.2016.1198499>.
- [224] J. Ma, C. Chen, F. Yu, Self-regenerative and self-enhanced smart graphene/Ag₃PO₄ hydrogel adsorbent under visible light, *New J. Chem.* 40 (2016) 3208–3215. <https://doi.org/10.1039/c5nj03404c>.
- [225] R. Davarnejad, S. Afshar, P. Etehadfar, Activated carbon blended with grape stalks powder: properties modification and its application in a dye adsorption, *Arab. J. Chem.* 13 (2020) 5463–5473. <https://doi.org/10.1016/j.arabjc.2020.03.025>.
- [226] Z. Li, H. Hanafy, L. Zhang, L. Sellaoui, M. Schadeck, M.L.S. Oliveira, M.K. Seliem, G. Luiz, A. Bonilla-petriciolet, Q. Li, Adsorption of congo red and methylene blue dyes on an ashitaba waste and a walnut shell-based activated carbon from aqueous solutions: experiments, characterization and physical interpretations, *Chem. Eng. J.* 388 (2020) 124263. <https://doi.org/10.1016/j.cej.2020.124263>.
- [227] C. Chiang, J. Chen, J. Lin, Preparation of pore-size tunable activated carbon derived from waste coffee grounds for high adsorption capacities of organic dyes, *J. Environ. Chem. Eng.* 8 (2020) 103929. <https://doi.org/10.1016/j.jece.2020.103929>.
- [228] Y. Zhu, B. Yi, S. Yan, Q. Yuan, Y. Wu, Removal of methylene blue from aqueous solution by cattle manure-derived low temperature biochar, *RSC Adv.* 8 (2018) 19917–19929. <https://doi.org/10.1039/C8RA03018A>.
- [229] G. Yang, L. Wu, Q. Xian, F. Shen, J. Wu, Y. Zhang, Removal of congo red and methylene blue from aqueous solutions by vermicompost-derived biochars, *PLoS One.* 11 (2016) e0154562. <https://doi.org/10.1371/journal.pone.0154562>.

- [230] S. Tang, D. Xia, Y. Yao, T. Chen, J. Sun, Y. Yin, W. Shen, Y. Peng, Dye adsorption by self-recoverable, adjustable amphiphilic graphene aerogel, *J. Colloid Interface Sci.* 554 (2019) 682–691. <https://doi.org/10.1016/j.jcis.2019.07.041>.
- [231] R. Rajumon, J.C. Anand, A.M. Ealias, D.S. Desai, G. George, M.P. Saravanakumar, Adsorption of textile dyes with ultrasonic assistance using green reduced graphene oxide: an in-depth investigation on sonochemical factors, *J. Environ. Chem. Eng.* 7 (2019) 103479. <https://doi.org/10.1016/j.jece.2019.103479>.
- [232] M. Harbi, M. Salih, H. Burhan, S. Demiroglu, Ö. Demirbas, F. Sen, Preparation, characterization and adsorption kinetics of methylene blue dye in reduced-graphene oxide supported nanoadsorbents, *J. Mol. Liq.* 309 (2020) 113171. <https://doi.org/10.1016/j.molliq.2020.113171>.
- [233] A.H. Jawad, A.S. Abdulhameed, Mesoporous Iraqi red kaolin clay as an efficient adsorbent for methylene blue dye: adsorption kinetic, isotherm and mechanism study, *Surfaces and Interfaces.* 18 (2020) 100422. <https://doi.org/10.1016/j.surfin.2019.100422>.
- [234] I. Chaari, E. Fakhfakh, M. Medhioub, F. Jamoussi, Comparative study on adsorption of cationic and anionic dyes by smectite rich natural clays, *J. Mol. Struct.* 1179 (2019) 672–677. <https://doi.org/10.1016/j.molstruc.2018.11.039>.
- [235] M. Atrous, M. Bouzid, E.C. Lima, P. Silas, A. Bonilla-petriciolet, A. Ben, Adsorption of dyes acid red 1 and acid green 25 on grafted clay: modeling and statistical physics interpretation, *J. Mol. Liq.* 294 (2019) 111610. <https://doi.org/10.1016/j.molliq.2019.111610>.
- [236] W. Choi, I. Lahiri, R. Seelaboyina, Y.S. Kang, Synthesis of graphene and its applications: a review, *Crit. Rev. Solid State Mater. Sci.* 35 (2010) 52–71. <https://doi.org/10.1080/10408430903505036>.
- [237] S. Ren, P. Rong, Q. Yu, Preparations, properties and applications of graphene in functional devices: a concise review, *Ceram. Int.* 44 (2018) 11940–11955. <https://doi.org/10.1016/j.ceramint.2018.04.089>.
- [238] M. Coros, F. Pogacean, L. Magerusan, C. Socaci, S. Pruneanu, A brief overview on synthesis and applications of graphene and graphene-based nanomaterials, *Front. Mater. Sci.* 13 (2019) 23–32.
- [239] S. Nasir, M.Z. Hussein, Z. Zainal, N.A. Yusof, Carbon-based nanomaterials/allotropes: a glimpse of their synthesis, properties and some applications, *Materials (Basel).* 11 (2018) 1–24. <https://doi.org/10.3390/ma11020295>.
- [240] Y. Chen, X. Xie, X. Xin, Z.R. Tang, Y.J. Xu, Ti3C2Tx-based three-dimensional hydrogel by a graphene oxide-assisted self-convergence process for enhanced photoredox catalysis, *ACS Nano.* 13 (2019) 295–304. <https://doi.org/10.1021/acsnano.8b06136>.
- [241] J. Li, G. Xiao, C. Chen, R. Li, D. Yan, Superior dispersions of reduced graphene oxide synthesized by using gallic acid as a reductant and stabilizer, *J. Mater. Chem. A.* 1 (2013) 1481–1487. <https://doi.org/10.1039/c2ta00638c>.
- [242] K. Yang, W. Yuan, Z. Hua, Y. Tang, F. Yin, D. Xia, Triazine-based two-dimensional organic polymer for selective NO₂ sensing with excellent performance, *ACS Appl. Mater. Interfaces.* 12 (2020) 3919–3927. <https://doi.org/10.1021/acsam.9b17450>.
- [243] J. Wu, K. Tao, Y.Y. Guo, Z. Li, X.T. Wang, Z.Z. Luo, S.L. Feng, C.L. Du, D. Chen, J.M. Miao, L.K. Norford, A 3D chemically modified graphene hydrogel for fast, highly sensitive, and selective gas sensor, *Adv. Sci.* 4 (2017) 1–9. <https://doi.org/10.1002/advs.201600319>.
- [244] H.N. Lim, N.M. Huang, S.S. Lim, I. Harrison, C.H. Chia, Fabrication and characterization of graphene hydrogel via hydrothermal approach as a scaffold for preliminary study of cell growth, *Int. J. Nanomedicine.* 6 (2011) 1817–1823. <https://doi.org/10.2147/ijn.s23392>.
- [245] G. Liao, J. Hu, Z. Chen, R. Zhang, G. Wang, T. Kuang, Preparation, properties, and applications of graphene-based hydrogels, *Front. Chem.* 6 (2018) 1–5. <https://doi.org/10.3389/fchem.2018.00450>.
- [246] T. Jiao, H. Zhao, J. Zhou, Q. Zhang, X. Luo, J. Hu, Q. Peng, X. Yan, Self-assembly reduced graphene oxide nanosheet hydrogel fabrication by anchorage of chitosan/silver and its potential efficient application toward dye degradation for wastewater treatments, *ACS Sustain. Chem. Eng.* 3 (2015) 3130–3139. <https://doi.org/10.1021/acssuschemeng.5b00695>.
- [247] F.T. Johra, W.G. Jung, Hydrothermally reduced graphene oxide as a supercapacitor, *Appl. Surf. Sci.* 357 (2015) 1911–1914. <https://doi.org/10.1016/j.apsusc.2015.09.128>.
- [248] Q. Luo, Y. Shan, X. Zuo, J. Liu, Anisotropic tough poly(vinyl alcohol)/graphene oxide nanocomposite hydrogels for potential biomedical applications, *RSC Adv.* 8 (2018) 13284–13291. <https://doi.org/10.1039/c8ra00340h>.
- [249] C. Pan, L. Liu, Q. Chen, Q. Zhang, G. Guo, Tough, stretchable, compressive novel

- polymer/graphene oxide nanocomposite hydrogels with excellent self-healing performance, *ACS Appl. Mater. Interfaces*. 9 (2017) 38052–38061. <https://doi.org/10.1021/acsami.7b12932>.
- [250] J.K. Wychowaniec, M. Iliut, M. Zhou, J. Moffat, M.A. Elsayy, W.A. Pinheiro, J.A. Hoyland, A.F. Miller, A. Vijayaraghavan, A. Saiani, Designing peptide/graphene hybrid hydrogels through fine-tuning of molecular interactions, *Biomacromolecules*. 19 (2018) 2731–2741. <https://doi.org/10.1021/acs.biomac.8b00333>.
- [251] K. Tadyszak, Ł. Majchrzycki, Ł. Szyller, B. Scheibe, Preparation and characterization of partially reduced graphene oxide aerogels doped with transition metal ions, *J. Mater. Sci.* 53 (2018) 16086–16098. <https://doi.org/10.1007/s10853-018-2770-x>.
- [252] G. Moon, H. Kim, W. Choi, Chemical-free growth of metal nanoparticles on graphene oxide sheets under visible light irradiation, *RSC Adv.* 2 (2012) 2205–2207. <https://doi.org/10.1039/c2ra00875k>.
- [253] M. Casa, M. Sarno, C. Cirillo, P. Ciambelli, Reduced graphene oxide-based silver nanoparticle-containing natural hydrogel as highly efficient catalysts for nitrile wastewater treatment, *Chem. Eng. Trans.* 47 (2016) 307–312. <https://doi.org/10.3303/CET1647052>.
- [254] D. Ghosh, S. Dhibar, A. Dey, S. Mukherjee, N. Joardar, S.P.S. Babu, B. Dey, Graphene oxide dispersed supramolecular hydrogel capped benign green silver nanoparticles for anticancer, antimicrobial, cell attachment and intracellular imaging applications, *J. Mol. Liq.* 282 (2019) 1–12. <https://doi.org/10.1016/j.molliq.2019.03.010>.
- [255] S. Jaworski, M. Wierzbicki, E. Sawosz, A. Jung, G. Gielerak, J. Biernat, H. Jaremek, W. Łojkowski, B. Woźniak, J. Wojnarowicz, L. Stobiński, A. Małolepszy, M. Mazurkiewicz-Pawlicka, M. Łojkowski, N. Kurantowicz, A. Chwalibog, Graphene oxide-based nanocomposites decorated with silver nanoparticles as an antibacterial agent, *Nanoscale Res. Lett.* 13 (2018) 1–17. <https://doi.org/10.1186/s11671-018-2533-2>.
- [256] E.F. Aboelfetoh, A.H. Gemeay, R.G. El-Sharkawy, Effective disposal of methylene blue using green immobilized silver nanoparticles on graphene oxide and reduced graphene oxide sheets through one-pot synthesis, *Environ. Monit. Assess.* 192 (2020) 1–20.
- [257] D. Dasler, R.A. Schäfer, M.B. Minameyer, J.F. Hitzengerger, F. Hauke, T. Drewello, A. Hirsch, Direct covalent coupling of porphyrins to graphene, *J. Am. Chem. Soc.* 139 (2017) 11760–11765. <https://doi.org/10.1021/jacs.7b04122>.
- [258] A.D. Adler, F. Longo, W. Shergalis, Mechanistic investigations of porphyrin syntheses. I. preliminary studies on ms-tetraphenylporphin, *J. Am. Chem. Soc.* 4315 (1964) 3145–3149.
- [259] I.N. Fedulova, N.A. Bragina, N. V Novikov, O.A. Ugol, A.F. Mironov, Synthesis of lipophilic tetraphenylporphyrins to design lipid-porphyrin ensembles, *Russ. J. Bioorganic Chem.* 33 (2007) 589–593. <https://doi.org/10.1134/S106816200706009X>.
- [260] Z. Xu, Q. Mei, Q. Hua, R. Tian, J. Weng, Y. Shi, W. Huang, Synthesis, characterization, energy transfer and photophysical properties of ethynyl bridge linked porphyrin – naphthalimide pentamer and its metal complexes, *J. Mol. Struct.* 1094 (2015) 1–8. <https://doi.org/10.1016/j.molstruc.2015.03.005>.
- [261] M. Rojkiewicz, P. Kuś, P. Kozub, M. Kempa, The synthesis of new potential photosensitizers, *Dye. Pigment.* 99 (2013) 627–635. <https://doi.org/10.1016/j.dyepig.2013.06.029>.
- [262] S. Sim, Y. Andou, H.A.A. Bashid, H. Lim, M. Altarawneh, Z. Jiang, K. Eksiler, S. Iikubo, Development of organo-dispersible graphene oxide via pseudo-surface modification for thermally conductive green polymer composites, *ACS Omega*. 3 (2018) 18124–18131. <https://doi.org/10.1021/acsomega.8b02478>.
- [263] M. Mar Bernal, E.M. Pérez, One-pot exfoliation of graphite and synthesis of nanographene/dimesitylporphyrin hybrids, *Int. J. Mol. Sci.* 16 (2015) 10704–10714. <https://doi.org/10.3390/ijms160510704>.
- [264] T. Han, J. Jin, C. Wang, Y. Sun, Y. Zhang, Y. Liu, Ag nanoparticles-modified 3D graphene foam for binder-free electrodes of electrochemical sensors, *Nanomaterials*. 7 (2017). <https://doi.org/10.3390/nano7020040>.
- [265] D.E. Watson, J.H.G. Ng, K.E. Aasmundtveit, M.P.Y. Desmulliez, In-situ silver nanoparticle formation on surface-modified polyetherimide films, *IEEE Trans. Nanotechnol.* 13 (2014) 736–742. <https://doi.org/10.1109/TNANO.2014.2318203>.
- [266] G. Ao, Z. Xiao, X. Qian, Z. Li, Y. Wang, X. Zhang, Y. Song, Nonlinear optical properties tuning in meso-tetraphenylporphyrin derivatives substituted with donor/acceptor groups in picosecond and nanosecond regimes, *Molecules*. 20 (2015) 5554–5565.

- <https://doi.org/10.3390/molecules20045554>.
- [267] G. Tuerdi, P. Nizamidin, N. Kari, A. Yimit, F. Wang, Optochemical properties of gas-phase protonated tetraphenylporphyrin investigated using an optical waveguide NH₃ sensor, *RSC Adv.* 8 (2018) 5614–5621. <https://doi.org/10.1039/c7ra11643h>.
- [268] S. Sunderrajan, L.R. Miranda, G. Pennathur, Improved stability and catalytic activity of graphene oxide/chitosan hybrid beads loaded with porcine liver esterase, *Prep. Biochem. Biotechnol.* 48 (2018) 343–351. <https://doi.org/10.1080/10826068.2018.1446153>.
- [269] A. Al Nafiey, P. Subramanian, A. Addad, B. Sieber, S. Szunerits, R. Boukherroub, Green synthesis of reduced graphene oxide-silver nanoparticles using environmentally friendly L-arginine for H₂O₂ detection, *ECS J. Solid State Sci. Technol.* 5 (2016) 3060–3066. <https://doi.org/10.1149/2.0121608jss>.
- [270] M. Lotya, A. Rakovich, J.F. Donegan, J.N. Coleman, Measuring the lateral size of liquid-exfoliated nanosheets with dynamic light scattering, *Nanotechnology.* 24 (2013). <https://doi.org/10.1088/0957-4484/24/26/265703>.
- [271] J. Amaro-Gahete, A. Benítez, R. Otero, D. Esquivel, C. Jiménez-Sanchidrián, J. Morales, Á. Caballero, F.J. Romero-Salguero, A comparative study of particle size distribution of graphene nanosheets synthesized by an ultrasound-assisted method, *Nanomaterials.* 9 (2019). <https://doi.org/10.3390/nano9020152>.
- [272] B. Chakrabarti, D. Nir, V. Yufit, F. Tariq, J. Rubio-Garcia, R. Maher, A. Kucernak, P. V. Aravind, N. Brandon, Performance enhancement of reduced graphene oxide-modified carbon electrodes for vanadium redox-flow systems, *ChemElectroChem.* 4 (2017) 194–200. <https://doi.org/10.1002/celec.201600402>.
- [273] K. Tseng, H. Ku, D. Tien, L. Stobinski, Novel preparation of reduced graphene oxide-silver complex using an electrical spark discharge method, *Nanomaterials.* 9 (2019) 1–12.
- [274] R. Bhujel, S. Rai, K. Baruah, U. Deka, J. Biswas, Capacitive and sensing responses of biomass derived silver decorated graphene, *Sci. Rep.* 9 (2019) 1–14. <https://doi.org/10.1038/s41598-019-56178-4>.
- [275] H. Zhao, T. Jiao, L. Zhang, J. Zhou, Q. Zhang, Q. Peng, X. Yan, Preparation and adsorption capacity evaluation of graphene oxide-chitosan composite hydrogels, *Sci. China Mater.* 58 (2015) 811–818. <https://doi.org/10.1007/s40843-015-0090-x>.
- [276] X. Zhang, G. Li, H. Zhang, X. Wang, J. Qu, P. Liu, Y. Wang, Enhanced adsorption capacity and selectivity towards salicylic acid in water by a cationic polymer, *Soft Matter.* 9 (2013) 6159–6166. <https://doi.org/10.1039/c3sm00096f>.
- [277] A. Elsagh, O. Moradi, A. Fakhri, F. Najafi, R. Alizadeh, V. Haddadi, Evaluation of the potential cationic dye removal using adsorption by graphene and carbon nanotubes as adsorbents surfaces, *Arab. J. Chem.* 10 (2017) S2862–S2869. <https://doi.org/10.1016/j.arabjc.2013.11.013>.
- [278] M. Ussia, E. Bruno, E. Spina, D. Vitalini, G. Pellegrino, F. Ruffino, V. Privitera, S.C. Carroccio, Freestanding photocatalytic materials based on 3D graphene and polyporphyrins, *Sci. Rep.* 8 (2018) 1–12. <https://doi.org/10.1038/s41598-018-23345-y>.
- [279] R. Chen, Y. Zhang, L. Shen, X. Wang, J. Chen, A. Ma, W. Jiang, Lead(II) and methylene blue removal using a fully biodegradable hydrogel based on starch immobilized humic acid, *Chem. Eng. J.* 268 (2015) 348–355. <https://doi.org/10.1016/j.cej.2015.01.081>.
- [280] T. Jiao, H. Guo, Q. Zhang, Q. Peng, Y. Tang, X. Yan, B. Li, Reduced graphene oxide-based silver nanoparticle-containing composite hydrogel as highly efficient dye catalysts for wastewater treatment, *Sci. Rep.* 5 (2015) 1–12. <https://doi.org/10.1038/srep11873>.
- [281] S. Khan, A.A. Edathil, F. Banat, Sustainable synthesis of graphene-based adsorbent using date syrup, *Sci. Rep.* 9 (2019) 1–14. <https://doi.org/10.1038/s41598-019-54597-x>.
- [282] A. Raja, P. Rajasekaran, K. Selvakumar, M. Arunpandian, K. Kaviyarasu, S. Asath Bahadur, M. Swaminathan, Visible active reduced graphene oxide-BiVO₄-ZnO ternary photocatalyst for efficient removal of ciprofloxacin, *Sep. Purif. Technol.* 233 (2020) 115996. <https://doi.org/10.1016/j.seppur.2019.115996>.
- [283] A. Raja, K. Selvakumar, P. Rajasekaran, M. Arunpandian, S. Ashokkumar, K. Kaviyarasu, S. Asath Bahadur, M. Swaminathan, Visible active reduced graphene oxide loaded titania for photodecomposition of ciprofloxacin and its antibacterial activity, *Colloids Surfaces A Physicochem. Eng. Asp.* 564 (2019) 23–30. <https://doi.org/10.1016/j.colsurfa.2018.12.024>.
- [284] D. Saravanakkumar, H.A. Oualid, Y. Brahmi, A. Ayeshamariam, M. Karunanaithy, A.M. Saleem, K.

- Kaviyarasu, S. Sivaranjani, M. Jayachandran, Synthesis and characterization of CuO/ZnO/CNTs thin films on copper substrate and its photocatalytic applications, *OpenNano*. 4 (2019) 100025. <https://doi.org/10.1016/j.onano.2018.11.001>.
- [285] A.L.T. Zheng, Y. Andou, Detection and remediation of bisphenol A (BPA) using graphene-based materials: mini-review, *Int. J. Environ. Sci. Technol.* (2021). <https://doi.org/10.1007/s13762-021-03512-x>.
- [286] A.L.T. Zheng, S. Boonyuen, G.Y. Li, L.H. Ngee, Y. Andou, Design of reduced graphene hydrogel with alkylamine surface functionalization through immersion/agitation method and its adsorption mechanism, *J. Mol. Struct.* (2021) 131008. <https://doi.org/10.1016/j.molstruc.2021.131008>.
- [287] S.M.F. Kabir, P.P. Sikdar, B. Haque, M.A.R. Bhuiyan, A. Ali, M.N. Islam, Cellulose-based hydrogel materials: chemistry, properties and their prospective applications, *Prog. Biomater.* 7 (2018) 153–174. <https://doi.org/10.1007/s40204-018-0095-0>.
- [288] K.K. Sadasivuni, A. Kafy, H.-C. Kim, H.-U. Ko, S. Mun, J. Kim, Reduced graphene oxide filled cellulose films for flexible temperature sensor application, *Synth. Met.* 206 (2015) 154–161. <https://doi.org/10.1016/j.synthmet.2015.05.018>.
- [289] M. Sabbaghan, D.S. Argyropoulos, Synthesis and characterization of nano fibrillated cellulose/Cu₂O films; micro and nano particle nucleation effects, *Carbohydr. Polym.* 197 (2018) 614–622. <https://doi.org/10.1016/j.carbpol.2018.06.011>.
- [290] D. Xiaolin, W. Zi, P. Jinjing, G. Wenli, L. Qiao, L. Lin, Y. Juming, High photocatalytic activity of Cu@Cu₂O/RGO/cellulose hybrid aerogels as reusable catalysts with enhanced mass and electron transfer, *React. Funct. Polym.* 138 (2019) 79–87. <https://doi.org/10.1016/j.reactfunctpolym.2019.02.016>.
- [291] H. Chen, Q. Chen, R. Hu, H. Wang, B.Z. Newby, Y. Chang, J. Zheng, Mechanically strong hybrid double network hydrogels with antifouling properties, *J. Mater. Chem. B*. 3 (2015) 5426–5435. <https://doi.org/10.1039/C5TB00681C>.
- [292] Q. Chen, H. Chen, L. Zhu, J. Zheng, Engineering of Tough Double Network Hydrogels, *Macromol. Chem. Phys.* 217 (2016) 1022–1036. <https://doi.org/10.1002/macp.201600038>.
- [293] Q. Chen, H. Chen, L. Zhu, J. Zheng, Fundamentals of double network hydrogels, *J. Mater. Chem. B*. 3 (2015) 3654–3676. <https://doi.org/10.1039/C5TB00123D>.
- [294] R. Xiong, H.S. Kim, L. Zhang, V.F. Korolovych, S. Zhang, Y.G. Yingling, V. V. Tsukruk, Wrapping Nanocellulose Nets around Graphene Oxide Sheets, *Angew. Chemie Int. Ed.* 57 (2018) 8508–8513. <https://doi.org/10.1002/anie.201803076>.
- [295] G.E. Lau, C.A. Che Abdullah, W.A.N. Wan Ahmad, S. Assaw, A.L.T. Zheng, Eco-Friendly Photocatalysts for Degradation of Dyes, *Catalysts*. 10 (2020) 1129. <https://doi.org/10.3390/catal10101129>.
- [296] A. Phuruangrat, A. Maneechote, P. Dumrongrojthanath, N. Ekthammathat, S. Thongtem, T. Thongtem, Effect of pH on visible-light-driven Bi₂WO₆ nanostructured catalyst synthesized by hydrothermal method, *Superlattices Microstruct.* 78 (2015) 106–115. <https://doi.org/10.1016/j.spmi.2014.11.038>.
- [297] P. Dumrongrojthanath, T. Thongtem, A. Phuruangrat, S. Thongtem, Synthesis and characterization of hierarchical multilayered flower-like assemblies of Ag doped Bi₂WO₆ and their photocatalytic activities, *Superlattices Microstruct.* 64 (2013) 196–203. <https://doi.org/10.1016/j.spmi.2013.09.028>.
- [298] K. Kaviyarasu, A. Ayeshamariam, E. Manikandan, J. Kennedy, R. Ladchumananandasivam, U. Umbelino Gomes, M. Jayachandran, M. Maaza, Solution processing of CuSe quantum dots: Photocatalytic activity under RhB for UV and visible-light solar irradiation, *Mater. Sci. Eng. B*. 210 (2016) 1–9. <https://doi.org/10.1016/j.mseb.2016.05.002>.
- [299] Y. Subba Reddy, C. Maria Magdalane, K. Kaviyarasu, G.T. Mola, J. Kennedy, M. Maaza, Equilibrium and kinetic studies of the adsorption of acid blue 9 and Safranin O from aqueous solutions by MgO decorated FLG coated Fuller's earth, *J. Phys. Chem. Solids*. 123 (2018) 43–51. <https://doi.org/10.1016/j.jpcc.2018.07.009>.
- [300] C. Maria Magdalane, K. Kaviyarasu, N. Matinise, N. Mayedwa, N. Mongwaketsi, D. Letsholathebe, G.T. Mola, N. AbdullahAl-Dhabi, M.V. Arasu, M. Henini, J. Kennedy, M. Maaza, B. Jeyaraj, Evaluation on La₂O₃ garlanded ceria heterostructured binary metal oxide nanoplates for UV/ visible light induced removal of organic dye from urban wastewater, *South African J. Chem. Eng.* 26 (2018) 49–60. <https://doi.org/10.1016/j.sajce.2018.09.003>.
- [301] C.M. Magdalane, K. Kaviyarasu, G.M.A. Priyadharsini, A.K.H. Bashir, N. Mayedwa, N. Matinise,

- A.B. Isaev, N. Abdullah Al-Dhabi, M.V. Arasu, S. Arokiyaraj, J. Kennedy, M. Maaza, Improved photocatalytic decomposition of aqueous Rhodamine-B by solar light illuminated hierarchical yttria nanosphere decorated ceria nanorods, *J. Mater. Res. Technol.* 8 (2019) 2898–2909. <https://doi.org/10.1016/j.jmrt.2018.11.019>.
- [302] N.M.I. Alhaji, D. Nathiya, K. Kaviyarasu, M. Meshram, A. Ayeshamariam, A comparative study of structural and photocatalytic mechanism of AgGaO₂ nanocomposites for equilibrium and kinetics evaluation of adsorption parameters, *Surfaces and Interfaces.* 17 (2019) 100375. <https://doi.org/10.1016/j.surfin.2019.100375>.
- [303] S. Panimalar, R. Uthrakumar, E.T. Selvi, P. Gomathy, C. Inmozhi, K. Kaviyarasu, J. Kennedy, Studies of MnO₂/g-C₃N₄ heterostructure efficient of visible light photocatalyst for pollutants degradation by sol-gel technique, *Surfaces and Interfaces.* 20 (2020) 100512. <https://doi.org/10.1016/j.surfin.2020.100512>.
- [304] N. Geetha, S. Sivaranjani, A. Ayeshamariam, M. Siva Bharathy, S. Nivetha, K. Kaviyarasu, M. Jayachandran, High Performance Photo-Catalyst Based on Nanosized ZnO–TiO₂ Nanoplatelets for Removal of RhB Under Visible Light Irradiation, *J. Adv. Microsc. Res.* 13 (2018) 12–19. <https://doi.org/10.1166/jamr.2018.1352>.
- [305] T. Ohno, K. Tokieda, S. Higashida, M. Matsumura, Synergism between rutile and anatase TiO₂ particles in photocatalytic oxidation of naphthalene, *Appl. Catal. A Gen.* 244 (2003) 383–391. [https://doi.org/10.1016/S0926-860X\(02\)00610-5](https://doi.org/10.1016/S0926-860X(02)00610-5).
- [306] T. Ohno, T. Tsubota, K. Nishijima, Z. Miyamoto, Degradation of Methylene Blue on Carbonate Species-doped TiO₂ Photocatalysts under Visible Light, *Chem. Lett.* 33 (2004) 750–751. <https://doi.org/10.1246/cl.2004.750>.
- [307] T. Ohno, M. Akiyoshi, T. Umebayashi, K. Asai, T. Mitsui, M. Matsumura, Preparation of S-doped TiO₂ photocatalysts and their photocatalytic activities under visible light, *Appl. Catal. A Gen.* 265 (2004) 115–121. <https://doi.org/10.1016/j.apcata.2004.01.007>.
- [308] T. Ohno, T. Mitsui, M. Matsumura, Photocatalytic Activity of S-doped TiO₂ Photocatalyst under Visible Light, *Chem. Lett.* 32 (2003) 364–365. <https://doi.org/10.1246/cl.2003.364>.
- [309] G. Beyene, G. Sakata, T. Senbeta, B. Mesfin, Effect of core size/shape on the plasmonic response of spherical ZnO@Au core-shell nanostructures embedded in a passive host-matrices of MgF₂, *AIMS Mater. Sci.* 7 (2020) 705–719. <https://doi.org/10.3934/matricsci.2020.6.705>.
- [310] A. Visibile, R.B. Wang, A. Vertova, S. Rondinini, A. Minguzzi, E. Ahlberg, M. Busch, Influence of Strain on the Band Gap of Cu₂O, *Chem. Mater.* 31 (2019) 4787–4792. <https://doi.org/10.1021/acs.chemmater.9b01122>.
- [311] D.C.T. Nguyen, K.Y. Cho, W.-C. Oh, A facile route to synthesize ternary Cu₂O quantum dot/graphene-TiO₂ nanocomposites with an improved photocatalytic effect, *Fullerenes, Nanotub. Carbon Nanostructures.* 25 (2017) 684–690. <https://doi.org/10.1080/1536383X.2017.1344648>.
- [312] L. Yang, Z. Li, H. Jiang, W. Jiang, R. Su, S. Luo, Y. Luo, Photoelectrocatalytic oxidation of bisphenol A over mesh of TiO₂/graphene/Cu₂O, *Appl. Catal. B Environ.* 183 (2016) 75–85. <https://doi.org/10.1016/j.apcatb.2015.10.023>.
- [313] Y. Wang, K. Zhou, Effect of OH⁻ on morphology of Cu₂O particles prepared through reduction of Cu(II) by glucose, *J. Cent. South Univ.* 19 (2012) 2125–2129. <https://doi.org/10.1007/s11771-012-1254-4>.
- [314] S. Ganesh Babu, R. Vinoth, P. Surya Narayana, D. Bahnmann, B. Neppolian, Reduced graphene oxide wrapped Cu₂O supported on C₃N₄: An efficient visible light responsive semiconductor photocatalyst, *APL Mater.* 3 (2015) 104415. <https://doi.org/10.1063/1.4928286>.
- [315] Zielińska-Jurek, Wei, Janczarek, Wysocka, Kowalska, Size-Controlled Synthesis of Pt Particles on TiO₂ Surface: Physicochemical Characteristic and Photocatalytic Activity, *Catalysts.* 9 (2019) 940. <https://doi.org/10.3390/catal9110940>.
- [316] S. Mustapha, Y. Andou, Tailored higher performance silicone elastomer with nanofibrillated cellulose through acidic treatment, *Polym. Compos.* (2021) 1–11. <https://doi.org/10.1002/pc.25976>.
- [317] I. Boukhoubza, M. Khenfouch, M. Achehboune, B.M. Mothudi, I. Zorkani, A. Jorio, X-ray diffraction investigations of nanostructured ZnO coated with reduced graphene oxide., *J. Phys. Conf. Ser.* 1292 (2019) 012011. <https://doi.org/10.1088/1742-6596/1292/1/012011>.
- [318] P. Zheng, T. Liu, Y. Su, L. Zhang, S. Guo, TiO₂ nanotubes wrapped with reduced graphene oxide as a high-performance anode material for lithium-ion batteries, *Sci. Rep.* 6 (2016) 36580. <https://doi.org/10.1038/srep36580>.

- [319] S. Mourdikoudis, R.M. Pallares, N.T.K. Thanh, Characterization techniques for nanoparticles: comparison and complementarity upon studying nanoparticle properties, *Nanoscale*. 10 (2018) 12871–12934. <https://doi.org/10.1039/C8NR02278J>.
- [320] B.S. Gonçalves, L.M.C. Silva, T.C.C. De Souza, V.G. De Castro, G.G. Silva, B.C. Silva, K. Krambrock, R.B. Soares, V.F.C. Lins, M. Houmard, E.H.M. Nunes, Solvent effect on the structure and photocatalytic behavior of TiO₂-RGO nanocomposites, *J. Mater. Res.* 34 (2019) 3918–3930. <https://doi.org/10.1557/jmr.2019.342>.
- [321] D. Yoon, J. Hwang, D.H. Kim, W. Chang, K.Y. Chung, J. Kim, One-pot route for uniform anchoring of TiO₂ nanoparticles on reduced graphene oxides and their anode performance for lithium-ion batteries, *J. Supercrit. Fluids*. 125 (2017) 66–78. <https://doi.org/10.1016/j.supflu.2017.02.005>.
- [322] Y. Deng, A.D. Handoko, Y. Du, S. Xi, B.S. Yeo, In Situ Raman Spectroscopy of Copper and Copper Oxide Surfaces during Electrochemical Oxygen Evolution Reaction: Identification of Cu III Oxides as Catalytically Active Species, *ACS Catal.* 6 (2016) 2473–2481. <https://doi.org/10.1021/acscatal.6b00205>.
- [323] S. Challagulla, K. Tarafder, R. Ganesan, S. Roy, Structure sensitive photocatalytic reduction of nitroarenes over TiO₂, *Sci. Rep.* 7 (2017) 8783. <https://doi.org/10.1038/s41598-017-08599-2>.
- [324] J.-B. Wu, M.-L. Lin, X. Cong, H.-N. Liu, P.-H. Tan, Raman spectroscopy of graphene-based materials and its applications in related devices, *Chem. Soc. Rev.* 47 (2018) 1822–1873. <https://doi.org/10.1039/C6CS00915H>.
- [325] K. Dong, J. He, J. Liu, F. Li, L. Yu, Y. Zhang, X. Zhou, H. Ma, Photocatalytic performance of Cu₂O-loaded TiO₂/rGO nanoheterojunctions obtained by UV reduction, *J. Mater. Sci.* 52 (2017) 6754–6766. <https://doi.org/10.1007/s10853-017-0911-2>.
- [326] H. Zhang, X. Wang, N. Li, J. Xia, Q. Meng, J. Ding, J. Lu, Synthesis and characterization of TiO₂/graphene oxide nanocomposites for photoreduction of heavy metal ions in reverse osmosis concentrate, *RSC Adv.* 8 (2018) 34241–34251. <https://doi.org/10.1039/C8RA06681G>.
- [327] V. Kuzmenko, N. Wang, M. Haque, O. Naboka, M. Flygare, K. Svensson, P. Gatenholm, J. Liu, P. Enoksson, Cellulose-derived carbon nanofibers/graphene composite electrodes for powerful compact supercapacitors, *RSC Adv.* 7 (2017) 45968–45977. <https://doi.org/10.1039/C7RA07533B>.
- [328] S. Tan, J. Li, L. Zhou, P. Chen, D. Xu, Z. Xu, Fabrication of a flexible film electrode based on cellulose nanofibers aerogel dispersed with functionalized graphene decorated with SnO₂ for supercapacitors, *J. Mater. Sci.* 53 (2018) 11648–11658. <https://doi.org/10.1007/s10853-018-2413-2>.
- [329] S. He, H. Hou, W. Chen, 3D porous and ultralight carbon hybrid nanostructure fabricated from carbon foam covered by monolayer of nitrogen-doped carbon nanotubes for high performance supercapacitors, *J. Power Sources*. 280 (2015) 678–686. <https://doi.org/10.1016/j.jpowsour.2015.01.159>.
- [330] H.S. Hassan, M.F. Elkady, A.A. Farghali, A.M. Salem, A.I.A. El-Hamid, Fabrication of novel magnetic zinc oxide cellulose acetate hybrid nano-fiber to be utilized for phenol decontamination, *J. Taiwan Inst. Chem. Eng.* 78 (2017) 307–316. <https://doi.org/10.1016/j.jtice.2017.06.021>.
- [331] I. Roy, A. Bhattacharyya, G. Sarkar, N.R. Saha, D. Rana, P.P. Ghosh, M. Palit, A.R. Das, D. Chattopadhyay, In situ synthesis of a reduced graphene oxide/cuprous oxide nanocomposite: a reusable catalyst, *RSC Adv.* 4 (2014) 52044–52052. <https://doi.org/10.1039/C4RA08127G>.
- [332] P. Benjwal, M. Kumar, P. Chamoli, K.K. Kar, Enhanced photocatalytic degradation of methylene blue and adsorption of arsenic(III) by reduced graphene oxide (rGO)-metal oxide (TiO₂/Fe₃O₄) based nanocomposites, *RSC Adv.* 5 (2015) 73249–73260. <https://doi.org/10.1039/c5ra13689j>.
- [333] M. El Achaby, F.Z. Arrakhiz, S. Vaudreuil, E.M. Essassi, A. Qaiss, Piezoelectric β -polymorph formation and properties enhancement in graphene oxide – PVDF nanocomposite films, *Appl. Surf. Sci.* 258 (2012) 7668–7677. <https://doi.org/10.1016/j.apsusc.2012.04.118>.
- [334] T. Soltani, B.-Kyu Lee, A benign ultrasonic route to reduced graphene oxide from pristine graphite, *J. Colloid Interface Sci.* 486 (2017) 337–343. <https://doi.org/10.1016/j.jcis.2016.09.075>.
- [335] H. Abdali, A. Ajjji, Preparation of Electrospun Nanocomposite Nanofibers of Polyaniline/Poly(methyl methacrylate) with Amino-Functionalized Graphene, *Polymers (Basel)*. 9 (2017) 453. <https://doi.org/10.3390/polym9090453>.
- [336] M. Xiang, R. Yang, J. Yang, S. Zhou, J. Zhou, S. Dong, Fabrication of polyamide 6/reduced graphene oxide nano-composites by conductive cellulose skeleton structure and its conductive behavior, *Compos. Part B Eng.* 167 (2019) 533–543.

- <https://doi.org/10.1016/j.compositesb.2019.03.033>.
- [337] U. Goikuria, A. Larrañaga, J.L. Vilas, E. Lizundia, Thermal stability increase in metallic nanoparticles-loaded cellulose nanocrystal nanocomposites, *Carbohydr. Polym.* 171 (2017) 193–201. <https://doi.org/10.1016/j.carbpol.2017.05.024>.
- [338] X. Wang, W. Xing, X. Feng, B. Yu, H. Lu, L. Song, Y. Hu, The effect of metal oxide decorated graphene hybrids on the improved thermal stability and the reduced smoke toxicity in epoxy resins, *Chem. Eng. J.* 250 (2014) 214–221. <https://doi.org/10.1016/j.cej.2014.01.106>.
- [339] C.D. Simão, J.S. Reparaz, M.R. Wagner, B. Graczykowski, M. Kreuzer, Y.B. Ruiz-Blanco, Y. García, J.-M. Malho, A.R. Goñi, J. Ahopelto, C.M. Sotomayor Torres, Optical and mechanical properties of nanofibrillated cellulose: Toward a robust platform for next-generation green technologies, *Carbohydr. Polym.* 126 (2015) 40–46. <https://doi.org/10.1016/j.carbpol.2015.03.032>.
- [340] K. Alamelu, V. Raja, L. Shiamala, B.M. Jaffar Ali, Biphasic TiO₂ nanoparticles decorated graphene nanosheets for visible light driven photocatalytic degradation of organic dyes, *Appl. Surf. Sci.* 430 (2018) 145–154. <https://doi.org/10.1016/j.apsusc.2017.05.054>.
- [341] M.E. Aguirre, R. Zhou, A.J. Eugene, M.I. Guzman, M.A. Grela, Cu₂O/TiO₂ heterostructures for CO₂ reduction through a direct Z-scheme: Protecting Cu₂O from photocorrosion, *Appl. Catal. B Environ.* 217 (2017) 485–493. <https://doi.org/10.1016/j.apcatb.2017.05.058>.
- [342] Z. Wang, W. Zhu, R. Huang, Y. Zhang, C. Jia, H. Zhao, W. Chen, Y. Xue, Fabrication and Characterization of Cellulose Nanofiber Aerogels Prepared via Two Different Drying Techniques, *Polymers (Basel)*. 12 (2020) 2583. <https://doi.org/10.3390/polym12112583>.
- [343] R.F. Faradilla, L. Lucia, M. Hakovirta, Remarkable Physical and Thermal Properties of Hydrothermal Carbonized Nanoscale Cellulose Observed from Citric Acid Catalysis and Acetone Rinsing, *Nanomaterials*. 10 (2020) 1049. <https://doi.org/10.3390/nano10061049>.
- [344] A.E. Ketola, M. Leppänen, T. Turpeinen, P. Papponen, A. Strand, A. Sundberg, K. Arstila, E. Retulainen, Cellulose nanofibrils prepared by gentle drying methods reveal the limits of helium ion microscopy imaging, *RSC Adv.* 9 (2019) 15668–15677. <https://doi.org/10.1039/C9RA01447K>.
- [345] H. Mahajan, S.K. Arumugasamy, A. Panda, V. Sada, M. Yoon, K. Yun, Well-Designed Au Nanorod-Doped Cu₂O Core-Shell Nanocube-Embedded Reduced Graphene Oxide Composite for Efficient Removal of a Water Pollutant Dye, *ACS Omega*. 5 (2020) 24799–24810. <https://doi.org/10.1021/acsomega.0c03487>.
- [346] Q. Zhang, Y. He, X. Chen, D. Hu, L. Li, T. Yin, L. Ji, Structure and photocatalytic properties of TiO₂-Graphene Oxide intercalated composite, *Chinese Sci. Bull.* 56 (2011) 331–339. <https://doi.org/10.1007/s11434-010-3111-x>.
- [347] M.J. Jackman, A.G. Thomas, C. Muryn, Photoelectron Spectroscopy Study of Stoichiometric and Reduced Anatase TiO₂ (101) Surfaces: The Effect of Subsurface Defects on Water Adsorption at Near-Ambient Pressures, *J. Phys. Chem. C*. 119 (2015) 13682–13690. <https://doi.org/10.1021/acs.jpcc.5b02732>.
- [348] W. Xie, R. Li, Q. Xu, Enhanced photocatalytic activity of Se-doped TiO₂ under visible light irradiation, *Sci. Rep.* 8 (2018) 8752. <https://doi.org/10.1038/s41598-018-27135-4>.
- [349] J. Li, Z. Mei, L. Liu, H. Liang, A. Azarov, A. Kuznetsov, Y. Liu, A. Ji, Q. Meng, X. Du, Probing Defects in Nitrogen-Doped Cu₂O, *Sci. Rep.* 4 (2015) 7240. <https://doi.org/10.1038/srep07240>.
- [350] J.-J. Zhang, Y.-H. Wu, J.-Y. Mei, G.-P. Zheng, T.-T. Yan, X.-C. Zheng, P. Liu, X.-X. Guan, Synergetic adsorption and photocatalytic degradation of pollutants over 3D TiO₂-graphene aerogel composites synthesized via a facile one-pot route, *Photochem. Photobiol. Sci.* 15 (2016) 1012–1019. <https://doi.org/10.1039/C6PP00133E>.
- [351] S. Ghattavi, A. Nezamzadeh-Ejhieh, A visible light driven AgBr/g-C₃N₄ photocatalyst composite in methyl orange photodegradation: Focus on photoluminescence, mole ratio, synthesis method of g-C₃N₄ and scavengers, *Compos. Part B Eng.* 183 (2020) 107712. <https://doi.org/10.1016/j.compositesb.2019.107712>.
- [352] T. Liu, L. Wang, X. Lu, J. Fan, X. Cai, B. Gao, R. Miao, J. Wang, Y. Lv, Comparative study of the photocatalytic performance for the degradation of different dyes by ZnIn₂S₄: adsorption, active species, and pathways, *RSC Adv.* 7 (2017) 12292–12300. <https://doi.org/10.1039/C7RA00199A>.
- [353] D. Wang, X. Pan, G. Wang, Z. Yi, Improved propane photooxidation activities upon nano Cu₂O/TiO₂ heterojunction semiconductors at room temperature, *RSC Adv.* 5 (2015) 22038–22043. <https://doi.org/10.1039/C4RA15215H>.
- [354] W. Wang, Z. Wu, E. Eftekhari, Z. Huo, X. Li, M.O. Tade, C. Yan, Z. Yan, C. Li, Q. Li, D. Zhao, High

- performance heterojunction photocatalytic membranes formed by embedding Cu₂O and TiO₂ nanowires in reduced graphene oxide, *Catal. Sci. Technol.* 8 (2018) 1704–1711. <https://doi.org/10.1039/C8CY00082D>.
- [355] S.-R. Kim, I. Ali, J.-O. Kim, Phenol degradation using an anodized graphene-doped TiO₂ nanotube composite under visible light, *Appl. Surf. Sci.* 477 (2019) 71–78. <https://doi.org/10.1016/j.apsusc.2017.12.024>.
- [356] W. Zhang, X. Li, Z. Yang, X. Tang, Y. Ma, M. Li, N. Hu, H. Wei, Y. Zhang, In situ preparation of cubic Cu₂O-RGO nanocomposites for enhanced visible-light degradation of methyl orange, *Nanotechnology*. 27 (2016) 265703. <https://doi.org/10.1088/0957-4484/27/26/265703>.
- [357] K. Dai, H. Chen, T. Peng, D. Ke, H. Yi, Photocatalytic degradation of methyl orange in aqueous suspension of mesoporous titania nanoparticles, *Chemosphere*. 69 (2007) 1361–1367. <https://doi.org/10.1016/j.chemosphere.2007.05.021>.
- [358] B. Sharma, R. Deswal, Single pot synthesized gold nanoparticles using Hippophae rhamnoides leaf and berry extract showed shape-dependent differential nanobiotechnological applications, *Artif. Cells, Nanomedicine, Biotechnol.* 46 (2018) 408–418. <https://doi.org/10.1080/21691401.2018.1458034>.
- [359] X. Sun, D. Xu, P. Dai, X. Liu, F. Tan, Q. Guo, Efficient degradation of methyl orange in water via both radical and non-radical pathways using Fe-Co bimetal-doped MCM-41 as peroxymonosulfate activator, *Chem. Eng. J.* 402 (2020) 125881. <https://doi.org/10.1016/j.cej.2020.125881>.
- [360] D. Ren, O. Merdrignac-Conanec, V. Dorcet, M. Cathelinaud, Z. Zheng, H. Ma, X. Zhang, In situ synthesis and improved photoelectric performances of a Sb₂Se₃/β-In₂Se₃ heterojunction composite with potential photocatalytic activity for methyl orange degradation, *Ceram. Int.* 46 (2020) 25503–25511. <https://doi.org/10.1016/j.ceramint.2020.07.021>.
- [361] R. Dou, H. Lin, M. Guo, J. Cao, C. Liu, S. Chen, Fabrication of Ag/RP composite with excellent photocatalytic activity for degrading high concentration of methyl orange solution, *Mater. Lett.* 268 (2020) 127612. <https://doi.org/10.1016/j.matlet.2020.127612>.
- [362] Z. Jia, Q. Chen, C. Li, Z. Li, D. Zhang, R. Chu, L. Wu, Facile in situ preparation of fibrous Ag/AgCl composites with efficient photocatalytic degradation of methyl orange under solar light, *J. Phys. Chem. Solids*. 140 (2020) 109360. <https://doi.org/10.1016/j.jpcs.2020.109360>.
- [363] X. Zheng, D. Zhang, Y. Gao, Y. Wu, Q. Liu, X. Zhu, Synthesis and characterization of cubic Ag/TiO₂ nanocomposites for the photocatalytic degradation of methyl orange in aqueous solutions, *Inorg. Chem. Commun.* 110 (2019) 107589. <https://doi.org/10.1016/j.inoche.2019.107589>.
- [364] R. Shan, L. Lu, J. Gu, Y. Zhang, H. Yuan, Y. Chen, B. Luo, Photocatalytic degradation of methyl orange by Ag/TiO₂/biochar composite catalysts in aqueous solutions, *Mater. Sci. Semicond. Process.* 114 (2020) 105088. <https://doi.org/10.1016/j.mssp.2020.105088>.
- [365] V.N. Nguyen, D.T. Tran, M.T. Nguyen, T.T.T. Le, M.N. Ha, M.V. Nguyen, T.D. Pham, Enhanced photocatalytic degradation of methyl orange using ZnO/graphene oxide nanocomposites, *Res. Chem. Intermed.* 44 (2018) 3081–3095. <https://doi.org/10.1007/s11164-018-3294-3>.
- [366] D. Wang, L. Zhao, H. Ma, H. Zhang, L.-H. Guo, Quantitative Analysis of Reactive Oxygen Species Photogenerated on Metal Oxide Nanoparticles and Their Bacteria Toxicity: The Role of Superoxide Radicals, *Environ. Sci. Technol.* 51 (2017) 10137–10145. <https://doi.org/10.1021/acs.est.7b00473>.
- [367] P. Kumar, P. Huo, R. Zhang, B. Liu, Antibacterial Properties of Graphene-Based Nanomaterials, *Nanomaterials*. 9 (2019) 737. <https://doi.org/10.3390/nano9050737>.
- [368] A. Mobeen, C. Maria Magdalane, S.K. Jasmine Shahina, D. Lakshmi, R. Sundaram, G. Ramalingam, A. Raja, J. Madhavan, D. Letsholathebe, A.K.H. Bashir, M. Maaza, K. Kaviyarasu, Investigation on antibacterial and photocatalytic degradation of Rhodamine-B dye under visible light irradiation by titanium molybdate nanoparticles prepared via microwave method, *Surfaces and Interfaces*. 17 (2019) 100381. <https://doi.org/10.1016/j.surfin.2019.100381>.

APPENDICES

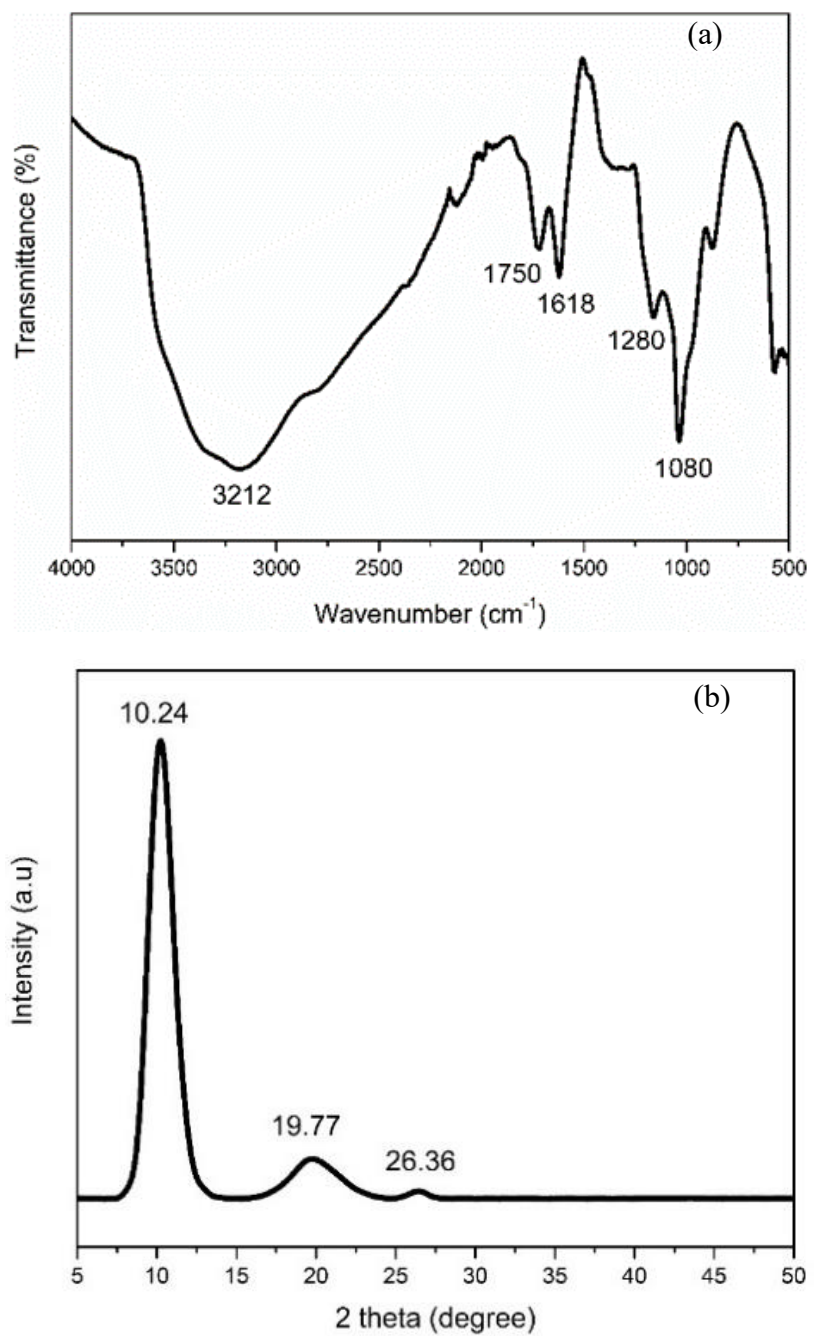


Fig. S2.1. (a) FTIR spectrum and (b) XRD spectra of GO

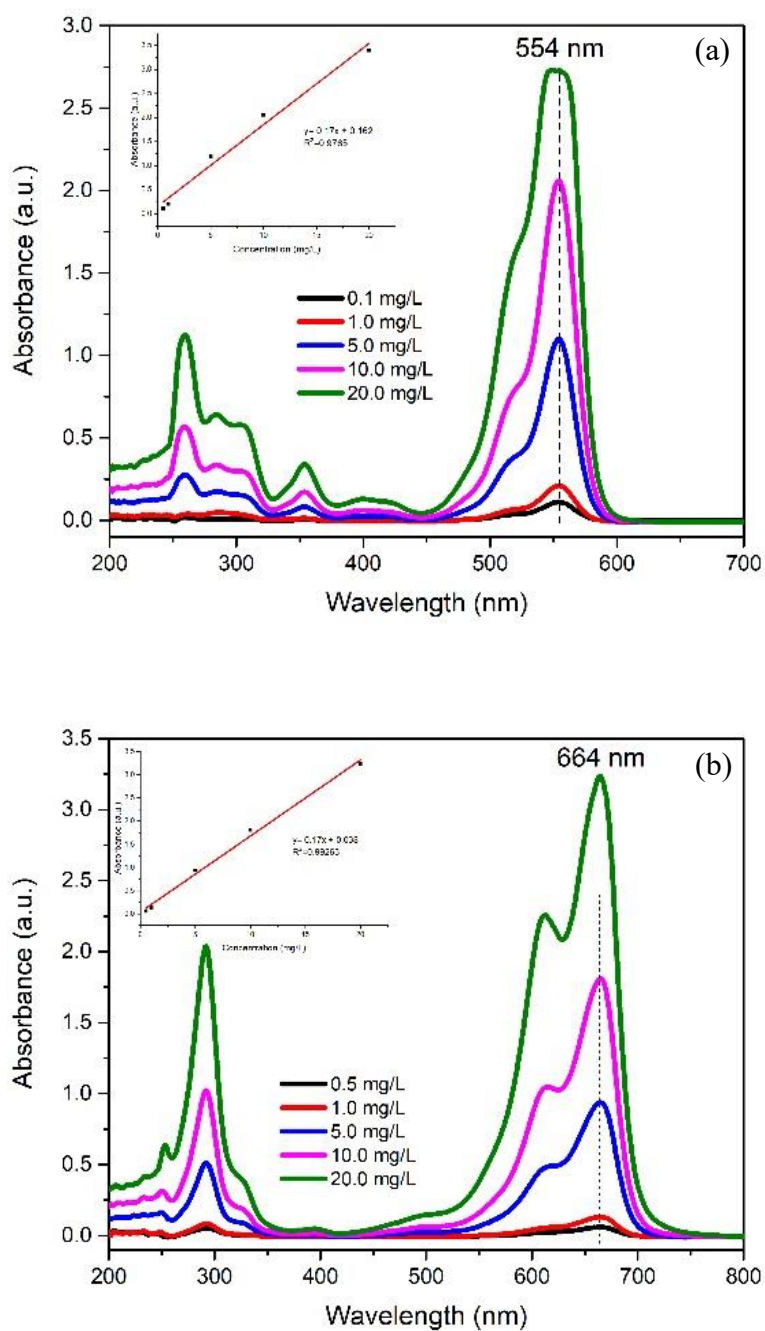


Fig. S3.1. The absorption spectrum and linear concentration curve of (a) RhB and (b) MB under varying concentration

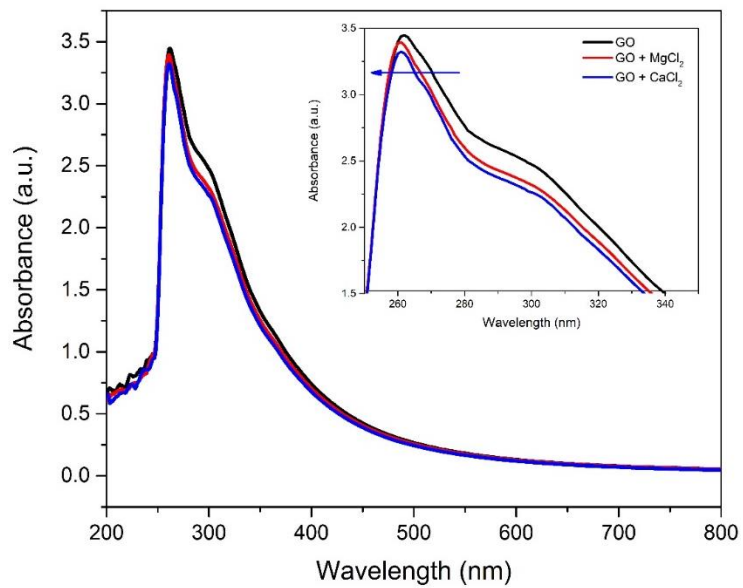


Fig. S3.2. UV-vis spectrum of GO suspension in the presence of MgCl_2 and CaCl_2

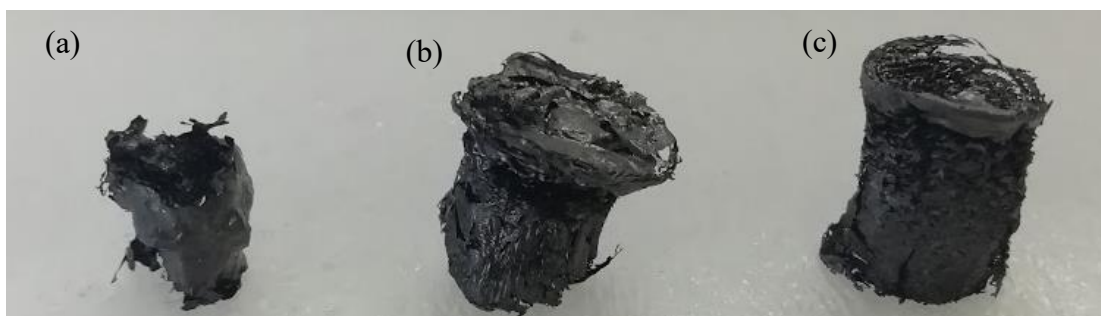


Fig. S3.3. Digital image of freeze dried (a) rGH, (b) rGH-Mg and (c) rGH-Ca

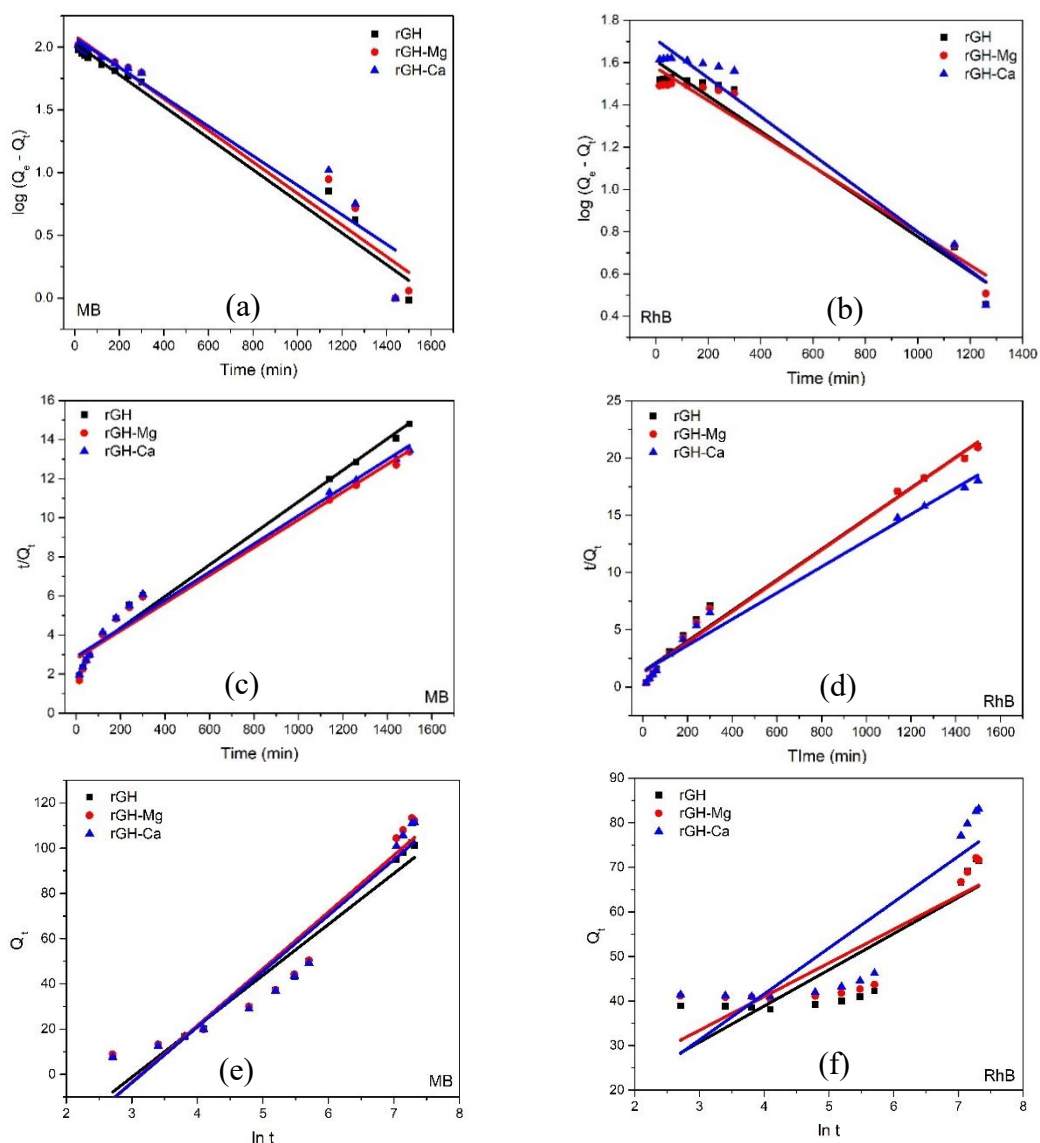


Fig. S3.4. Pseudo first order (a,b), Pseudo-second order (c,d) and Elovich kinetic model (e,f) of MB and RhB adsorption on the hydrogels

Table S3.1. The parameters of the intraparticle diffusion model by the hydrogels

Sample	Step 1			Step 2	
	C (mg/g)	K_1	R_1^2	K2	R_2^2
MB					
rGH	-34.30	13.98	0.95590	2.70	0.99942
rGH-Mg	-33.84	13.97	0.94378	3.22	0.99932
rGH-Ca	-34.41	13.94	0.95567	3.12	0.99325
RhB					
rGH	37.06	0.2503	0.74803	1.48175	0.99998
rGH-Mg	39.69	0.18771	0.68891	1.39418	0.99991
rGH-Ca	38.90	0.36242	0.81394	1.85871	0.99955

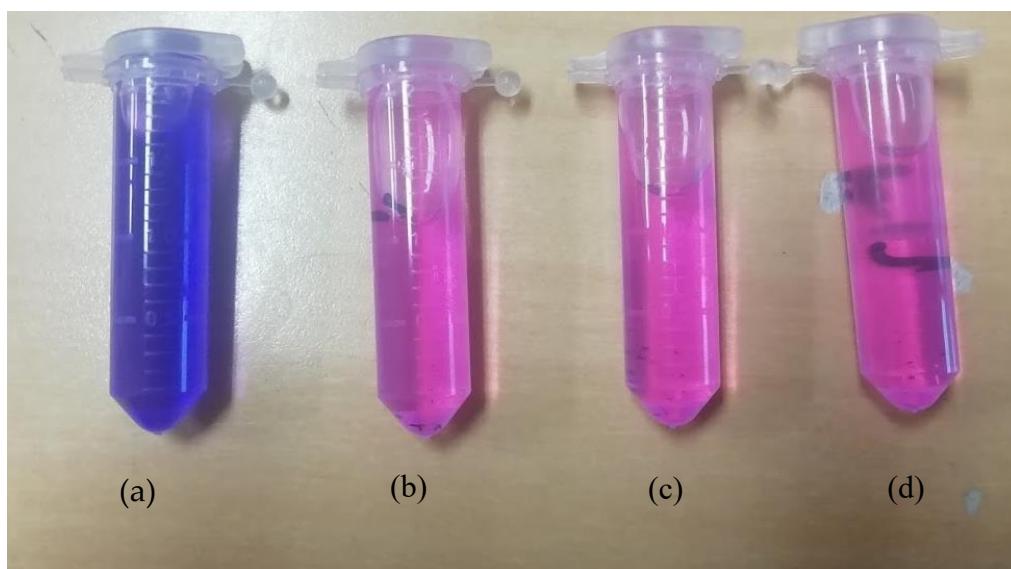


Fig. S3.5. Digital image of the dye solution before (a) and after for (b) rGH, (c) rGH-Mg and (d) rGH-Ca in the simultaneous adsorption of MB and RhB

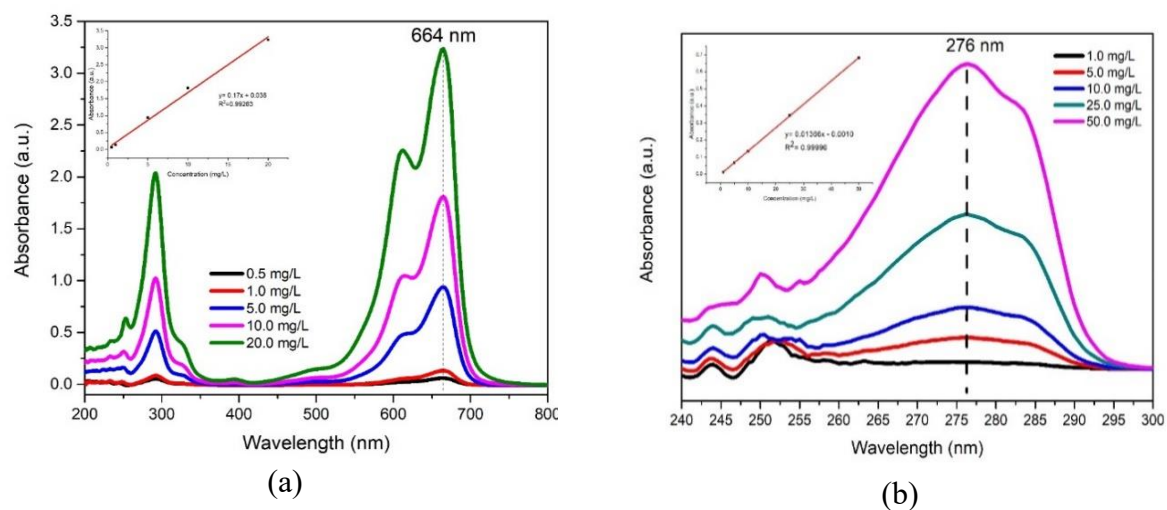


Fig. S4.1. UV-vis spectra of varying concentration of (a) BPA and (b) MB. *Inset.* Calibration curve of absorbance against concentration

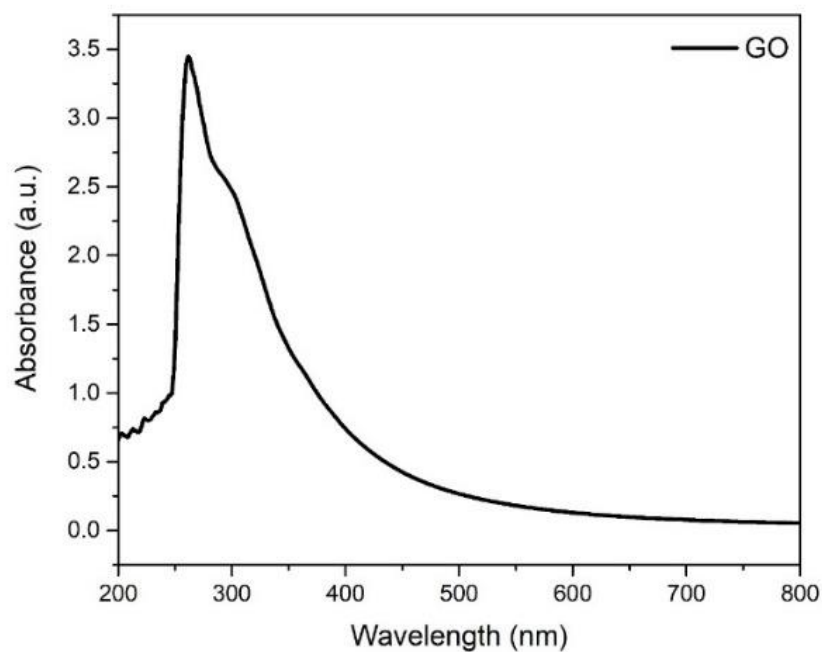


Fig. S4.2. UV-Vis spectrum of GO

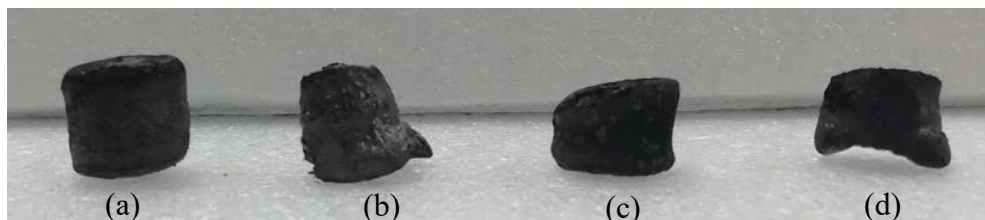


Fig. S4.3. Digital image of the freeze-dried hydrogel. (a) rGH, (b) rGH-OA, (c) rGH-DA and (d) rGH-DDA

Table S4.1. Specific surface area and texture properties of the reduced graphene samples obtained using BET and BJH analysis, respectively

Sample	Specific surface area (m ² /g)	Pore radius (nm)	Pore volume (cc/g)
rGH	12.125	1.981	0.069
rGH-OA	17.693	1.971	0.140
rGH-DA	20.220	1.717	0.193
rGH-DDA	16.688	1.968	0.125

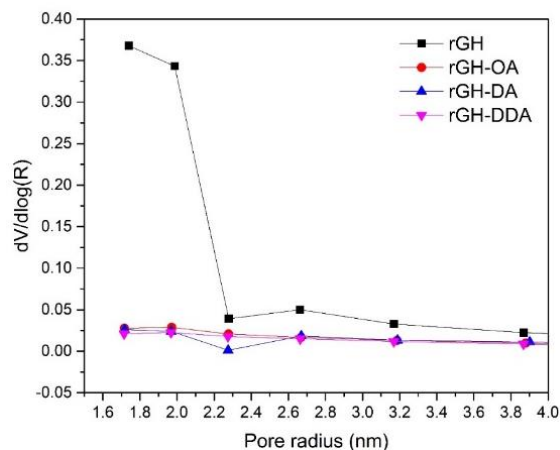


Fig S4.4. Pore size distribution of the freeze-dried hydrogels

Table S4.2. Chemical bonding and atomic percentage obtained from the high resolution C1s spectra of the hydrogels

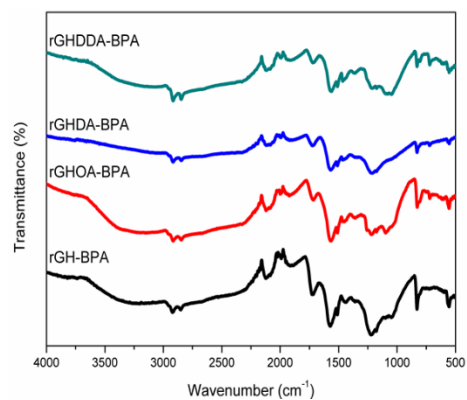
Sample	Binding energy	Bond assignment	Atomic (%)
rGH-OA	284.3	C-C/C=C	59.72
	285.5	C-N	16.85
	286.3	C-O	10.70
	287.6	C=O	6.83
	289.1	O-C=O	5.90
rGH-DA	284.5	C-C/C=C	60.81
	285.7	C-N	16.92
	286.5	C-O	11.46
	287.8	C=O	5.97
	289.3	O-C=O	4.84
rGH-DDA	284.6	C-C/C=C	55.85
	285.8	C-N	23.44
	286.6	C-O	9.13
	287.9	C=O	5.52
	289.4	O-C=O	6.06
rGH	284.6	C-C/C=C	57.00
	285.8	C-O	31.55
	287.9	C=O	6.13
	289.2	O-C=O	5.32

Table S4.3. Fitted kinetic parameters for the BPA adsorption onto the hydrogels

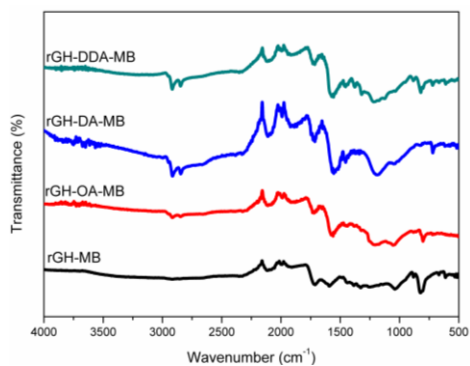
Sample	Pseudo-First Order Model			Pseudo-Second Order Model		
	Q _e	K ₁	R ²	Q _e	K ₂	R ²
rGH	181.70	0.000818	0.95502	180.18	0.00000714	0.96564
rGH-OA	184.81	0.000651	0.93341	179.86	0.00000938	0.95981
rGH-DA	261.54	0.000707	0.89667	546.45	0.00000433	0.90726
rGH-DDA	130.42	0.000472	0.90842	134.05	0.00001425	0.96645

Table S4.4. Fitted kinetic parameters for the MB adsorption onto the hydrogels

Sample	Pseudo-First Order Model			Pseudo-Second Order Model		
	Q _e	K ₁	R ²	Q _e	K ₂	R ²
rGH	122.87	0.000342	0.948	283.29	0.0000371	0.99283
rGH-OA	91.80	0.000465	0.93546	381.68	0.0000378	0.99658
rGH-DA	104.76	0.000327	0.89145	454.55	0.0000395	0.99685
rGH-DDA	67.32	0.000465	0.93547	280.11	0.0000514	0.99658



(a)



(b)

Fig S4.5. FTIR spectrum of the hydrogel after the adsorption of (a) BPA and (b) MB

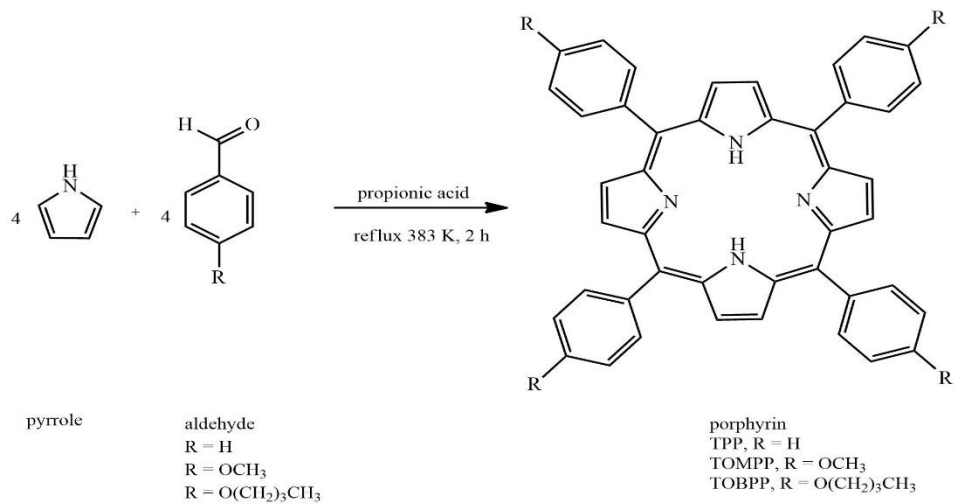
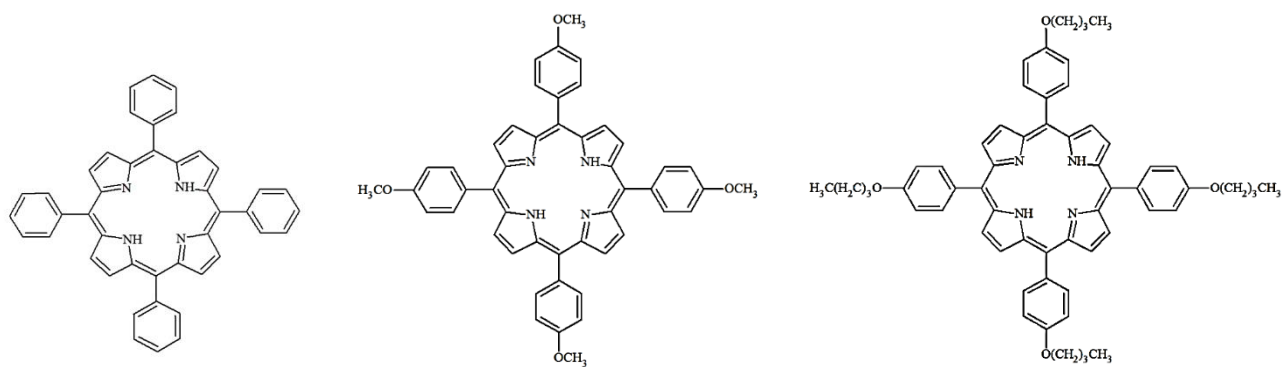


Fig. S5.1. General scheme for the synthesis of the porphyrin complexes.



(a) Tetraphenylporphyrin
(TPP)

(b) Tetrakis(4-
methoxyphenyl)phenylporphyrin

(c) Tetrakis(4-
butyloxyphenyl)phenylporphyrin

Fig. S5.2. Structure of (a) TPP (b) TOMPP and (c) TOBPP

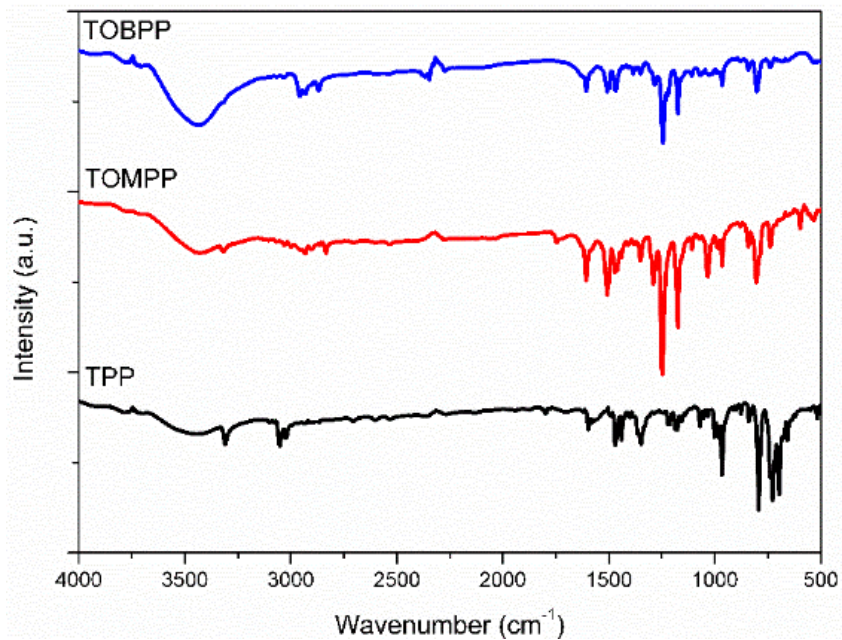
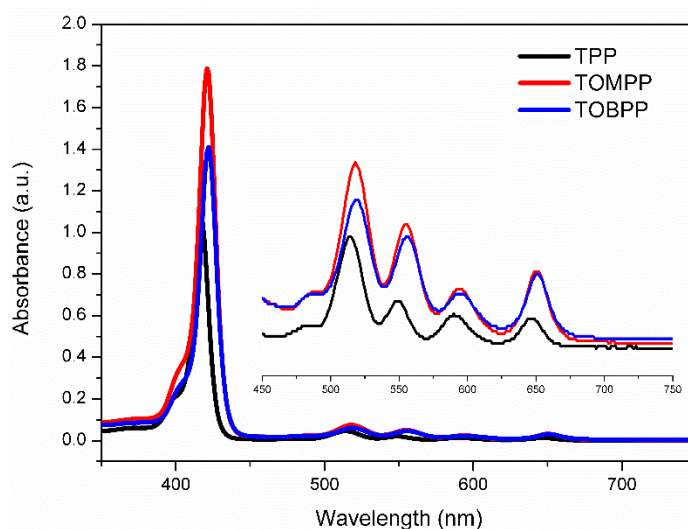


Fig. S5.3. FT-IR spectrum of TPP, TOMPP and TOBPP

Table S5.1. FT-IR data of free base porphyrin complexes.

Compounds	N-H str. in porphyrin	C-H str. in phenyl and long chain	C=C str. in phenyl	C-N str. in porphyrin	C-O str. in long chain	N-H bend in porphyrin	C-H bend in porphyrin
TPP	3310	-	1597, 1469	1212	-	966	794
TOMPP	3316	2931, 2834	1607, 1509	1248	1174	966	804
TOBPP	3320	2931, 2868	1607, 1509	1245	1174	966	802

**Fig. S5.4.** The UV-Vis absorption spectra of TPP, TOMPP and TOBPP in CH₂Cl₂**Table S5.2.** The absorption data molar extinction coefficient (ϵ) of all compounds

Porphyrin	Dichloromethane ^a				
	S band (nm)	Q band (nm), ϵ (M ⁻¹ cm ⁻¹)			
		Q ₁	Q ₂	Q ₃	Q ₄
TPP	417	514, 14122	548, 6140	590, 4605	649, 3991
TOMPP	421	518, 11941	555, 8266	595, 3980	650, 5205
TOBPP	422	519, 22955	556, 17310	595, 8655	651, 11665

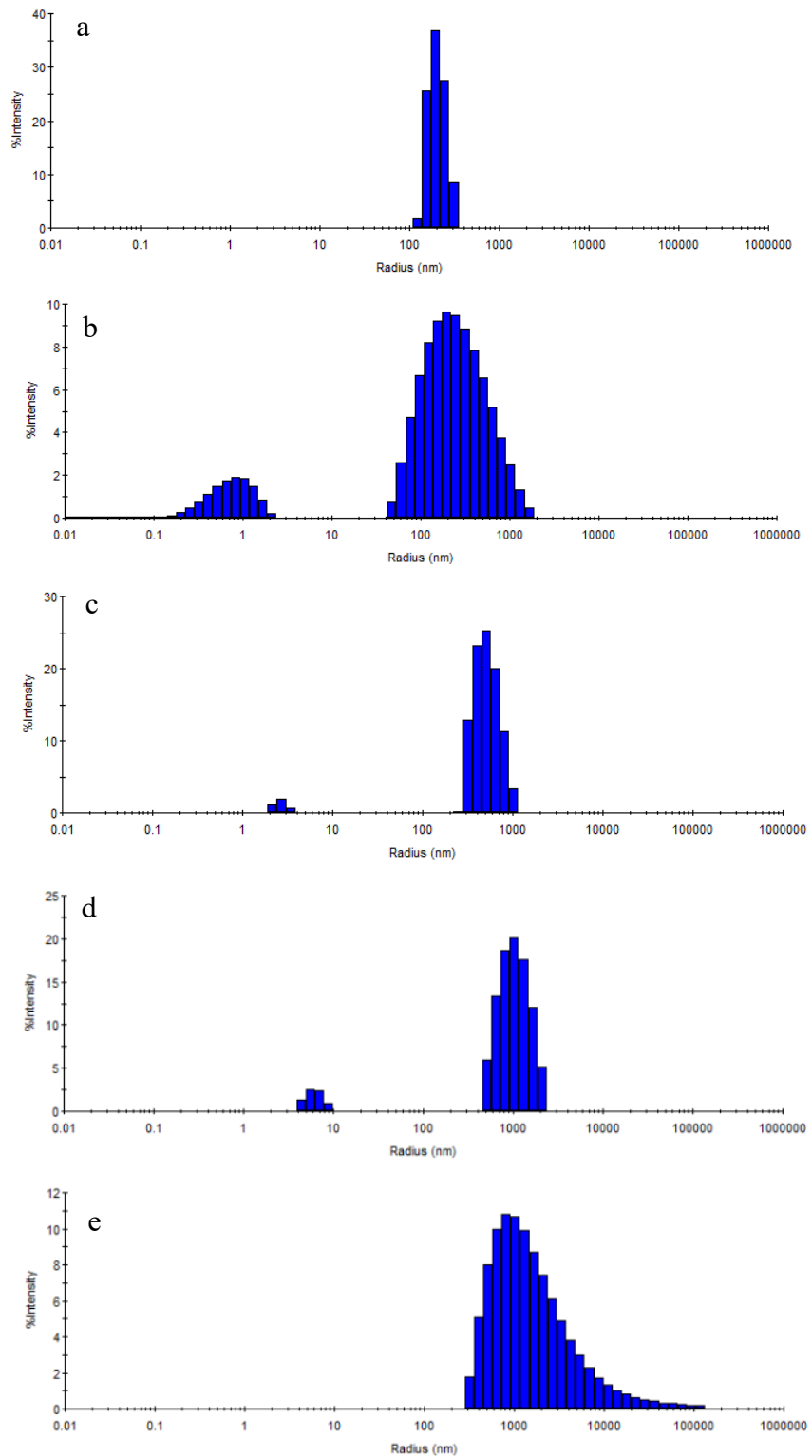


Fig. S5.5. Plot of Size distribution in scattering intensity as measured by DLS: (a) rGH, (b) Ag/rGH, (c) Ag/TPP/rGH, (d) Ag/TOMPP/rGH and (e) Ag/TOBPP/rGH

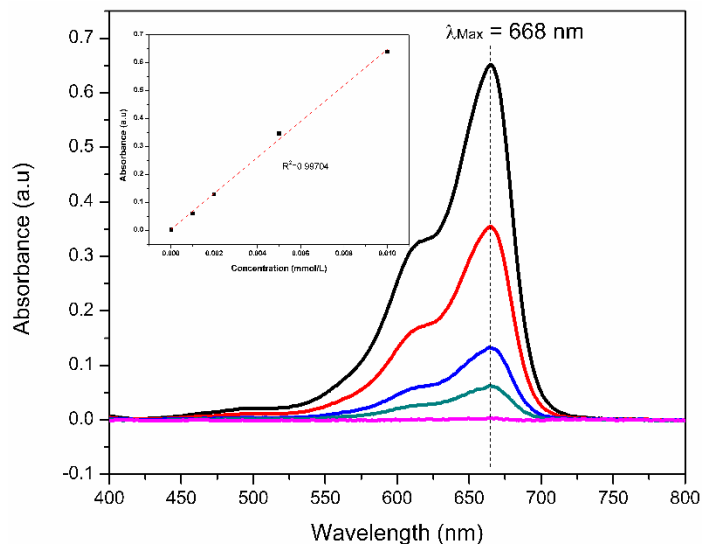
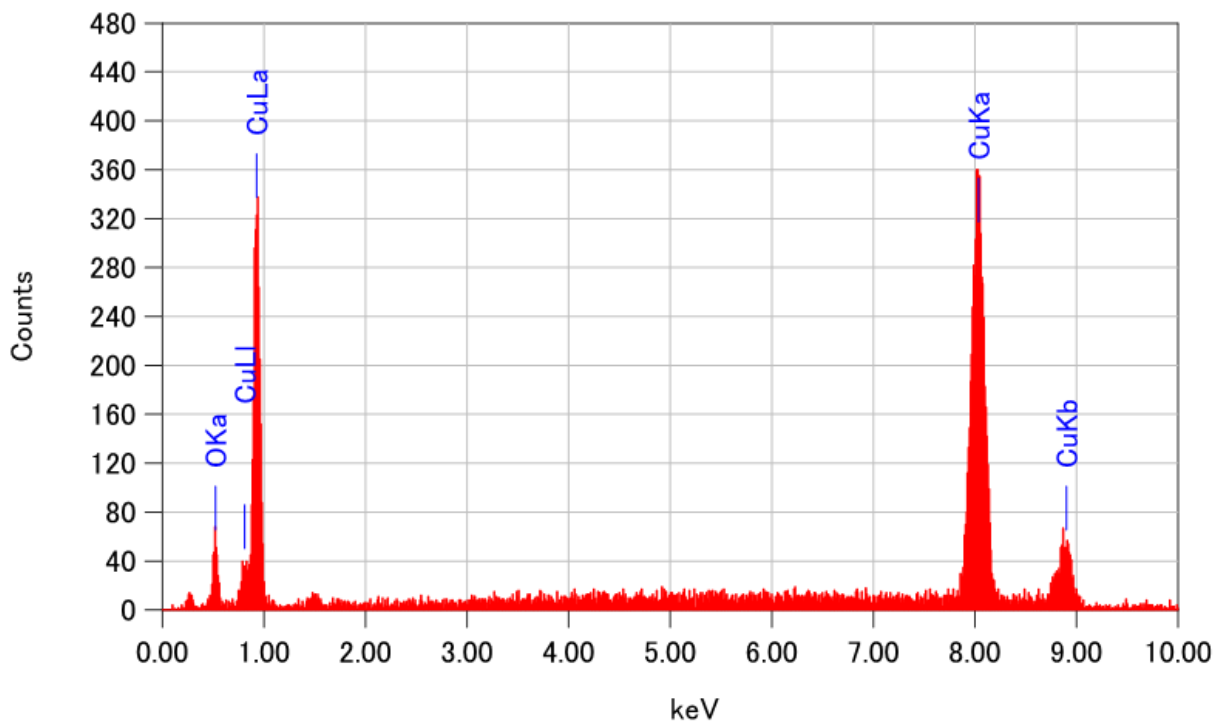


Fig. S5.6. UV -Vis spectrum of methylene blue at concentration range from 0.01 mg/L to 20 mg/L at room temperature. *Inset:* Standard curve for the adsorption of MB onto hydrogels

Table S5.3. Kinetic parameters for the adsorption of MB at 298 K

Sample	Pseudo-First Order Model			Pseudo-Second Order Model		
	Q_e	K_1	R^2	Q_e	K_2	R^2
rGH	73.77	0.0021082	0.95808	92.00	0.00002798	0.97156
Ag/rGH	100.05	0.0021572	0.95102	122.85	0.00002078	0.96864
Ag/TPP/rGH	69.57	0.0034545	0.97752	138.89	0.00008422	0.99970
Ag/TOMPP/rGH	85.83	0.0024412	0.95630	115.47	0.00004052	0.99083
Ag/TOBPP/rGH	104.32	0.0025563	0.98755	142.45	0.00003252	0.99688



ZAF法 簡易定量分析

フィッティング係数 : 0.1117

元素	(keV)	質量%	σ	原子数%	化合物	質量%	カチオン数	K
O K	0.525	3.29	0.15	11.90				1.6645
Cu K	8.040	96.71	1.46	88.10				98.3355
合計		100.00		100.00				

Fig S6.1. EDX analysis of the as-prepared Cu₂O nanospheres

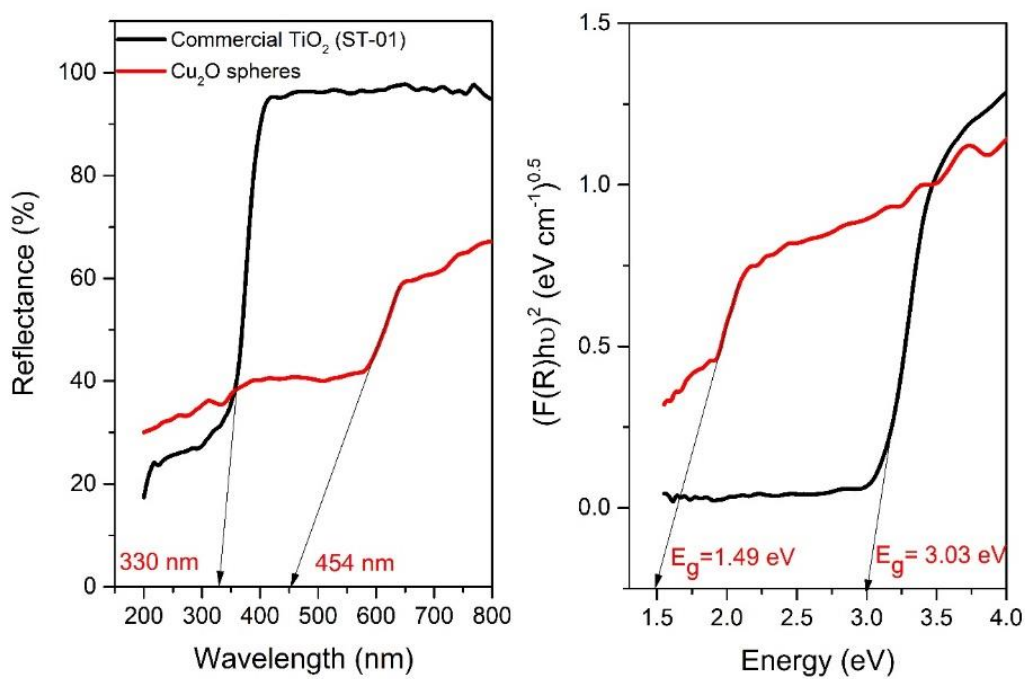


Fig S6.2. (a) UV-DRS absorption spectra and (b) Tauc plots of the TiO₂ and Cu₂O spheres

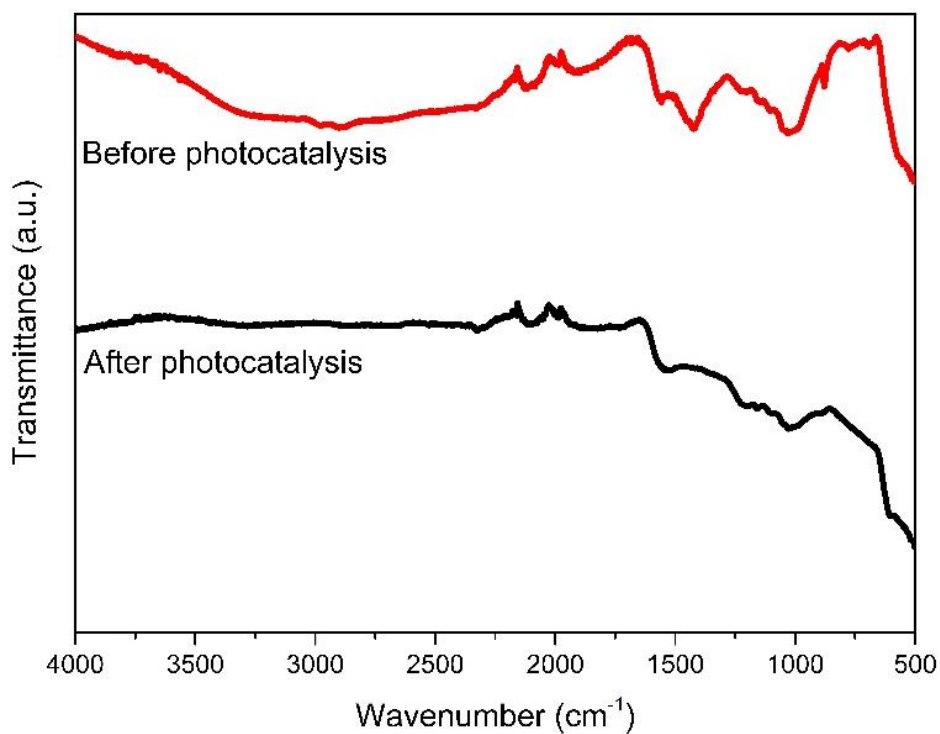


Fig S6.3. FTIR spectrum of the Cu₂O/TiO₂/CNF/rGH before and after the photocatalytic degradation of MO

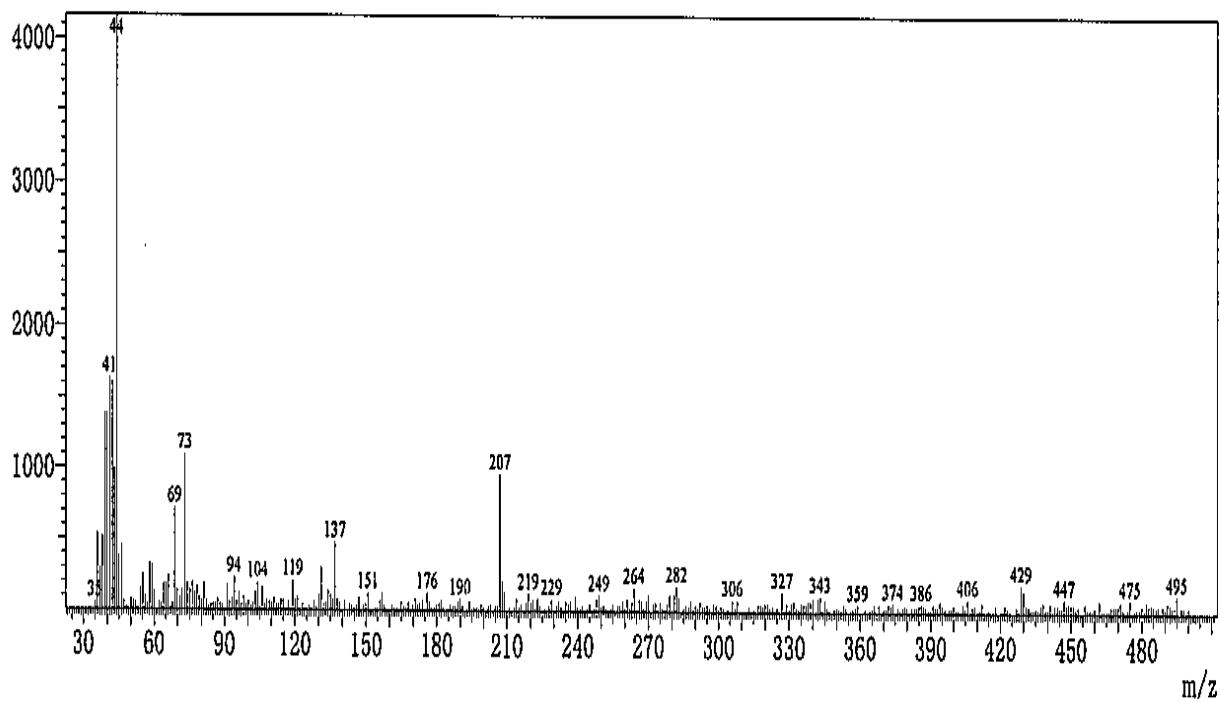


Fig S6.4. MS spectrum of MO solution using GC-MS after 2 h of irradiation.

LIST OF ACHIEVEMENTS

Publications related to the thesis

Refereed Journal Articles:

1. **A.L.T. Zheng**, T. Phromsatit, S.Boonyuen, Y. Andou (2020). Synthesis of silver nanoparticles /porphyrin/reduced graphene oxide hydrogel as dye adsorbent for wastewater treatment, *FlatChem* 23,10764. <https://doi.org/10.1016/j.flatc.2020.100174>. **JCR- IF:5.227**
2. **A.L.T. Zheng**, S. Boonyuen, T. Ohno, Y. Andou (2021). Hydrothermally Reduced Graphene Hydrogel Intercalated with Divalent Ions for Dye Adsorption Studies. *Processes* 9, 169, <https://doi.org/10.3390/pr9010169>. **JCR- IF: 2.847**
3. **A.L.T. Zheng**, S. Boonyuen, T. Ohno, Y. Andou (2021). Accessing the physical and chemical changes of hydrothermally reduced graphene hydrogel in the presence of aliphatic dicarboxylic acid, *Journal of Porous Materials*. <https://doi.org/10.1007/s10934-021-01072-6> **JCR-IF: 2.496**
4. **A.L.T. Zheng**, Y. Andou (2021). Detection and remediation of bisphenol-A (BPA) using graphene-based materials: mini-review, *International Journal of Environmental Science and Technology* <https://doi.org/10.1007/s13762-021-03512-x> **JCR-IF: 2.860**
5. A.L.T. Zheng, Y.L. Gan, H.N Lim, S. Boonyuen, Y. Andou (2021). Design of reduced graphene hydrogel with alkylamine surface functionalization through immersion/agitation method and its adsorption mechanism, *Journal of Molecular Structure*. <https://doi.org/10.1016/j.molstruc.2021.131008> **JCR-IF: 3.196**
6. **A.L.T. Zheng**, S. Sabidi, T. Ohno, T. Maeda, Y. Andou (2021). Low-temperature surfactant-free hydrothermal synthesis of Cu₂O/TiO₂ decorated on cellulose nanofiber/reduced graphene hydrogel for enhanced photocatalytic activity and its antibacterial applications, *Chemosphere*. 286 (2) 131731. <https://doi.org/10.1016/j.chemosphere.2021.131731> **JCR-IF: 7.086**

Refereed Book Chapters:

1. **A.L.T. Zheng**, C.A Che Abdullah, Y. Andou (2021). Graphene-based nanomaterials for water-remediation applications. Handbook of Green and Sustainable Nanotechnology, Springer Publications **(Accepted)**

2. **A.L.T. Zheng**, T. Ohno, Y. Andou (2021). Hybrid three-dimensional graphene architectures for photocatalytic degradation of noxious pollutants. *Green Nanoarchitectonics*, Jenny Stanford Publisher, Routledge & CRC Press (**Under Review**)

Publications not related to the thesis

1. G.E. Lau, C.A Che Abdullah, W.A.N. Wan Ahmad, S. Assaw, **A.L.T. Zheng** (2020). Eco-Friendly Photocatalysts for Degradation of Dyes. *Catalysts* 10, 1129. <https://doi.org/10.3390/catal10101129>
JCR-IF: 4.146
2. R.M. Zawawi, **A.L.T. Zheng** (2020). Zinc oxide/vancomycin-based electrochemical chiral sensor for the recognition of penicillamine enantiomers, *International Journal of Electrochemical Science* 15 (2020) 3255 – 3267. <https://doi:10.20964/2020.04.39> **JCR-IF: 1.765**
3. **A.L.T. Zheng**, H. N. Farrag, S. Sabidi, T. Kato, T. Maeda, Y. Andou (2021). Accessing the anti-microbial activity of cyclic peptide immobilized on reduced graphene oxide. *Materials Letters*. **304**, **130621**
<https://doi.org/10.1016/j.matlet.2021.130621> **JCR-IF: 3.423**
4. **A.L.T. Zheng**, S. Boonyuen, T. Ohno, Y. Andou (2021). Recent progress in visible light doped ZnO photocatalyst in photodegradation applications. *Environmental Nanotechnology, Monitoring and Management*. (**Submitted**)

Presentation at Academic Conferences and Symposiums

1. **A.L.T. Zheng**, T. Ohno, Y. Andou (2021). Cu₂O/TiO₂ orientate on CNF/reduced graphene hydrogel template for improved photocatalytic degradation. ACS Fall 2021. Atlanta, 22 – 26 August 2021 (Oral)
2. **A.L.T. Zheng**, & Y. Andou (2021). N-doped graphene nanoplatelets/reduced graphene hydrogel (N-GNP/rGH): Preparation and physicochemical analysis. 12th International Fundamental Science Congress (IFSC). Universiti Putra Malaysia, 26-28 August 2021 (Oral)
3. **A.L.T. Zheng**, & Y. Andou, “Preparation of photo-solidification electrically conductive polymer using graphene” 70th SPSJ Meeting Annual Meeting. Nagoya Congress Center, 26 May 2021 (Poster)
4. **A.L.T. Zheng**, H. N. Farrag, T. Kato, Y. Andou, “Novel cyclic undecapeptides immobilized on reduced graphene oxide surface for antibacterial applications” International Summits and Conference on

Materials Science, Nanotechnology & Bio-Manufacturing (ISCMNB' 2021), IKBN Sepang, 25 May 2021
(Oral)- *Best Invited Short Lecture Award*

5. S. Jongpuarkklang, P. Nongharn, M. Kandiah, **A.L.T. Zheng**, Y. Andou, P. Arpornmaeklong, S.Boonyuen, "One-Pot Synthesis of Gold Nanocatalyst Using Crude Oroxyllum Indicum". The 21st International Union of Materials Research Societies-International Conference in Asia (IUMRS-ICA 2020), Chiang Mai University, Thailand, 25 February 2021 (Poster)
6. **A.L.T. Zheng**, T. Maeda & Y. Andou, "Facile fabrication of 3D Cu₂O/TiO₂/cellulose nanofiber-reduced graphene aerogel with enhanced photocatalytic activity" 6th International Conference on Nanoscience and Nanotechnology (ICONN). SRM Institute of Science and Technology, 3 February 2021 (Oral)
7. **A.L.T. Zheng**, & Y. Andou, "Effect of Chain Length of Aliphatic Dicarboxylic Acid on Hydrothermally Reduced Graphene Hydrogels" 7th International Symposium on Applied Engineering and Sciences (SAES2020). Universiti Putra Malaysia, December 2020 (Oral)
8. **A.L.T. Zheng**, & Y. Andou, "Facile nitrogen doping using alkylamine on reduced graphene hydrogel for improved adsorption of wastewater pollutants" 3rd World Congress on Nanomaterials. August 28-29, 2020. (Oral)
9. **A.L.T. Zheng**, T. Phromsatit., S. Boonyuen., & Y. Andou, "Facile One-pot Synthesis of Silver nanoparticle /Porphyrin/Reduced Graphene Hydrogel via Hydrothermal Treatment: Preparation and Characterization" Pure and Applied Chemistry International Conference (PACCON) 2020. Impact Forum, Bangkok Thailand, 14 February 2020 (Oral)
10. **A.L.T. Zheng**, & Y. Andou, "Facile Synthesis and Characterization of Alkylamine-Functionalized Reduced Graphene Hydrogel" 18th Asian Chemical Congress 2019. Taipei International Convention Center, Taipei, December 2019 (Poster)- *Top 10 in the 'Best of Best Competition'*
11. **A.L.T. Zheng**, Ohno, T & Y. Andou, "Effect of Chain Length of Aliphatic Dicarboxylic Acid on Hydrothermally Reduced Graphene Hydrogels" 7th International Symposium on Applied Engineering and Sciences (SAES2019). Universiti Putra Malaysia, November 2019 (Oral)
12. **A.L.T. Zheng**, & Y. Andou, "Hydrothermally Reduced Graphene Hydrogel-Divalent Metal Carbonates as Efficient Dye Adsorbents for Methylene Blue" 55th Kyushu Area Joint Meeting of the Chemistry-Related Societies. Kitakyushu International Conference Centre, July 2019 (Poster)

BIOGRAPHY

Alvin Lim Teik Zheng was born on 29 October 1992 in Alor Setar, the capital of Kedah, Malaysia. He did his early education in Iskandar National School and his secondary education in Pokok Sena Science High School and Sultan Abdul Hamid College. In 2010, he gained admission into Universiti Putra Malaysia (UPM) for his foundation studies in the Centre of Foundation Studies for Agricultural Science (ASPER) before pursuing his Bachelor's in the same university under the Academician Special Scholarship (BKTA) program, Ministry of Higher Education, Malaysia. He did his internship stint in the State Department of Agriculture, Malaysia before his graduation. His work there mainly focused on conducting physicochemical analysis (Organic C, total N, C/N ratio, available phosphorus, pH, and electrical conductivity) of soil and leaf samples. He also participated in the International Field Science Course at Kochi University, Japan.

He decided to pursue his Masters's degree (Analytical Chemistry) under the MyBrainSc scholarship, Ministry of Higher Education, Malaysia, and Graduate Research Fund (GRF) in the same university. In the duration of his studies, he served as laboratory instructors for undergraduate courses such as Inorganic and Physical Chemistry (CHM 3010) and Inorganic Chemistry 1 (CHM 3301) in the Department of Chemistry. His Masters' dissertation is on sensor development for chiral molecules using ZnO nanoparticles under the supervision of Dr. Ruzniza Zawawi. He briefly joined the Short Term Exchange Program (Research Collaboration), Japan Student Services Organization (JASSO). His short-term project focused on biodegradable polymer from waste materials under guidance of Associate Professor Dr. Yoshito Andou. After he completed his Masters's degree program, he briefly served in the same university as an administrative officer in the Student Affairs Division.

He continued his doctoral degree studies under the Monbukagakusho (MEXT) Scholarship, Japan in the Graduate School of Life Science and Systems Engineering, Kyushu Institute of Technology in Andou Research Group. His Ph.D. studies mainly focused on three-dimensional graphene architectures for wastewater remediation. He carried out his brief internship stint in the Department of Chemistry, Faculty of Science and Technology, Thammasat University under the guidance of Associate Professor Dr. Supakorn Boonyuen during his Ph.D. studies. His work mainly focused on the green synthesis and characterizations of metal nanoparticles and porphyrin-based complexes. He has participated in numerous national and international conferences to share the findings of his work. His notable achievement was when he was

crowned the 'Best of Best' in the oral presentation in the Asian Chemical Congress 2018, Taiwan. He is actively seeking opportunities and possibilities to further improve himself as a researcher. He hoped to be a great educator and researcher for the benefit of his nation, MALAYSIA.